

See discussions, stats, and author profiles for this publication at: <https://www.researchgate.net/publication/253418363>

# Cellular pattern formation

Article · January 1998

---

CITATIONS

9

READS

136

1 author:



Yi Jiang

Georgia State University

195 PUBLICATIONS 4,302 CITATIONS

SEE PROFILE

CELLULAR PATTERN FORMATION

A Dissertation

Submitted to the Graduate School  
of the University of Notre Dame  
in Partial Fulfillment of the Requirements  
for the Degree of

Doctor of Philosophy

by

Yi Jiang, B.S.

---

James A. Glazier, Director

Department of Physics

Notre Dame, Indiana

August 1998

© Copyright by

Yi Jiang

1998

All rights reserved

# CELLULAR PATTERN FORMATION

Abstract

by

Yi Jiang

This thesis studies the formation and evolution of cellular patterns in foams and living organisms using the extended large- $Q$  Potts model. Specific problems include grain growth, foam drainage, foam rheology, and patterning and cell sorting in the mound phase of the slime mold *Dictyostelium discoideum*.

In a wide range of cellular materials, surface-energy-driven diffusion leads to boundary motion which causes some grains to expand and others to shrink. Two-dimensional large- $Q$  Potts model simulation of the evolution of a disordered cluster developed from a hexagonal grain array with a defect shows that abnormal grain growth can occur without strong anisotropy of surface energy. The grains at the boundary of the disordered cluster reach a special scaling state with no scale change.

In three-dimensional liquid foams, drainage occurs due to gravity. Large- $Q$  Potts model simulations, extended to include gravity in three dimensions, agree with both experimental and analytical results for various kinds of foam drainage, and also predict new phenomena.

Foams exhibit a unique rheological transition from solid-like to fluid-like. Simulations using the large- $Q$  Potts model, extended to apply shear to a two-dimensional foam, show three different types of hysteresis in foam's stress-strain relationship, which correspond to the elastic, viscoelastic and viscous fluid properties. This wide-ranging mechanical response depends on the structure and dynamics of local topo-

logical rearrangement of foam cells.

Biological tissues resemble foams and the large- $Q$  Potts model can also simulate sorting in biological cell aggregates. In *Dictyostelium* mound, two types of cells are initially randomly distributed. In time, one cell type sorts to form a tip. Simulations show that both differential adhesion and chemotaxis are required for sorted tip formation. With only differential adhesion, no tip forms. With only chemotaxis, a tip forms containing both cell types. Thus simulations can provide a method to determine the processes necessary for biological patterning.

## CONTENTS

FIGURES . . . . .	iv
CHAPTER 1: SUMMARY . . . . .	1
CHAPTER 2: INTRODUCTION . . . . .	5
2.1 Overview . . . . .	5
2.2 Dynamics of Cellular Patterns . . . . .	9
CHAPTER 3: POTTS MODEL . . . . .	16
3.1 Introduction . . . . .	16
3.1.1 Overview . . . . .	16
3.1.2 Original Potts Model For Grain Growth . . . . .	17
3.1.3 Small- $Q$ Simulations . . . . .	20
3.1.4 Lattice Anisotropy . . . . .	22
3.1.5 Algorithms . . . . .	26
3.2 Extensions . . . . .	27
3.2.1 Interaction Between Spins . . . . .	27
3.2.2 Coupling to an External Field . . . . .	31
3.2.3 Constraints . . . . .	33
CHAPTER 4: GRAIN GROWTH . . . . .	38
4.1 Background . . . . .	38
4.2 Mean Field Theories . . . . .	48
4.3 Abnormal Grain Growth . . . . .	52
4.4 Defect Growth . . . . .	56
4.5 Bamboo Formation . . . . .	66
4.6 Grain Growth in Three Dimensions . . . . .	71
CHAPTER 5: FOAM DRAINAGE . . . . .	76
5.1 Introduction . . . . .	76
5.2 Experiments . . . . .	80
5.3 Theory . . . . .	82
5.3.1 Forced Drainage . . . . .	88
5.3.2 Free Drainage . . . . .	90

5.3.3 Pulsed Drainage . . . . .	91
5.4 Simulations . . . . .	93
CHAPTER 6: FOAM RHEOLOGY . . . . . 101	
6.1 Introduction . . . . .	101
6.1.1 Background . . . . .	101
6.1.2 Overview . . . . .	103
6.2 Model . . . . .	109
6.3 Hysteresis . . . . .	114
6.3.1 Ordered Foams . . . . .	116
6.3.2 Disordered Foams . . . . .	127
6.4 T1 Avalanches . . . . .	131
6.5 Structural Disorder . . . . .	139
6.6 Effective Foam Viscosity . . . . .	147
6.7 Conclusions . . . . .	149
CHAPTER 7: CELL SORTING . . . . . 153	
7.1 Introduction . . . . .	153
7.2 <i>Dictyostelium</i> . . . . .	154
7.3 Differential Adhesion . . . . .	157
7.3.1 Experiments . . . . .	157
7.3.2 Model . . . . .	158
7.4 Chemotaxis . . . . .	165
7.4.1 Experiments . . . . .	166
7.4.2 Models . . . . .	168
7.5 <i>Dictyostelium</i> Mound Formation . . . . .	169
7.5.1 Experiments . . . . .	169
7.5.2 A Model of <i>Dictyostelium</i> . . . . .	171
7.5.3 Simulation Results . . . . .	177
7.6 Cellular Automata . . . . .	191
CHAPTER 8: CONCLUSIONS AND OUTLOOK . . . . . 195	
8.1 Grain Growth . . . . .	195
8.2 Foam Drainage . . . . .	196
8.3 Foam Rheology . . . . .	198
8.4 Cell Sorting . . . . .	199

## FIGURES

<p>2.1 Photograph of soap bubbles confined between two glass plates: a typical two-dimensional cellular pattern in a quasi-static equilibrium with three-fold vertices and <math>120^\circ</math> contact angles. Walls curve due to the pressure difference between adjacent cells. . . . .</p> <p>2.2 A four-fold vertex decays into two three-fold vertices because the total boundary length decreases. . . . .</p> <p>2.3 A dragonfly's wing, top, can be mimicked by two-dimensional soap films in a suitable frame (thick lines), bottom. Notice that the walls form <math>90^\circ</math> angles with the frame but meet at <math>120^\circ</math> angles among themselves. [From Hildebrandt and Tromba [29]]. . . . .</p> <p>3.1 Schematic of a two-dimensional cellular pattern represented in the large-<math>Q</math> Potts model. Numbers show different spin values. Heavy black lines indicate grain boundaries. . . . .</p> <p>3.2 Snapshots of the patterns in Potts model simulations on a triangular lattice at low <math>T</math> for: (a) <math>Q = 3</math>, (b) <math>Q = 6</math>, (c) <math>Q = 12</math>, and (d) <math>Q = 64</math>. [From Anderson <i>et al.</i> [44]]. . . . .</p> <p>3.3 Wulff plots of lattice anisotropy in two dimensions: (a) sq-1 [11], (b) sq-2 [11], (c) sq-3, (d) sq-4 correspond to nearest, 2nd nearest, 3rd nearest, and 4th nearest neighbors on a square lattice; (e) tr-1 [39], (f) tr-2 correspond to nearest and 2nd nearest neighbors on a triangular lattice, respectively. . . . .</p> <p>3.4 Asymmetric coupling strength in the Potts model: <math>\mathcal{J}_{12} \neq \mathcal{J}_{21}</math>. Case (a) corresponds to cell-2 expanding into cell-1. Case (b) corresponds to cell-1 expanding into cell-2. <math>\Delta\mathcal{H}</math> is the energy difference after the spin flip. . . . .</p> <p>3.5 Effect of an external gravitational field in the Potts model. Spin 1 is a liquid subject to gravity and spin 2 is a gas. <math>z</math> is the height of the spins. <math>\Delta\mathcal{H}</math> is the energy difference after the spin flip. . . . .</p> <p>3.6 Energy sketch for the volume constraint. The solid line is the quadratic volume constraint. The dotted line is the linear surface energy term. . . . .</p>	<p>6</p> <p>10</p> <p>13</p> <p>18</p> <p>21</p> <p>23</p> <p>29</p> <p>32</p> <p>35</p>
---	--

4.1	Crystal morphology of a cross section of a low-carbon alloy steel ( $10\%Cr - 2.6\%Si - 0.35\%Al$ ), with average grain size $10^{-2}cm$ . Arrows indicate some non-equilibrium features of the pattern. [From Nagai, Kawasaki and Nakamura [70]]. . . . .	44
4.2	T1 process: the wall between bubbles <b>b</b> and <b>d</b> disappears and a new wall forms between bubble <b>a</b> and <b>c</b> . Bubbles <b>a</b> and <b>c</b> become neighbors and both gain one side. . . . .	44
4.3	T2 processes: disappearance of a triangle, a square and a pentagon. . . . .	45
4.4	Topological distribution functions for a two-dimensional soap foam [11], an aluminum foil [26] and a Potts model simulation on a nearest-neighbor triangular lattice [84]. . . . .	46
4.5	Potts model simulations of pinned microstructures for four pinning particle concentrations. [From Srolovitz <i>et al.</i> [41]]. . . . .	54
4.6	Schematic showing grain boundary curvature elimination. The vertex with three particle-pinned boundaries translates and rotates. The curved lines are the initial grain boundary shape and the dotted straight lines are the grain boundary configuration following the vertex translation and rotation. [Redrawn from Srolovitz <i>et al.</i> [41]]. . . .	54
4.7	Snapshots of the time evolution of an initially hexagonal pattern with a single defect: (a) 0 MCS, (b) 5000 MCS, (c) 10000 MCS. Figures show the center 1/4 of the whole pattern. . . . .	58
4.8	Evolution of the disordered cluster. The total area of the cluster ( $\circ$ ) grows quadratically while the number of grains in the cluster (*) grows linearly. . . . .	59
4.9	The second moment of $\rho(n)$ of the cluster ( $\mu_2$ , bullets) and the boundary ( $\mu'_2$ , circles). . . . .	60
4.10	Topological distribution, $\rho(n)$ , excluding the large center grain, averaged over six different times between 6000MCS and 10600MCS. Error bars indicate standard deviation from the mean. . . . .	61
4.11	Schematic illustration of the technique used to prepare a monolayer hexagonal foam. The monolayer foam is formed between the surface of a surfactant solution and a parallel glass plate above it. [Redrawn from Vaz and Fortes [101]]. . . . .	63
4.12	Pictures of a typical evolving foam containing an initial isolated larger bubble, constituting a topological defect: (a) $t = 0$ , (b) $t = 25h$ , (c) $t = 28h$ , (d) $t = 32h$ . [From Kader and Earnshaw [102]]. . . . .	63
4.13	Topological distributions for an evolving foam from a single defect: numbers show the number of sides of the center bubble ( $n_c$ ). The distributions omit the data points at $n_c$ . [From Kader and Earnshaw [102]]. . . . .	65

4.14	The large center grain in Potts model simulations becomes hexagonal when the initial hexagons align with the underlying square lattice. . .	65
4.15	Snapshots of the time evolution of a defect in a hexagonal pattern rotated by $45^\circ$ with respect to the underlying square lattice. Numbers indicate time in MCS. . . . .	67
4.16	Evolution of grains with strip width $w = 3.0$ (initial average grain size 1.0). $\tau$ is simulation time in arbitrary units. By $\tau = 0.2$ some grains traverse the width and the strip breaks into clusters. Eventually the clusters develop into bamboo. [From Walton <i>et al.</i> [104]]. . . . .	68
4.17	A two-dimensional foam experiment on bamboo formation in a ring: (a) $t = 0$ , (b) $t = 24h$ , (c) $t = 180h$ , (d) $t = 200h$ . Diameters of the rings are 63.9mm and 71.8mm. The width of the ring is 7.9mm. [From Rosa and Fortes [111]]. . . . .	70
4.18	A three dimensional MRI image of foam obtained using the 14 Tesla MRI at the NHMFL, FL. The voxel resolution is $86\mu m$ and the height of the foam is 10mm. The line in the center of the tube is an artifact of the image reconstruction algorithm. [Courtesy of B. Prause]. . . . .	74
5.1	A three-dimensional standing foam: liquid drains and accumulates at the bottom of the foam. Bubbles closer to the bottom contain more liquid, with thicker films and Plateau borders. [Courtesy of B. Prause].	77
5.2	A Plateau border in three dimensions. [From Weaire and Pittet [135]].	78
5.3	Liquid density profiles from segmented AC capacitance measurements. The $x$ -axis covers a range of 70cm. Left (right) corresponds to the top (bottom) position of the standing foam, but does not include the top and the bottom of the foam. (a) Forced drainage in an initially dry foam: a solitary wave moves at constant velocity downward; (b) Free drainage: initially homogeneously distributed liquid drains when the liquid input stops. (c) Pulsed drainage: a fixed amount of liquid travels down into an initially dry foam. The pulse decays and spreads. [Courtesy of D. Weaire. After Hutzler <i>et al.</i> [139]]. . . . .	83
5.4	Liquid profiles for free drainage (MRI experiment data). . . . .	84
5.5	Cross section of an ideal Plateau border channel. . . . .	86
5.6	A solitary wave travels down the foam - solution given by Equation 5.11. At the left side (top of the foam) the liquid fraction tends to a constant, corresponding to a wet foam. At the right side (bottom of the foam) the liquid fraction is zero, corresponding to a dry foam. The interface between wet and dry foams is sharp. [Redrawn from Weaire <i>et al.</i> [129]]. . . . . .	89
5.7	Sketched evolution of the liquid profile for free drainage. [From Verbiest <i>et al.</i> [131]]. . . . . .	92

5.8	Liquid profiles for simulated free drainage in a three-dimensional foam. Arrow indicates the direction of time. . . . .	94
5.9	Liquid profiles for simulated pulsed drainage in a three-dimensional foam <i>vs.</i> time (MCS). The leading fronts of the traveling pulse are fitted with the traveling wave solution, Equation 5.11, at 4000 MCS and 6000 MCS (*). . . . .	96
5.10	Snapshots of vertical cross sections of simulated pulsed drainage in a three-dimensional foam: (a) 3000 MCS, (b) 8000 MCS, (c) 12000 MCS. . . . .	97
5.11	Liquid profiles for simulated forced drainage in an initially dry three-dimensional foam. The interval between each profile is 200 MCS. . . . .	98
5.12	Liquid profiles for simulated forced drainage in an initially wet three-dimensional foam. The interval between each profile is 200 MCS. . . . .	99
5.13	Snapshot of drainage in a simulated disordered foam, showing a vertical cross section of a three-dimensional standing foam. . . . .	100
6.1	Schematic illustration of the stress-strain diagram of a liquid foam. . . . .	104
6.2	Princen-Prud'homme model showing the strain dependence of bubble morphology for simple shear with initial hexagon orientation at zero. (a) Undeformed equilibrium network: strain $\epsilon = 0$ . (b) Strain $\epsilon = 1/\sqrt{3}$ . (c) Yield strain $\epsilon = 2/\sqrt{3}$ . (d) Relaxation, $\epsilon = 2/\sqrt{3}$ ; the foam recovers its initial equilibrium configuration but the bubbles have all undergone T1 processes [From Khan and Armstrong [164]]. . . . . .	104
6.3	Stress-strain curves for simple shear flow in ordered foams show periodic behavior. In Khan <i>et al.</i> 's notation, $\gamma$ is the applied strain, $\hat{\tau}_{xy}$ is the shear stress and $\hat{N}_1$ is the normal stress. Points (a)(b)(c)(d) correspond to the bubble morphologies in Figure 6.2 [From Khan and Armstrong [164]]. . . . . .	105
6.4	Schematic illustration of a Rheometric Mechanical Spectrometer (RMS7200). A foam sample is sandwiched between two parallel plates with both surfaces covered with sandpaper to avoid slippage. The top plate rotates at a constant angular velocity $\omega$ and the force/torque $T$ on the bottom plate is measured. [Redrawn from Khan <i>et al.</i> [173]]. . . . . .	108
6.5	Snapshots of an ordered foam under shear. Colors encode bubble topologies (lattice size $256 \times 256$ ): (a) boundary shear, (b) bulk shear (shear rate $\beta = 0.01$ ), (c) bulk shear (shear rate $\beta = 0.05$ ). Six-sided bubbles are blue, five-sided green and seven-sided yellow, four-sided (edge bubbles) are red. . . . .	117
6.6	Stress-strain curve for an ordered foam under steady boundary shear, corresponding to case (a) shown in Figure 6.5. The number of T1 events is histogrammed in 50 MCS bins. . . . .	118

6.7 Stress-strain curves for ordered foam under periodic boundary shear with $\mathcal{J}_{ij} = 3$ , $T = 0$ and $\alpha = 1.7 \times 10^{-3}$ . Numbers above the figures are $\gamma_0$ , the shear amplitude. Progressively increasing $\gamma_0$ leads to transitions among three types of hysteresis: $\gamma_0 = 1.0$ corresponds to elastic response, $\gamma_0 = 3.5$ shows viscoelastic response (before any T1 event occurs), $\gamma_0 = 7.0$ is a typical response when only one T1 event occurs during one cycle of strain loading. The intermediate steps show that the transition between these three types is smooth.	. 120
6.8 Stress-strain curves for ordered foam under periodic boundary shear with $\gamma_0 = 7$ , $T = 0$ and $\alpha = 1.7 \times 10^{-3}$ . Numbers above the figures are $\mathcal{J}_{ij}$ , which is inversely related to liquid viscosity. Progressively decreasing $\mathcal{J}_{ij}$ produces transitions from elastic ( $\mathcal{J}_{ij} = 10$ ), to viscoelastic ( $\mathcal{J}_{ij} = 5$ ) and to viscous flow due to T1 events. For $\mathcal{J}_{ij} = 3$ , all the edge bubbles undergo one T1 during half a strain cycle. For $\mathcal{J}_{ij} = 1$ , all the edge bubbles undergo three T1s during half a strain cycle.	. . . . . 121
6.9 Phase diagram of hysteresis in the parameter space $\gamma_0$ vs. $\mathcal{J}_{ij}$ , with $T = 0$ and $\alpha = 1.7 \times 10^{-3}$ .	. . . . . 122
6.10 Effect of progressively increasing temperature, $T$ ( $\mathcal{J}_{ij} = 3$ , $\gamma_0 = 4$ , and $\alpha = 1.7 \times 10^{-3}$ ). All data shown are averages over 10 periods.	. . . . . 123
6.11 Stress-strain curve for an ordered foam under bulk shear at shear rate $\beta = 0.01$ . The magnified view in the box shows the correlation between stress releases and individual avalanches of T1 events.	. . . . . 125
6.12 Stress-strain curve for an ordered foam under bulk shear at shear rate $\beta = 0.05$ . The magnified view in the box shows the correlation between stress releases and overlapping avalanches of T1 events.	. . . . . 126
6.13 Snapshots of a disordered foam under shear. Colors encode bubble topologies (lattice size $256 \times 256$ ): (a) boundary shear, (b) bulk shear.	. . . . . 128
6.14 Stress-strain curves for a disordered foam under steady boundary shear, corresponding to Figure 6.13(a).	. . . . . 129
6.15 Stress-strain curves for a disordered foam under steady bulk shear at shear rate $\beta = 0.01$ , corresponding to Figure 6.13(b).	. . . . . 130
6.16 Power spectra of the time series of the number of T1 events in an ordered foam for three shear rates, $\beta = 0.01, 0.02$ and $0.05$ , respectively.	. . . . . 134
6.17 Power spectra of the time series of the number of T1 events in a disordered foam ( $\mu_2(n) = 0.81, \mu_2(a) = 7.25$ ) for five shear rates $\beta$ from 0.001 to 0.05.	. . . . . 136
6.18 Power spectra of the time series of the number of T1 events in a very disordered foam ( $\mu_2(n) = 1.65, \mu_2(a) = 21.33$ ) for three shear rates.	. . . . . 137

6.19 Number of T1 events per unit shear per bubble, $\overline{N}$ , as a function of shear rate, $\beta$ , for four samples. Squares correspond to a foam of 180 bubbles, with $\mu_2(n) = 1.65$ , $\mu_2(a) = 21.33$ . Stars correspond to a foam of 246 bubbles with $\mu_2(n) = 1.72$ , $\mu_2(a) = 15.1$ . Triangles correspond to a foam of 377 bubbles, with $\mu_2(n) = 1.07$ , $\mu_2(a) = 2.50$ . Circles correspond to a foam of 380 bubbles, with $\mu_2(n) = 0.95$ , $\mu_2(a) = 2.35$ . The inset shows on a log-log scale that the $\overline{N}$ values differ by several orders of magnitude. . . . .	138
6.20 Power spectra of the energy for an ordered foam under steady bulk shear for three shear rates, $\beta = 0.01, 0.02$ , and $0.05$ . . . . .	140
6.21 Power spectra of the energy for a disordered foam [ $\mu_2(n) = 0.81$ , $\mu_2(a) = 7.25$ ] for five shear rates, $\beta = 0.001, 0.005, 0.01, 0.02$ , and $0.05$ . . . . .	141
6.22 Power spectra of the energy for a very disordered foam [ $\mu_2(N) = 1.65$ , $\mu_2(a) = 21.33$ ] for five shear rates, $\beta = 0.001, 0.005, 0.01, 0.02$ , and $0.05$ . . . . .	142
6.23 Yield strain as a function of shear rate. . . . .	144
6.24 Evolution of $\mu_2(n)$ under steady bulk shear. Legend denotes the initial $\mu_2(n)$ . . . . .	145
6.25 Evolution of $\mu_2(n)$ under steady simple shear for an ordered foam, showing the correlation between the stress decreases and $\mu_2(n)$ . . . . .	146
6.26 Schematic of the Kelvin Model for linear viscoelasticity. . . . .	147
6.27 Schematic of the generalized Kelvin model. . . . .	150
6.28 Terminal velocity as a function of density in simulations of dropping a “heavy bubble” through an ordered foam (lattice size $256 \times 256$ ). Simulation parameters are $T = 0$ , $\mathcal{J}_{ij} = 3$ , and $\Gamma = 1$ . The stars (*) and the circles (o) correspond to two different directions of the gravitational field with respect to the orientation of the hexagonal pattern. Straight lines are linear fits. . . . .	150
 7.1 Life cycle of <i>Dictyostelium</i> . The individual cells are about $10\mu\text{m}$ in diameter. The fruiting body is about $3\text{mm}$ high. Aggregation starts $6\text{h}$ after starvation; a tight mound forms at about $10\text{h}$ ; tip formation finishes by $12\text{h}$ ; culmination takes 6 hours from $18\text{h}$ to $24\text{h}$ [Courtesy of W. Loomis]. . . . .	156
7.2 Sorting of an aggregate of neural retinal (light) and pigmented retinal cells (dark) obtained from 10-day old chick embryos. (a) Aggregate $5\text{h}$ after mixing of dissociated cells. (b) After $10\text{h}$ , the neural retinal cells form an external layer. (c) After $72\text{h}$ , the neural retinal cells surround an internal dark core of pigmented retinal cells. [After Mombach <i>et al.</i> [207]]. . . . . .	159

7.3	Reconstitution of <i>Dictyostelium</i> pre-stalk and pre-spore cell aggregates. Pre-stalk and pre-spore cells were dissociated from the slug stage. After indicated times, pre-stalk cells first formed a cluster inside pre-spore cells (dark), then moved to the surface of the aggregate. Except for the aggregate at 2h, the aggregates were encased by slime sheath. [After Takeuchi <i>et al.</i> [209]. Copyright ©1988 John Wiley & Sons Inc., used by permission of Wiley-Liss, a division of John Wiley & Sons, Inc.]. . . . .	160
7.4	Schematic of spin change on a two-dimensional square lattice with fourth nearest neighbor interaction. . . . .	163
7.5	Potts model simulation of cell sorting with differential adhesion. Dark cells adhere to each other more strongly than light cells do: (a) 0 MCS, (b) 100 MCS, (c) 13500 MCS. [From Glazier and Graner [206]].	164
7.6	A dark field image of aggregating fields of <i>Dictyostelium</i> on an agar substrate. White bands are excited cells, corresponding to the wave-front of cAMP waves. Note the signaling spirals and the onset of streams at the aggregation edges. [Courtesy of H. Levine]. . . . .	167
7.7	Time sequence of the aggregation, mound and slug phases of a simulation of <i>Dictyostelium</i> . (a) Initial random mixture of prestalk (light) and prespore (dark) cells on a substrate. (b) Cells start to stream into a mound. (c-d) Mound forms. (e) Mound falls to the ground. (f) Slug migrates. [From Savill <i>et al.</i> [244]]. . . . . .	173
7.8	Sorting with differential adhesion only. (a-1) A vertical cross section view of the mound at time zero. About 20% pre-stalk cells (red) are randomly distributed among pre-spore cells (blue); cell surfaces are colored black. (a-2) A three-dimensional surface plot of the mound at time zero. (b) A vertical section view and a surface plot of the mound with pre-stalk cells more cohesive than pre-spore cells. Both cell types have the same adhesivity with sheath ( $\mathcal{J}_{psp,psp} = 15, \mathcal{J}_{pst,pst} = 5$ , i.e. pre-stalk cells five times more cohesive than pre-spore cells, $\mathcal{J}_{psp,sheath} = \mathcal{J}_{pst,sheath} = 10$ ), at 20000 Monte Carlo steps (MCS). (c) Same as (b) but with pre-stalk cells less cohesive than pre-spore cells ( $\mathcal{J}_{psp,psp} = 1, \mathcal{J}_{pst,pst} = 3, \mathcal{J}_{psp,sheath} = \mathcal{J}_{pst,sheath} = 10$ ), at 6000 MCS. (d) A vertical section view and a surface plot of the mound with pre-stalk cells more adhesive to sheath than pre-spore cells ( $\mathcal{J}_{pst,sheath} = 10, \mathcal{J}_{psp,sheath} = 25$ , i.e. pre-stalk cells are 2.5 time more adhesive to sheath than pre-spore cells). Pre-stalk cells are more cohesive ( $\mathcal{J}_{psp,psp} = 15, \mathcal{J}_{pst,pst} = 5$ , i.e. pre-stalk cells are three times more cohesive than pre-spore cells), at 2000 MCS: pre-stalk cells move to the surface of the mound, leaving some small clusters of pre-stalk cells in the bulk. (e) Same as (d) but with pre-spore cells more cohesive than pre-stalk cells ( $\mathcal{J}_{psp,psp} = 1.0, \mathcal{J}_{pst,pst} = 3$ , i.e., pre-spore cells are three times more cohesive than pre-stalk cells), at 200 MCS. . . . .	180

7.9	Initial configuration for simulations with both differential adhesion and chemotaxis ( $\mathcal{J}_{psp,psp} = 1.0$ , $\mathcal{J}_{pst,pst} = 3.0$ , $\mu = 20$ ). (a) A three-dimensional surface plot of the mound showing different states of the cells: green represents quiescent, purple active, and yellow refractory. (b) A three-dimensional surface plot of the mound showing cell type distribution: pre-spore cells are blue and pre-stalk cells red. (c) A vertical cross section of the mound showing cell type distribution: pre-spore cells are blue and pre-stalk cells red. Cell surface is black. (d) A projection from the top, of the chemical concentration on the surface of the substrate. The chemical field is zero at time zero. . . . .	184
7.10	The same mound as in Figure 7.9 at 2000 MCS for simulations with both differential adhesion and chemotaxis. . . . .	185
7.11	Vertical section views of the evolution of a mound ( $\mathcal{J}_{psp,psp} = 1$ , $\mathcal{J}_{pst,pst} = 3$ , $\mu = 20$ ). Numbers show time in MCS. . . . .	186
7.12	Vertical section views of the mounds at 2000 MCS for different relative strengths of chemotaxis and differential adhesion. Numbers show the values of the control parameter $\phi$ . $\phi = 0$ corresponds to pure differential adhesion, $\phi = \infty$ to pure chemotaxis. . . . .	188
7.13	The evolution of tip size (fraction of cells in the tip) as a function of time for different $\phi$ . . . . .	189
7.14	The fraction of pre-stalk cells in contact with sheath as a function of time for different $\phi$ . $\phi = \infty$ corresponds to the case of pure chemotaxis, with pre-stalk and pre-spore cells having the same surface tensions. . . . .	190

## Acknowledgments

First and foremost, I would like to thank my supervisor, James Glazier, not only for his advice and support, but also his patience and the latitude he has allowed me.

Thanks are due to many members of the research group: Mark, Marius, Burke, Sridhar, Arpita and Istvan, for all the wonderful and inspiring discussions and collaborations, and unselfish help over the years. Much of the work here was connected, in one way or another, to those discussions. Special thanks to Mark and Marius who have constantly encouraged me and shared their intelligence and experience.

I appreciate the hospitality of the Center for Nonlinear Studies and Theoretical Division of Los Alamos National Laboratory for the productive and fun summers in the high desert of New Mexico. Rafi Bloomenfeld first opened the door for me. The work on foam rheology and hysteresis was done in collaboration with Pieter Swart and Avadh Saxena of LANL. I also owe special thanks to Avadh Saxena, whose complete devotion to science and unlimited enthusiasm will always be a source of inspiration to me.

I would also like to thank Herbert Levine for introducing and guiding me into the wonderland of slime mold *Dictyostelium*. The hospitality of Herbert Levine who invited me to UCSD and the generosity of Bill Loomis who let me play in his molecular biology lab gave me the chance to get hands-on experience with *Dictyostelium* and made the work on *Dictyostelium* possible.

I would also like to thank Gerald Jones and Uri Sarid for useful discussions and questions; François Graner, Florence Elias, Denis Weaire and Jim McNally for most

stimulating correspondence.

Last but by no means least, I thank my husband - Li Zheng, who fills my life with love and sunshine.

This work has been supported in part by NSF DMR-92-57001-006, the ACS/PRF and NSF INT 96-03035-0C, and in part by the US Department of Energy.

## CHAPTER 1

### SUMMARY

This thesis treats the formation and evolution of cellular patterns in foams and living organisms using the extended large- $Q$  Potts model. Specific problems include two-dimensional anomalous grain growth from inhomogeneous initial conditions, liquid drainage under gravity in three-dimensional wet foams, foams' mechanical response and topological rearrangements under external stress, and pattern formation and cell sorting in the mound stage of the slime mode *Dictyostelium*.

Two-dimensional coarsening occurs in a wide range of materials. In spite of a few complications, the simple and well understood von Neumann's law governs the evolution of grains. Surface energy drives diffusion which causes boundary motion, some grains expand and other shrink and eventually disappear. Experiments show that most homogeneous initial conditions evolve into a scaling state where the statistics of the ensemble of grains remain the same while the average area of grains increases linearly in time. For highly inhomogeneous initial conditions, the evolution differs. The large- $Q$  Potts model on a two-dimensional lattice simulates the evolution of the disordered cluster developed from a perfect hexagonal grain array with a single defect. The distribution functions are not stable, while the average area and the number of grains in the cluster grow linearly in time. However, the grains at the boundary of the cluster form a well defined region which reaches a special scaling state with time invariant distributions and no scale change. Abnormal grain growth can occur without anisotropy of surface energy, contrary to previous belief.

It requires only widely spaced topological defects in an initially homogeneous array of grains.

Studies of foams with a small liquid fraction often ignore the role of Plateau borders, the liquid-filled regions at the intersections of cell walls. For three-dimensional liquid foams, an additional complication is the vertical drainage of the liquid due to gravity. Often drainage, rather than diffusion, determines foam stability and properties. Many applications require detailed understanding of drainage. The large- $Q$  Potts model extended to include gravity on a three-dimensional lattice simulates the vertical liquid profile of foam drainage. For ordered foams, a constant profile develops for forced drainage with liquid input from the top of the foam at a constant rate. In free drainage, without liquid input from the top, homogeneously distributed liquid drains to the bottom of the foam until capillary effects and gravity balance, while for pulsed drainage, as liquid drains from the top of the foam into the dry foam, a sharp interface between the wet and dry foam develops. The fixed profile moves downward at a constant velocity with a flat interface. The simulations agree with both experimental data and analytical results. In a disordered foam or when coarsening is not negligible, the wetting front is no longer sharp and stable, challenging current theories and experiments.

Foams have unique rheological properties that range from solid-like to fluid-like. The large- $Q$  Potts model, extended to apply shear to a two-dimensional foam, simulates two-dimensional non-coarsening foam under shear. Simulations of periodic shear show three different types of hysteresis in the stress-strain relationship, which correspond to the elastic, viscoelastic and fluid-like properties of foams. This wide-ranging mechanical response of foams depends on the structural disorder and local topological rearrangement of foam cells. The effects of structural disorder on the dynamics of topological rearrangements are studied by applying steady shear on

disordered foams. Structural disorder decreases the yield strain; sufficiently high disorder practically eliminates the elastic and viscoelastic regimes. Larger shear rates have effects similar to larger structural disorder. The statistics and dynamics of local topological rearrangement events (avalanches) depend sensitively on the degree of polydispersity of the foam structure. As the structural disorder increases, the topological rearrangements become more correlated and their power spectra change from white noise to  $1/f$  noise. Intriguingly, the power spectra of the total stored energy exhibit the same  $1/f$  trend. While avalanches of T1s globally reduce the stored elastic energy, leading to foam flow, isolated single T1 events locally reduce the elongation of cells. Studying the effects of single T1s may help explain the connection between microscopic topological rearrangements and macroscopic mechanical response.

While biological tissues differ from foams in many aspects, their structures are similar. The large- $Q$  Potts model can also simulate cell sorting in biological cell aggregates. *Dictyostelium discoideum* is a classic model for biological pattern formation. Its life cycle alternates between solitary amoebae and multicellular fruiting body. Propagating extracellular chemical waves supply chemotactic signals which control collective cell motion. In the multicellular mound, cells differentiate into two major types, pre-stalk and pre-spore. The initially randomly distributed pre-stalk cells, in time, sort to the top of the mound to form a cylindrical, nipple-like tip. Two possible mechanisms could govern relative cell motion: differential adhesion, in which differences in contact energy at cell interfaces bias the direction of cell motion, and chemotactic motion of cells along a chemical gradient. Simulations of both differential cell adhesion and chemotaxis show that with differential adhesion only, pre-stalk cells move to the surface of the mound but form no tip. With chemotaxis driven by an outgoing circular wave only, a tip forms but contains both pre-stalk and

pre-spore cells. Only for a narrow range of parameter values does a tip form which contains only pre-stalk cells. These simulations provide a method to determine the processes necessary for patterning and suggest a series of further experiments.

## CHAPTER 2

### INTRODUCTION

#### 2.1 Overview

The formation and evolution of patterns which arise from spontaneous instabilities in a driven, initially homogeneous medium by symmetry breaking and wavelength selection, have attracted considerable attention. In systems as diverse as Rayleigh-Bénard convection, diffusion-limited aggregation, solidification fronts, the Belusov-Zhabotinsky reaction, vibrated liquids (Faraday experiment), vibrated granular materials, and many others, patterns arise as a result of a nonlinear or a non-equilibrium mechanism [1]. A different class of non-equilibrium disordered patterns, known collectively as *cellular patterns*, begins with an intrinsically patterned state with defined domains which then evolve.

Cellular patterns take their name from their resemblance to living tissue. As shown in Figure 2.1, they consist of domains separated from each other by distinct boundaries. Already in the 17th century, researchers across several different disciplines noted that the appearance of many cellular materials was almost identical [2, 3]. Geologists found cellular patterns in crack networks in lava slopes [3, 4] and stone arrangements due to convection during freeze-thaw cycles [5]; biology offered a huge variety of cellular patterns of different length scales, from territorial patterns in ecology to cellular structures in tissues [6]; materials science offered polycrystalline structures in metals and sintered ceramics, cracks in glazes and fracture in polymer films above their glass transition temperature [7]; finally, cellular patterns are also

characteristic of some nonlinear convection problems like solar granulation [8] and Bénard-Marangoni convection [9]. More examples can be found in Glazier's thesis [11] and several review papers [10, 12]. Sir D'Arcy Thompson [13] guessed, quite rightly, that the ubiquity of cellular patterns is not the result of detailed, system dependent interactions, but is the outcome of competition between a minimization process and global constraints of a geometric nature. However, he did not proceed to a general theory of cellular patterns, but chose to apply these insights to explain biological structures.

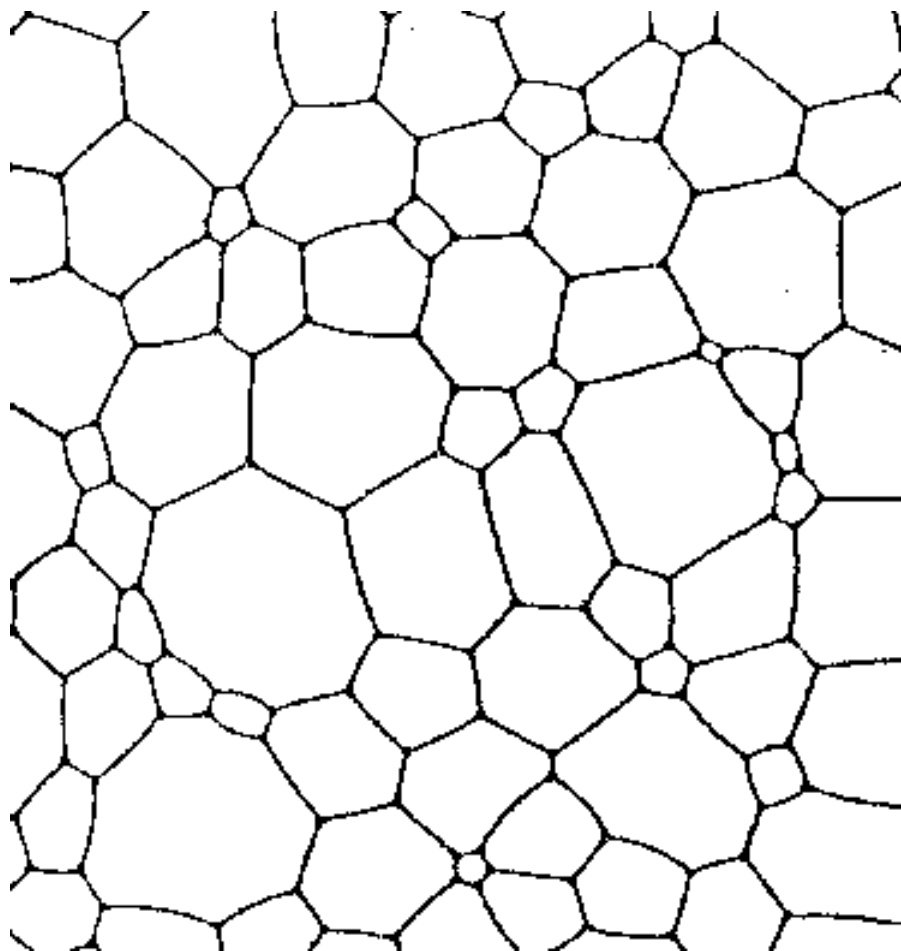


Figure 2.1: Photograph of soap bubbles confined between two glass plates: a typical two-dimensional cellular pattern in a quasi-static equilibrium with three-fold vertices and  $120^\circ$  contact angles. Walls curve due to the pressure difference between adjacent cells.

The modern history of the subject begins with C. S. Smith [14], who at a metallurgy conference in Cleveland, proposed the study of two-dimensional soap froth as a means of understanding a problem of vast practical importance: the evolution of grains inside a metal. J. von Neumann was at the seminar and he immediately derived the equation for the growth of polygonal bubbles in two-dimensional soap froth now known as von Neumann's Law [15]. Ever since, the formation and evolution of two-dimensional cellular patterns has attracted considerable attention. Experiments have studied a variety of materials including soap froth [16, 17, 18], magnetic bubbles [19, 20, 21], Langmuir films [22, 23], lipid monolayer foams [24] and ferrofluid foams [25]. Theoretical studies of two dimensional cellular patterns proceed mostly in three distinct branches: area dominated (mean field theories using von Neumann's law), boundary dominated (motion induced by boundary curvature) and vertex dominated (motion induced by tangent forces) [10, 26, 27]. A great deal of understanding has been achieved about the evolution from a nearly ordered foam to a disordered **scaling state**, where the length scale of the pattern grows but the statistics stay the same. The statistical distributions, including the topological distribution  $\rho(n)$  (where  $n$  is the number of sides of a domain), and the normalized area distribution  $\rho(a/\langle a \rangle)$  (where  $a, \langle a \rangle$  are the area of domains and the average domain area), and the various topology and area correlations characterize the pattern disorder. Questions, however, remain whether the scaling state is universal and why a wide range of materials select the same scaling distribution from a family of possible solutions. In those materials where coarsening does not reach a scaling state, *e.g.* in abnormal grain growth, where some domains grow at a much faster rate than the rest, what are the necessary conditions for these anomalies? We will attempt to answer (partially) these questions by presenting a special scaling state evolved from a single topological defect on a homogeneous lattice [Chapter 3].

Recently, research on cellular patterns has extended from two-dimensional to three-dimensional, from quasi-static coarsening in single phase systems to multi-phase, more dynamic problems, including drainage and rheology.

Foam drainage, while extremely important in foam applications, had only been described by empirical rules. In a charming book “*Soap Bubbles: their colors and forces which mold them*,” C. V. Boys [126] in the early 20th century, discussed the thickness of bubble walls after demonstrating many interesting and entertaining experiments. Bikerman [127] in his book “*Foams: Theory and Industrial Applications*,” reported early experiments measuring the amount of liquid drained from a foam and gave no less than five different functional forms for the volume of liquid draining out of a standing foam [127]. Mysels *et al.* [128] investigated different types of thin film drainage, concentrating on vertical films formed by withdrawal of glass frames from pools of surfactant solution. Only recently has foam drainage been systematically studied. Weaire *et al.* performed a series of experiments which measured the evolution of the liquid profile during different kinds of drainage [129]. A theory has emerged in the form of the drainage equation [130, 131] to explain some of the experimental observations and to predict others, which in turn, were verified in experiments. But both experiments and theories are limited to ordered foams, where effects can be averaged. We will describe our Monte Carlo model, which reproduces both experimental and theoretical results in ordered foams and predicts new phenomena in disordered foams [132, 133]. Our model represents “an interesting change of direction for theory” [129] [Chapter 4].

A growing interest in the complex behavior of driven simple systems has resulted in ever increasing research on the rheology of cellular and granular materials. Many soft materials, including foams and emulsions, have intriguing rheological properties [161]. They behave as elastic solids for small applied shear due to their linear

deformation, recovering their initial shape and size when the shear is released, but flow like viscous liquids at large applied shear due to nonlinear and collective local rearrangements. While analytical study is only possible for periodic structures or linear responses, computer modeling has provided important insights into the rheology of foams. Several models have been developed: constitutive models based on local mechanical interactions [162, 163, 164], a vertex model treating foams as a collection of interacting vertices [165], a center model based on Voronoi reconstruction of foams [166] and a “bubble” model where bubbles interact as elastic disks with viscous dissipation [167]. These models make different assumptions and have different regimes of applicability. The phenomenology of foam flow is well-established but experiments revealing the connection between detailed structure and mechanical response have been scant [Chapter 5].

## 2.2 Dynamics of Cellular Patterns

As the following pages will emphasize, a part of this thesis treats cellular patterns of a particular kind: in two-dimensions, all vertices are three-fold (except during topological changes) and the walls connecting them meet each other at  $120^\circ$  angles. Simple geometry shows that a three-fold vertex with non- $120^\circ$  angles has larger boundary length than one with  $120^\circ$  angles. Minimization of the total boundary length makes a pair of three-fold vertices energetically more favorable than a four-fold vertex, and walls become circular arcs [28]. Figure 2.2 shows a four-fold vertex decaying into a pair of three-fold vertices with  $120^\circ$  contact angles; the boundary length in the latter is about 3.4% shorter than that in the former. This decay is just a simple example of the centuries-old Steiner’s problem: given  $n$  points, find a spanning tree that includes every point with minimal total length. Fermat posed the basic problem in 1646 but it was Steiner (1796-1863) who devised this formulation [29]. A minimal spanning tree is called a Steiner tree, and arises frequently in

problems concerning network design, optimal location of facilities *etc.* [30]. While Steiner's problem is a well known NP-complete problem [31], soap films naturally “solve” it by minimizing their surface energy. Note that a soap froth spanning tree is not necessarily Steiner's tree – it can be a local minimum in configuration space. Topology and dynamics relate intimately in cellular patterns. A three-fold vertex is topologically stable, *i.e.* a small displacement of one wall does not destroy it, whereas moving a wall at a four-fold vertex immediately forms two three-fold (not necessarily with  $120^\circ$  angles) vertices.

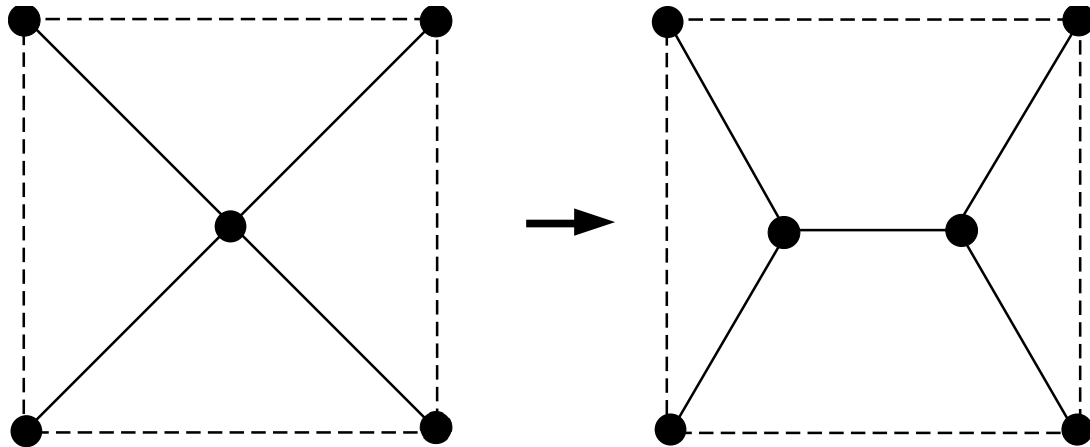


Figure 2.2: A four-fold vertex decays into two three-fold vertices because the total boundary length decreases.

In Summary, at equilibrium:

- The pattern has a vertex connectivity of three (higher connectivity is unstable).
- Walls are minimal surfaces (with constant mean curvatures).
- Walls meet each other at  $120^\circ$  angles at vertices.
- The curvature of a wall is proportional to the difference in pressure across it.

The last point is the Young-Laplace law:

$$\Delta P = \frac{2\sigma}{r}, \quad (2.1)$$

where  $\sigma$  is the coefficient of surface tension and  $r$  the radius of curvature of the wall.

In foams, pressure differences between adjacent bubbles, given by Equation 2.1, cause gas to flow through the walls from higher pressure bubbles to lower pressure ones. Note that the gas pressure difference caused by film curvature is negligible compared to the mean pressure within bubbles, so the amount of gas inside a bubble is nearly proportional to its area. Hence, assuming that the diffusion rate is linearly proportional to the pressure difference, the rate of area change through a wall is proportional to the wall length  $l_{ij}$  and pressure difference:

$$\Delta a_{i \rightarrow j} = \kappa'(p_i - p_j)l_{ij}, \quad (2.2)$$

where  $\kappa'$  is a diffusion constant. In the soap froth, this relation is essentially Fick's diffusion equation [77].

From these assumptions, elementary trigonometry shows that:

$$\frac{da_n}{dt} = \kappa(n - 6), \quad (2.3)$$

where  $a_n$  is the area of a cell of  $n$  sides and  $\kappa$  is a coefficient depending on  $\kappa'$  and  $\sigma$ . Equation 2.3 is known as von Neumann's law which is exact under these assumptions. von Neumann's law also holds for metallic polycrystals where the boundaries are not always at equilibrium, provided that locally the boundary velocity is proportional to local curvature. Considering the force balance on a point at the boundary with no inertia [77]:

$$p_i - p_j = \sigma/r - \lambda v_\perp, \quad (2.4)$$

where  $\sigma$  is the surface tension,  $r$  is the local radius of curvature,  $\lambda$  is the coefficient of viscous drag and  $v_\perp$  is the normal velocity of the boundary, which relates to the area change of a bubble through:

$$\frac{da_i}{dt} = \oint_{\text{bubble } i} v_\perp dl. \quad (2.5)$$

Using equations 2.2 and 2.4, and a geometrical identity,

$$\oint_{\text{bubble } i} \frac{1}{r} dl = 2\pi - n\pi/3 = (6 - n)\pi/3, \quad (2.6)$$

we recover von Neumann's law with:

$$\kappa = \frac{\pi\kappa'\sigma}{3(1 + \lambda\kappa')}. \quad (2.7)$$

In the limit  $\lambda \rightarrow 0$ , this relation is the original von Neumann's derivation for soap foams; in the limit  $\lambda \rightarrow \infty$  we obtain idealized metallic grain growth, since the pressure differences become negligible and boundary velocities are simply proportional to local curvature. In both cases, von Neumann's law states that coarsening does not depend on domain areas or on the local configuration, except through the number of sides.

The walls meet the boundaries of the container or any second phase object at  $90^\circ$  because of the symmetry in contact angles. This angle difference is best illustrated in the picture of dragon fly wings in Figure 2.3, where walls meet at  $120^\circ$  angles among themselves but form  $90^\circ$  angles with the wire frame. Studies of coarsening, often neglect boundary effects. But in thin film strips, the boundaries strongly influence the microstructural evolution, which may have important consequences for the performance of the material. Vaidya and coworkers [103] observed a “bamboo” microstructure develop as individual grains spanned the width of a thin film conductor strip; Walton *et al.* [104, 105] simulated grain growth in thin film strips; Fortes

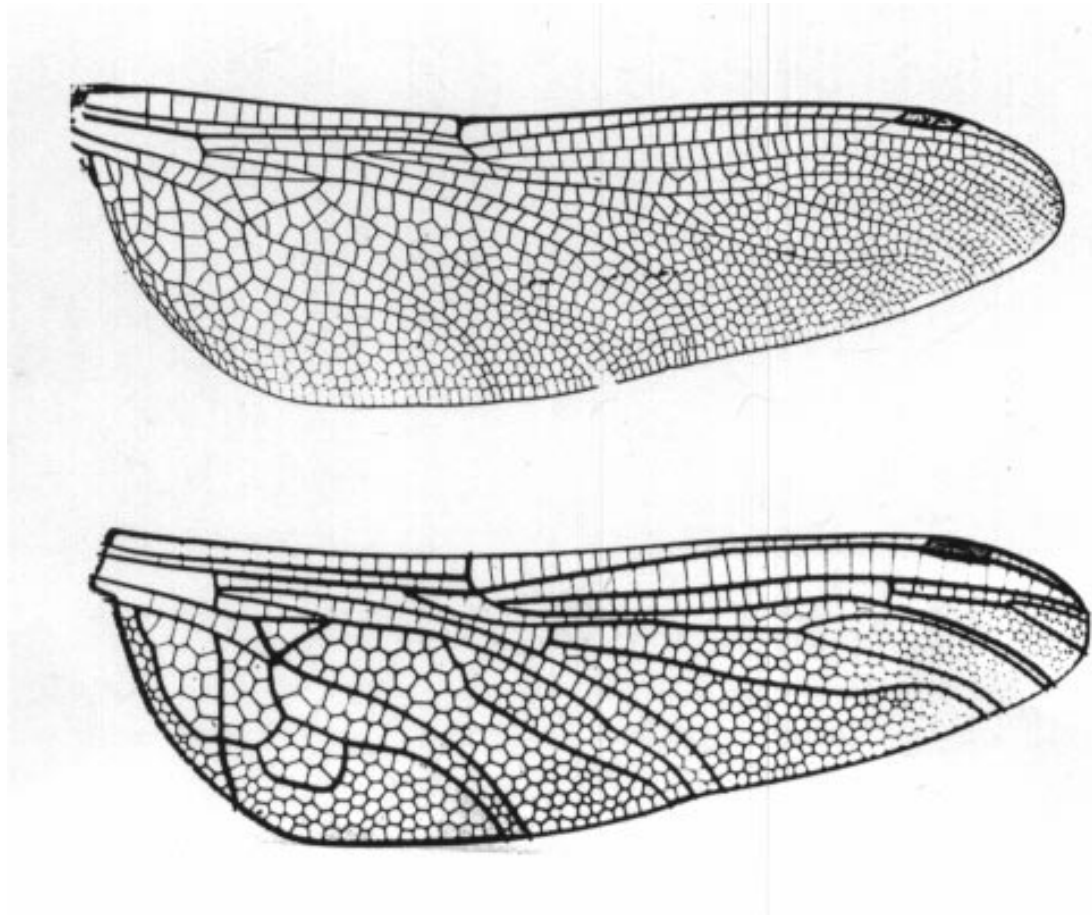


Figure 2.3: A dragonfly’s wing, top, can be mimicked by two-dimensional soap films in a suitable frame (thick lines), bottom. Notice that the walls form  $90^\circ$  angles with the frame but meet at  $120^\circ$  angles among themselves. [From Hildebrandt and Tromba [29]].

and Rosa [110, 111] investigated similar bamboo formation in soap froth confined in long tubes [Section 3.5].

While surface tension drives foam dynamics, the competition between surface minimization and conservation constraints gives rise to complex patterns. Similar rules hold in three dimensions: walls have constant mean curvatures ( $\frac{1}{r_1} + \frac{1}{r_2}$ ), and vertices are four-fold with  $109.47^\circ$  internal angles (the tetrahedral angle,  $\cos^{-1}(-1/3)$ ). However, some of the geometrical constraints are relaxed in three dimensions, considerably complicating the problem. Glazier has proposed from

simulations a coarsening law for three-dimensional cellular structures in analogy with von Neumann’s law [113]. Sire has developed a compatible mean field theory [114]. Experimental three-dimensional coarsening studies have used various new techniques such as diffusion wave spectroscopy [115, 116], magnetic resonance imaging [117, 118], and optical tomography [119] [Section 3.6].

We will first present our research on foams, including foam coarsening (grain growth) [Chapter 3], foam drainage (phase separation)[Chapter 4] and foam rheology (mechanical response under external driving) [Chapter 5]. We have employed a Monte Carlo simulation, the large- $Q$  Potts model and extended it to all these problems [Chapter 2]. As Sir D’Arcy Thompson did, we then go back to the realm of biology. The obvious similarity in appearance between the cells of a soap foam and the cells in a living organism leads to many attempts to connect the two more formally. In his book *On Growth and Forms*, Sir D’Arcy Thompson expressed the analogy succinctly: “...surface tension is of great and is probably of paramount importance” in the determination of the shapes of simple organisms and cells [13]. We apply the same model and a general understanding of physical mechanisms to study cell sorting.

Cell sorting is critical to life. Cells move extensively in embryonic development, wound healing and metastasis of cancer. When cells of two or more types are randomly intermingled and aggregated, they are able to migrate over long distances to re-establish homogeneous cell masses and sometimes to re-construct functional tissues [192]. Living organisms, even adult animals such as *Hydra*, can regenerate from an aggregate of randomly mixed cells of different types [193, 194]. Cell migration and sorting *in vivo* usually require a high degree of organization and complex cellular interactions. The driving mechanisms for cell sorting fall into two categories: short range interactions where cells interact through direct contact, and

long range interactions where cells interact through the external environment. We seek to understand how cells migrate and sort by studying these interactions in a simple organism, slime mold amoebae *Dictyostelium discoideum*, which are easy to manipulate experimentally. We will focus our discussion on explaining cell sorting and patterning in the mound stage of *Dictyostelium*, based on direct (differential adhesion) and indirect (chemotactic) cell interactions [Chapter 6].

Except in the discussions of cell sorting, we use the word *foam* as broadly as possible – to describe a cellular structure. Only in specific contexts will we distinguish between wet and dry foams, ordered and disordered foams. We neglect all chemical aspects of foams in our study: that is, we describe them mainly by one parameter,  $\gamma$ , the surface tension, whose value will not be specified. While the rate at which gas diffuses across bubble walls and the rate at which bubble walls relax when perturbed both depend on the chemical makeup, especially the viscosity, of the foam, we usually assume that the walls relax much faster than other processes, such as gas diffusion or liquid drainage. In this respect, foams and concentrated emulsions may differ only in their degree of wetness or average bubble size. The terms grain, bubble, cell and domain are more or less interchangeable, as are film, wall, boundary, grain boundary, and membrane.

## CHAPTER 3

### POTTS MODEL

#### 3.1 Introduction

##### 3.1.1 Overview

Potts introduced the Potts model in 1952 [32], as a generalization of the Ising model to more than two components. Historically, Ashkin and Teller first studied a four-component version of the model [33], so the model is sometimes called the Ashkin-Teller-Potts model. The general  $Q$ -state model gained its current name after Domb [34] proposed it to his then student Potts as a thesis topic. It became a subject of intense research interest in the 70's and 80's because it has a much richer phase structure than the Ising model. Its critical behavior is also richer and more general than that of the Ising model. In the ensuing effort to explore its properties, the Potts model became an important testing ground for different methods and approaches in critical point theory [35]. The phase transitions of the low  $Q$  Potts model are still studied [36].

The phase transition literature is strikingly replete with “models:” the Ising model, the Heisenberg model, the Potts model, the chiral Potts model, the XY model, the Baxter model, the Zamolodchikov model, the F model and even the non-linear sigma model, to name just a few. For these models, we can often compute the partition functions exactly or at least reduce them to a finite number of integrals [37]. The Potts model is the generalized Ising model, having discrete degenerate spin values (except in the  $Q = \infty$  limit); the XY (or O(2)) model consists of a set of

continuous valued spins regularly arranged on a two-dimensional square lattice; the Heisenberg model is the three-dimensional version of the XY model, where spins obey a continuous symmetry in three dimensions.

The early 80's saw the pioneering work of Anderson, Grest, Sahni and Srolovitz who developed the  $Q$ -state Potts model to study cellular pattern coarsening [38, 39, 40, 41, 42, 43, 45, 46, 47, 48, 50, 51]. They used the Potts model to simulate metallic grain pattern relaxation at low temperatures, very different from most high temperature phase transition problems. A quasi-microscopic view of grain growth naturally led metallurgists to think of the interior of a grain as being composed of a lattice of "atoms" (corresponding to spins), and the grain boundaries as the interfaces between different types of atoms or different crystal orientations (corresponding to mismatched lattice bonds).

### 3.1.2 Original Potts Model For Grain Growth

As mentioned in chapter 1, the basic driving force in coarsening is surface energy. Unlike a molecular dynamics model that requires the detailed interaction potentials among the atoms, or a mean field theory that begins with von Neumann's law [Equation 2.3], the Potts model minimizes total surface energy and essentially solves the minimal surface equations. The Potts model puts surface energy on a lattice by defining a free energy proportional to the total area of grain boundary. Mathematically, each site on the lattice has a spin  $\sigma$ . All the lattice sites within a given grain have the same spin  $\sigma$ , with a different spin for each grain. The difference between spins defines the grain boundaries. Figure 3.1 shows a schematic of the model in two dimensions. The energy of interaction between like spins is zero, and between unlike spins one. Thus the Potts Hamiltonian - the total energy - is:

$$\mathcal{H} = \sum_{\vec{i}, \vec{j}} [1 - \delta_{\sigma(\vec{i}), \sigma(\vec{j})}], \quad (3.1)$$

where  $\vec{i}$  and  $\vec{j}$  are neighboring lattice sites. The neighbor range (discussed below) affects the nature of the interaction.

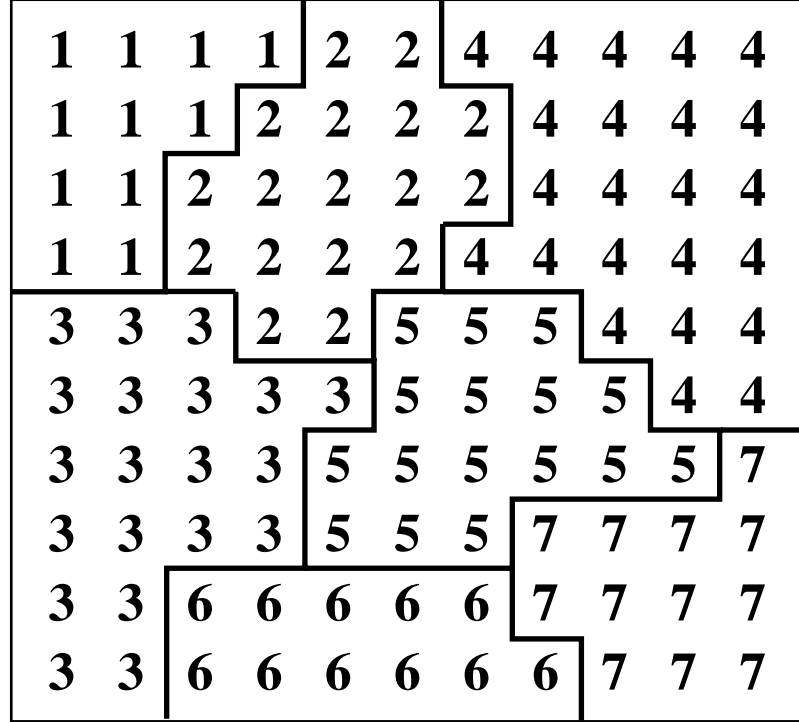


Figure 3.1: Schematic of a two-dimensional cellular pattern represented in the large- $Q$  Potts model. Numbers show different spin values. Heavy black lines indicate grain boundaries.

Monte Carlo simulations of  $Q$ -state Potts models have traditionally used local algorithms such as that of Metropolis *et al.* [52]. A lattice site is chosen at random and a new trial spin is also chosen at random from one of the other  $Q - 1$  spins. The probability of accepting such a reassignment is:

$$\mathcal{P} = \begin{cases} 1 & \Delta\mathcal{H} \leq 0 \\ \exp(-\Delta\mathcal{H}/T) & \Delta\mathcal{H} > 0 \end{cases}, \quad (3.2)$$

where  $\Delta\mathcal{H} = \mathcal{H}_{\text{after}} - \mathcal{H}_{\text{before}}$  denotes the difference between the total energy before and after the spin reassignment, and  $T$  is the magnitude of fluctuations. Simulation time is measured by Monte Carlo steps (MCS), where one MCS corresponds to as many spin flip attempts as the total number of lattice sites  $N$ . Note that this definition of time is somewhat arbitrary, as the spin configuration and energy are updated instantaneously with every spin flip. The updating rules are exactly the same for each lattice site and the evolution is continuous. Thus the relative timing of events, for example two spin flips, is uncertain within one MCS. While this uncertainty is insignificant for well separated events, it can change the measured interval between frequent events.

On average the maximum velocity of boundary motion is 1 lattice site per MCS. However, for pathological updating sequences, the velocity can range from zero to  $N$  lattice sites per MCS. Thus velocity is intrinsically a statistical distribution. Correct calculation requires averaging over replicas. In practice, these pathologies are rare. Hence time averages can substitute for replica averages. Successful spin flips at the grain boundaries correspond to boundary migration. A segment of boundary therefore moves with a velocity  $v_i$  related to the local energy difference,  $\Delta\mathcal{H}_i$ , by

$$v_i = C[1 - \exp(-\Delta\mathcal{H}_i/T)], \quad (3.3)$$

where  $C$  is a constant corresponding to a boundary mobility [44]. Equation 3.3 is equivalent to the boundary velocity derived from classical reaction rate theory [54].

This algorithm makes the crucial assumption that the boundary motion is Brownian, described by Boltzmann dynamics. This assumption is true for metallic materials, where atoms jump back and forth across the boundary if the thermal energy is high. Mombach *et al.* [208] showed in chicken embryo cell experiments that certain cell membranes also perform thermal fluctuations. But soap foams are essentially

fluctuation free. Many of our simulations accept only reassessments that lower the total energy, *i.e.*,

$$\mathcal{P} = \begin{cases} 1 & \Delta\mathcal{H} \leq 0 \\ 0.5 & \Delta\mathcal{H} = 0 \\ 0 & \Delta\mathcal{H} > 0 \end{cases}, \quad (3.4)$$

corresponding to the zero temperature limit, which is appropriate for soap froth. However, even zero temperature simulations have fluctuations due to Monte Carlo updating.

### 3.1.3 Small- $Q$ Simulations

Early simulations by Anderson *et al.* used small  $Q$  values, shown in Figure 3.2 for  $Q = 3, 6, 12$ , and  $64$  on a triangular lattice at  $T \sim 0$ .

Obviously low- $Q$  configurations consist of very irregular and asymmetric grains while the high- $Q$  configurations consist of more compact and symmetric grains. In the low- $Q$  limit, when grains meet and coalesce with other grains of the same spin value (same orientations), their areas have large discontinuous changes. The probability for two like grains to meet scales as:

$$1 - (1 - 1/Q)^Z, \quad (3.5)$$

which for large  $Q$  reduces to  $Z/Q$ , where  $Z$  is the number of neighbors on the lattice [44]. For  $Q = 64$ , on a next-nearest neighbor triangular lattice where  $Z = 12$ , the probability of grain coalescence is about 0.172 which is not negligible. Since coalescence events are strictly forbidden in most real metallic grain growth [53], only the large- $Q$  limit can successfully model grain growth. In unstable foams, wall breakage sometimes occurs and two bubbles sharing the same wall coalesce. While the topological distribution and von Neumann's law determine the rate of diffusive

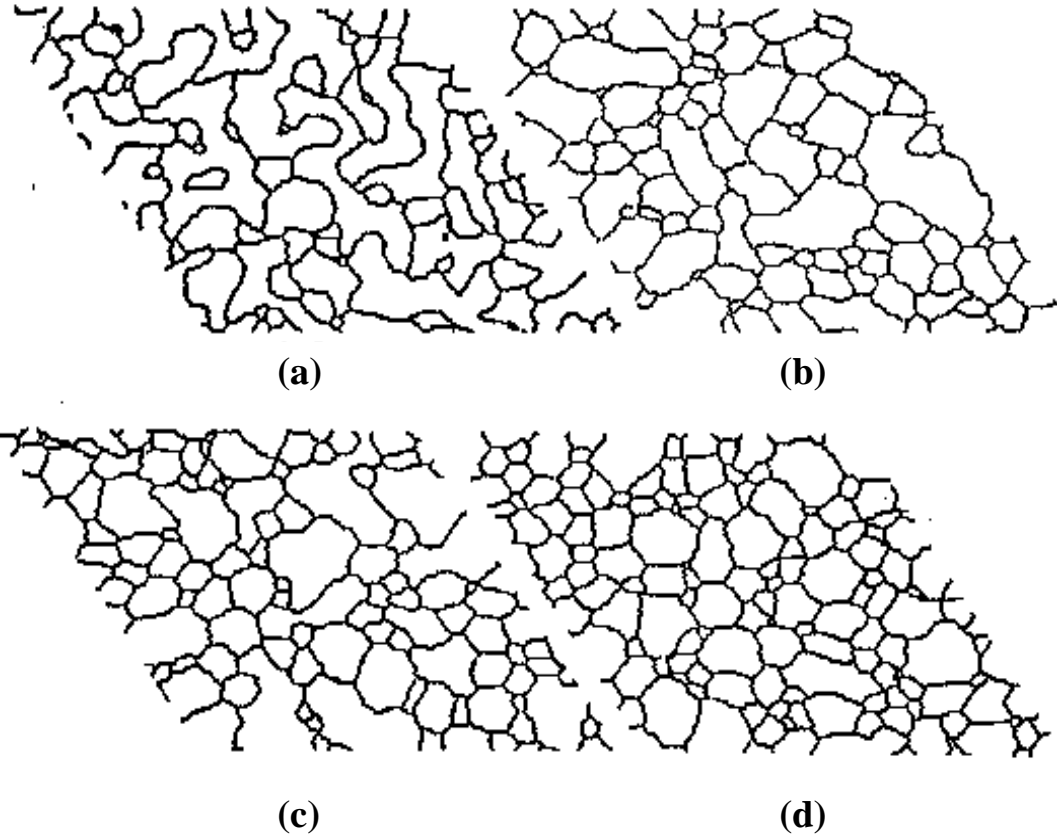


Figure 3.2: Snapshots of the patterns in Potts model simulations on a triangular lattice at low  $T$  for: (a)  $Q = 3$ , (b)  $Q = 6$ , (c)  $Q = 12$ , and (d)  $Q = 64$ . [From Anderson *et al.* [44]].

bubble disappearances, coalescence depends on different mechanisms and thus has rates independent of diffusional coarsening. Also, wall breakage usually appears as a cascade, strongly correlated in space and time [55], rather than being uncorrelated and probabilistic as in the low- $Q$  Potts model. Coalescence can be modeled in the large- $Q$  limit by assigning the same spin value to the two merging grains.

### 3.1.4 Lattice Anisotropy

In practice, lattice simulation of surface energy runs into difficulties when lattice discretization results in strong lattice anisotropy. The lattice anisotropy can be characterized by the ratio of lowest to highest surface energies per unit boundary length as a function of orientation, usually shown in a Wulff plot (surface energy *vs.* surface orientation). Figure 3.3 shows that longer range spin interactions smooth the Wulff plot. Table 3.1 gives the values of lattice anisotropy and the corresponding orientations of energy extrema:  $\theta_M$  for energy maxima and  $\theta_m$  for energy minima. In low temperature Potts model simulations, boundaries tend to align preferentially along low-energy orientations. For example, if we use a simple nearest neighbor interaction on a square lattice, boundaries tend to be horizontal and vertical, allowing stable vertices to deviate from the  $120^\circ$  rule. As a result, coarsening gradually slows down and finally stops altogether (as observed in many real metals with a high anisotropy), rather than continuing indefinitely. Moreover, the Potts model with strong lattice anisotropy consistently yields wider side and area distributions than soap froth [56]. One way to treat this problem is to work at a higher temperature where thermal activation allows the boundaries to overcome anisotropy pinning. Experimentally in metals, higher temperatures result in higher growth rates. Therefore this choice is reasonable in simulating grain growth. As mentioned, soap froth, free of boundary fluctuations, should be simulated in the zero temperature limit. A better solution is therefore to reduce the lattice anisotropy by using a triangular

Figure 3.3: Wulff plots of lattice anisotropy in two dimensions: (a) sq-1 [11], (b) sq-2 [11], (c) sq-3, (d) sq-4 correspond to nearest, 2nd nearest, 3rd nearest, and 4th nearest neighbors on a square lattice; (e) tr-1 [39], (f) tr-2 correspond to nearest and 2nd nearest neighbors on a triangular lattice, respectively.

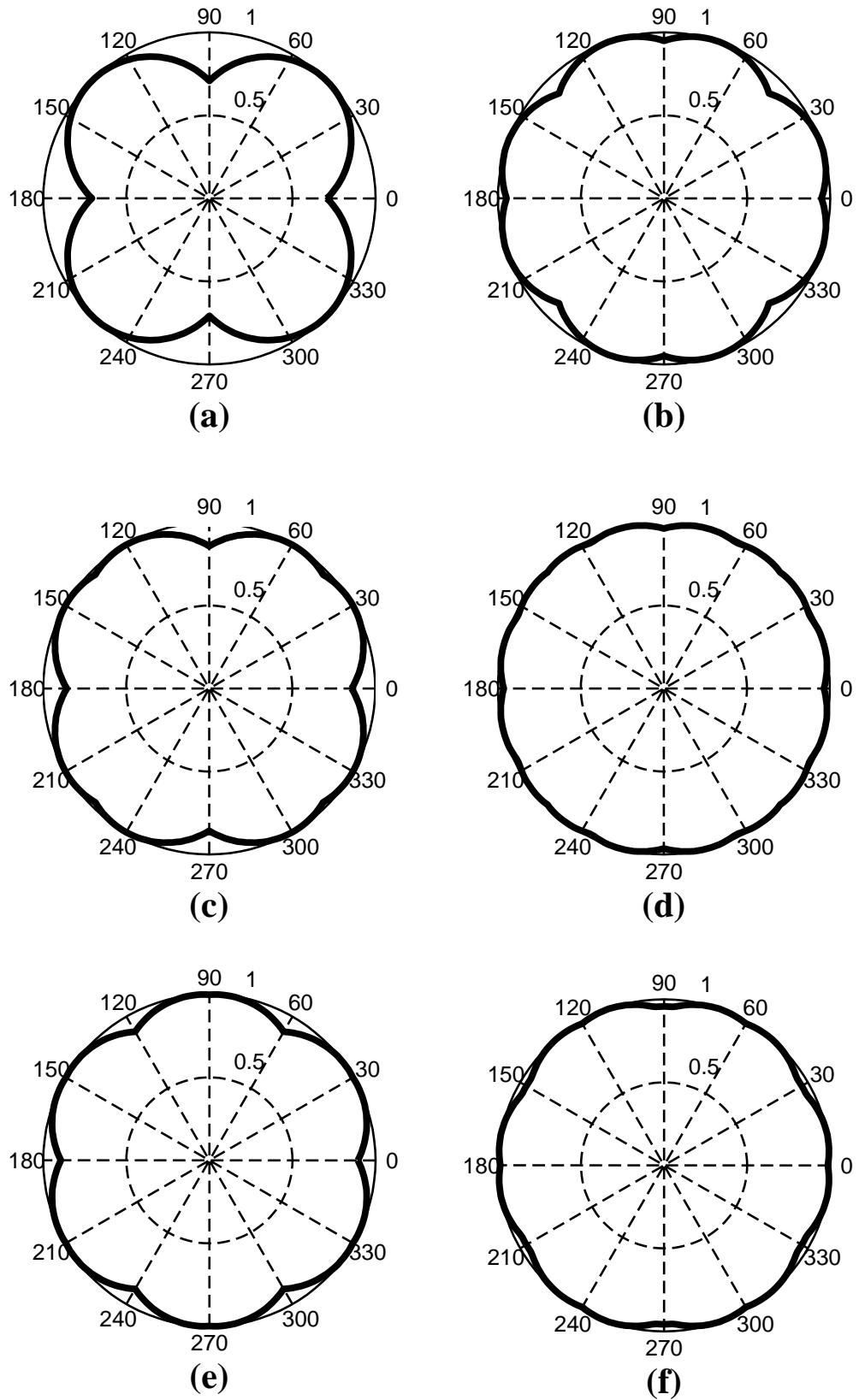


Table 3.1: LATTICE ANISOTROPY IN THE POTTS MODEL

# of Neighbors		$\theta_M$	$\theta_m$	$\Phi = E_M/E_n$
sq-1	4	45.0	0.0	1.414
sq-2	8	19.5	45.0	1.190
sq-3	12	31.5	0.0	1.166
sq-4	20	16.5	0.0	1.037
tr-1	6	27.0	0.0	1.119
tr-2	12	10.5	45.0	1.077

lattice, or increasing the range of interaction. We generally use a fourth nearest neighbor interaction on a two-dimensional square lattice, which corresponds to a lattice anisotropy of 1.037 [see Table 3.1], a good approximation to the ideal, isotropic 1.00 but not too computationally expensive. An alternative approach is to use different weights for different order of neighbors, which can provide low anisotropy with fewer neighbors but is not necessarily more computationally efficient, as it involves using non-integer numbers.

Holm *et al.* [56] have studied the effects of lattice anisotropy and temperature on coarsening in the large- $Q$  Potts model. Although by very different mechanisms, increasing temperature and smoothing the Wulff plot of the lattice both can overcome the anisotropy inherent in discrete lattice simulations, resulting in continuous coarsening that obeys von Neumann's law (Equation 2.3).

When using long range interactions, size limits become more significant: *e.g.* in a fourth nearest neighbor two-dimensional square lattice, for any cells of area  $a \leq 21$ , all lattice sites are surface sites. For small size cells, von Neumann's law fails because the surface to volume ratio does not follow  $r : r^2$ . For a fourth nearest neighbor interaction on a two-dimensional square lattice,  $a = 35$  is the minimum area. In general, cell areas must be larger than  $Z^2/4\pi$ , where  $Z$  is the number of neighbors, for the surface to volume ratio to be approximately correct.

### 3.1.5 Algorithms

The standard Metropolis algorithm selects a site at random with uniform probability, and tries to change the spin at the site to another randomly selected spin. At zero temperature, no spins can change except those at the boundaries, because creating an unlike spin inside a domain can only increase the total surface energy which is not accepted. However, finite temperature simulations can cause heterogeneous grain nucleation, which does not occur during normal grain growth. We employ a new algorithm: we randomly choose lattice sites at the boundaries only, and try to reassign to them one of their neighbors' spin values. In real materials, grain boundaries migrate as a result of thermally activated atomic jumps across a boundary. The atoms added to a growing crystallite assume its orientation. Hence from microscopic considerations, a chosen lattice site should attempt to reorient into one of its neighbor's orientations. This algorithm considerably speeds coarsening and eliminates heterogeneous nucleation. Recently, a detailed comparison between this algorithm and the standard Metropolis algorithm has shown that they have the same growth exponents  $\alpha$  ( $\langle r \rangle \sim t^\alpha$ ) and distributions of grain sides and sizes [53]. A further improvement of the algorithm keeps only the list of boundary sites instead of the entire lattice configuration, and selects trial spins from local neighbors. To keep the rate of time evolution constant as the number of boundary sites changes, the definition of MCS changes: one MCS is as many spin flip attempts as the total number of boundary spin sites. Hence, one new MCS : one old MCS = boundary length : area. This new algorithm is much faster than the old ones when grains are large, for example, in late stage coarsening.

### 3.2 Extensions

The large- $Q$  Potts model has been extended in many ways to incorporate different aspects of cellular materials. In analogy to other spin models, the extensions fall into the following categories:

- coupling between spins,
- coupling to external fields,
- constraints.

We shall describe in detail how we implement these in due course. Here we give only an overview.

#### 3.2.1 Interaction Between Spins

When more than one type of cell (more than one phase) is present in a cellular material, surface tensions at boundaries between like types and unlike types differ. To incorporate these differences in surface energies, instead of using a constant coupling strength for all unlike spin pairs, we introduce different coupling strengths for different “types” of spins. Graner and Glazier [215, 206] first proposed this extension of the Potts model in their simulations of cell sorting, where they included three types of cells: dark cells (d), light cells (l) and a fluid medium (M) treated as a generalized cell. Low surface energy corresponds to a smaller value of coupling constant. The total energy becomes:

$$\mathcal{H}_1 = \sum_{\vec{i}, \vec{j}} \mathcal{J}_{\tau(\sigma(\vec{i})), \tau(\sigma(\vec{j}))} (1 - \delta_{\sigma(\vec{i}), \sigma(\vec{j})}), \quad (3.6)$$

where  $\tau(\sigma)$  is the type of cell  $\sigma$ . The summation is always over all neighboring sites on the lattice. The coupling constants can be mapped into surface tensions,  $\gamma_{\tau\tau'}$  [214]:

$$\gamma_{dl} = \mathcal{J}_{dl} - \frac{\mathcal{J}_{dd} + \mathcal{J}_{ll}}{2}, \quad (3.7)$$

$$\gamma_{dM} = \mathcal{J}_{dM} - \frac{\mathcal{J}_{dd}}{2}, \quad (3.8)$$

$$\gamma_{lM} = \mathcal{J}_{lM} - \frac{\mathcal{J}_{ll}}{2}. \quad (3.9)$$

The total surface energy  $\mathcal{H}$  can be rewritten as:

$$\mathcal{H} = \gamma_{dl} I_{dl} + \gamma_{dM} I_{dM} + \gamma_{lM} I_{lM} + \sum_{\text{cells}} A_i \frac{\mathcal{J}_{ii}}{2}, \quad (3.10)$$

where  $I_{dM}$ ,  $I_{lM}$  and  $I_{dl}$  are the total interface areas between the respective types, and  $A_i$  is the total surface area of cell  $i$ . The last term is constant if all cell surface areas stay the same.

For cell sorting in the *Dictyostelium* mound [Chapter 6], we include four cell types: prestalk, prespore, sheath and substrate, and model the different surface tensions by using type dependent coupling strengths.

As the coupling strength describes the interaction between spins,  $\mathcal{J}_{ij}$  usually is symmetric, *i.e.*  $\mathcal{J}_{ij} = \mathcal{J}_{ji}$ . But it does not have to be symmetric. In fact, an asymmetric coupling strength effectively exerts a force [57]. When  $\mathcal{J}_{ij} > \mathcal{J}_{ji}$ , a spin flip from  $i$  to  $j$  has a different energy from that from  $j$  to  $i$ .  $\mathcal{J}_{ij} - \mathcal{J}_{ji}$  contributes to  $\Delta\mathcal{H}$ , and therefore biases the probability of a spin flip between  $i$  and  $j$ , favoring  $i$  to  $j$ . Figure 3.4 illustrates this bias on a nearest neighbor square lattice. In case (a), the change in configuration energy is  $\Delta\mathcal{H}_a = 3\mathcal{J}_{21} - \mathcal{J}_{12}$ , when the circled spin 1 flips to its neighbor spin 2; in case (b),  $\Delta\mathcal{H}_b = 3\mathcal{J}_{12} - \mathcal{J}_{21}$ , when the circled spin 2 flips to its neighbor spin 1.

Hence the ratio of the probabilities for (a) and (b) is:

$$\exp(-\Delta\mathcal{H}_a/T) : \exp(-\Delta\mathcal{H}_b/T) = \exp[4(\mathcal{J}_{12} - \mathcal{J}_{21})/T], \quad (3.11)$$

(a)

1	1	2	2
1	1	2	2
1	1	2	2

  
 $J_{12}$ 

1	1	2	2
1	2	2	2
1	1	2	2

  
 $3 J_{21}$

$$\Delta H = 3 J_{21} - J_{12}$$

(b)

1	1	2	2
1	1	2	2
1	1	2	2

  
 $J_{21}$ 

1	1	2	2
1	1	1	2
1	1	2	2

  
 $3 J_{12}$

$$\Delta H = 3 J_{12} - J_{21}$$

Figure 3.4: Asymmetric coupling strength in the Potts model:  $\mathcal{J}_{12} \neq \mathcal{J}_{21}$ . Case (a) corresponds to cell-2 expanding into cell-1. Case (b) corresponds to cell-1 expanding into cell-2.  $\Delta\mathcal{H}$  is the energy difference after the spin flip.

which can be generalized to an arbitrary lattice by replacing 4 with the total neighbor number  $Z$ . This ratio reflects the net velocity of the segment of boundary, as given in Equation 3.3. If  $\mathcal{J}_{12} > \mathcal{J}_{21}$ , the probability of cell-2 protruding into cell-1 is higher than the other way around. Since in highly damped motions such as cell movements, motion stops as soon as the applied force stops, the velocity, rather than the acceleration, is proportional to the applied force, or  $\vec{v} \propto \vec{F}$ . So in the Potts model, we can treat the forces as derived from an effective potential energy. Hence,

$$\vec{F} \propto \vec{v} \propto [1 - \exp(-\Delta\mathcal{H}/T)] \frac{\vec{\nabla}\mathcal{H}_p}{|\vec{\nabla}\mathcal{H}_p|}. \quad (3.12)$$

Via the spin flip probabilities, the Potts model translates energy into forces.

Since the probability is  $\exp(-\Delta\mathcal{H}/T)$ , the above arguments hold true for asymmetric temperatures  $T$  as well. Although the term “asymmetric temperature” may sound odd, it occurs often in biological cells. Different types of cells have different intrinsic membrane fluctuation amplitudes. Stronger membrane fluctuations correspond to higher temperatures. When two different membranes touch, the asymmetric membrane fluctuations at the contact surface can be described by “asymmetric temperature,” *i.e.* a spin flip from  $i$  to  $j$  is driven by a stronger force than that from  $j$  to  $i$ .

More generally, to apply force through coupling strengths, we can make  $\mathcal{J}$  a tensor ( $2 \times 2$  in two dimensions) which relates to the stress tensor:

$$\mathcal{J} = \begin{pmatrix} \mathcal{J}_{xx} & \mathcal{J}_{xy} \\ \mathcal{J}_{yx} & \mathcal{J}_{yy} \end{pmatrix}. \quad (3.13)$$

The detailed form of  $\mathcal{J}$  can be as complicated as desired for different effects, *e.g.* asymmetric and time dependent. For example, when we apply uniaxial stress,  $\mathcal{J}$  has perpendicular basis vectors, with diagonal components only:

$$\mathcal{J} = \begin{pmatrix} e^{-\alpha} & 0 \\ 0 & e^\alpha \end{pmatrix}, \quad (3.14)$$

where  $\alpha$ , which can depend on time,  $\alpha = \alpha(t)$ , is a convenient measure of the applied stress field. This choice of  $\mathcal{J}_{xx}, \mathcal{J}_{yy}$  conserves the total area, since extension in the  $x$  direction is compensated by contraction in the  $y$  direction and *vice versa*. Hydrostatic pressure can be readily included if  $\mathcal{J}_{xx} \times \mathcal{J}_{yy} \neq 1$ .

We should emphasize that coupling between spins exerts forces locally, different from a globally applied field.

### 3.2.2 Coupling to an External Field

When an external field acts on the cells, or some subset of cell types, the spins need to couple to the external field. But unlike magnetic materials where spins flip to align or anti-align with the magnetic field, in our extended Potts model, since the spins do not correspond to any microscopic properties, cells keep their identity in the field. The coupling only exerts force on the cell boundaries and the boundary migration results in cell motion. For example, in the case of wet soap foams, where cells have two types, gas and liquid, liquid drains under gravity [chapter 4]. One spin value corresponds to the liquid phase, which is subject to an external gravitational field. The total energy therefore has a potential term, in addition to  $\mathcal{H}_1$  [132]:

$$\mathcal{H}_2 = \mathcal{H}_1 + \sum_{liquid} g z_i, \quad (3.15)$$

where  $g$  is the weight per unit volume and  $z_i$  is the height of the liquid spin. As the foam tries to minimize the total energy, lower positions for liquid spins are favorable. Therefore, the spin flip probability is higher for liquid spins to move downward than in any other directions, as illustrated in Figure 3.5 on a nearest neighbor square lattice.

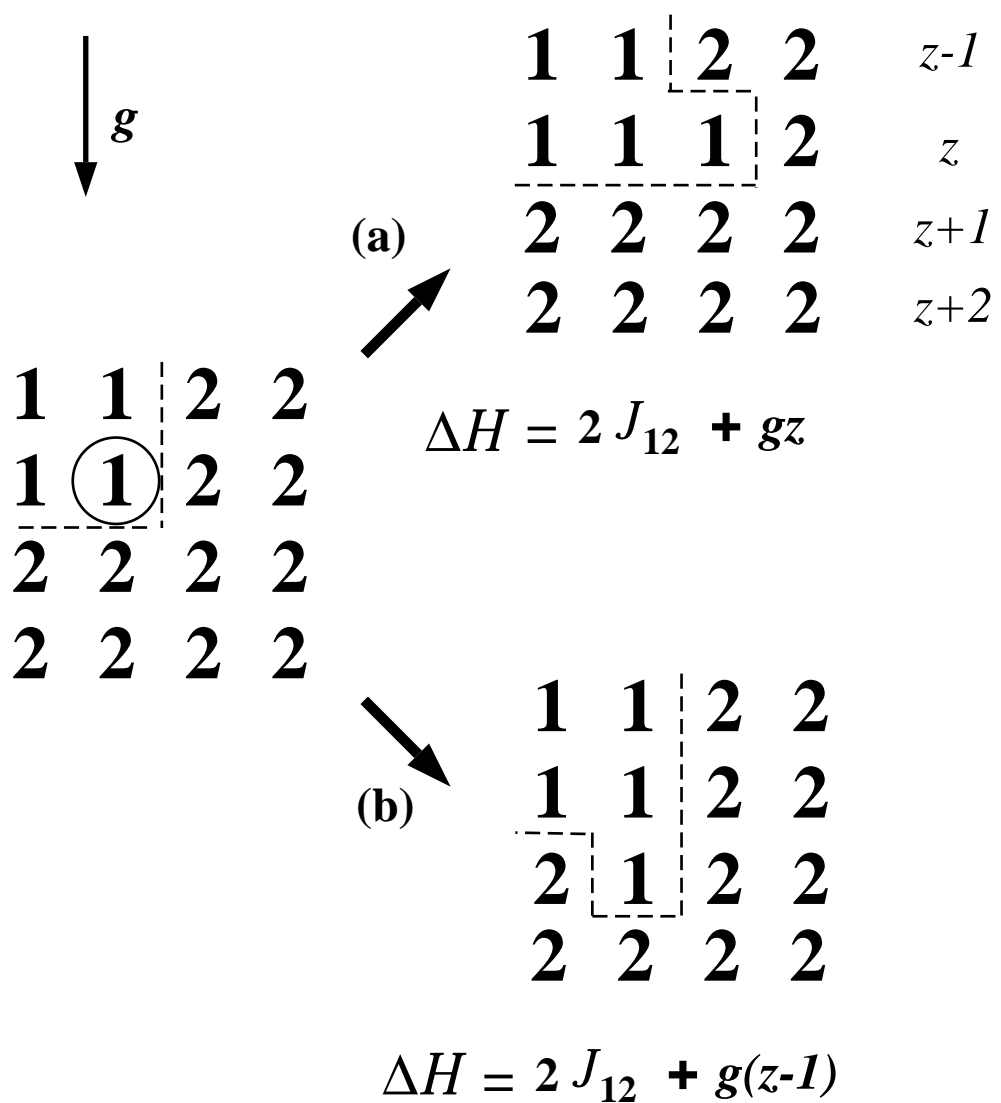


Figure 3.5: Effect of an external gravitational field in the Potts model. Spin 1 is a liquid subject to gravity and spin 2 is a gas.  $z$  is the height of the spins.  $\Delta\mathcal{H}$  is the energy difference after the spin flip.

The ratio between the probabilities of a side-ways flip and a downward flip is:

$$\exp(-\Delta\mathcal{H}_a) : \exp(-\Delta\mathcal{H}_b) = \exp(-g) < 1. \quad (3.16)$$

The coupling between liquid spins and the gravitational field does not change the liquid spins to other values if their total volume is constrained, but rather biases the probable direction their motion.

Similar terms can model biological cell chemotactic motion when external chemical gradients guide cell movement in the direction of higher or lower chemical concentration. Given that the cell velocity is proportional to the local chemical gradient [245], the modification is

$$\mathcal{H}'_2 = \mathcal{H}_1 + \mu \sum_i C_i, \quad (3.17)$$

where  $\mu$  is the chemical potential,  $C_i$  is the chemical concentration at site  $i$ , and the summation is over lattice sites experiencing chemotaxis. A spin flip causes an energy change  $\Delta\mathcal{H}' = \Delta\mathcal{H} + \mu(C'_i - C_i)$ . For a positive  $\mu$ , if  $C > C'$  then  $\Delta\mathcal{H}' < \Delta\mathcal{H}$  and the probability of accepting the reassignment increases; if  $C < C'$  then  $\Delta\mathcal{H}' > \Delta\mathcal{H}$  and the probability decreases; if  $C = C'$  the probability does not change. So, over time, boundaries move more often into sites with higher concentrations than with lower concentrations, and the cell migrates up the chemical gradient. The direction can be changed by simply changing the sign of  $\mu$ . Chapter 6 discusses cell chemotaxis.

### 3.2.3 Constraints

In the Potts model, coupling between spins and coupling to external fields both exert local forces that depend only on local spin configurations. Non-local forces such as those depending on global properties, like cell volume or substrate curvature, can be treated as constraints. In general, we can add a constraint to the total energy,

just as a constraint is included in the Lagrangian:

$$\mathcal{H}_c = \sum_{\sigma} \sum_{\alpha=1}^{\infty} \Gamma_{\alpha} [f(\sigma) - F(\tau(\sigma))]^{\alpha}, \quad (3.18)$$

where  $\Gamma$  is the equivalent Lagrange multiplier,  $f$  is the actual value of some property of cell  $\sigma$ ,  $F$  is the constrained value, and  $\alpha$  indicates different orders of constraints. When the pattern satisfies the constraint,  $\mathcal{H}_c = 0$ , with an energy penalty increasing for worse constraint violation.

Biological cells generally have a fixed range of sizes. They do not grow unboundedly nor shrink and disappear like coarsening soap bubbles. We include this constraint in the form of an elastic term with elastic constant  $\Gamma$ , and a fixed target size  $V$ , which may depend on cell type. The total energy becomes:

$$\mathcal{H}_3 = \mathcal{H}_1 + \sum_{\sigma} \Gamma(\tau(\sigma)) [v(\sigma) - V(\tau(\sigma))]^2, \quad (3.19)$$

where  $v(\sigma)$  is the volume of cell  $\sigma$  and  $V(\tau(\sigma))$  is the type dependent target volume. Deviation from the target volume increases the total energy and therefore is not favored. This term is the lowest order expansion of the volume energy, the elastic approximation. More sophisticated volume energy needs higher powers (4, 6...) for nonlinear features. In practice, unless the total volume of all cells are strictly constrained, all the cells at equilibrium are slightly smaller than their target volumes. This bias can be understood by looking at the total energy  $\mathcal{H}_3$ . As shown in the schematic in Figure 3.6, the volume constraint term (II) is quadratic, an even function of the target volume,  $V^2 \sim r^6$ , *i.e.* the same deviation from the target volume is equally energetically unfavorable, regardless of whether it is larger or smaller than the target volume. The surface area term (I) in  $\mathcal{H}_3$ , however, is a linear function of the total surface area  $\sim r^2$ , which favors smaller total surface areas, hence smaller volume.

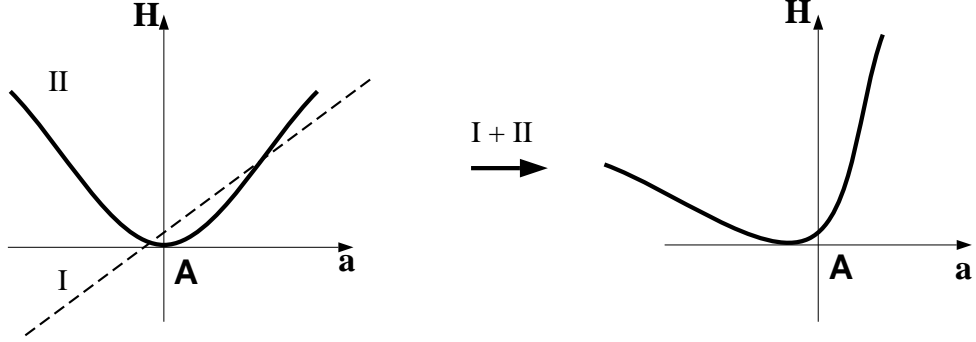


Figure 3.6: Energy sketch for the volume constraint. The solid line is the quadratic volume constraint. The dotted line is the linear surface energy term.

We can rewrite  $\mathcal{H}$  as:

$$\mathcal{H} = Ar^2 + B(r^3 - R^3)^2, \quad (3.20)$$

where  $A$  and  $B$  are constants,  $r$  and  $R$  are the radius of the cell and its target radius, respectively. If we expand  $r = R + \epsilon$  to  $O(\epsilon^2)$ ,

$$\mathcal{H} = A(R + \epsilon)^2 + B[(R + \epsilon)^3 - R^3]^2 = AR^2 + 2AR\epsilon + (A + 9BR^4)\epsilon^2. \quad (3.21)$$

If  $\epsilon < 0$ , the second term can cancel the last one, *i.e.* the loss in total surface energy balances the increase in volume energy. Surface energy minimization lowers the cell volumes. The same arguments hold true in two dimensions. The competition between surface and bulk energy results in smaller areas than the target areas.

For two cells which satisfy their constraints, if a spin flip occurring at the cell boundary causes Cell- $A$  to lose one pixel and Cell- $B$  to gain one, the increased volume energy results in a higher probability for Cell- $A$  to gain one pixel, when the next spin  $A$  at the boundary of Cell- $A$  is chosen for flipping, and for Cell- $B$  to shed one pixel when a boundary spin  $B$  is chosen. Although all the spin updates still occur locally, the volume constraint is non-local, which imposes a long range (of the order of the cell size) interaction on the cells.

Weaire *et al.* [58] modeled foam coarsening using an area constraint term in two dimensions, including von Neumann's law explicitly to control the dynamics in the calculations, and using the hexagonal lattice Potts model only to relax the grain boundaries. Their energy looked very much like  $\mathcal{H}_3$ :

$$\mathcal{H} = \frac{1}{2N} \sum_{\vec{i}, \vec{j}} (1 - \delta_{\sigma_{\vec{i}}, \sigma_{\vec{j}}}) + \frac{\lambda}{N} \sum_n (a_n - A_n)^2, \quad (3.22)$$

where  $A_n$  is the von Neumann's law determined target area for cell  $n$  in two dimensions, and  $N$  is the total number of cells. Surface energy minimization under area constraint leads to minimal surfaces with each cell having a fixed target area. The target areas were updated according to von Neumann's law at each time step.

However, because the Potts Model obeys the Young-Laplace law in a probabilistic fashion, von Neumann's law arises spontaneously. So, Weaire's model is actually redundant. But it has the advantage over the original Potts model,  $\mathcal{H}_1$ , that even cells small relative to the lattice constant properly obey von Neumann's law.

More importantly, this method separates boundary relaxation from gas diffusion. In foams, boundary relaxation is much faster than boundary diffusion, while in metallic grains the two timescales are of the same order. But the conventional Potts model does not distinguish these two timescales. Hence the Potts model can give non-minimal surfaces if the boundaries are not fully relaxed, especially when temperature is high or there is a fast external driving force (*e.g.* drainage [Chapter 4] or shear [Chapter 5]). We can change our model as follows: (1) at time 0, switch off the area constraint by letting  $\lambda = 0$  and evolve the pattern to time  $t$ ; (2) turn on the area constraint and relax the boundaries by letting  $\lambda = \lambda$ , and  $A_n = A_n(t)$ . Repeating steps (1) and (2), the Potts model can produce von Neumann coarsening with fully relaxed patterns.

If we let the target volume be time dependent,  $V = V(t)$ , we can model a

whole variety of growth dynamics. Examples include cell growth as a function of nutrient supply (cancerous cell growth [59]), and foam-making from reacting chemicals (sponge making processes [60]).

A completely different class of geometric constraints includes coarsening on a curved surface. Grest *et al.* extended the Potts model to include a linear Gaussian curvature term [61]:

$$\mathcal{H}_k = -c \sum_{\vec{i}} \sum_{\vec{j}} K_{\vec{j}} \delta_{\sigma_{\vec{i}} \sigma_{\vec{j}}}, \quad (3.23)$$

where  $c$  is a constant,  $K_{\vec{j}}$  is the local Gaussian curvature of a surface element at site  $\vec{j}$ . Their simulations on a sphere, torus and a pseudo-sphere agree with the generalized von Neumann's law on curved surfaces [62].

## CHAPTER 4

### GRAIN GROWTH

#### 4.1 Background

The complete prediction of microstructural development in polycrystalline solids as a function of time and temperature is a major objective in materials science, but is not yet possible, primarily due to the complexity of the grain interactions. The evolution of the polycrystalline structure depends on the coordinates of the grain boundary network, the crystallographic orientations of the grains, and the microscopic mechanisms by which elements of the boundaries move [46].

The term grain growth describes the increase in grain size which occurs upon annealing a polycrystalline aggregate after primary recrystallization is complete. Two different types of grain growth have been distinguished – **normal grain growth** and **abnormal grain growth** (or secondary recrystallization) [63]. Normal grain growth refers to the microstructure homogeneously increasing in scale, while abnormal grain growth refers to the rapid increase in size of a few grains, with the maximum grain size increasing at a rate much faster than the mean growth rate [64].

Smith proposed almost half a century ago that coarsening foams can model grain growth in polycrystals [14]. Pressure difference driven gas diffusion in foams and interface energy driven particle motion in polycrystals both result in boundary motion, causing some grains to expand and others to shrink and eventually disappear. The net result of this coarsening is a continual decrease in total boundary length (or interface area), and an increase in mean grain size. The statistical and dynamical

properties of soap froth and metallic polycrystals are rather similar in spite of the different underlying mechanisms. In a soap froth, gas diffusion through the walls determines the motion of cellular boundaries, and the rate of diffusion and therefore the rate of evolution depends on the thickness, composition and surface tension of the soap films. On the other hand, polycrystals are made of monocrystalline grains, and the boundary or interface between two grains has an interface energy. The energy per unit length of the boundary depends on the mis-orientation of the neighboring grains and on the orientation of the boundary itself with respect to the two grain orientations, two aspects of the anisotropy of boundaries in polycrystals. The boundary moves due to rearrangements of the atoms and tends to reduce the interface energy.

Due to the difficulty of visualizing the interior structure of three-dimensional foams and polycrystals, most experiments have been two-dimensional, *e.g.* coarsening dynamics in two-dimensional foams made between two parallel glass plates [11] or in thin film growth [65, 66, 67].

Besides technical applications, a strong theoretical motivation for studying coarsening in cellular structures is that cellular structures provide an example of disordered constrained patterns where a set of rather simple “microscopic” rules produces a nontrivial global nonequilibrium dynamics. The dynamics of the cellular structure is fully deterministic, *i.e.* the evolution is completely determined by the initial configuration. Nevertheless, statistical approaches are very useful. A variety of statistical mechanical models can be built and compared with experiments. Statistical characteristics of the cellular structure are the area distribution and the side distribution (also called the topological distribution). We can also study the corresponding correlation functions among these variables, such as Lewis’ law and Aboav-Weaire’s law (see below).

A few well known experimental facts concerning the dynamics of soap froth and polycrystals are:

1. They are far from equilibrium:

They are not stationary except for some very special initial conditions, *e.g.* a perfect hexagonal array of bubbles in two dimensions. The simple thermodynamic reason for coarsening in cellular patterns is that cell boundaries have an additional free energy proportional to their length or surface area, which drives the evolution to continuously minimize the total surface energy until the pattern becomes a single domain. This equilibrium state is not interesting, so we always study the transient.

2. They obey von Neumann's law in two dimensions:

Foams have two very different dynamic timescales. A fast timescale driven by surface tension minimizes the total length of the network while keeping constant the areas of the domains. The pattern achieves a quasi-static equilibrium. A much slower timescale is the gas diffusion driven by pressure differences across cell boundaries. In metallic polycrystals, however, these two timescales are comparable. The boundaries are not always at equilibrium, and they are not always minimal surfaces but can be significantly irregular. Figure 4.1 shows a cross section of a low carbon steel, arrows indicating a few non-equilibrium features: boundaries do not have constant curvature and contact angles are not  $120^\circ$  degrees.

Smith [69], supported by a series of experiments, proposed that the irregularities of the metal boundaries averaged out over a sufficiently large population of grains. Hence, both soap froth and metals obey von Neumann's law, Equation 2.3.

von Neumann's law states that cells with more than six sides expand, while cells with fewer than six neighbors shrink and eventually disappear. Coarsening depends only on  $n$ , the coarsest topological quantity.

3. Topological requirements:

The **topological charge** is  $\tau \equiv n - 6$ . The sum of topological charge over the pattern is a constant by virtue of Euler's theorem, which gives a conservation law for the faces ( $F$ ), edges ( $E$ ) and vertices ( $V$ ) of any cellular structure, provided that the face or cell at infinity is not counted:

$$F - E + V = 1. \quad (4.1)$$

In two dimensions, topologically stable patterns have coordination number (number of edges meeting at the same vertex) 3, so the average number of edges  $\langle n \rangle$  can be determined as follows. Three cells share each vertex and each cell has  $\langle n \rangle$  edges or vertices on average, so,

$$\langle n \rangle F = 3V. \quad (4.2)$$

Two cells share each edge,

$$\langle n \rangle F = 2E. \quad (4.3)$$

Applying Euler's theorem, we have:

$$F - \frac{1}{2}\langle n \rangle F + \frac{1}{3}\langle n \rangle F = 1. \quad (4.4)$$

So  $\langle n \rangle = 6\frac{F-1}{F}$ , which tends towards 6 for an infinite system,  $F \rightarrow \infty$ . Hence the topological charge summed over all cells:

$$\sum_i \tau_i = \sum_i n_i - 6F = -6, \quad (4.5)$$

is a constant, independent of the number of cells, *i.e.* topological charge cannot be destroyed, it can only be redistributed [27].

In three dimensions, the analogy fails since the number of polyhedra,  $P$ , is an extra degree of freedom:

$$-P + F - E + V = 1. \quad (4.6)$$

The topological charge is undetermined. For a three-dimensional cellular pattern where all vertices have coordination number 4, the average number of faces  $\langle f \rangle$  and the average number of sides per face  $\langle n \rangle$  have the relation:

$$\langle f \rangle = \frac{12}{6 - \langle n \rangle}. \quad (4.7)$$

#### 4. Topological rearrangements:

At first glance von Neumann's law appears to lead to the disappearance of all the cells with fewer than 6 sides and thus a large size separation among the cells with different numbers of sides. However, when a cell disappears, its neighbors can either gain or lose sides (*i.e.* change from one topological class to another). On average, the neighbors lose sides to preserve the topological charge. These topological rearrangements exchange cells between topological classes. Recall that Euler's theorem implies that  $\langle n \rangle = 6$ , so cells with fewer than six sides are always present in the foam unless all the cells are hexagons.

Cell rearrangements fall into two classes, the T1 process and the T2 process. Shown in Figure 4.2, neighbor switching (the T1 process) preserves the number of cells. Two cells gain one side and the other two lose one side; the local topological charge stays constant. The disappearance of a triangle, square, or a pentagon (T2 process), shown in Figure 4.3, decreases the number of cells and the local topological charge redistributes. In a T2(3) process, all three neighbors lose one side. In a T2(4) process, the four-sided cell first shrinks to a four-fold vertex, which then splits into a pair of three-fold vertices. Two cells lose sides while two stay unchanged. Constraints from neighboring cells determine the orientation of the new wall, except in the low probability completely symmetric case where the symmetry breaking

would be probabilistic.

### 5. Scaling regime:

Although these cellular patterns are far from equilibrium, experiments reveal that the patterns evolve into a **scaling state** in which they evolve self-similarly. Standard measurements for cellular patterns are the topological distributions, area distributions, correlations and boundary lengths – all quantities which can be measured in experiments. The topological distribution function,  $\rho(n)$ , the probability of a cell having  $n$  sides, and the rescaled size distribution functions  $\rho(a/\langle a \rangle)$ , where  $\langle a \rangle$  is the mean area, remain constant in the scaling state, while the length scale increases in time. The  $m$ th moments of the distributions are:

$$\mu_m(x) \equiv \sum_x \rho(x)(x - \langle x \rangle)^m, \quad (4.8)$$

among which  $\mu_2(n)$  is the most commonly used. The scaling regime was observed in experiments on aluminum foils [26] as well as soap foams [17]. The topological distribution tends to a stationary scaling form and  $\mu_2(n)$  assumes a roughly constant value. Two-dimensional soap froth experiments with up to 10000 bubbles in the initial state [11, 17] and early smaller simulations [71] gave a value of  $\mu_2(n) = 1.4$  in the scaling regime. Other simulations showed a slightly lower value of  $\mu_2 = 1.2$  [79].

The scaling hypothesis can be expressed as:

$$\frac{N_n(a, t)}{N(t)} = \frac{1}{a} f_n\left(\frac{a}{\langle a \rangle}\right), \quad (4.9)$$

where  $N_n$  is the number of  $n$ -sided cells with areas between  $a$  and  $a+da$ ,  $N(t)$  is the total number of cells and  $f_n(x)$  is some function. Experiments and simulations suggest that the distribution function  $f_n(x)$  is universal, independent of the microscopic mechanisms underlying the dynamics. Figure 4.4 shows  $\rho(n)$  for a two-dimensional

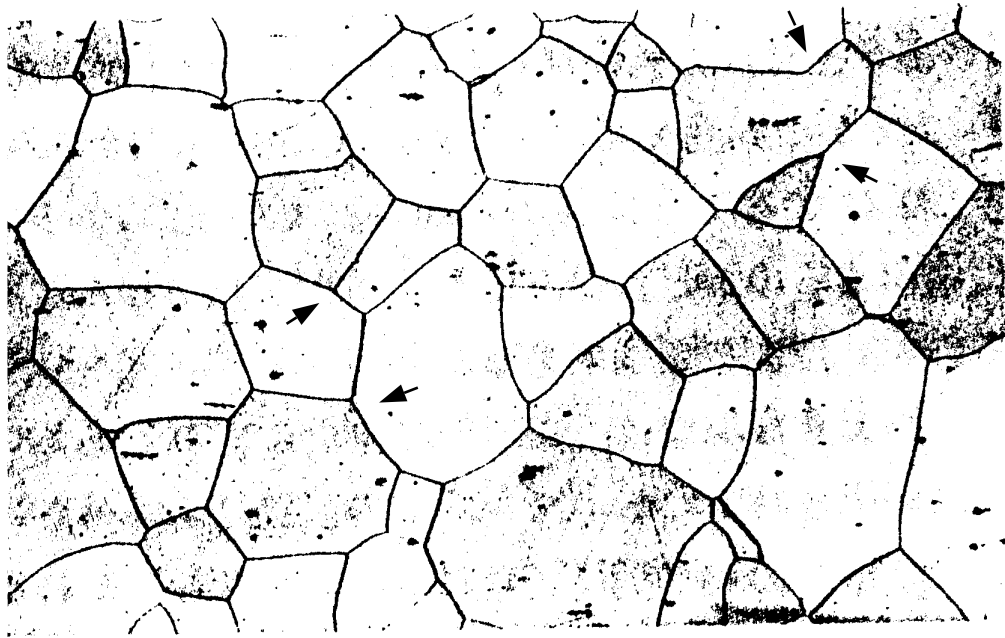


Figure 4.1: Crystal morphology of a cross section of a low-carbon alloy steel ( $10\%Cr - 2.6\%Si - 0.35\%Al$ ), with average grain size  $10^{-2}cm$ . Arrows indicate some non-equilibrium features of the pattern. [From Nagai, Kawasaki and Nakamura [70]].

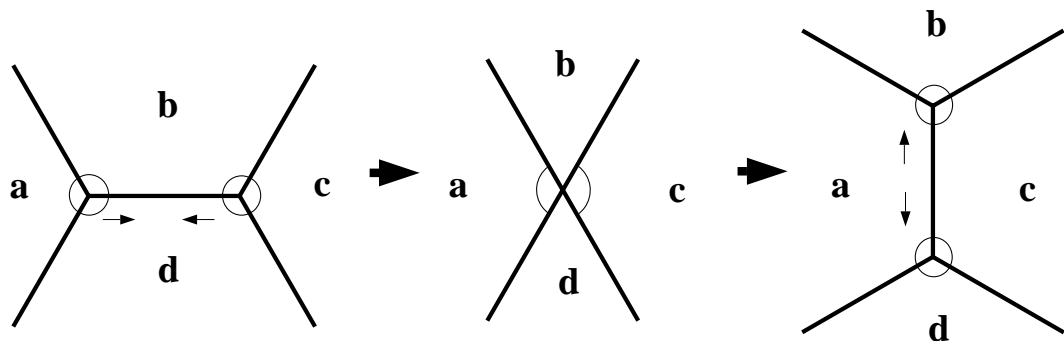


Figure 4.2: T1 process: the wall between bubbles **b** and **d** disappears and a new wall forms between bubble **a** and **c**. Bubbles **a** and **c** become neighbors and both gain one side.

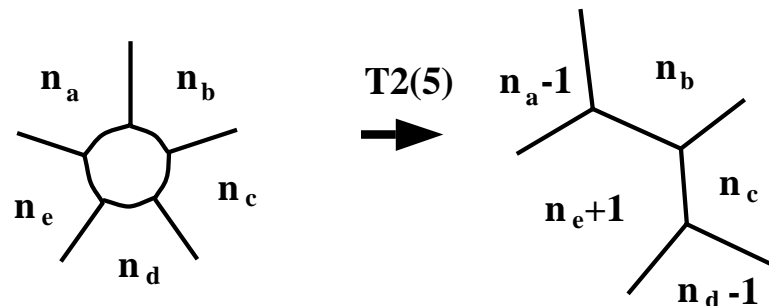
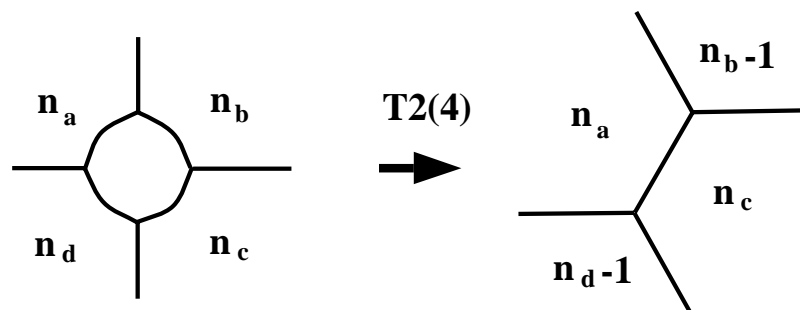
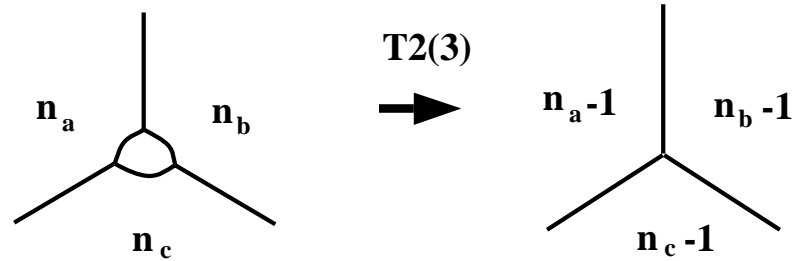


Figure 4.3: T2 processes: disappearance of a triangle, a square and a pentagon.

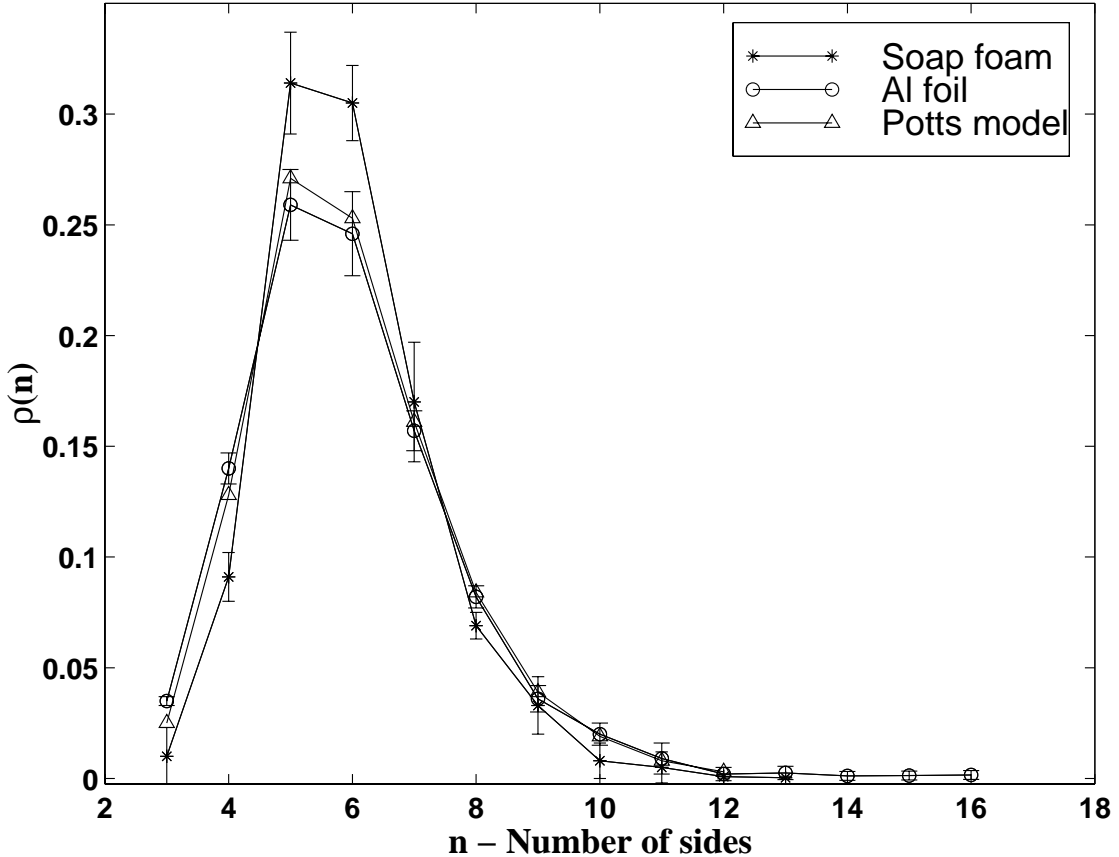


Figure 4.4: Topological distribution functions for a two-dimensional soap foam [11], an aluminum foil [26] and a Potts model simulation on a nearest-neighbor triangular lattice [84].

soap froth [11], an aluminum thin film [26] and a Potts model simulation on a triangular lattice with nearest neighbor interaction [84].

Combining von Neumann's law and the scaling hypothesis, from dimensional arguments, the average cell area grows as [72]:

$$\langle a(t) \rangle \sim t^\alpha, \quad (4.10)$$

where  $\alpha = 1$ . The same linear area growth in the scaling regime applies to both two-dimensional metallic polycrystals and soap froth. But this linear growth occurs only for pure metals with low surface energy anisotropy and for specially prepared

dry soap foams (where the bubble walls maintain the same width, *i.e.* no liquid drainage, accumulation, or wall rupture, throughout the evolution). For dirty metals (*e.g.* with impurities) and usual soap froth (wet foam) the growth exponent  $\alpha$  is less than 1.

## 6. Correlations: Lewis's Law and Aboav-Weaire's Law:

Lewis discovered a simple linear relationship between cell area and topology in cucumber skin, human amnion and pigmented epithelium of the retina [73, 74]:

$$\langle a_n \rangle = c_1 + c_2 n, \quad (4.11)$$

where  $a_n$  is the area of an  $n$ -sided cell and  $c_1$  and  $c_2$  are fitting parameters. Most undifferentiated biological tissues seem to obey this phenomenological law, though the evidence is not conclusive [75]. Rivier and Lissowski [76], using a maximum entropy argument applied to the topological distribution  $\rho(n)$ , derived Lewis's law. But Equation 4.11 fails for both soap froth and metal grains [11]. From two-dimensional soap froth data and Potts model simulations, Glazier and Weaire [77] concluded that Lewis's law holds only for materials which have a constrained area distribution, while for coarsening cellular patterns the average radius of cells with  $n$  sides linearly depends on  $n$ :

$$\langle r_n \rangle = c_1 + c_2 n. \quad (4.12)$$

Iglesias and de Almeida have given a maximum entropy argument for a similar perimeter law [78]

$$a_n / \langle a_n \rangle \propto n^2. \quad (4.13)$$

Herdle and Aref's simulations of ideal dry froth found that a linear relation could fit both average areas and average perimeters, though for small  $n$  the perimeter fit

was slightly better [79]. Flyvbjerg [80], based on a random neighbor mean field model, argued that Lewis's law is asymptotically true for large  $n$ .

Aboav [81] suggested an inverse correlation between a cell's number of sides  $n$  and the number of sides of its neighbors  $m(n)$ , the nearest-neighbor topological correlation of bubbles, with the basic form:

$$m(n) = A + \frac{B}{n}, \quad (4.14)$$

where  $m(n)$  is the mean topology of nearest neighbors of an  $n$ -sided cell and the values of  $A$  and  $B$  were empirically determined to be 5 and 8 respectively. Weaire developed this relation into what is known as Aboav-Weaire's law:

$$m(n) = 6 - \alpha + [6\alpha + \mu_2(n)]/n, \quad (4.15)$$

where  $\alpha$  is a constant of order 1 [81, 82, 83]. Stavans *et al.* measured  $m(n)$  for a scaling state of a two-dimensional helium froth and found excellent agreement with Aboav-Weaire's law with  $\mu_2(n) = 1.4, \alpha = 1$  [17]. A detailed comparison between  $m(n)$  for soap froth and the Potts model simulations can be found in [11, 84].

The correct description of pattern evolution should include these neighbor correlations. But we often use the distribution functions and their second moments to describe the pattern.

## 4.2 Mean Field Theories

The analytical treatment of the evolution of cellular patterns is very difficult because of the random nature of foams and the topological correlations between cells. However, neglecting the topological correlations by effectively replacing  $m(n)$  with  $m(6)$ , allows various mean field theories [85]. This approximation is worse for cells with fewer sides, which fortunately are rare [80].

Fradkov [86, 87] and Beenakker [88] suggested a mean field description and derived the corresponding kinetic (Master) equations for the distributions using a “gas” approximation, *i.e.* no correlations for cells. Flyvbjerg and Jeppesen [89, 80] used a very similar description. The main simplifying assumption is that all the cells are completely uncorrelated. The cells then can behave as points moving in a two-dimensional phase space  $a - n$  (area *vs.* side or topological class). The area is the coordinate of a particle while  $n - 6$  corresponds to its velocity, as determined by von Neumann’s Law. The velocities of particles are different for different topological classes and the points can change their velocities due to collisions when they transfer from one class to another. When a particle reaches  $a = 0$ , it disappears and the consequent T2 process results in a transition to new topological classes for randomly selected cells. The Master equation for the concentrations  $\rho(n) = N_n(a, t)/N(t)$  takes the form:

$$\frac{\partial \rho(n)}{\partial t} + \dot{a} \frac{\partial \rho(n)}{\partial a} = [C_-(n+1)\rho(n+1) - (C_- + C_+)n\rho(n) + C_+(n-1)\rho(n-1)] + 2\rho(n), \quad (4.16)$$

where  $\dot{a}$  is determined by von Neumann’s Law;  $C_-$  and  $C_+$  are the rates at which an  $n$ -sided cell loses or gain one side, due to T2 processes. Since T2s involve the disappearance of triangles, squares and pentagons, these rates depends on the corresponding concentrations  $\rho(3), \rho(4), \rho(5)$  at  $a = 0$ . T1-processes can be included but only with an arbitrary rate constant which is a major shortcoming for mean field models. The expression in square brackets stands for the transition probability between the topological classes due to a *T2* process while the addition of the last term guarantees  $\sum_n \rho(n) = 1$ . In the scaling regime  $\langle a(t) \rangle$  is expected to grow linearly in time. The scaling distributions can be obtained by substituting,

$$\rho(n, a) = \frac{1}{t} f_n\left(\frac{a}{t}\right), \quad (4.17)$$

where the scaling function  $f_n$  follows

$$\frac{\partial f_n}{\partial t} + (n - 6 - x) \frac{\partial f_n}{\partial x} = C_-(n+1)f_{n_1} - [(C_- + C_+)n - 2]f_n + C_+(n-1)f_{n-1}, \quad (4.18)$$

where  $x = a / < a >$  is the rescaled area. Equation 4.18 is both nonlinear and nonlocal, since  $C_-$  and  $C_+$  are functions of  $f_3(0)$ ,  $f_4(0)$  and  $f_5(0)$ . However, it can be treated as a linear equation by considering constant  $C_-$  and  $C_+$ , and then solved for  $C_-$  and  $C_+$  self-consistently.

Fradkov [86] was first to derive an equation of this kind but did not try to solve it. He characterized the Master equation as “very difficult for analytical treatment” (because of the nonlinearity) and used it only to derive a few simple relations and did not attempt to solve it numerically, restricting himself to Monte Carlo simulations.

Instead of solving the Master equation or doing Monte Carlo simulations, we can simulate the “molecular dynamics” of the “gas” particles directly as follows. The particles are characterized by their areas and their number of sides. The initial values are taken such that the average number of sides is 6 while the areas are random. At each time step the areas change according to von Neumann’s law. When some of the areas reach zero, some randomly chosen particles change their topology according to the T2 rules. For example, when a pentagon vanishes, pick at random three particles, two of them lose a side and the third gains a side. To conserve the total number of particles, new particles have to be created in such a way that the topological and area distributions are not disturbed. The simplest way is just to duplicate a randomly chosen particle. This process is described by the Master equation and its realizations are solutions. Conserving the total number of particles eliminates restrictions on simulation time.

This model can take into account explicitly the effects of topological correlations: instead of randomly picking the cells affected by the T2 processes, only the neighboring cells change their topological classes. The “topological network models” [80, 88] maintain a list of neighboring cells at all times and consider the nearest neighbor correlations of bubbles. But they assume the neighbors of the vanishing cell randomly gain or lose sides, while the choice in real materials depends in a complex but deterministic way on the detailed geometry rather than the topological distributions and correlations.

The difficulties in solving equations 4.16 and 4.11 called for a simpler description of coarsening. Indeed, it is possible to separate the topological and area components of the dynamics. Stavans, Domany and Mukamel [90] proposed a mean field model which describes the dynamics of the soap froth in terms of the topological distribution  $\rho(n)$  without considering the areas. The advantage of this model is that instead of differential equations for the distribution  $f_n(a)$ , it has only algebraic equations which can be solved analytically. The model changes cell sides according to the rules for T2 processes. The relative probabilities of the vanishing of a triangle, square and pentagon are  $W_3$ ,  $W_4$  and  $W_5$ , which in principle can be determined experimentally. Only two of these rates are independent because the sum  $W_3 + W_4 + W_5$  determines the time scale. The rate of disappearance of an  $n$ -sided cell is:

$$\frac{dN_n(t)}{dt} = -W_n N_n(t). \quad (4.19)$$

Notice that this equation represents only the rate of disappearance of  $n$ -sided cells due to their areas vanishing. The rates are proportional to the number of  $n$ -sided cells which have zero area  $N_n(a, t)|_{z=0}$ . Hence:

$$\frac{dN_n(t)}{dt} = N_n(0, t) \frac{da_n}{dt} = N_n(0, t) k(n-6), \quad (4.20)$$

where the second step uses von Neumann's law. Therefore,

$$W_n = -k(n-6) \frac{N_l(0,t)}{N_n(t)} = \frac{N_n(0,t)}{N(t)} \frac{N(t)}{N_n(t)}. \quad (4.21)$$

In the scaling regime,

$$\frac{N_n(a,t)}{N(t)e} = \frac{1}{\langle a \rangle} f_n\left[\frac{a}{\langle a \rangle}\right], \quad (4.22)$$

and

$$\frac{N_n(t)}{N(t)} = \int \frac{1}{\langle a \rangle} f_n\left[\frac{a}{\langle a \rangle}\right] da = \int f_n(x) dx. \quad (4.23)$$

Since this calculation does not depend on the initial conditions, all initial conditions reach a scaling state at long times in this mean field model. The scaling function,  $f_n$ , represents a family of stable scaling solutions, raising intriguing questions about the mechanism by which soap froth, polycrystals and the Potts model all select one particular solution [11, 80, 90, 71, 91, 92].

### 4.3 Abnormal Grain Growth

In addition to the rate of equilibration, the other main distinction between soap foams and polycrystals is anisotropy. In foams, the surface energy is isotropic while in polycrystals, surface anisotropy plays an important role in growth and can not be ignored. von Neumann's law does not consider boundary anisotropy.

Abnormal grain growth occurs when the boundaries surrounding a few grains move relatively rapidly while other boundaries are relatively stationary, *i.e.* a few grains grow much faster than the rest.

Often abnormal grain growth requires normal grain growth to be impeded, with the exception of a few grains which act as nuclei for abnormal grain growth [93].

Several factors have been suggested to contribute to the inhibition of normal grain growth [94]:

- Grain boundary grooving in thin films and sheets.
- Impurity particle induced pinning of boundaries.
- Texture inhibition in a material with strong preferred orientation.
- Impurity inhibition by zone refining.

Srolovitz *et al.* modeled two-dimensional grain growth in the presence of a second-phase particle dispersion using the large- $Q$  Potts model [41]. They randomly select lattice sites and assign to them spins that do not interact with the rest of the spins. Each particle occupies one lattice site. The particle concentration and spatial location are fixed during grain growth. Simulations for different particle concentrations show that grains exhibit normal growth at first, followed by an abrupt transition to a pinned state. Figure 4.5 shows the pinned patterns for four different particle concentrations. During the normal growth phase, mean grain size grows as  $r \sim t^\alpha$  with  $\alpha = 0.39 \pm 0.02$ , close to that in the absence of particles. The average grain area at pinning is inversely proportional to the particle concentration, which is attributed to the eliminating of boundary curvature by particles when they intersect boundaries, as illustrated in Figure 4.6. The shifting of boundary curvature halts further grain boundary movement, leading to pinning of the entire pattern when, on average, each boundary has one particle or equivalently three particles per grain. Yabushita *et al.* [95] used the same model but with different sizes of particles and found that larger particles reside exclusively in the grain boundaries, which they interpreted as an increased pinning effect.

Hillert [96] and Detert [64] suggested that removing second-phase particles from

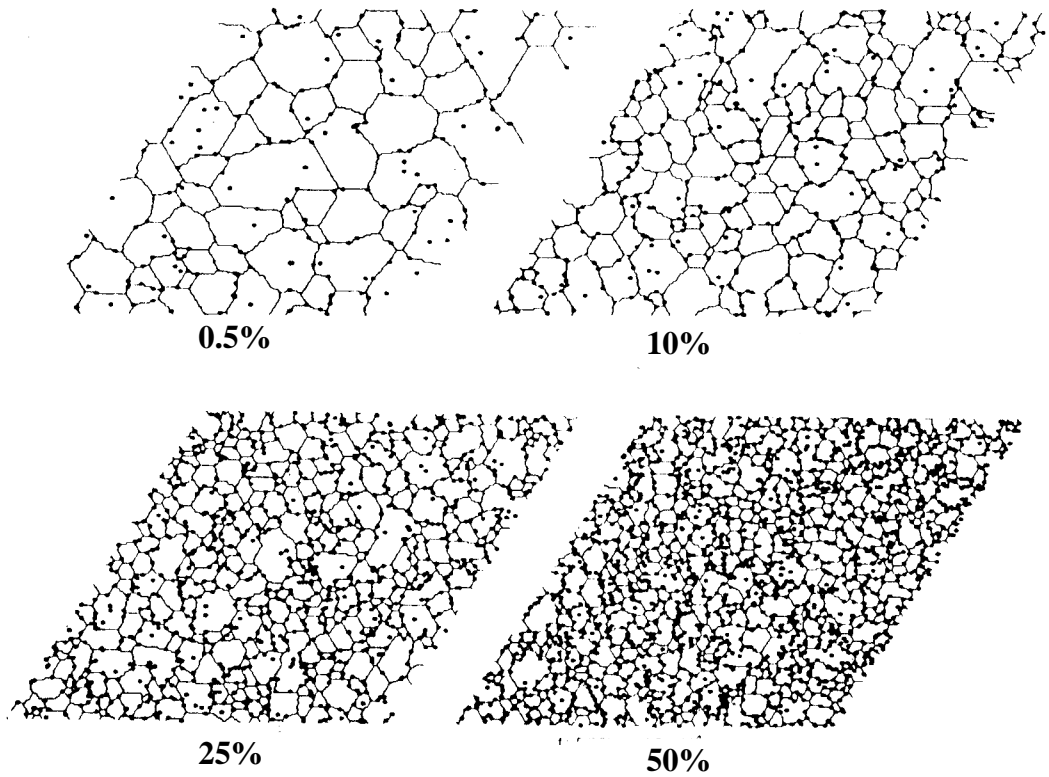


Figure 4.5: Potts model simulations of pinned microstructures for four pinning particle concentrations. [From Srolovitz *et al.* [41]].

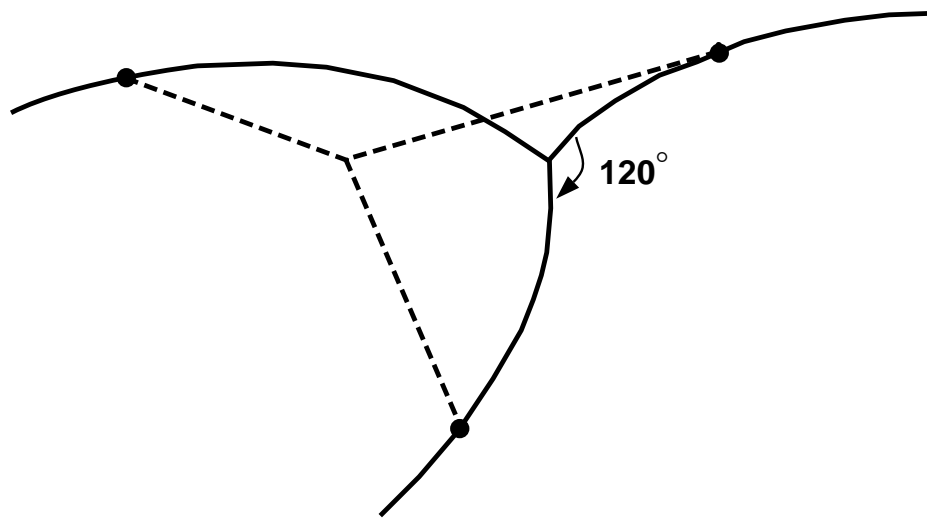


Figure 4.6: Schematic showing grain boundary curvature elimination. The vertex with three particle-pinned boundaries translates and rotates. The curved lines are the initial grain boundary shape and the dotted straight lines are the grain boundary configuration following the vertex translation and rotation. [Redrawn from Srolovitz *et al.* [41]].

the pinned stage can lead to abnormal growth. Srolovitz *et al.* [42] tested this idea by gradually decreasing the particle density. They found that homogeneous decrease of particles does not lead to abnormal grain growth. However, in real materials, particles may disappear preferentially in one part of the microstructure due to non-uniformities in temperature, solute concentration, stress, *etc...* The simulations indeed show that grain growth proceeds within the particle free region but is restrained by the neighboring pinned grains.

Since the boundary velocity is a driving force times a boundary mobility, the standard belief is that abnormal grain growth results from spatial variation in forces or mobility. “Abnormal grain growth may then result either from an abnormally high mobility, or from the existence of a higher driving force. We may note that abnormal growth is not expected to occur solely as a result of an initial size advantage” [109]. The reasoning is the following: although an extra-large grain may grow faster than its neighbors, it will not grow relatively faster than the average size of normal grains. Also, in a moderately disordered pattern, many-sided cells tend to lose sides as they grow, *i.e.* the topological distribution regresses to the mean. If the initial structure does not contain any abnormally large grains, they should not develop from geometrical considerations alone.

Simulations of the abnormal growth of a grain due to the enhanced mobility of all its boundaries were reported in [108, 49, 42]. The result of such abnormal growth is that the abnormal grain grows relative to the average normal grain size until its relative size asymptotically reaches a certain value. Another possible source of abnormal grain growth is a difference in the driving force for abnormal grains. One likely source of driving forces in addition to grain boundary capillarity is that different grains, with different crystallographic orientations, may have different surface energies for the interfaces between the film and its exterior surroundings, either

free-surface energies or film-to-substrate interface energies. If the free-surface energy of one grain is different from that of a neighboring grain, then an additional force drives the boundary which separates the two grains to migrate to expand the lower-energy surface at the expense of the higher-energy one.

In our simulations of grain growth from a single defect, we show a new source of abnormal grain growth: topological defects. As long as the topological defects are widely spaced, abnormal grain growth can occur with isotropic and homogeneous surface energy.

#### 4.4 Defect Growth

In a recent model of the time evolution of two-dimensional soap froth with a single defect [97], Levitan challenged the common wisdom that the scaling state dynamics does not depend on the initial condition. Using a mean-field treatment, he claimed that the long-time distribution function  $\rho(n)$  from generic initial conditions differs from that for an initial hexagonal lattice with only one defect. He also found the scaling law that the number of cells in the evolving cluster follows  $N(t) \sim t$ . This work excited considerable interest and some controversy [98, 99]. We used the large- $Q$  Potts model to examine the evolution of a single defect in a lattice of perfect hexagonal foam in two dimensions and study its scaling state [100],

A perfect hexagonal foam is stable for all time. We put in the center of the lattice a grain with area somewhat greater than the mean area of the hexagons so that it has more than six sides at time zero. The defect functions as a seed for the evolution. Therefore the pattern consists of two parts: the evolving neighborhood of the defect, and the rest of the lattice which does not evolve. As the pattern evolves in time, the boundary of the disordered region propagates outwards.

We used the Potts Hamiltonian, Equation 3.1, in the  $T = 0$  limit on a  $2000 \times 2000$  lattice, running until the disordered cluster reached the boundaries of the lattice. For

our simulations, we chose a fourth nearest neighbor square lattice (lattice anisotropy 1.037, see Table 3.1), which is known to evolve in a manner very close to ideal grain growth [56].

In agreement with Levitan [97], we defined the disordered cluster to consist of all grains with at least one non-hexagonal neighbor, yielding a large grain in the center and a boundary of grains around it. Figure 4.7 shows snapshots of the evolution.

As we can see from the figures, the center grain grows much faster than the grains at its boundary, whose average area randomly fluctuates around a value  $\langle a \rangle' = (0.88 \pm 0.08)a_0$ , where  $a_0$  is the initial area of the hexagons. The grains outside the cluster remain unchanged. The disordered cluster maintains a bilayer of grains around the large grain; that is, the large grain grows at the same rate as disorder propagates outward in the pattern. The diameter of the cluster grows linearly in time, while the area of the cluster grows quadratically. This result is trivial if we consider a big grain growing without affecting neighboring non-evolving small grains. Its number of sides (number of neighbors) is proportional to its perimeter, *i.e.*,  $n \sim d$ , with  $d$  being the diameter of the big grain, *i.e.* the normal velocity of the propagating front is constant. Using von Neumann's law:

$$\frac{da_n}{dt} \sim n \sim d \sim \sqrt{a_n} . \quad (4.24)$$

Equation 4.24 gives  $a \sim t^2$  and  $d \sim t$ . Also, the large center grain determines the diameter and the total area of the cluster. Therefore the cluster grows like the large center bubble, as shown in Figure 4.8.

The number of grains in the cluster grows linearly, as shown in Figure 4.8. This result is again trivial, although not obvious, since the total number of grains in the cluster  $n_c \sim n$  (the number of neighbors of the center grain),  $n_c \sim t$ , agrees with [97].

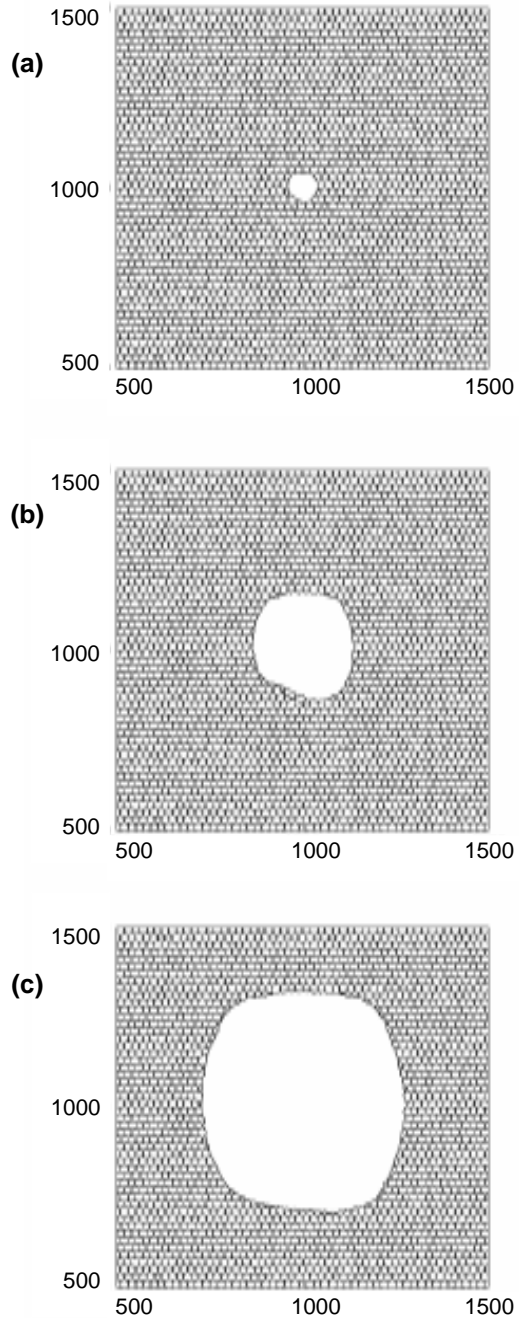


Figure 4.7: Snapshots of the time evolution of an initially hexagonal pattern with a single defect: (a) 0 MCS, (b) 5000 MCS, (c) 10000 MCS. Figures show the center 1/4 of the whole pattern.

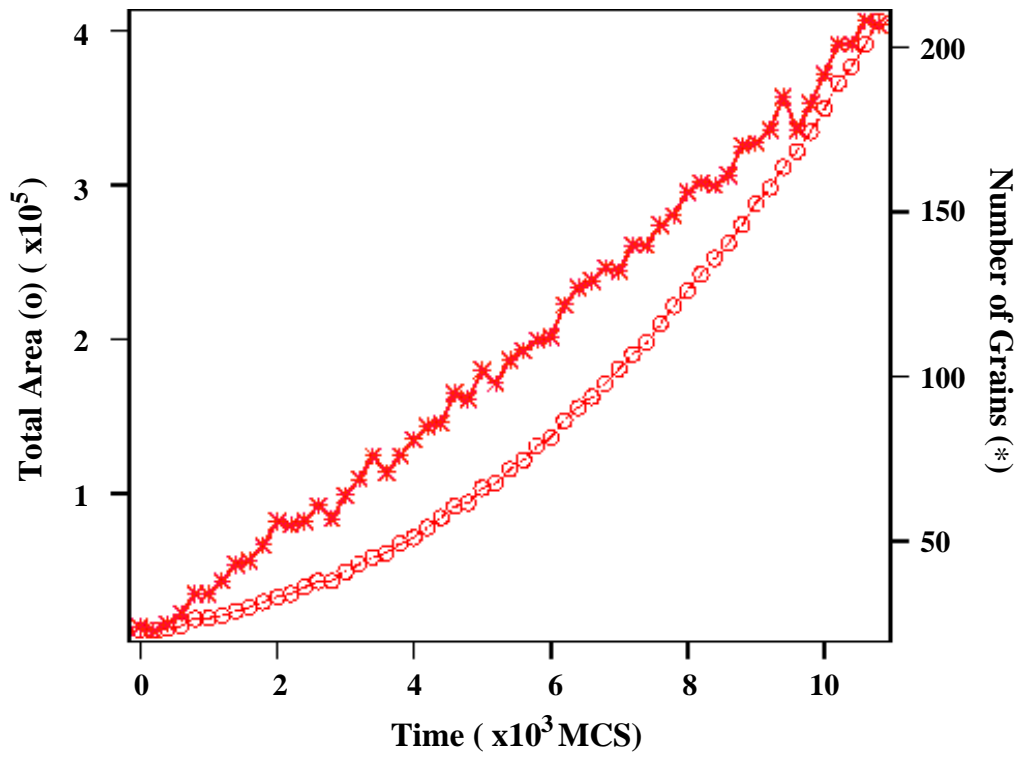


Figure 4.8: Evolution of the disordered cluster. The total area of the cluster ( $\circ$ ) grows quadratically while the number of grains in the cluster ( $*$ ) grows linearly.

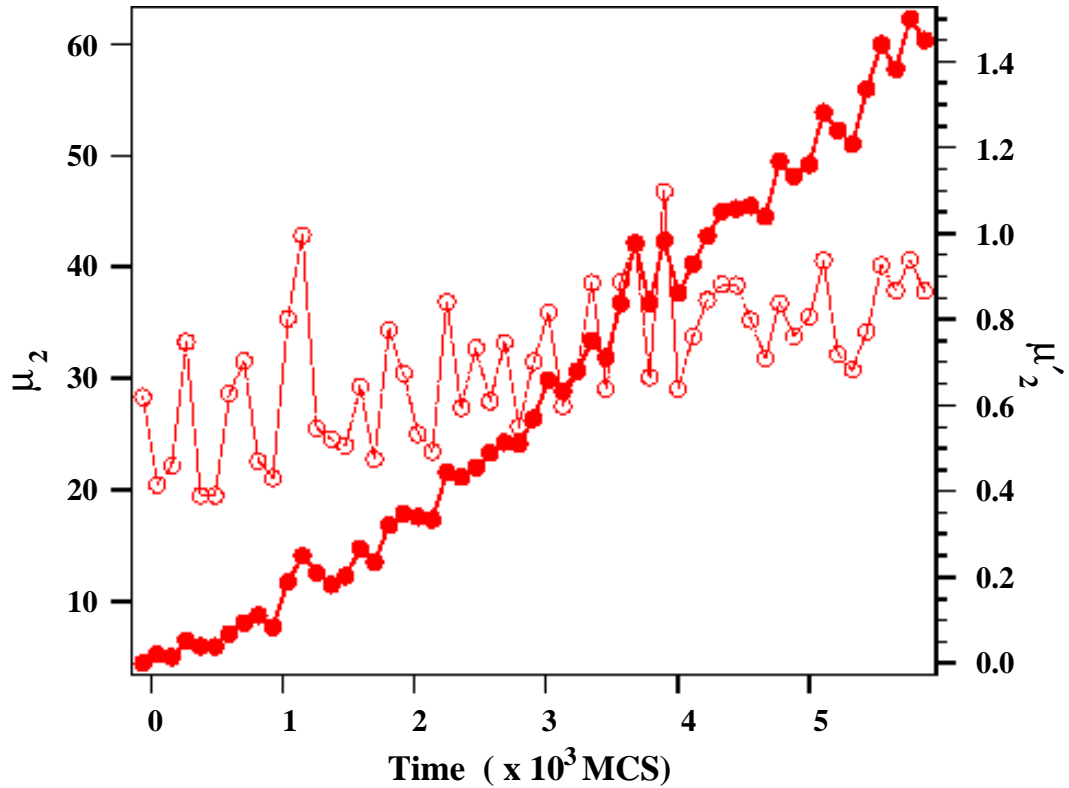


Figure 4.9: The second moment of  $\rho(n)$  of the cluster ( $\mu_2$ , bullets) and the boundary ( $\mu'_2$ , circles).

The average area of the grains in the cluster, as we predict, ( $\langle a \rangle = \langle a/n \rangle \sim t^2/t \sim t$ ) grows linearly, accidentally mimicking a normal scaling state, whereas the average area of the grains in the cluster boundary is constant.

The tail of the topological distribution function,  $\rho(n)$ , extends towards larger and larger values of  $n$ , corresponding to the large center grain. The peak stays at  $n = 6$  due to our definition of the cluster. The second moment of the topological distribution, dominated by the large grain, grows linearly (Figure 4.9), consistent with the data of Aboav [83], for the transient behavior of samples which are initially almost hexagonal. If we exclude the large grain in the center, the rest of the cluster presents a  $\mu'_2$  fluctuating around a constant value of about 0.7 (Figure 4.9) and

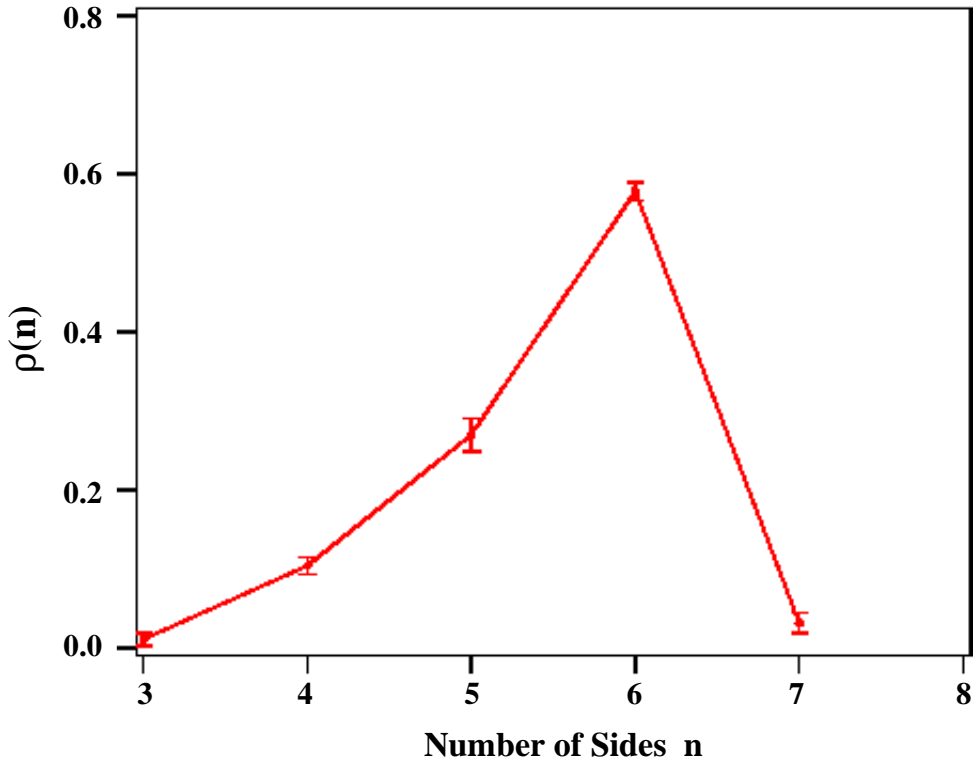


Figure 4.10: Topological distribution,  $\rho(n)$ , excluding the large center grain, averaged over six different times between 6000MCS and 10600MCS. Error bars indicate standard deviation from the mean.

the topological distribution is constant (Figure 4.10). Thus, the boundary of the cluster preserves self-similar growth, yielding a special scaling state of constant length scale. We never reach a normal scaling state. The mean field theory fails because in this pattern, the large grain, the boundary grains and the remaining hexagonal grains form three distinct classes with fixed spatial relations: exactly opposite to the homogeneous mean field assumption.

The transient time to reach a scaling state strongly depends on the randomness of the initial conditions [77]. To quickly reach the scaling regime in computer simulations requires a sufficiently random initial lattice of grains. A very regular array

with a few widely spaced defects has a few grains grow rapidly, until the sizes of the few large grains reach the initial separation between defects, as in abnormal grain growth. In the evolution of a single defect in an isotropic hexagonal lattice, the large grain (from the defect) grows at the same rate as disorder propagates outward. The statistics of the disordered cluster show that the topological distribution diverges in time, while the average area of the grains in the cluster grows linearly, a result supported by Aboav's data and previous simulations. However, excluding the large center grain, side and area distributions are steady for the boundary of the cluster.

Contrary to general belief, our results also show that abnormal grain growth can occur in materials provided they have well spaced topological defects, and their crystallites are highly uniform and ordered, even without any anisotropy or fluctuations of surface energy.

The recent experiments of Fortes *et al.* [101] and Earnshaw *et al.* [102] on bubble rafts confirmed our results on both the special scaling state and abnormal grain growth. Both experiments generated ordered foams by sandwiching bubbles between the surface of a soap solution and a glass cover plate, as shown in Figure 4.11. A steady air flow into soap liquid generates a nearly uniform bubble size distribution. Since the foams are wet, bubbles are round rather than polygonal. It is difficult to avoid grain boundaries in such experiments. Confining the two-dimensional foam in a hexagonal frame helps enforce the desired crystalline symmetry. By systematically sweeping the tip of a needle to and fro along the lines of bubbles, Kader and Earnshaw created within the hexagonal cell, a nearly perfect six-fold coordinated lattice comprising several thousand bubbles about 2mm in diameter [102]. Using a syringe and needle, they introduced a large bubble that had more than six nearest neighbors. Figure 4.12 shows a typical evolving ordered foam with a single topological defect.

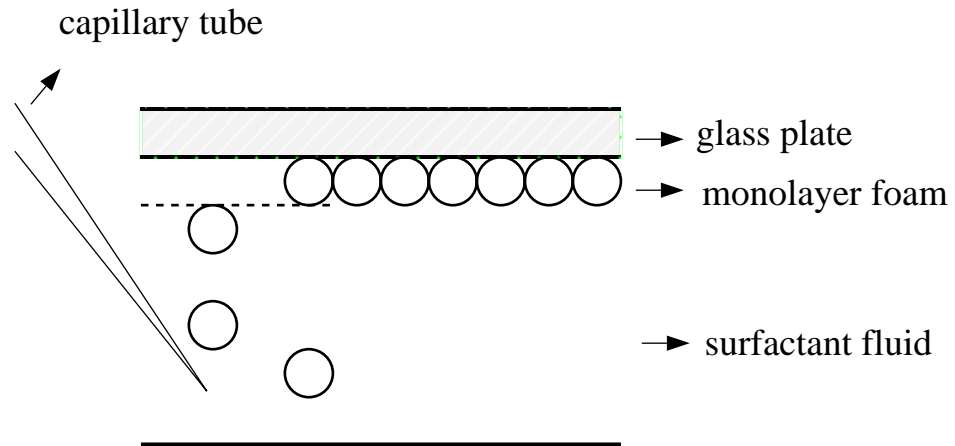


Figure 4.11: Schematic illustration of the technique used to prepare a monolayer hexagonal foam. The monolayer foam is formed between the surface of a surfactant solution and a parallel glass plate above it. [Redrawn from Vaz and Fortes [101]].

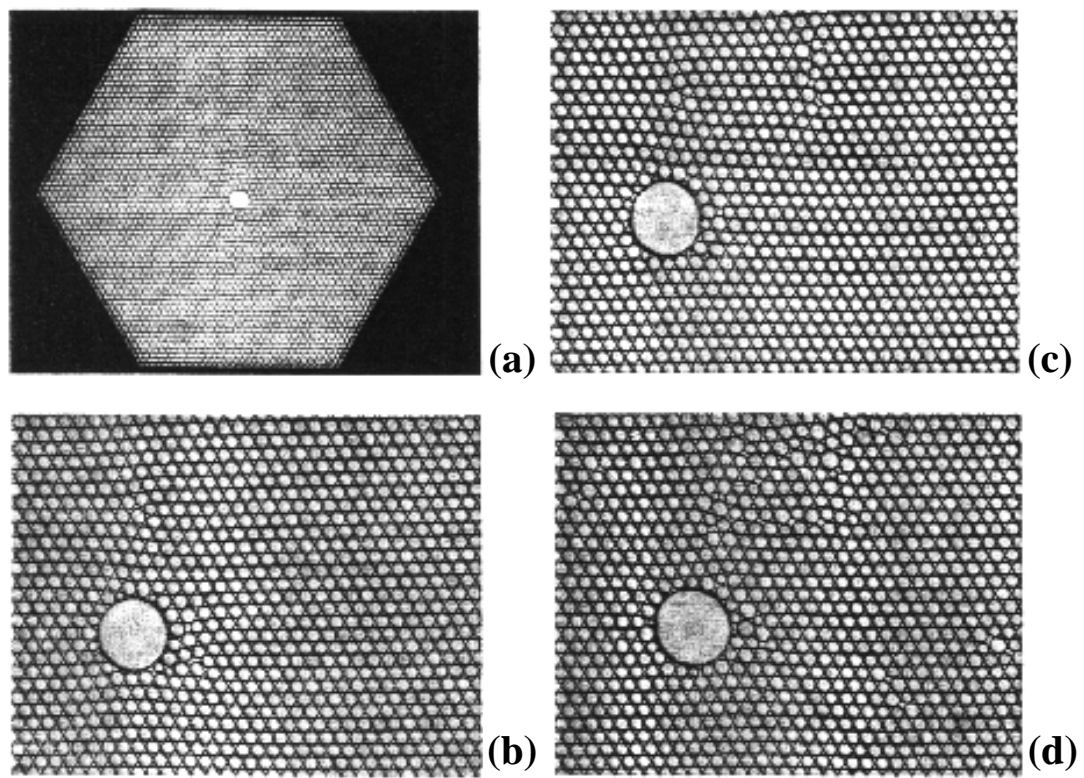


Figure 4.12: Pictures of a typical evolving foam containing an initial isolated larger bubble, constituting a topological defect: (a)  $t = 0$ , (b)  $t = 25h$ , (c)  $t = 28h$ , (d)  $t = 32h$ . [From Kader and Earnshaw [102]].

Experiments show that the disordered cluster grows, but those bubbles comprising the area of disorder around the center large bubble reach a stationary state in which the topological and area distributions are constant, supporting our simulations. Quantitative differences, however, arise. In the topological distribution of the boundary of the disordered cluster, shown in Figure 4.13, an unusual feature is the significant population at  $n = 3$  [102]. In conventional two-dimensional foams, such bubbles disappear through T2(3) processes. In the bubble raft experiments, the threefold-coordinated bubbles are small and lie around the center large bubble, adjacent to two more normal sized bubbles. The difference from the simulations clearly lies in the wetness of the experimental foams. The experiments failed to determine whether  $\mu'_2$  reached a steady value because of coarsening-induced disorder elsewhere in the foam, as shown in Figure 4.12(b). Another difference appears in the final steady value of  $\langle a/a_0 \rangle$ , the average area of the bubbles in the boundary of the disordered cluster. It is  $0.88 \pm 0.08$  in the simulations and  $0.77 \pm 0.04$  in the bubble raft experiments [102]. The difference is small and may again be due to the wetness of the experimental foams. Also the simulations have much better statistics than the experiments.

In our simulations, the center grain gradually becomes hexagonal. A closer observation shows that the final hexagon is a  $90^\circ$  rotation of the initial hexagons, as illustrated in Figure 4.14, whereas in experiments, the large center bubble remains circular [101, 102].

This shape development is an artifact of the lattice simulation. On the square lattice, when the hexagon boundaries align with the underlying lattice, boundary mobility is slightly impeded. Thus the boundary of the large center grain migrates more rapidly along the hexagon boundaries, and more slowly perpendicular to the hexagon boundaries, which explains why the hexagonal shape of the center grain is

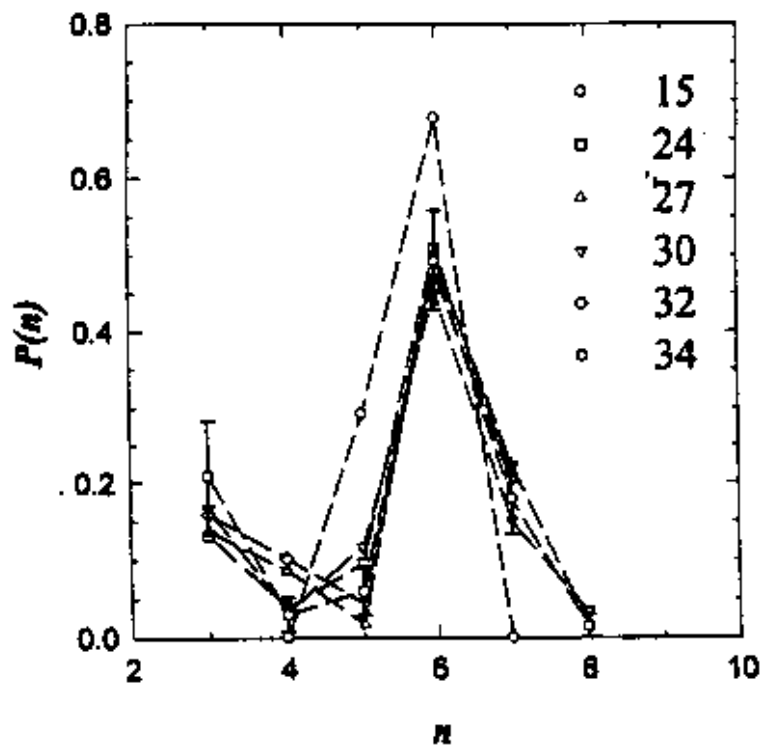


Figure 4.13: Topological distributions for an evolving foam from a single defect: numbers show the number of sides of the center bubble ( $n_c$ ). The distributions omit the data points at  $n_c$ . [From Kader and Earnshaw [102]].

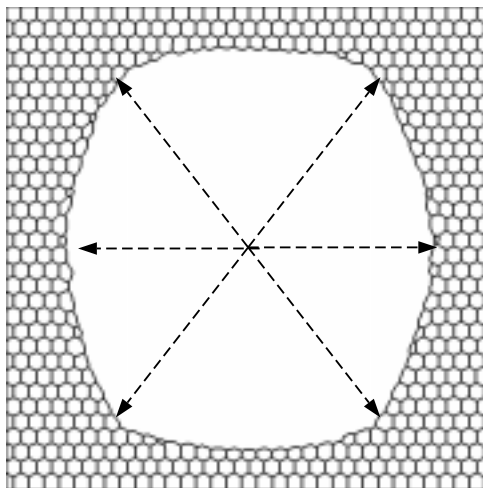


Figure 4.14: The large center grain in Potts model simulations becomes hexagonal when the initial hexagons align with the underlying square lattice.

$90^\circ$  rotated from the initial hexagons. If we rotate the initial hexagonal pattern  $45^\circ$  so that no hexagon boundaries align with the lattice, the center defect no longer develops a hexagonal shape, as shown in Figure 4.15.

Since we used fixed boundary conditions because of the difficulty of applying periodic boundary condition to the rotated pattern, the edge grains were also non-hexagonal defects and coarsened in time. Before the edge grains destroy the ordered pattern, the center grain grows relatively homogeneously. The final state shown is strongly reminiscent of many examples of abnormal grain growth in metals, in which the background grains slowly coarsen.

#### 4.5 Bamboo Formation

The effect of solid walls on grain growth and foam coarsening is poorly understood. Most studies have ignored boundary effects by either assuming infinite or periodic boundary conditions. However, boundary effects sometimes are significant. For example, many of the interconnects in integrated circuits are patterned metallic thin films, particularly aluminum alloys [104]. Experiments show that formation of a “bamboo” microstructure, in which grains traverse the width of the metal strip, increases the rate of electromigration-induced failure of thin film strip conductors [103]. Walton and coworkers [104, 105] used a boundary migration model to simulate the formation of bamboo structure. Their model treated grain boundary segments as arrays of points, which move so that the Mullins’s rate equation holds [106]:

$$\vec{v} = \mu \vec{\kappa} \quad (4.25)$$

where  $\vec{v}$ , the local boundary velocity is proportional to the local curvature  $\vec{\kappa}$ , with  $\mu$ , the mobility constant, depending on the grain boundary energy. The model alternates between moving the boundary segments and relaxing the vertices to con-

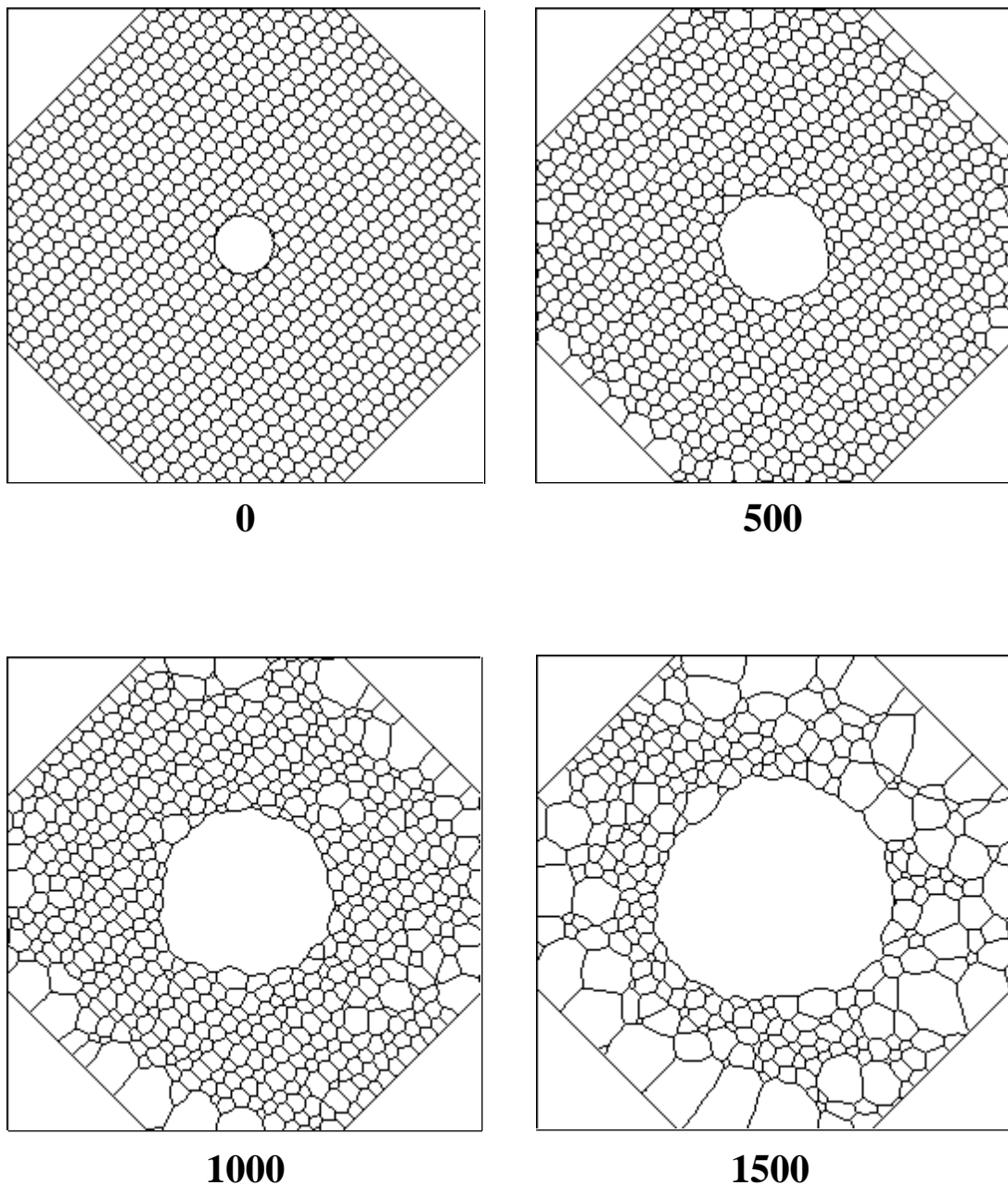


Figure 4.15: Snapshots of the time evolution of a defect in a hexagonal pattern rotated by  $45^\circ$  with respect to the underlying square lattice. Numbers indicate time in MCS.

figurations with  $120^\circ$  contact angles. This model was first used to simulate two-dimensional grain growth in continuous thin films [66, 107, 108]. They began with a standard initial condition and then patterned the structure into a long strip of a specified width. The strip has periodic boundary conditions in the direction of its length and forces the grain walls to be perpendicular to the top and bottom surfaces of the film. Figure 4.16 shows a sequence of grains evolving into a bamboo structure.

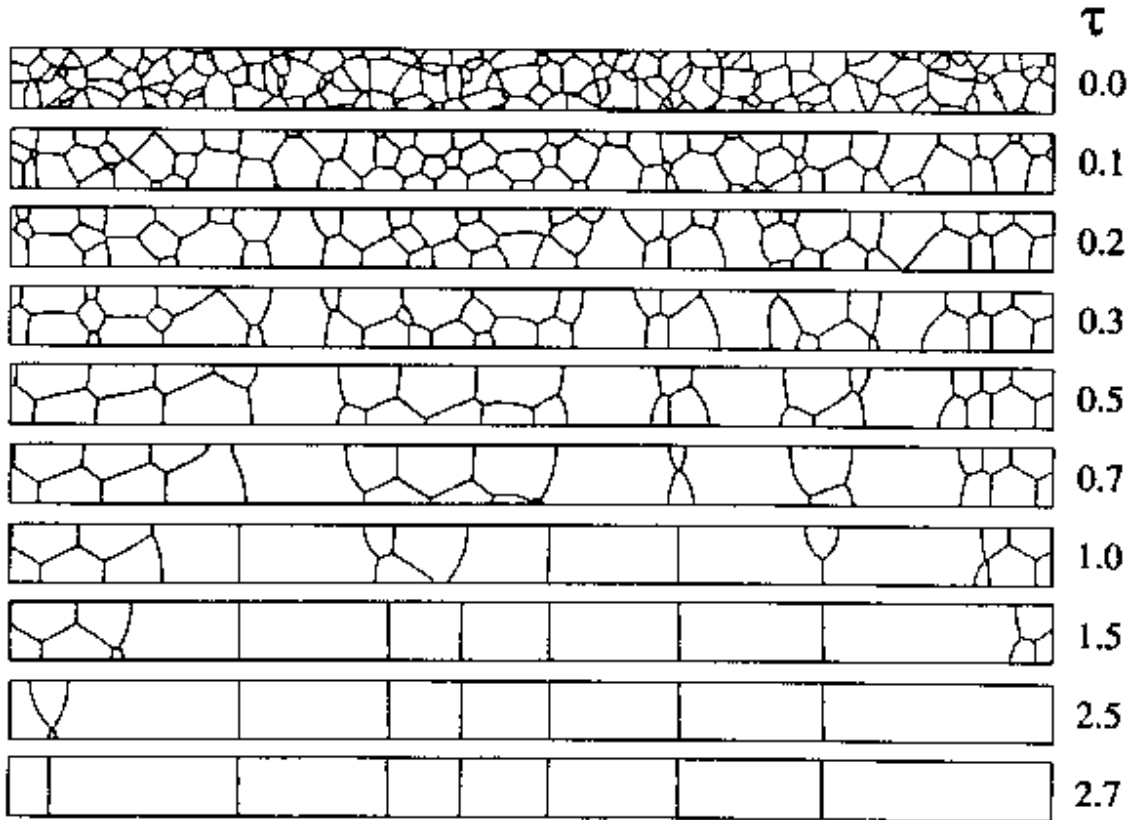


Figure 4.16: Evolution of grains with strip width  $w = 3.0$  (initial average grain size 1.0).  $\tau$  is simulation time in arbitrary units. By  $\tau = 0.2$  some grains traverse the width and the strip breaks into clusters. Eventually the clusters develop into bamboo. [From Walton *et al.* [104]].

They found that the rate of bamboo formation is inversely proportional to the square of the strip width  $w$ :  $t \propto w^2$ . The fully developed bamboo-like domains

have average aspect ratio (length to width ratio)  $\gamma = 2.3$ . If the initial grains are much smaller than the strip width, normal grain growth occurs until some grains grow large enough to traverse the entire strip width, creating sections of bamboo structure, which then expand and consume the grain clusters separating them, until all grains completely span the width.

Fortes *et al.* [110] used glass tubes with diameters between 7.5 and 15.0 mm, and nominal length 50 cm. They created nearly monodisperse three-dimensional foams with an initial average diameter around 2 mm and observed the bamboo formation in the middle 40 cm of the tube. They found an average aspect ratio  $\gamma = 0.97$ , different from Walton *et al.*'s result. To investigate whether this difference is due to the dimensionality, Rosa and Fortes [111] performed a two-dimensional soap froth experiment in a narrow ring (Figure 4.17) and found  $\gamma = 1.43$ , which does not coincide with either of the previous results. They tried to collect information on  $\gamma$  from arbitrary slices of a simulated two dimensional foam image, but arbitrary slices of a two-dimensional pattern do not have grain boundaries perpendicular to the slice lines.

In their simulations, Walton *et al.* started with an initial condition with three grains across the width of the strip. In the three-dimensional foam experiments, Fortes *et al.* varied the diameter of the tubes which contained from three to seven bubbles across the width. For larger tubes,  $\gamma$  was found to be larger. The ring geometry nicely avoided boundary effects in the length direction but the effects of its curved walls are not understood. All these differences make comparison difficult. To fully investigate boundary effects on coarsening dynamics, more controlled experiments and corresponding detailed simulations [112] of bamboo formation are desirable.

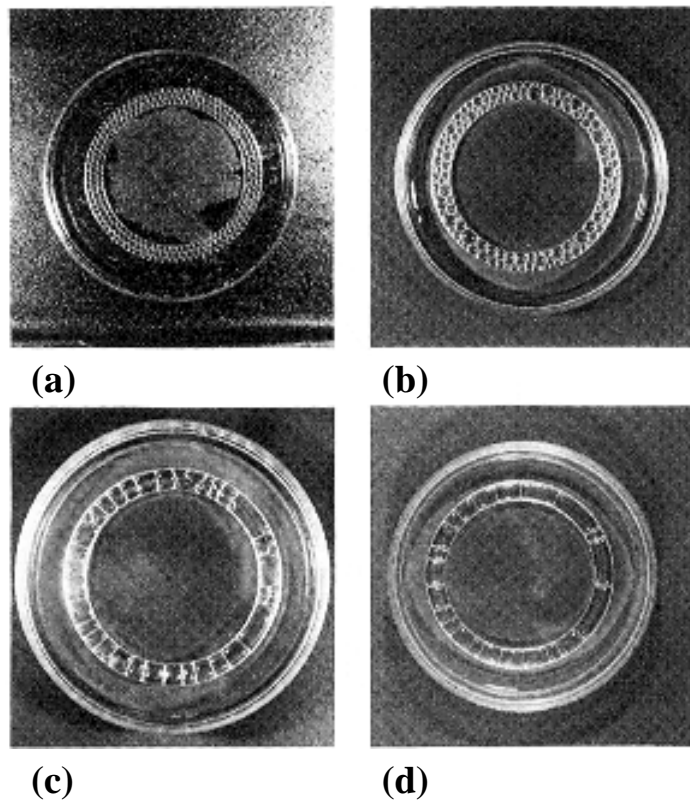


Figure 4.17: A two-dimensional foam experiment on bamboo formation in a ring: (a)  $t = 0$ , (b)  $t = 24h$ , (c)  $t = 180h$ , (d)  $t = 200h$ . Diameters of the rings are 63.9mm and 71.8mm. The width of the ring is 7.9mm. [From Rosa and Fortes [111]].

## 4.6 Grain Growth in Three Dimensions

In soap froth, minimization of surface energy results in grain boundaries that are minimal surfaces with constant mean curvature,  $k \equiv \frac{1}{r_1} + \frac{1}{r_2}$ , where  $r_1$  and  $r_2$  are the two independent radii of curvature. The mean curvature determines the pressure difference across the grain boundary via the Young-Laplace law:

$$\Delta P = \kappa_0 \left( \frac{1}{r_1} + \frac{1}{r_2} \right), \quad (4.26)$$

where  $\kappa_0$  is a diffusion constant [28]. In a quasi-two-dimensional soap froth, all films stretch between top and bottom plates. The equality of contact angles between the films and plates ( $90^\circ$ ) means that  $r_2$  is infinite. Thus  $1/r_2 \sim 0$ , and all films are circular arcs, reducing Equation 4.26 to Equation 2.1. Equation 4.26, together with geometric considerations, results in von Neumann's law, Equation 2.3. In three dimensions the derivation for von Neumann's law fails. The topology does not determine the mean curvature  $k$  but the Gaussian curvature  $G \equiv \frac{1}{r_1 r_2}$ . The two curvatures are independent in three dimensions. Walls need not be spherical sections. In addition, the mean number of faces in an infinite three dimensional polyhedral foam can vary (Equation 4.7), while in a two dimensional foam, the mean number of sides is exactly 6.

Early three-dimensional grain growth simulations by Anderson *et al.* [46, 50] used the Potts model but only focused on the evolution of a cross-section which was essentially a two-dimensional problem. Indeed, they found the same growth exponent and scaling distributions for the cross-section as for two-dimensional coarsening. Later they used the same model for three-dimensional growth and found the growth exponent  $\alpha$  of the average grain volume  $\langle v \rangle \propto t^\alpha$ ,  $\alpha = 1.5$  [48]. Kawasaki *et al.* used a vertex model which treated the cellular pattern as a collection of vertices moving to minimize surface energy [120, 121] and found a similar growth exponent.

This  $3/2$  exponent, however, can be derived from a simple dimensional argument if we assume a scaling state in which topological and area distributions are time independent [121, 113]. Since the Young-Laplace law implies [113]:

$$\frac{dv}{dt} = \kappa_1 a \langle 1/r_1 + 1/r_2 \rangle, \quad (4.27)$$

where  $a$  is the surface area of the grain,  $\kappa_1$  a diffusion constant, and the average is over the grain surface, when the grain shape distributions are constant,

$$\frac{dv}{dt} \propto 1/r \propto v^{-1/3}, \quad (4.28)$$

yielding  $\alpha = 3/2$ . This average growth exponent, however, says little about the dynamics of individual grains. Glazier, using a large- $Q$  Potts model simulation, concluded that the average growth rate of three-dimensional grains depends linearly on their number of faces [113]:

$$\langle \frac{dv_f}{dt} \rangle = \kappa v^{1/3} (f - f_0), \quad (4.29)$$

where  $\langle \rangle$  is an average over all grains in a topological class. Equation 4.29 is analogous to von Neumann's law, but with  $f_0 = 15.8$  rather than  $\langle f \rangle$ . Because the Potts model is discrete and statistical, it cannot directly determine if Equation 4.29 holds for individual grains in the continuum limit. Weaire and Glazier [122] also showed that volume conservation requires:

$$f_0 = \langle f \rangle \left( 1 + \frac{\mu_2}{\langle f \rangle^2} \right), \quad (4.30)$$

where  $\mu_2 = \langle f^2 \rangle - \langle f \rangle^2$  describes the foam disorder. Sire [114] in a mean field model reproduced Equation 4.29. Assuming a three-dimensional scaling state to investigate possible scaling properties, de Almeida *et al.* [123] used a maximum entropy approach, but did not try to study the coarsening dynamics.

Experimentally, because of the strong scattering of light, which gives foams their familiar white appearance, optical photographs can only probe the surface layers of bubbles. The foam structure, distribution, and dynamics of coarsening remain largely inaccessible to traditional experimental measurements such as surface observation, freeze fracture, or electrical conductivity *etc.* [169]. Insertion probe sampling provides foam volume distributions but destroys the sample [124]. Recently, several non-invasive experimental techniques have been developed to probe the dynamics and interior structure of foams.

Durian *et al.* [115, 116] developed a non-invasive technique, using multiple light-scattering (diffusing wave spectroscopy or DWS), and measured the average bubble diameter in a three-dimensional shaving cream foam. They found that after a transient of a few minutes, the growth followed  $r \propto t^\alpha$ ,  $\alpha = 0.45 \pm 0.05$  up to times of the order of 1000 minutes, yielding  $\alpha = 1.35 \pm 0.15$ . However, this technique does not provide direct information on bubble size or topology distributions.

Magnetic resonance imaging (MRI) provides non-destructive visualization of the foam by sampling the polarization density of the nuclear moment (protons) as a function of position. Gonatas *et al.* [117] used a 1.8 Tesla medical MRI spectrometer with a spatial resolution of  $100\mu\text{m}$  to probe the interior of a foam, and studied the topological distribution in two-dimensional sections. While they claimed that the foam coarsening did not reach a scaling state up to  $50h$  (over a decade of growth in the mean length scale), since  $\mu_2(a)$  increased linearly over time, their observed area growth was compatible with  $\langle a \rangle \sim t$ , *i.e.*  $v \sim t^{3/2}$ . However, the finite resolution of their measurement introduced a systematic error by missing substantial numbers of small bubbles, which skewed their estimates of mean bubbles sizes and distributions and affected  $\mu_2$ . When the small bubbles dominate the distribution, under-counting them lowers  $\mu_2(a)$ . As the foam coarsens, the length scale increases and the fraction

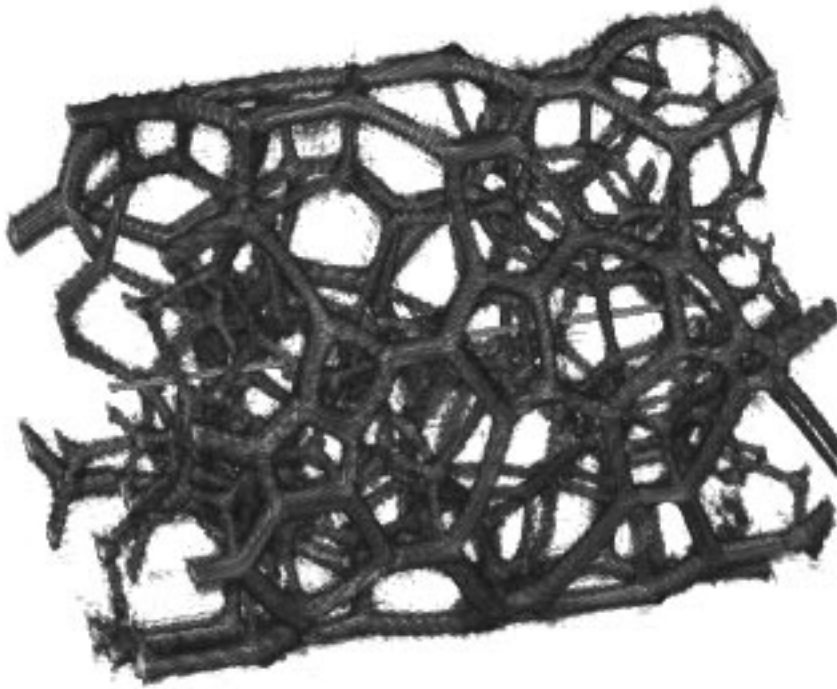


Figure 4.18: A three dimensional MRI image of foam obtained using the 14 Tesla MRI at the NHMFL, FL. The voxel resolution is  $86\mu m$  and the height of the foam is 10mm. The line in the center of the tube is an artifact of the image reconstruction algorithm. [Courtesy of B. Prause].

of bubbles below the cutoff length decreases, resulting in increasing  $\mu_2(a)$ . In other words, under-counting small bubbles can result in increasing  $\mu_2(a)$  even if the true distribution is constant. Checking the shape of the tail of the distribution would help to directly verify if a scaling state exists, which, however, was not possible with their limited statistics. Thus higher spatial resolution is required to improve the technique. Prause *et al.* [118] used a protein gelatin foam to produce the first full three-dimensional image of a liquid foam and showed the potential for studies of time evolution and drainage in three dimensions. Figure 4.18 shows a three-dimensional MRI foam image.

Monnereau and coworkers in a very recent paper [119] used optical tomography

and a foam reconstruction algorithm based on Surface Evolver software (minimization software developed by Brakke [125]) to measure the mean volumes for  $f$ -faced bubbles. Their data suggest that:

$$\frac{d\langle v_f \rangle}{dt} = \langle v_f \rangle^{-1/3} \kappa'(f - f_0), \quad (4.31)$$

where  $f_0$  was found to be  $\langle f \rangle = 13.4$ . This work was the first experimental investigation of Equation 4.29, but limited data render the results hard to interpret.

It is still unclear whether three-dimensional coarsening reaches a scaling state. Glazier's Potts model simulation used a small lattice ( $100^3$ ) and collected statistics only over a decade of growth [113]. Simulations on a larger lattice and experimental investigations over a few decades of growth should clarify this point. If yes, what are the dynamics of individual grains? What is the value of  $f_0$  and why? If not, what causes the difference between two-dimensional and three-dimensional coarsening? Many questions are unanswered for three-dimensional coarsening. Experiments using the high-field (7 Tesla) large-bore MRI facility in Glazier's group will try to answer these questions.

## CHAPTER 5

### FOAM DRAINAGE

#### 5.1 Introduction

Concentrated emulsions (bi-liquid foams) are a family of materials composed of one liquid dispersed in another. In this chapter, the term “foams” and “concentrated emulsions” can be used interchangeably, as many of the principles discussed here apply equally to both cases.

Foams are metastable. Besides diffusional coarsening, wet foams also show a spontaneous tendency to separate into their two distinct bulk phases: liquid and gas for foam, two liquids for concentrated emulsions. The time scale for the disintegration, however, varies widely [134]. Foams can persist from a few minutes to many days even years, depending on the conditions such as surfactants, air humidity and foam structure.

To effectively use foams and concentrated emulsions in any application, requires some control over their stability. A detailed understanding of the mechanisms involved in foam persistence and decay is therefore desirable.

For foams with homogeneous size distributions, under some conditions no liquid drains from the foam. Three possible equilibrium scenarios are: separation of a single phase (separation of the continuous phase liquid by drainage, or separation of the dispersed phase gas via film rupture), separation of both phases (both drainage and film rupture occur) or no phase separation (neither drainage nor film rupture occurs). The rate of drainage depends on a single dimensionless parameter which

measures the relative magnitudes of the gravitational and capillary forces [134].

Using a standing foam to study foam stability is simple and convenient. Typically, a certain volume of foam is prepared by blowing gas into surfactant liquid. The height of the foam decreases over time and the liquid phase accumulates at the bottom. Figure 5.1 shows a picture of a draining foam. Usually at the same time, the mean size of the bubbles increases, resulting in decreasing interfacial area. A successful model for the stability of standing foam should be able to predict the foam height, the bubble sizes and the liquid fraction of the foam as a function of time.

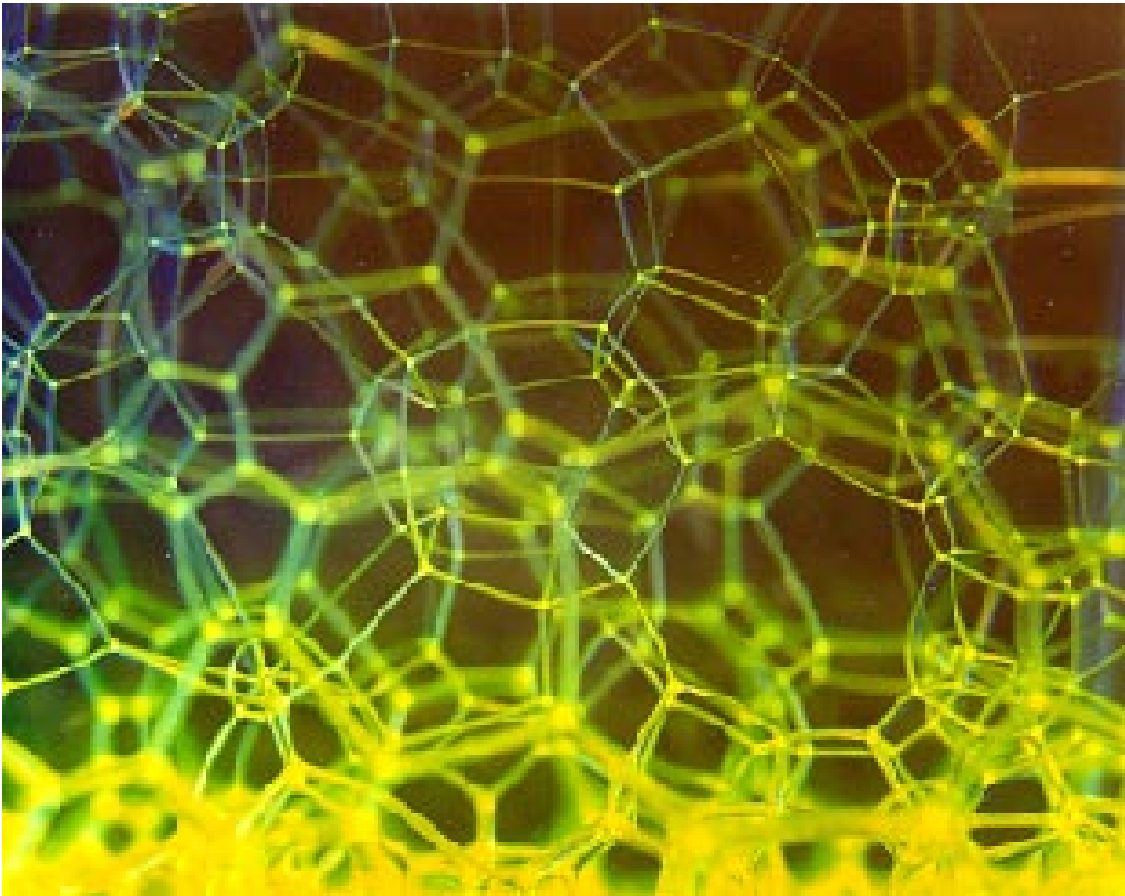


Figure 5.1: A three-dimensional standing foam: liquid drains and accumulates at the bottom of the foam. Bubbles closer to the bottom contain more liquid, with thicker films and Plateau borders. [Courtesy of B. Prause].

The continuous phase liquid in a foam is present in the liquid films between the faces of the polyhedral bubbles, and in the channels, the so called Plateau borders, where films meet. A sketch of a Plateau border is shown in Figure 5.2. These Plateau borders form a complex interconnected network through which liquid flows out of the foam under gravity. At the same time, liquid in the films is sucked into the Plateau borders. As a result, the films become thinner and more subject to rupture. In soap froth, film rupture at the foam boundary also causes loss of the dispersed gas phase from the foam. When a film ruptures, the bubbles sharing the film coalesce, leading to an increase in the average bubble size. Drainage of the continuous phase liquid therefore plays a pivotal role in foam stability.

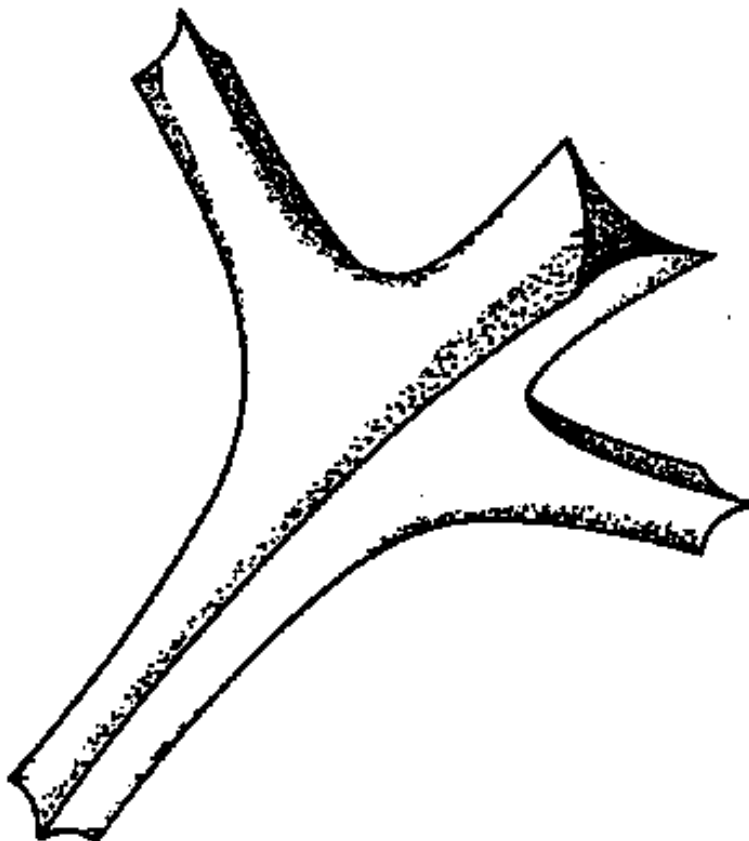


Figure 5.2: A Plateau border in three dimensions. [From Weaire and Pittet [135]].

Mysels *et al.*, in their book *Soap Films: Studies of Their Thinning* [128], first published in 1959, best presented the thinning of soap films in dry foams. They argued that liquid flows from films into Plateau borders. Their argument is as follows: the curved Plateau surface indicates that the liquid inside the border is at a lower pressure than the surrounding gas, whereas the flat parallel surfaces of the films indicate that the contained liquid is at a pressure close to that of the gas. Therefore a negative pressure gradient exists between the liquid in the films and in the Plateau borders. The film, due to its relative thinness, “... is a stable structure in which little liquid can flow.” As a result of this negative pressure gradient and the immobility of the liquid in the films, liquid will tend to flow out of the film into the border but not vice versa. Therefore liquid flows through the foam predominately in the Plateau border network. In addition, film rupture can be prevented in foams by placing them in a shock free and humid environment, for example, in a sealed-off glass container. Choices of surfactant also stabilize foams against rupture. High viscosity liquid thickens films and slow-diffusing gas like  $N_2$  slows down diffusional coarsening. Therefore we focus on liquid drainage through the Plateau channels only, neglecting film rupture and foam coarsening, assuming they do not occur on the time scale we investigate.

Weaire and coworkers’ experiments studied different types of foam drainage [136, 139], and Verbist *et al.* [130, 131] developed a theoretical model to calculate the liquid fraction as a function of foam height, the **liquid profile**. We extended the large- $Q$  Potts model to include two phases, liquid and gas, and incorporated gravitational forces to act on the liquid phase. The simulation results agree with both experimental data and analytical calculations [132]. Without adding liquid, initially uniformly distributed liquid drains to the bottom of the foam until capillary effects balance gravity. In an ordered dry foam, if a fixed amount of liquid is added

from the top, a sharp flat interface between the wet and dry foam develops. The wetting front profile forms a downward moving pulse, with a constant velocity. The pulse decays over time, while its leading edge over a brief period behaves like a solitary wave. With continuous liquid addition from the top, the pulse does not decay and we observe a solitary wave front moving with a constant velocity. Continuously adding liquid to an initially wet foam keeps the liquid profile constant. Our simulations also predict an unstable interface for the wetting front in disordered foams, which challenges current experiment and theory [133].

This chapter is organized as follows: Section 5.2 introduces experiments that are relevant to our study. Section 5.3 describes the micro-channel flow theory. In Section 5.4, we present the details of the model and compare the simulation results with experiments and theory.

## 5.2 Experiments

The traditional drainage experiment is to create a foam by blowing a given amount of gas through a given amount of surfactant solution, then measure the amount of liquid draining out of the foam as a function of time. This type of experiment is termed **free drainage** [136]. Notice that in three-dimensional foams, the bubbles are usually polyhedral, because normal foams have gas fractions more than 90% while the highest gas volume fraction for which identical spheres can occur is 74%. However, with polydisperse foams, the small bubbles can remain spherical at much higher volume fractions. Bikerman [127], almost half a century ago in his book “*Foams: Theory and Industrial Applications*,” reported early experiments measuring the amount of drained liquid as a function of time [127]. Variations of this procedure are widely used in the brewing industry [137, 138]. Unfortunately, the empirical functional forms describing the rate of drainage as a function of time never offered much insight into the physics of drainage.

Mysels *et al.* were the first to investigate the different types of thin film drainage [128], concentrating on vertical films formed by withdrawing glass frames from pools of surfactant solution. Information concerning the history of drainage measurements can be found in the review article by Weaire *et al.* [129].

The experiments relevant to our modeling were mainly done by Weaire and company. Weaire *et al.* performed a new type of drainage experiment, called **forced drainage**. Once the foam is created inside a tube by blowing nitrogen through a surfactant solution, it drains to reach its equilibrium. Then surfactant solution is added at the top of the foam column at a constant flow rate  $Q$ . Weaire *et al.* first monitored the shape of the interface between wet and dry foam by introducing two partially stripped wire electrodes into a tube of foam, and measuring the local resistance as a function of time. The resistance could be converted into liquid fraction. By increasing the number of electrodes, they developed a segmented resistance measurement of the foam. Later, they developed segmented AC capacitance measurements. The segment capacitance depends on the liquid fraction of the foam at the measured vertical position averaged over a finite vertical range which determines the vertical resolution. Scanning the capacitor segments yields the vertical liquid fraction profile of the foam.

They performed various kinds of drainage experiments with AC capacitance measurement [139]. Figure 5.3(a) shows the liquid fraction profile of the foam under forced drainage as a function of vertical position and time. A sharp interface between wet and dry foam develops, and travels downwards with a constant velocity. Figure 5.3(b) shows the liquid fraction profile for free drainage. Initially uniformly distributed liquid drains out of the foam, so the foam dries from the top. Figure 5.3(c) shows liquid fraction profiles for pulsed drainage, when a fixed amount of liquid is added at the top of the foam. The pulse spreads out as it travels downwards

with a constant velocity.

Other experiments trying to study the dynamics of foam drainage used magnetic resonance imaging (MRI) to obtain the average liquid concentration as a function of vertical position, German and McCarthy *et al.* in beer foams and whipped cream [140] and Glazier's group in soap foams [117, 118]. Figure 5.4 shows a set of MRI data obtained by Prause *et al.* with soap froth.

More detailed experiments are ongoing in Glazier's group. Current efforts include imaging the interface between wet and dry foam, and studying the effects of foam polydispersity on interface shape and stability. This study will test the predictions of our simulations [133].

### 5.3 Theory

Foam drainage research has suffered from a lack of communication between scientific disciplines. The recent foam drainage equation theory by Verbist and Weaire [130] was developed independently by Gol'dfarb [141], and many of the details have been covered elsewhere [142, 143, 144].

These models assume that the drainage occurs mainly along the Plateau borders, neglecting the contribution of the films. A further refinement to this type of model is to analyze the geometry of the Plateau border network in addition to the local flow properties. Hass and Johnson [145] proposed the most relevant among the earlier models, recognizing that most of the drainage occurs through the Plateau border channels. But they assumed the Plateau channels to be cylinders of uniform cross-section with immobile walls. In engineering literature, three recent models consider triangular channels with mobile walls [146, 147, 148]. However, some important differences between these models need to be recognized. First, only Narsimhan [148] considered the gradient of Plateau border capillary pressure which

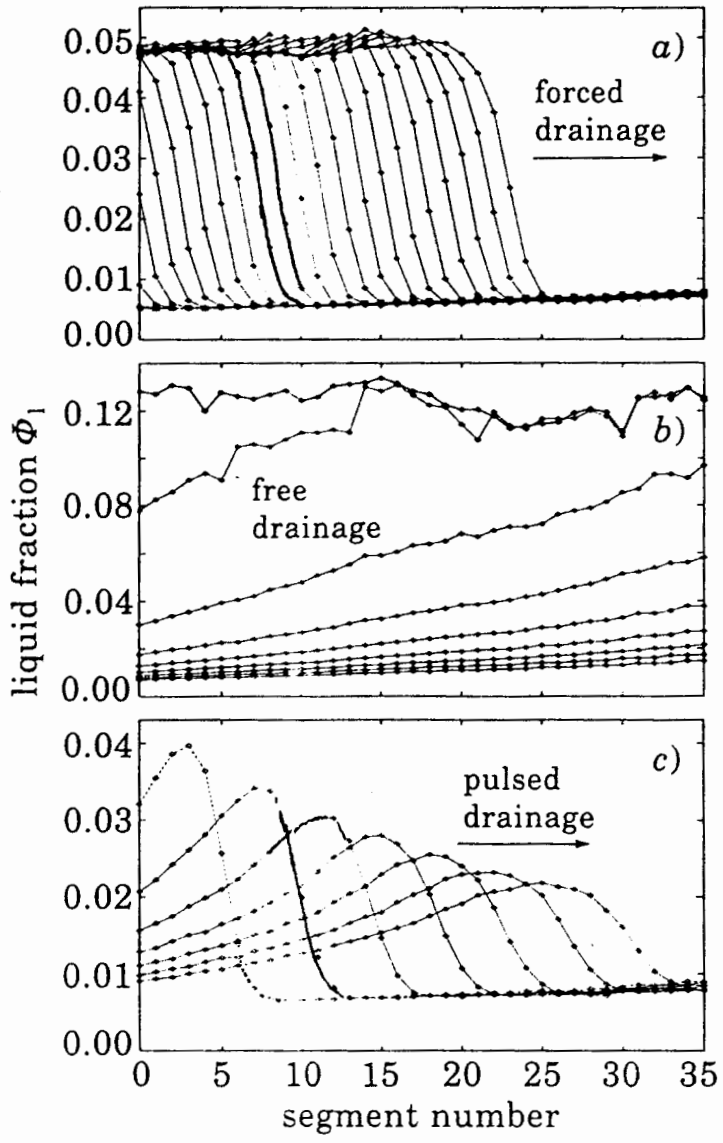


Figure 5.3: Liquid density profiles from segmented AC capacitance measurements. The  $x$ -axis covers a range of 70cm. Left (right) corresponds to the top (bottom) position of the standing foam, but does not include the top and the bottom of the foam. (a) Forced drainage in an initially dry foam: a solitary wave moves at constant velocity downward; (b) Free drainage: initially homogeneously distributed liquid drains when the liquid input stops. (c) Pulsed drainage: a fixed amount of liquid travels down into an initially dry foam. The pulse decays and spreads. [Courtesy of D. Weaire. After Hutzler *et al.* [139]].

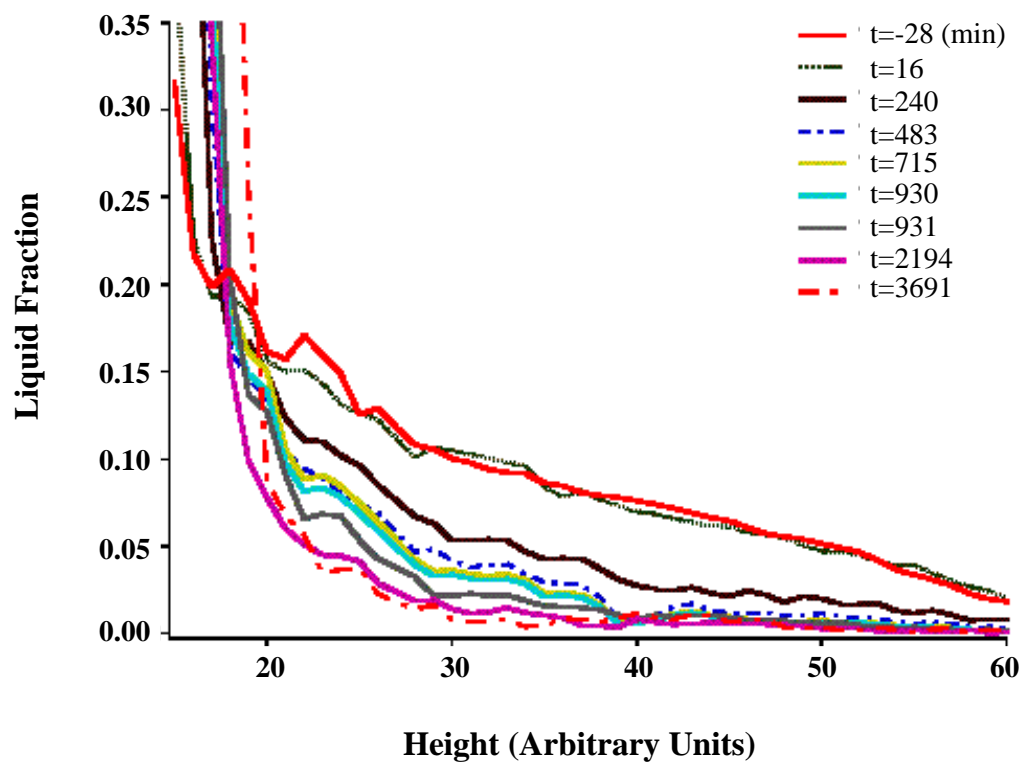


Figure 5.4: Liquid profiles for free drainage (MRI experiment data).

opposes gravity, thus predicting an equilibrium. The other two models predicted that drainage continues until all the liquid in the foam has drained out. Second, the model of Bhakta *et al.* [147] is microscopic, *i.e.* flow balances are written over individual Plateau channels. The other models use a macroscopic approach in which balances are written over differential volumes containing a large number of bubbles. Third, the models treated different initial conditions. However, the complexity of these models prevents their application to realistic situations.

The theoretical model we present here follows Verbist *et al.* [130, 131] and Gol'dfarb *et al.* [141, 144]. We study the propagation of liquid in the network of Plateau channels.

Before going into the details, keep in mind that the key assumption of the model is that drainage occurs only along the Plateau borders. This assumption is only valid for relatively dry foams. In the wet limit, flow can also occur through the films, whose thickness is no longer negligible compared to that of the Plateau borders [149]. Furthermore, a monomolecular layer of surfactant on the film surfaces reduces the surface tension and retards liquid flow, resulting in non-slip conditions on the boundaries of channels [150]. Thus the flow through the channels resembles Poiseuille flows. But unlike in solid pipes or in porous media, the cross section of the Plateau borders is not fixed in time but depends on the flow. In fact, because the cross sectional area is directly proportional to the liquid content, liquid propagation in the foam can be described by the evolution of the cross sectional area.

More simplifying assumptions include:

- The network of Plateau border channels is random and homogeneous.
- The liquid is incompressible.
- The liquid viscosity is constant.

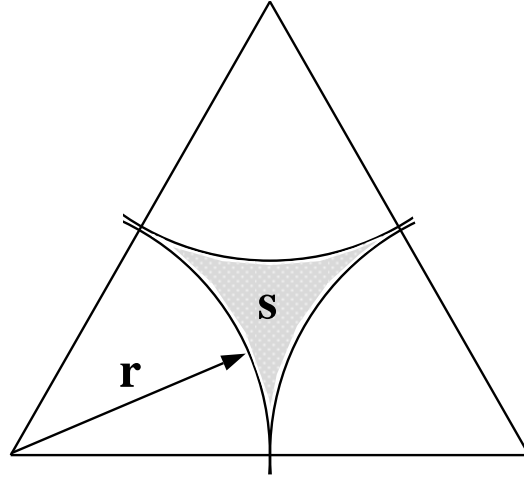


Figure 5.5: Cross section of an ideal Plateau border channel.

- The gas pressure is constant throughout the foam.

The Plateau borders, through which drainage proceeds, have curved triangular cross sections shown in Figure 5.5. The capillary pressure, *i.e.* the pressure across the liquid-gas interface, is:

$$P_{capillary} = P_l - P_g = \frac{2\gamma \cos \theta}{r}, \quad (5.1)$$

where  $\gamma$  is the surface tension,  $\theta$  is the contact angle between liquid and gas, and  $P_l$  and  $P_g$  are the pressures of the liquid and gas, respectively.

For an incompressible liquid, the derivative of Equation 5.1 yields the relation between the change of gas pressure,  $\delta P$ , and the change in the channel area,  $\delta s$ :

$$\delta P = \gamma \alpha s^{-3/2} \delta s, \quad (5.2)$$

where  $\alpha$  is a constant determined by the curvature of the lateral surface of the channel. For ideal Plateau channels, the radius of curvature of the lateral surface,  $r$ , relates to the area of the Plateau channel,  $s$ , as  $s = (\sqrt{3} - \pi/2)r^2$ , yielding,  $\alpha = (\sqrt{3} - \pi/2)^{\frac{1}{2}}$ .

Now we apply the continuity equation to the channel flow:

$$\frac{\partial s}{\partial t} + u \frac{\partial s}{\partial x} + s \frac{\partial u}{\partial x} = 0, \quad (5.3)$$

where  $u$  is the speed of the flow and  $s$  is the cross sectional area which is directly proportional to the liquid fraction as a function of position,  $x$ .

For Poiseuille type micro-channel flow, we can write the solution of the Navier-Stokes equation for massive fluid in a straight tube of arbitrary cross section with vanishing velocity on all interfaces as:

$$u = -\frac{s}{\beta\eta} \left[ \frac{1}{3} \frac{\partial P}{\partial x} - \rho g \right], \quad (5.4)$$

where  $\eta$  is the viscosity of the fluid, the factor  $1/3$  comes from averaging over the directions of motion of the liquid, and  $\beta$  is a numerical coefficient depending only on the shape of the cross section of the channel: *e.g.*  $\beta = 8\pi$  for a tube of circular section,  $\beta = 49.1$  for a cross section in the form of a Plateau triangle [141]. This equation can also be viewed as the force balance between the capillary force, the pressure gradient and gravity [130]:

$$\rho g - \frac{1}{3} \frac{\partial P}{\partial x} - \frac{\beta\eta u}{S} = 0. \quad (5.5)$$

Eliminating  $P$  and  $u$  from the above equations and introduce  $x_0 \equiv \sqrt{\gamma/\rho g}$  and  $t_0 \equiv \beta\eta/\sqrt{\gamma\rho g}$ , the equations reduce to a nonlinear PDE:

$$\frac{\partial S}{\partial \tau} - \frac{\partial}{\partial X} \left[ \alpha S^{1/2} \frac{\partial S}{\partial X} - S^2 \right] = 0, \quad (5.6)$$

with dimensionless variables  $X \equiv x/x_0$ ,  $\tau \equiv t/t_0$  and  $S \equiv s/x_0^2$ . Equation 5.6 is called the “foam drainage equation” [130].

In a moving frame,  $\xi = X - v\tau$ :

$$\frac{\partial}{\partial \xi} \left[ vS + \alpha S^{1/2} \frac{\partial S}{\partial \xi} - S^2 \right] = 0. \quad (5.7)$$

Neglecting the term which represents the variation of pressure along the Plateau border due to capillarity, the drainage equation can be reduced to a first order equation which was first proposed by Kraynik [142]:

$$\frac{\partial S}{\partial \tau} + \frac{\partial S^2}{\partial X} = 0. \quad (5.8)$$

Having arrived at these equations, we will look at their major numerical and analytical solutions for different types of drainage.

### 5.3.1 Forced Drainage

When liquid is added to the top of an initially dry foam, a sharp interface between the wet and dry foam develops and moves down the foam with a constant velocity. The dependence of this velocity  $v$  on the flow rate of liquid  $Q$  is  $v \propto Q^{1/2}$  [151].

For a constant downward flow at the top of the foam and accumulation of liquid at the bottom, namely,  $x \rightarrow -\infty, v = \text{const}; x \rightarrow +\infty, v = 0$ , Equation 5.7 yields the following three solutions:

$$S = v, \quad (5.9)$$

$$s = v \coth^2 \left[ \frac{\sqrt{v}}{\beta} (X - v\tau) \right], \quad (5.10)$$

$$s = v \tanh^2 \left[ \frac{\sqrt{v}}{\beta} (X - v\tau) \right]. \quad (5.11)$$

We consider only steady state solutions, for which the constant of the first integral is zero. The first solution to the channel area describes a steady state, in which the drainage balances the influx of liquid. The second solution is not physical as it diverges at  $X - v\tau = 0$ . The last one, a solitary wave traveling at a constant

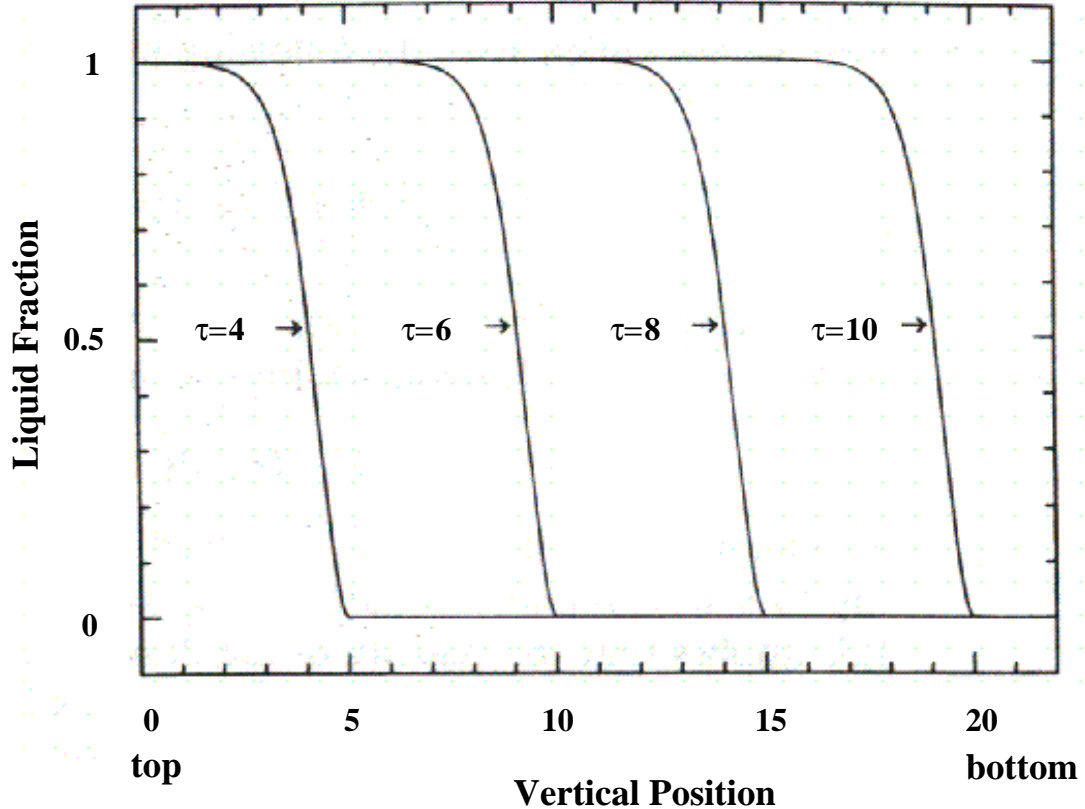


Figure 5.6: A solitary wave travels down the foam - solution given by Equation 5.11. At the left side (top of the foam) the liquid fraction tends to a constant, corresponding to a wet foam. At the right side (bottom of the foam) the liquid fraction is zero, corresponding to a dry foam. The interface between wet and dry foams is sharp. [Redrawn from Weaire *et al.* [129]].

velocity, plotted in Figure 5.6, agrees with experimental results for forced drainage where liquid is continuously added at the top of the foam [139, 136].

Slightly disturbing a constant profile, we may expand the profile as:

$$S(X, \tau) = S_0(X, \tau) + \epsilon S_1(X, \tau), \quad (5.12)$$

and linearize Equation 5.7 with respect to the small parameter  $\epsilon$ , leading to:

$$\frac{\partial S_1}{\partial \tau} + \frac{\partial}{\partial X} \left[ 2S_0 S_1 - \alpha S_0^{1/2} \frac{\partial S_1}{\partial X} \right] = 0. \quad (5.13)$$

Equation 5.13 is a linear wave equation, which can be directly integrated to yield:

$$S_1 = \frac{1}{2S_0} \left[ e^{(X-v\tau)/(S_0^{1/2}\alpha)} + v \right]. \quad (5.14)$$

The perturbation  $S_1(X, \tau)$  decays exponentially in time, so  $S_0$  is indeed a stable steady-state traveling wave solution.

Another solution can be found for finite flow rate at both  $X \rightarrow +\infty$  and  $X \rightarrow -\infty$ , only in an implicit form[131]:

$$X - v\tau = \frac{1}{v - 2v_a} \left\{ \frac{\sqrt{v - v_a}}{2} \ln \left| \frac{\sqrt{S} - \sqrt{v - v_a}}{\sqrt{S} + \sqrt{v - v_a}} \right| - \frac{\sqrt{v_a}}{2} \ln \left| \frac{\sqrt{S} - \sqrt{v_a}}{\sqrt{S} + \sqrt{v_a}} \right| \right\}, \quad (5.15)$$

where  $v$  is the wave velocity and  $v_a$  is the velocity for  $X \rightarrow +\infty$ . When wetting an initially dry foam from the top with a flow rate  $q_a = v_a^2$ , a solitary wave develops as in the original forced drainage case. If the flow rate is then increased to a value  $q_b = v_b^2$ , resulting in a second solitary wave of a higher velocity, the second wave will catch up with the first, forming a final solitary wave with velocity  $v_b$ . The catch up speed  $v = v_a + v_b$  according to equation 5.15. Results for solitary wave experiments agree qualitatively with theory [139].

### 5.3.2 Free Drainage

In free drainage, liquid drains out of an initially uniformly wet foam ( $S = S_0$  everywhere) until it reaches equilibrium. Its complexity prevents an analytical solution for free drainage in its entirety [129]. Nevertheless, based on numerical solutions of the drainage equation together with insight from experiments, we can understand the key features of free drainage. The sketch in Figure 5.7 distinguishes four different regimes.

In the first regime (a), the liquid fraction rises to a critical value at the bottom, where the profile stays constant, *i.e.* the foam releases hardly any liquid. The second regime (b) has a constant drainage rate due to the contraction of the uniform part of the liquid fraction profile. This part can be described well by a linear increase of liquid fraction towards the bottom of the foam, with a slope inversely proportional to time. This linear regime corresponds to the solution to Kraynik's equation (Equation 5.8), given by:

$$S(X, \tau) = \frac{1}{2} \frac{X - X_a}{\tau - \tau_a}. \quad (5.16)$$

The third regime (c) starts when the central constant wetness regime has contracted to zero size. The advancing edge of the Kraynik solution, Equation 5.16, then merges with the steady state profile at the bottom of the foam. Eventually, the liquid profile tends toward its equilibrium shape (d). The drainage rate in this fourth and last regime is presumably exponential.

### 5.3.3 Pulsed Drainage

In pulsed drainage, a fixed amount of liquid flows into a dry foam at the top  $X = 0, \tau = 0$ . This pulse travels downwards with a front resembling that of the solitary wave.

Conservation of area (liquid volume) predicts, for the peak of the pulse,

$$S_{peak}(\tau) = \sqrt{\lambda_0} \tau^{-1/2}, \quad (5.17)$$

where  $\lambda_0$  is the total amount of liquid in the foam. The position of the peak is given by:

$$X_{peak}(\tau) = 2\sqrt{\lambda_0} \tau^{-1/2}. \quad (5.18)$$

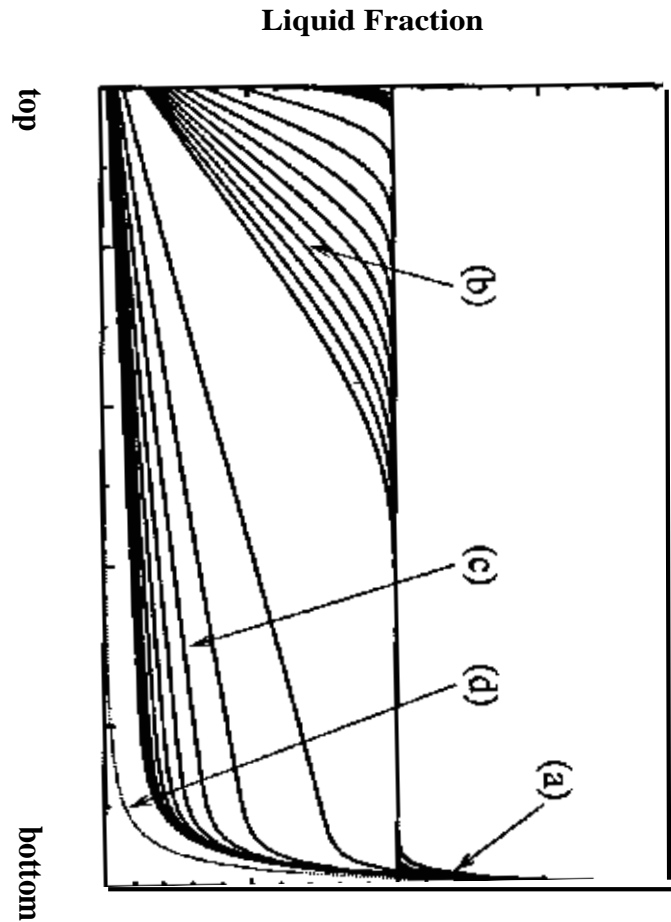


Figure 5.7: Sketched evolution of the liquid profile for free drainage. [From Verbist *et al.* [131].]

This result agrees well with experiments [129].

## 5.4 Simulations

We extend the large- $Q$  Potts model to include two phases, liquid and gas, with liquid subject to a gravitational field [132].

The foam is partitioned on a three-dimensional square lattice with  $Q > 5000$ , *i.e.* we have over 5000 bubbles in these simulations. We treat liquid and gas as two types, with the liquid forming a single bubble subject to a gravitational field. The extended Potts Hamiltonian of the system is then:

$$\mathcal{H} = \sum_{\vec{i}, \vec{i}' \text{ neighbors}} \mathcal{J}_{\tau(\sigma), \tau(\sigma')} [1 - \delta_{\sigma(\vec{i}), \sigma(\vec{i}')} ] + \sum_{\text{liquid}} g h_{\text{liquid}}, \quad (5.19)$$

where the coupling strengths  $\mathcal{J}_{\text{gas,gas}} > \mathcal{J}_{\text{gas,liquid}} > \mathcal{J}_{\text{liquid,liquid}}$  so that the surface energy is progressively higher for gas-gas and gas-liquid and liquid-liquid;  $g$  is the force of gravity per unit density and  $h_{\text{liquid}}$  is the height of the liquid spin. The second term in  $\mathcal{H}$  applies to liquid only. The ratio  $g : \mathcal{J}_{ij}$  controls the ratio between the rate of drainage and that of coarsening.

We evolve the pattern by the standard Metropolis algorithm. We use periodic boundary conditions in the horizontal direction to mitigate finite size effects, but no-flux conditions in the vertical direction, the direction of the gravitational field. To match Weaire *et al.*'s experiments, we use a very ordered initial foam, which affects the shape of the wetting interface. We monitor the mean liquid fraction as a function of vertical position.

Figure 5.8 shows the time evolution of the liquid profiles in free drainage. With no liquid input, the initially homogeneously distributed liquid drains downwards until gravity balances capillary effects, to produce an equilibrium profile. Drainage profiles from MRI experiments by McCarthy [140] and our group (Figure 5.4) are

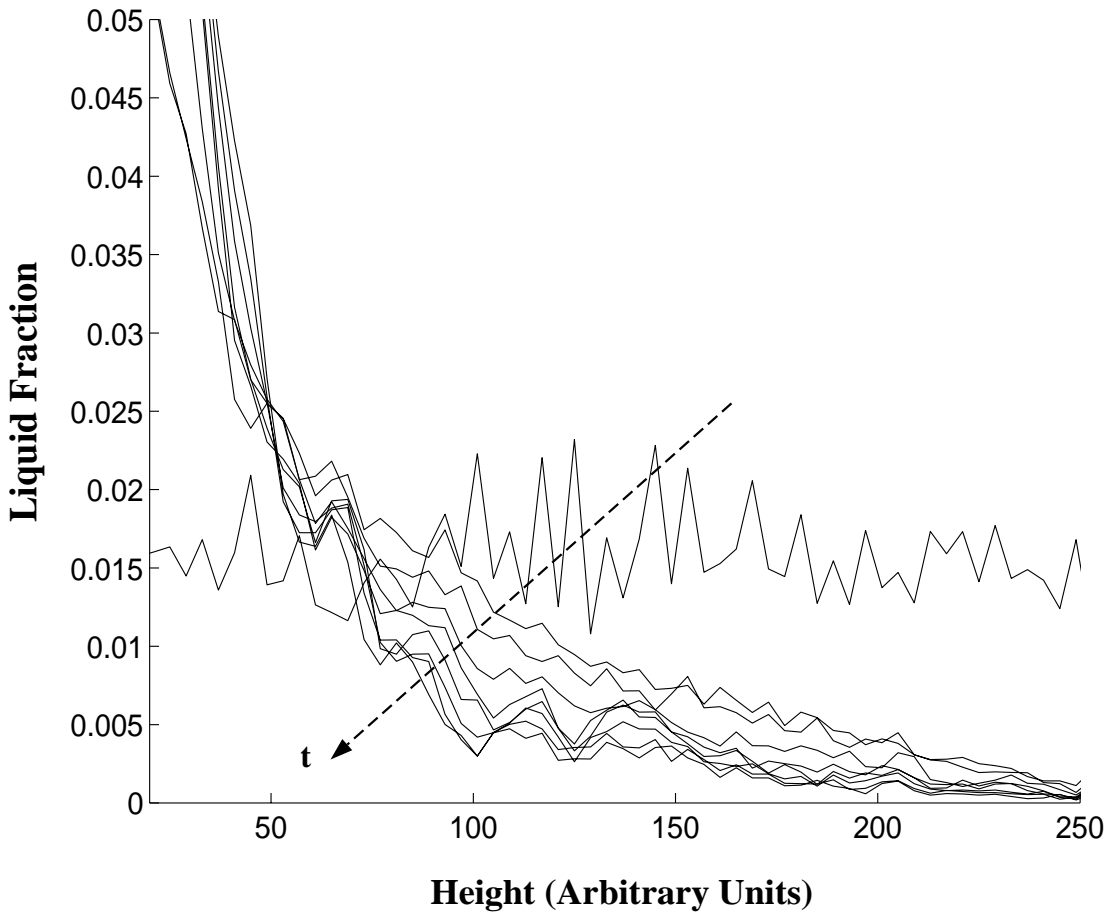


Figure 5.8: Liquid profiles for simulated free drainage in a three-dimensional foam. Arrow indicates the direction of time.

very similar, though quantitative comparison is difficult. Efforts to quantify the slope of the linear part of the profile have not had much success.

Figure 5.9 plots the liquid profiles for pulsed drainage. When drainage is much faster than coarsening, the interface is flat, within a band thinner than the dimension of a bubble. We monitor the pulse as it descends. The leading edge of the pulse, over short intervals such that decay is negligible, is quantitatively identical to the soliton in [139, 136]. In Figure 5.9, we fit the leading edges of the liquid profiles to the same soliton solution. A longer time simulation (with longer vertical distance

for the pulse to travel) allows us to see liquid transfer from the peak of the soliton to the tail, resulting in pulse spreading. In addition, the width of the wave front spreads over time, as predicted in [151]. The ordered structure of the simulated foams generates the high frequency structure of the profiles, shown in the vertical cross sections in Figure 5.10.

Naturally, for a continuous liquid supply, the soliton has a non-decaying fixed profile (Figure 5.11), matching both the analytic solution and the experimental results. The wave front of the soliton moves at a constant velocity, in good agreement with [139].

On the other hand, if the foam is initially wet, continuously adding liquid does not change the shape of the profiles except to increase the foam wetness (Figure 5.12), indicating equilibrium between the liquid input, gravity and capillary forces, corresponding to the steady state solution  $S = v = \text{constant}$ .

In polydisperse foams, where the Plateau channel network is no longer ordered, as liquid penetrates into the disordered network, the sharp interface between the wet and dry foam is no longer stable. Our large- $Q$  Potts model simulations predict an unstable interface resembling viscous fingering. When the rate of coarsening is comparable to that of drainage, the interface between the wet and dry foam is diffuse due to the disordered structure. The liquid forms clusters or droplets in the middle of the foam (Figure 5.13). Structural distributions become important in liquid flow. The simplified pipe flow calculation, which does not consider the spatial disorder, can no longer capture the flow properties. Drainage of a disordered foam is actually a porous medium problem with evolving pore sizes and shapes.

The extended large- $Q$  Potts model simulations produce results comparable to

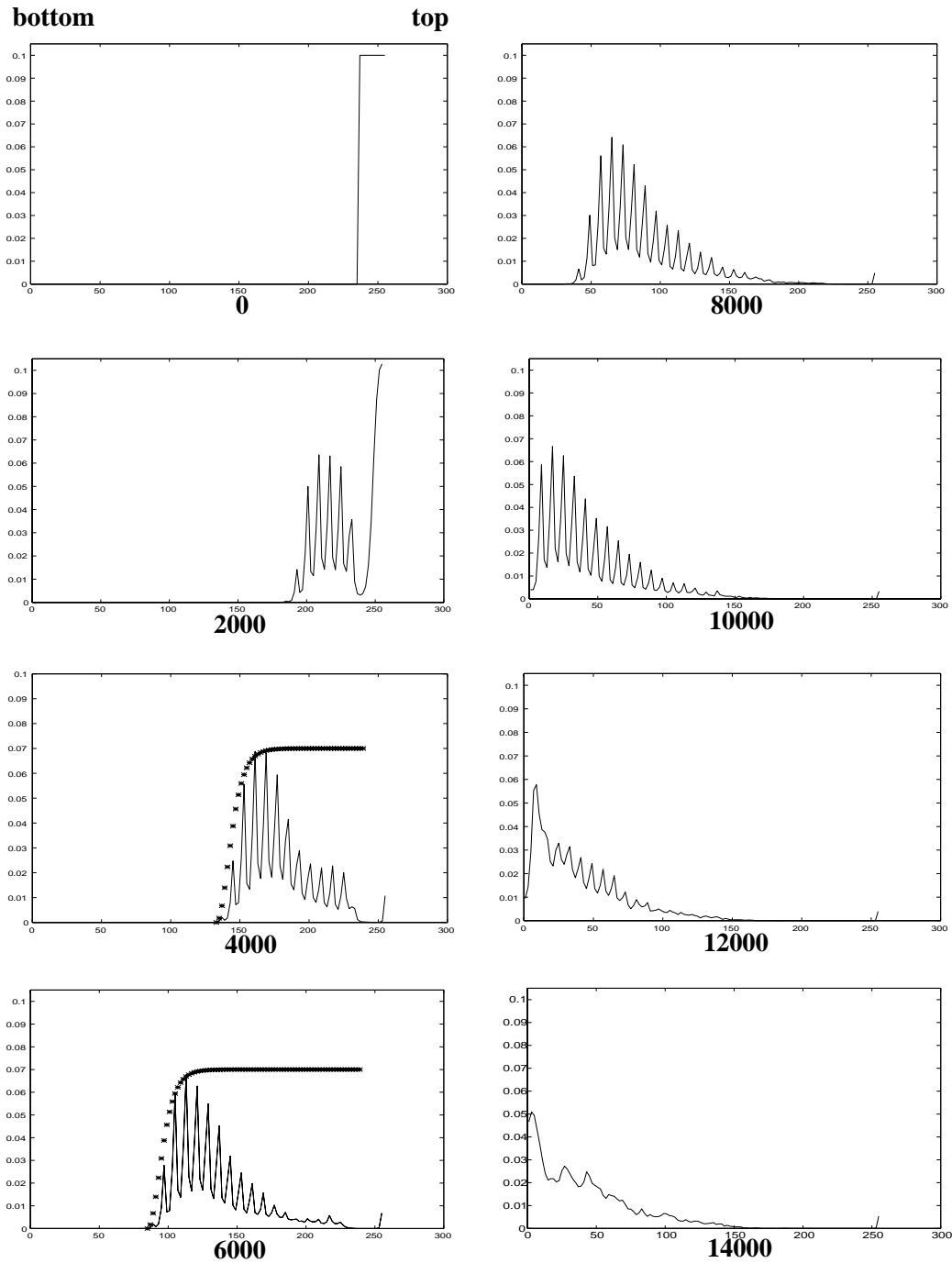


Figure 5.9: Liquid profiles for simulated pulsed drainage in a three-dimensional foam *vs.* time (MCS). The leading fronts of the traveling pulse are fitted with the traveling wave solution, Equation 5.11, at 4000 MCS and 6000 MCS (\*).

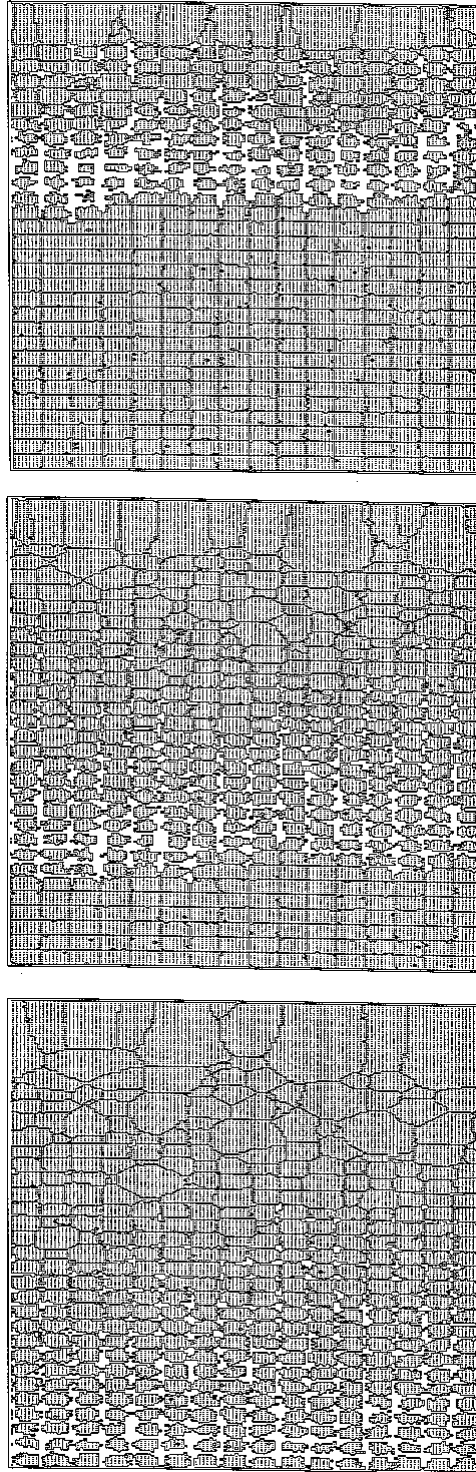


Figure 5.10: Snapshots of vertical cross sections of simulated pulsed drainage in a three-dimensional foam: (a) 3000 MCS, (b) 8000 MCS, (c) 12000 MCS.

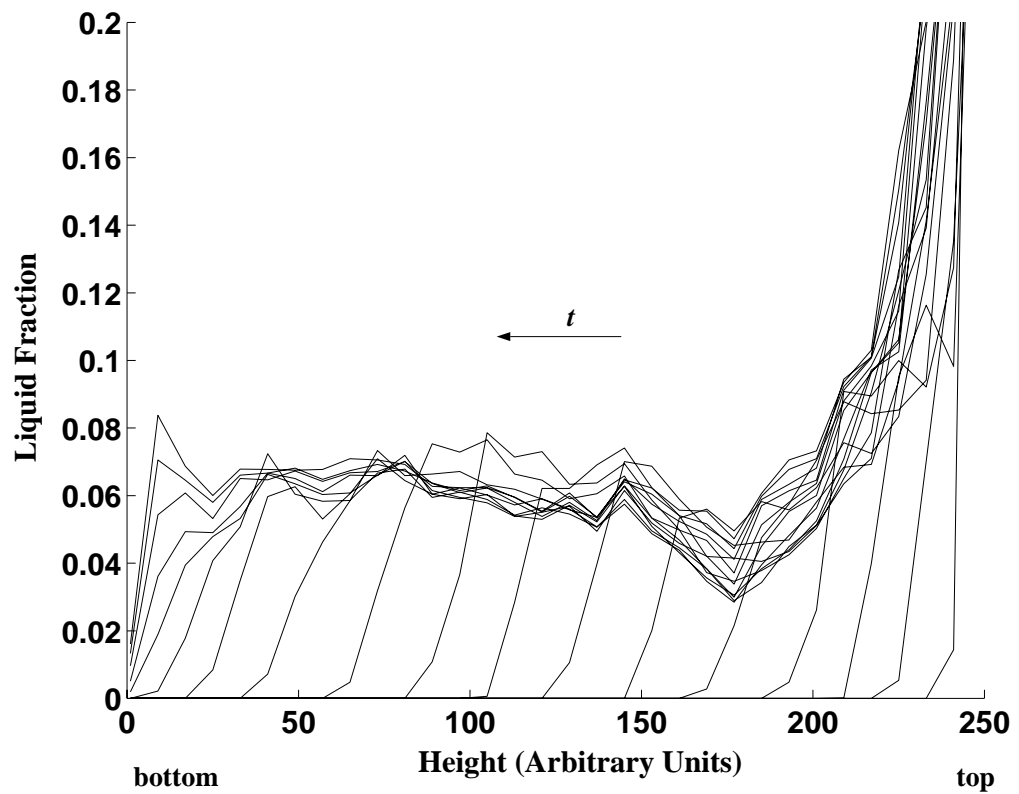


Figure 5.11: Liquid profiles for simulated forced drainage in an initially dry three-dimensional foam. The interval between each profile is 200 MCS.

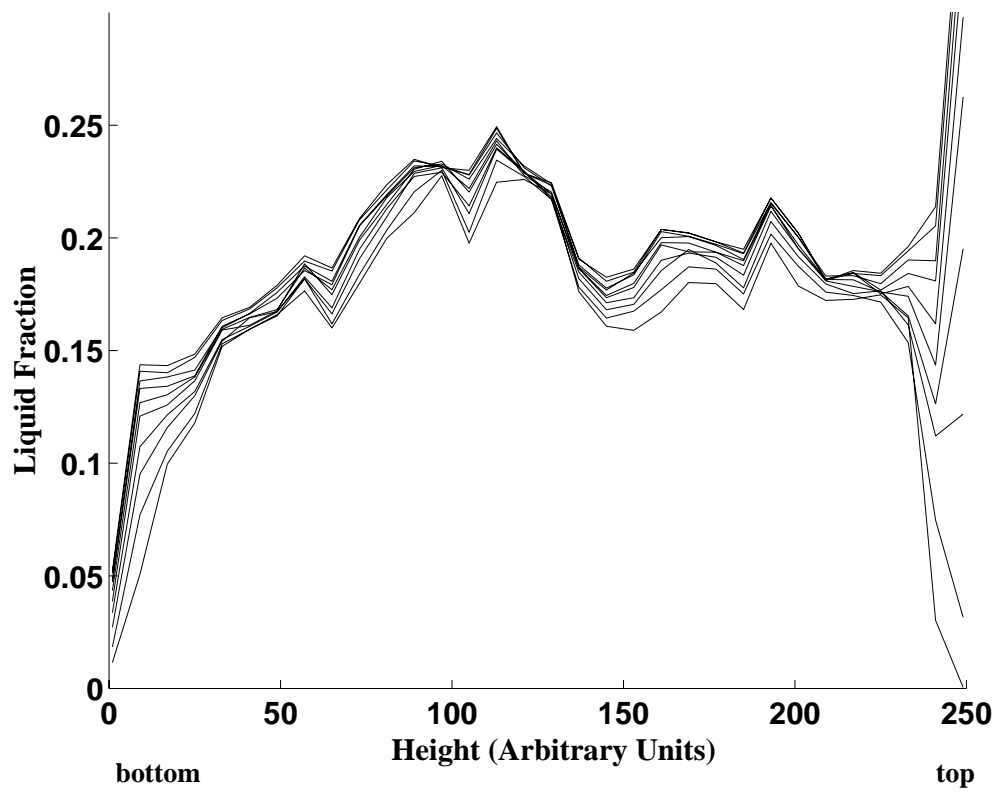


Figure 5.12: Liquid profiles for simulated forced drainage in an initially wet three-dimensional foam. The interval between each profile is 200 MCS.

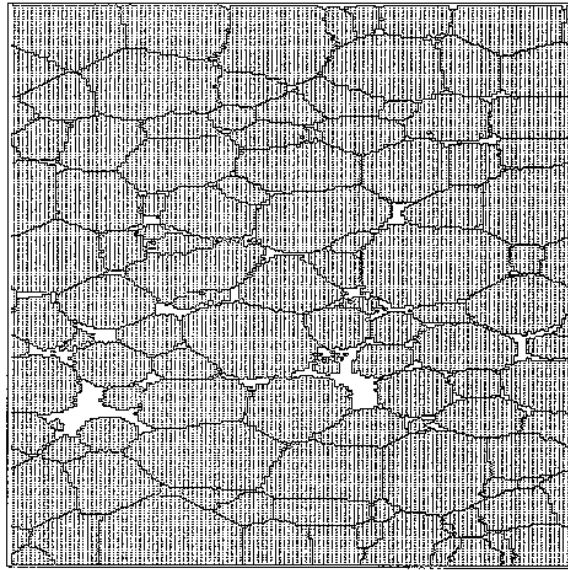


Figure 5.13: Snapshot of drainage in a simulated disordered foam, showing a vertical cross section of a three-dimensional standing foam.

experiments and also validate the drainage theory for ordered foams. This model represents a new direction for drainage theory, allowing us to continuously vary the liquid content, the strength and range of interactions between like and unlike phases, and the rate of drainage *vs.* coarsening. A detailed quantitative comparison between the experiments and simulations should help determine realistic parameters in the simulations.

## CHAPTER 6

### FOAM RHEOLOGY

#### 6.1 Introduction

##### 6.1.1 Background

Invented by Bingham in the beginning of this century, “rheology” is “the branch of physics that studies the deformation and flow of matter” (*Hypertext Webster*).

As a macroscopic form of matter, liquid foams, in which a small volume fraction of fluid forms a continuous network separating gas bubbles [169], exhibit striking mechanical properties which are different from their liquid and gas components. If pushed gently, they resist deformation elastically like a solid, obeying Hook’s law of **linear elasticity**. If pushed hard, they yield – flow and deform arbitrarily like a liquid, described by **viscosity**. Furthermore, if their pressure, temperature or volume is changed, they respond roughly as  $PV/T = \text{constant}$ . Thus, they are neither solid, liquid, nor vapor, yet can exhibit the hallmark features of all three basic states of matter. Exactly how this behavior occurs is not yet understood.

Our approach to study foam rheology is to correlate the microscopic details, *e.g.* structural disorder and topological rearrangements of individual bubbles, to the macroscopic mechanical properties of foams. This study also covers the wide range of emulsions and slurries, which are other classes of materials that exhibit similar rheology.

In foams, when shear stress is present, a pair of adjacent bubbles can be squeezed apart by another pair, as shown in Figure 4.2, a so-called T1 switching event [10].

This local but abrupt topological change results in bubbles rearranging from one metastable configuration to another. The resulting macroscopic dynamics is highly nonlinear and complex, involving large local motions that depend on structure at the bubble scale. The spatio-temporal statistics of T1 events are fundamental to the plastic yielding of two-dimensional liquid foams.

The relation between the **stress** (force  $F$  divided by cross-sectional area) and the **strain** (dimensionless deformation) is the most common and preferred measure for determining the mechanical properties of structural materials [170]. The proportionality between stress and strain is the **Young's Modulus**. For an elastic solid, the stress accumulates linearly as the applied strain increases. The slope is the **elastic modulus**. For a plastic solid, the stress is nonlinearly proportional to the applied strain and the stress saturates at a critical point, the **yield stress**, above which brittle materials fracture and ductile materials slowly releases stress. Fluids, on the other hand, deform and flow arbitrarily upon the smallest applied strain. No stress can accumulate. The stress in fluids depends not on the strain, but on the strain rate. The proportionality between stress and strain relates to the coefficient of **viscosity**.

Figure 6.1 shows a schematic illustration of the stress-strain plot of a liquid foam. At low strain, a foam is like an elastic solid, characterized by the linear response of the foam. Above the yield point, a foam is like a viscous fluid, defined by an effective viscosity. In the intermediate regime, a foam has both elastic and viscous properties, thus behaving visco-elastically.

We apply constant shear strain to study foam's solid-like behavior (linear and nonlinear response) and periodic shear strain to study foam's fluid-like behavior (rate dependence). We plot the stress-strain diagrams, and study their correlations to T1 dynamics and effects of structural disorder.

### 6.1.2 Overview

Previous theoretical studies of foam rheology fall into three classes: constitutive models, vertex models, and center models.

The constitutive models evolved from the ideas of Princen [163] and Prud'homme [162]. They modeled foam as a two-dimensional periodic array of hexagonal bubbles, as illustrated in Figure 6.2, where T1 events happen instantaneously and simultaneously for the entire foam.

Khan and Armstrong *et al.* developed a theoretical framework for treating shear (simple shear and uniaxial shear) for arbitrarily oriented hexagonal networks. They recognized that linear, homogeneous deformations of periodic networks require affine displacement of bubble and film midpoints. They studied the stress-strain relationships as a function of hexagon orientation and liquid viscosity [164]. Figure 6.3 shows a stress-strain curve for shear flow corresponding to hexagons under shear, shown in Figure 6.2. Reinelt and Kraynik [171], using the same model, studied a hexagonal foam with a size distribution and derived explicit relations between stress and strain tensors.

While analytical calculations exist only for periodic structures or for linear response, foams are naturally disordered with an inherent nonlinear response. Vertex models include the effect of stress on structure and the propagation of defects in dry foams. Okuzono and Kawasaki [165] studied the effect of finite shear rate by approximating the force on each vertex, a term which depends on the local motion and is based on the work of Schwartz and Princen [174], and predicted that rearrangements in a slowly driven foam have a broad, power law distribution of avalanche size *vs.* energy release, and thus exhibit self-organized criticality. However, in a vertex model, the walls (films) connecting the vertices adiabatically follow

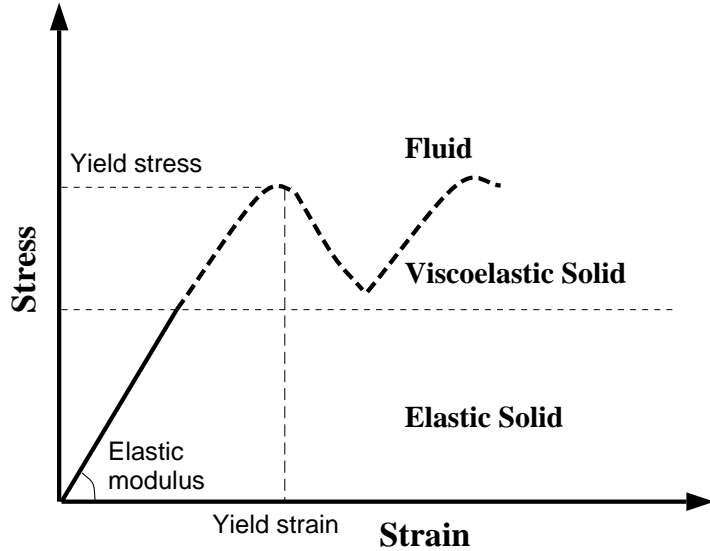


Figure 6.1: Schematic illustration of the stress-strain diagram of a liquid foam.

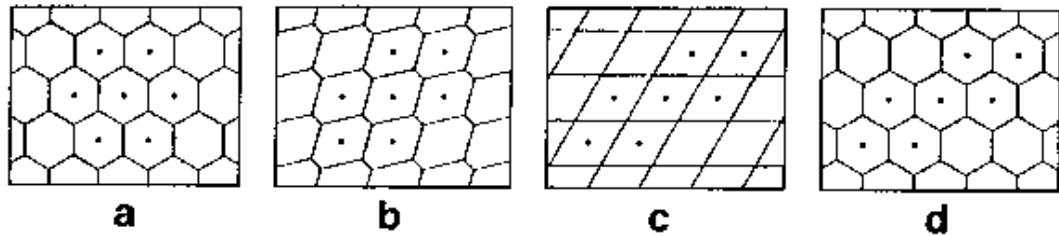


Figure 6.2: Princen-Prud'homme model showing the strain dependence of bubble morphology for simple shear with initial hexagon orientation at zero. (a) Undeformed equilibrium network: strain  $\epsilon = 0$ . (b) Strain  $\epsilon = 1/\sqrt{3}$ . (c) Yield strain  $\epsilon = 2/\sqrt{3}$ . (d) Relaxation,  $\epsilon = 2/\sqrt{3}$ ; the foam recovers its initial equilibrium configuration but the bubbles have all undergone T1 processes [From Khan and Armstrong [164]].

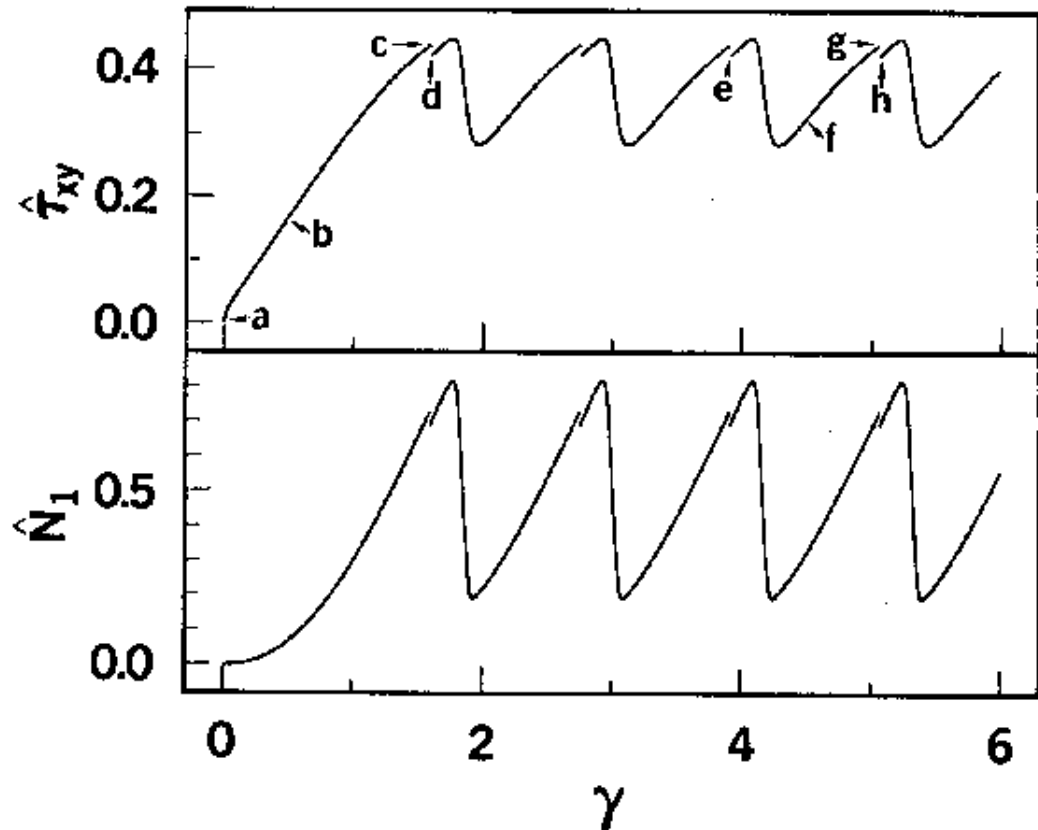


Figure 6.3: Stress-strain curves for simple shear flow in ordered foams show periodic behavior. In Khan *et al.*'s notation,  $\gamma$  is the applied strain,  $\hat{\tau}_{xy}$  is the shear stress and  $\hat{N}_1$  is the normal stress. Points (a)(b)(c)(d) correspond to the bubble morphologies in Figure 6.2 [From Khan and Armstrong [164]].

an out-of-equilibrium, slowly-relaxing vertex. In such a model, the walls are straight and vertices typically have arbitrary angles. In essence, the deviation of the vertex angles from the equilibrium value represents the integrated curvature of the bubble walls. A pure vertex model with straight walls does not handle T1 events correctly.

Weaire and Bolton [166], in a center model based on Voronoi reconstruction from the bubble centers, applied extensional deformation and simple shear to a two-dimensional foam and concluded that stress and topological rearrangements can induce ordering in a disordered foam. Using a similar model, Weaire and Hutzler [179] also found that only in the wet foam limit do foam rearrangements follow a power law. Durian's [167] center model, treating bubbles as disks connected by springs, measured the linear rheological properties as a function of polydispersity and liquid fraction. He found similar distributions for the avalanche-like rearrangements with a high frequency cutoff. But in such center models, the coherence length of a bubble is comparable to its diameter. Contact angles are correct at equilibrium but approach and remain near  $90^\circ$  during a T1 event, since the centers are essentially uninfluenced by topological details such as the difference between a fourfold vertex and a pair of three-fold vertices.

A further problem with both vertex and center models is that they do not directly count T1 events. Instead, they measure the size of rearrangement events by the associated decreases in energy. As we will discuss later, the energy decrease is not directly proportional to the number of T1 events. The correlation between energy decreases (macroscopic) and T1 dynamics (microscopic) is essential to understanding foam rheology.

A review by Weaire and Fortes [175] includes a brief overview of some of the computer models (up to 1993) of the mechanical and rheological properties of liquid and solid foams. Few models have attempted to relate the structural disorder and

configuration energy to foam rheology. Only recently, Sollich *et al.* [161], studying mechanisms for storing and dissipating energy, showed that the rheology of “soft glassy” materials, including foams, depends on structural disorder and metastability. Langer and Liu [172], using a bubble model similar to Durian’s, found that foam packing randomness has a strong effect on the linear shear response of a foam. One of our goals is to quantify the extent of metastability by measuring hysteresis.

Experimentally, rearrangement events are difficult to study in three dimensions because of the difficulty of direct visualization of foams. Most studies were limited to two dimensions. Khan *et al.* [173] applied simple shear to a foam trapped between two concentric parallel plates. They rotated the top plate and measured the torque on the bottom plate. Figure 6.4 shows a sketch of their mechanical spectrometer.

They found that foam viscosity decreases linearly with strain rate, and that the yield strain stays nearly constant for strain rates between 0 and  $1.8\text{s}^{-1}$ . Princen and Kiss [176], applying shear in a concentric cylinder viscometer (*i.e.* boundary shear), determined the yield stress and shear viscosity of highly concentrated water/oil emulsions. With the help of diffusing wave spectroscopy (DWS), experiments by Gopal and Durian on shaving creams showed that the rate of rearrangements is proportional to the strain rate, and that the rearrangements are spatially and temporally uncorrelated [177]. None of these experiments directly observed changes in bubble topology. Dennin and Knobler [178] performed a shear experiment on a monolayer Langmuir foam and counted the number of bubble side swapping events. Limited statistics, however, rendered their results hard to interpret.

Here we extend our Potts model to include the application of shear and to study the mechanical response of two-dimensional dry foams under stress.

Simulations of periodic shear using the extended large- $Q$  Potts model show three different types of hysteresis in the stress-strain relationship, elastic, viscoelastic and

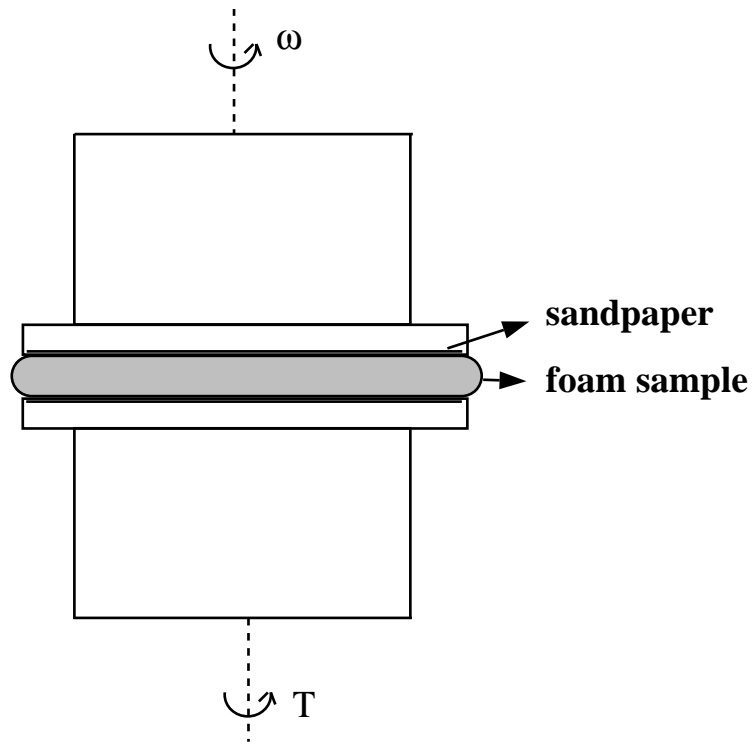


Figure 6.4: Schematic illustration of a Rheometric Mechanical Spectrometer (RMS7200). A foam sample is sandwiched between two parallel plates with both surfaces covered with sandpaper to avoid slippage. The top plate rotates at a constant angular velocity  $\omega$  and the force/torque  $T$  on the bottom plate is measured. [Redrawn from Khan *et al.* [173]].

fluid-like. This wide-ranging mechanical response of foams depends on the structural disorder and local topological rearrangement of foam cells. For steady shear the yield strain is much higher for an ordered foam than for a disordered foam and the statistics and dynamics of topological rearrangement events (avalanches) depend sensitively on the degree of polydispersity of the foam. As the structural disorder increases, the topological rearrangements become more correlated and their power spectra change from that of white noise towards  $1/f$  noise. Intriguingly, the power spectra of the total stored energy exhibit the same  $1/f$  trend.

In the next section, Section 6.2 we describe simulation details. Section 6.3 presents results on hysteresis. Section 6.4 contains discussions on dynamics and statistics of topological changes (T1 events). We discuss structural disorder in Section 6.5 and effective foam viscosity in Section 6.6.

## 6.2 Model

The nonlinear and collective nature of bubble rearrangement dynamics makes analytical studies difficult, except under rather special assumptions. Computer simulation therefore provides important insights into the full range of foam behavior. Both bubble surface properties and structure are fundamental to understanding foam flow. Previous models [165, 166, 167] were based on different special assumptions for the energy dissipation. Since the energy dissipation is poorly understood and hard to measure in experiments, the exact ranges of validity for these models are not clear. Not surprisingly, these models result in conflicting predictions, *e.g.*, for the distribution of avalanche-like rearrangements (to be discussed in Section 6.4). None of these models alone captures the full complexity of real foams.

The extended large- $Q$  Potts model, where bubbles have geometric properties as well as surface properties, is not based on any *a priori* energy dissipation assumption. In addition, it has the advantage of simultaneously incorporating many interactions,

including temperature effects, for foams with arbitrary disorder and liquid content.

In a real evolving pattern, the equilibrium contact angle occurs only for slow movement in which the vertices are adiabatically equilibrated. Whenever a topological rearrangement (a T1 event) occurs, the contact angles are far from their equilibrium values. The boundaries then adjust rapidly to re-establish equilibrium. The same holds true for the other possible topological change, the disappearance of a bubble, known as a T2 event [10]. However, disappearance only occurs in foams that do not conserve bubble number and area, which we do not consider in this study. We define the equilibrium contact angle so that any infinitesimal displacement of the vertex causes a second-order variation of the surface energy, while during a T1 event the energy must vary macroscopically over a small but finite coherence length, typically the rigidity length of a bubble. In our simulations, a bubble under stress can be stretched or compressed up to 60% of its original length, with its area conserved.

In our extended large- $Q$  Potts model, films are free to fluctuate, which is not true in vertex models; the contact angles during the T1 event are correct, which is not true in center models. Our model can also provide information about individual T1 events as well as averaged macroscopic measures such as total boundary length, which offers new insights into the connection between foam structure and mechanical response.

Before describing the details of the Potts model, we ought to mention its limitations. Viscosity is one of the basic physical properties of foam (both liquid viscosity and effective foam viscosity), but it is not easily defined in the Potts model. Although the effective viscosity and the viscoelasticity of films can be extracted from simulations and we understand the qualitative effects of parameters on viscosity, we do not yet have an explicit relationship between the model parameters and viscosity.

Adjusting this property quantitatively in our model is nontrivial. Another drawback is that the Metropolis algorithm results in uncertainties in the relative timing of events on the order of a few percent of a Monte Carlo step. While this uncertainty is insignificant for well separated events, it can change the measured interval between frequent events, especially when computing the size of T1 avalanches.

To focus on shear driven topological rearrangements, we prohibit foam coarsening by applying an area constraint on individual bubbles (see Chapter 2 for detailed discussions of the area constraint). In practical applications, foam deformation and rearrangement under stress is often much faster than gas diffusion, so neglecting coarsening is reasonable. The Potts Hamiltonian, the total energy of the foam, then includes a surface energy and an elastic bulk energy. We can extend this Hamiltonian to apply shear:

$$\mathcal{H} = \sum_{\vec{i}\vec{j}} \mathcal{J}_{\vec{i}\vec{j}} (1 - \delta_{\sigma_i \sigma_j}) + \Gamma \sum_n (a_n - A_n)^2 + \sum_{\vec{i}} \gamma(\vec{y}_i, t) x_{\vec{i}} (1 - \delta_{\sigma_i \sigma_{\vec{i}}}), \quad (6.1)$$

where  $\mathcal{J}_{\vec{i}\vec{j}}$  and  $\sigma_i$  are the coupling strength and spin;  $a_n$  is the area of the  $n$ th bubble and  $A_n$  its corresponding area under zero applied strain, as described in Chapter 2. The second term is the area constraint which prevents coarsening. The strength of the constraint,  $\Gamma$ , is inversely proportional to the gas compressibility; Coarsening can be included by setting the strength of the area constraint to zero. The last term corresponds to applying shear, with  $\gamma$ , the strain field and,  $x_{\vec{i}}$ , the position of the spin in the direction of the strain. The system evolves by our Potts model algorithm.

The shear term biases the probability of spin reassignment in the direction of increasing ( $\gamma < 0$ ) or decreasing ( $\gamma > 0$ )  $x_{\vec{i}}$ . The strain field  $\gamma$  has units of force. But because in the Potts model, the bubble boundary (film) speed is proportional to the reassignment probability  $P$  and we do not allow boundary slip, this term

effectively enforces a velocity  $v$ , *i.e.* applies a strain rate to the foam. The strain  $\epsilon(t)$  is proportional to a time integral of  $v$ ,

$$\epsilon \propto \int_0^t \sqrt{\gamma} (1 - e^{-\gamma(t') \Delta x_i}) dt'. \quad (6.2)$$

The prefactor  $\sqrt{\gamma}$  sets the unit and relates  $\gamma$  to the amplitude of strain.

If we limit this term to the edge layer of spins, we apply boundary shear, equivalent to moving the top and bottom plates of the foam with edge bubbles glued to the plates, namely:

$$\gamma = \begin{cases} \gamma_0 G(t) & y_i = 1 \\ -\gamma_0 G(t) & y_i = y_{max} \\ 0 & otherwise \end{cases}, \quad (6.3)$$

where  $\gamma_0$  is the amplitude of the strain field and  $G(t)$  is a function of time. On the other hand, the choice,

$$\gamma = \beta y_i G(t), \quad (6.4)$$

corresponds to applying bulk shear with shear rate  $\beta$ . The corresponding experiment would be trapping the foam between two parallel plates and rotating the plates with respect to a fixed point with no-slip edge boundary conditions. In all our studies we use  $G(t) = 1$  for steady shear, and  $G(t) = \sin(\alpha t)$  for periodic shear. Since for steady shear, the strain is a constant times time,  $\sqrt{\gamma}(1 - P)t$ , stress-time plots are equivalent to stress-strain curves.

Experimentally, the mechanical response, including yield strain, the elastic moduli, and topological rearrangements, is sensitive to the liquid volume fraction [135]. Especially, the simulation results of both Weaire [166] and Durian [167] showed a critical liquid fraction at which the foam undergoes a “melting transition.” However,

although different liquid content and drainage effects can be readily incorporated in the Potts model [132], we consider only the dry foam limit.

We use a periodic boundary condition in the  $\hat{x}$  direction, the direction of strain, to mitigate finite size effects, and a no-flux boundary condition in the  $\hat{y}$  direction. All our runs use a fourth nearest neighbor interaction on a square lattice, which has a lattice anisotropy of 1.03, very close to an isotropic situation.

For ordered foams under boundary shear, we use a  $400 \times 100$  lattice with each bubble containing  $20 \times 20$  lattice sites. For ordered foams under bulk shear, we use a  $256 \times 256$  lattice with  $16 \times 16$  sites for each bubble. When unstressed, all the bubbles are hexagons, except for those touching the top and bottom boundaries which are truncated, with four sides in the bulk. In the case of disordered foams, we use a  $256 \times 256$  lattice with various area distributions. We have tried a few runs using a lattice of size  $1024 \times 1024$  with  $64 \times 64$  bubbles. The results did not appear to differ.

The topological and area distributions characterize the foam disorder. Since the bubble areas are constrained, the evolution of the area distribution is not useful. We use a variety of disordered samples with different distributions characterized by  $\mu_2(n)$  and  $\mu_2(a)$ .

In practice, we generate the initial configuration by partitioning the lattice into equal sized square domains, each containing  $16 \times 16$  lattice sites. The squares are offset in every other row, so the pattern resembles a brick wall. We then run the simulation with area constraints but without strain at finite temperature for a few Monte Carlo steps, and then decrease the temperature to zero and let the pattern relax. The minimization of total surface energy (and hence the total boundary length) results in a hexagonal pattern, the initial configuration for the ordered foam. For disordered initial configurations, we continue to evolve the hexagonal pattern with-

out area constraints at finite temperature so that the bubbles coarsen. We monitor  $\mu_2(n)$  of the evolving pattern, and stop the evolution at any desired distribution or structural disorder, then relax the pattern at zero temperature with area constraint to guarantee that all our initial patterns have equilibrated, *i.e.* without adding external strain or stress, the bubbles would not deform or rearrange.

For all our simulations,  $\Gamma = 1$ , and  $\mathcal{J}_{ij} = 3$ , unless noted. All the simulations shown are run at zero temperature except when we study temperature effects on hysteresis. Finite temperature speeds the simulations, but does not appear to change the results qualitatively.

We keep a list of neighbors for each bubble. A change in the neighbor list indicates a topological change, which, since bubbles do not disappear, has to be a T1 event.

### 6.3 Hysteresis

Foam flow involves a collection of bubbles rearranging from one metastable configuration to another. The configurations therefore are important in understanding the flow behavior. Since foams are non-equilibrium, they can stick in metastable configurations for a long time unless perturbed. We study the metastability by hysteresis measurement.

Hysteresis is “a retardation of the effect when the forces acting upon a body are changed (as if from viscosity or internal friction); *esp.*: a lagging in the values of resulting magnetization in a magnetic material (as iron) due to a changing magnetizing force.” (Webster). Hysteresis occurs when the parameters have a non-linear and delayed response to a changing external field, resulting in memory effects. Hysteresis commonly appears in systems with many metastable states due to (but not limited to) interfacial phenomena or domain dynamics. The classic example of the former is that the contact angle between a liquid and a solid surface depends

on whether the front is advancing or retreating. The classic example of the latter is ferromagnetic hysteresis, in which the magnetization lags behind the change in applied magnetic field. In foams, hysteresis can have multiple microscopic origins, including stick-slip interfacial and vertex motion, local symmetry-breaking bubble rearrangements (T1 events), and the nucleation and annihilation of bubbles. In all of these, noise and disorder play an intrinsic role in selecting among the many possible metastable states when the foam is driven away from mechanical equilibrium. If the disordered systems have many metastable states with large energy barriers, *i.e.* a very rugged free energy landscape, they can relax extremely slowly towards the global energy minimum. On long length scales and practical time scales, a pattern driven by an external field will move from one metastable local energy minimum to the next. The global free energy minimum and the thermal fluctuations that drive the pattern toward it are, in this case, irrelevant. The state will instead depend on its history. By focusing on non-coarsening foams, we rule out nucleation and annihilation as sources for hysteresis. A two-dimensional dry foam is therefore an ideal testing ground for improving our understanding of hysteresis arising from local rearrangements and interfacial dynamics.

Finding a good order parameter is always the key problem for describing patterns with many degrees of freedom. In accordance with [165], we define the quantity:

$$\phi \equiv \frac{1}{A} \sum_{\vec{i}, \vec{j}} \theta_{\vec{i}, \vec{j}} (1 - \delta_{\sigma_{\vec{i}}, \sigma_{\vec{j}}}), \quad (6.5)$$

as the total stored elastic energy, in which sites  $\vec{i}, \vec{j}$  are neighbors and  $\theta_{\vec{i}, \vec{j}}$  is the wall thickness which is 1 in all our simulations (dry foam limit); the summation is over the whole lattice.  $\phi$  gives the total boundary length,  $L$ , rescaled by the total lattice area  $A$ . As the energy resides on the surfaces of bubbles only,  $\phi$  is proportional to the total surface energy, differing by a constant (surface tension).

In the deformation of bubbles, we shall assume that the gas is nearly incompressible (large  $\Gamma$ ), so any external forces concentrate at the films. Values of stress can be calculated by taking numerical derivatives of the total surface energy [166]. The calculation via derivatives is not suitable for foams undergoing many topological changes, since the stored elastic energy is discontinuous when topological changes occur. The alternative is to calculate stress directly, as given in [179], by the sum of forces acting on the boundary, which locally is proportional to the boundary length of a bubble. The total shear stress  $\sigma$  is proportional to the change of total boundary length in the foam, or  $\sigma(t) \propto L(t) - L(0)$ , with  $L(0)$  the initial equilibrium boundary length.

### 6.3.1 Ordered Foams

The simplest topological rearrangement occurs for boundary shear applied to an ordered foam. In such a foam the deformation affects only the edge layer bubbles and all the T1 events are easily localized. As the applied boundary shear increases, the bubbles in the edge layer distort, giving rise to a stored elastic energy. Figure 6.5(a) shows snapshots of the pattern. When a pair of vertices are pushed together to form a four-fold vertex, the number of sides changes for the cluster of bubbles involved. Colors in Figure 6.5 reflect the topologies of the bubbles. Note that a five-sided (green) and a seven-sided (yellow) bubble always appear in pairs except during the short lifetime of a four-fold vertex when the numbers of sides are ambiguous because of lattice discretization.

Once the strain exceeds a critical value, the yield strain, the edge bubbles undergo almost simultaneous rearrangements, which release the stress. The stored elastic energy,  $\phi$ , and stress,  $\sigma$ , increase during the time when the bubbles deform, then drop rapidly when the bubbles rearrange and release stress. Accumulation of stress

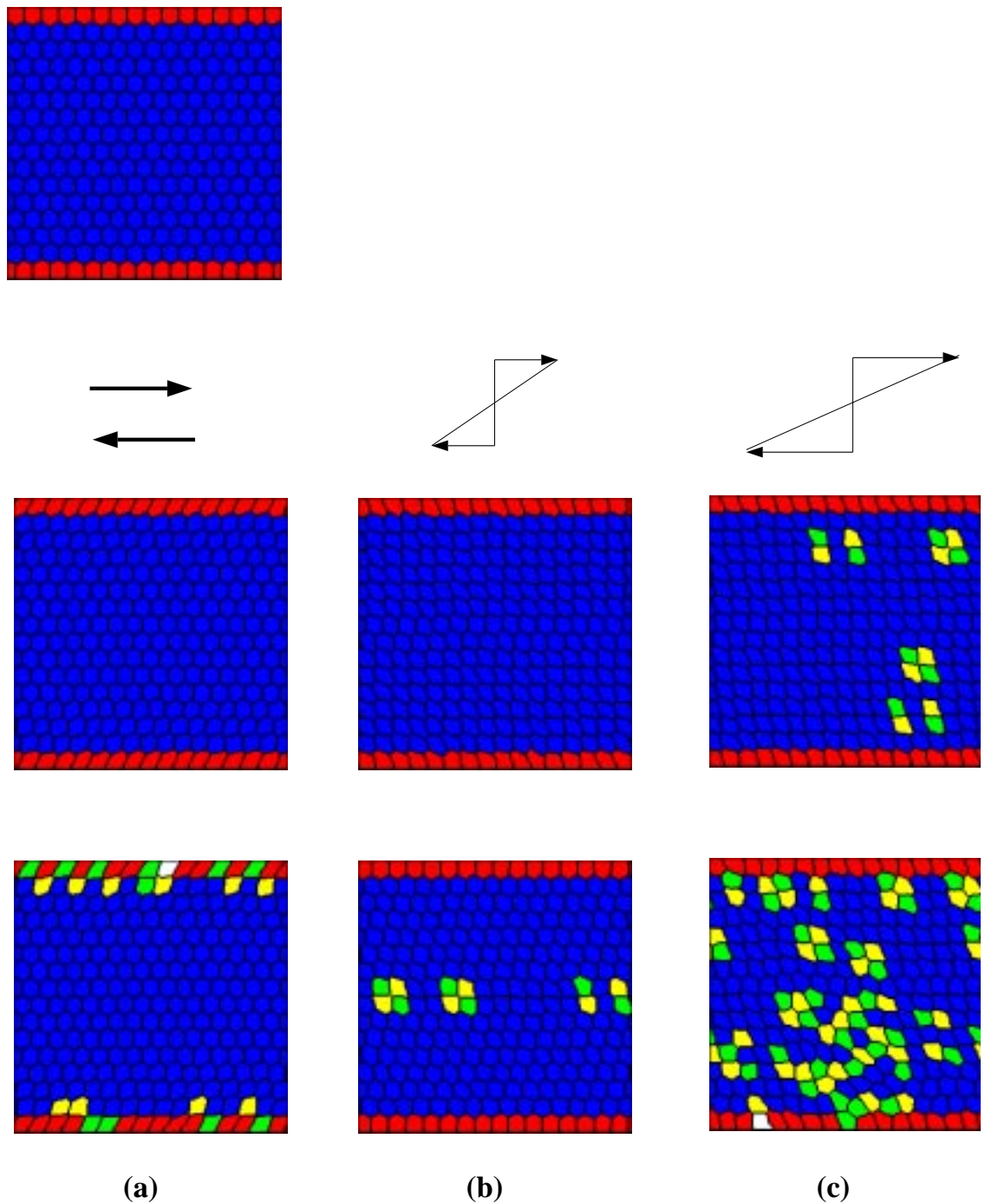


Figure 6.5: Snapshots of an ordered foam under shear. Colors encode bubble topologies (lattice size  $256 \times 256$ ): (a) boundary shear, (b) bulk shear (shear rate  $\beta = 0.01$ ), (c) bulk shear (shear rate  $\beta = 0.05$ ). Six-sided bubbles are blue, five-sided green and seven-sided yellow, four-sided (edge bubbles) are red.

stays within the edge layer of bubbles, and never propagates into the interior of the foam. The whole process repeats periodically, due to the periodic bubble structure, as shown in Figure 6.6, the stress-strain plot. This result corresponds to the stress-strain curves obtained in the model of Khan *et al.* with periodic hexagonal bubbles oriented at zero degrees with respect to strain as shown in Figure 6.3 [164].

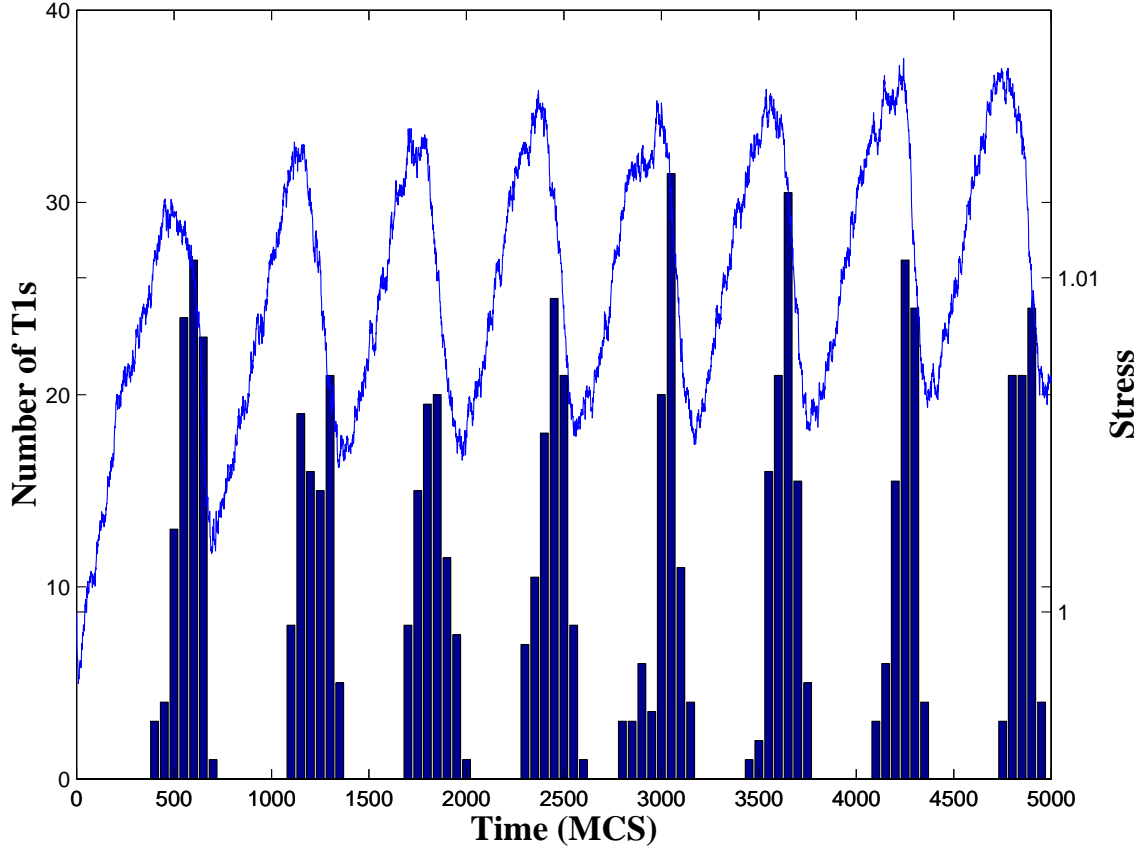


Figure 6.6: Stress-strain curve for an ordered foam under steady boundary shear, corresponding to case (a) shown in Figure 6.5. The number of T1 events is histogrammed in 50 MCS bins.

When applying periodic shear  $\gamma(t) = \gamma_0 \sin(\alpha t)$ , we keep the period  $2\pi/\alpha$  fixed and vary the amplitude  $\gamma_0$ . Under periodic (sinusoidal) shear, when the strain amplitude is small, bubbles deform when stress accumulates linearly and recover their shapes when stress is released. No topological rearrangement occurs. The stress-

strain plot is linear, corresponding to an elastic response. This result is in perfect agreement with the experimental result of DWS in [180]. As the strain amplitude increases, the stress-strain curve forms a small butterfly shaped hysteresis loop before any topological rearrangements occur, indicating a macroscopic viscoelastic response. For increasing strain amplitude, the hysteresis loop increases in size. When the applied strain amplitude exceeds a critical value, T1 events occur, which change the shape of the hysteresis loop. Even larger strain amplitude introduces more T1 events per period, adding small loops to the “wings” of the hysteresis loop. Figure 6.7 shows the transition between the three types of hysteresis in the stress-strain curve.

Changing the coupling strength,  $\mathcal{J}_{ij}$ , changes the viscosity of the bubble walls. Small coupling strength corresponds to lower viscosity. Similar transitions from elastic, to viscoelastic to fluid-like flow behavior occur for progressively lower values of viscosity, shown in Figure 6.8. The phase diagram in Figure 6.9 shows the elastic, viscoelastic and fluid-like behavior (as derived from the hysteretic response), as a function of the coupling strengths,  $\mathcal{J}_{ij}$  (*i.e.* viscosity) and strain amplitude,  $\gamma_0$ . A striking feature is the linear nature of all the boundaries (This figure contains 44 data points which are not shown).

Figure 6.10 shows the effect of finite temperature on the stress-strain curves. With progressively increasing temperature, noise becomes more dominant and eventually destroys the hysteresis loop. This result implies diminished metastability at finite temperature. However, it does not seem to change the qualitative mechanical response.

A more conventional experiment is the application of bulk shear [165, 167, 176, 178], with the shear strain varying linearly as a function of the vertical coordinate,

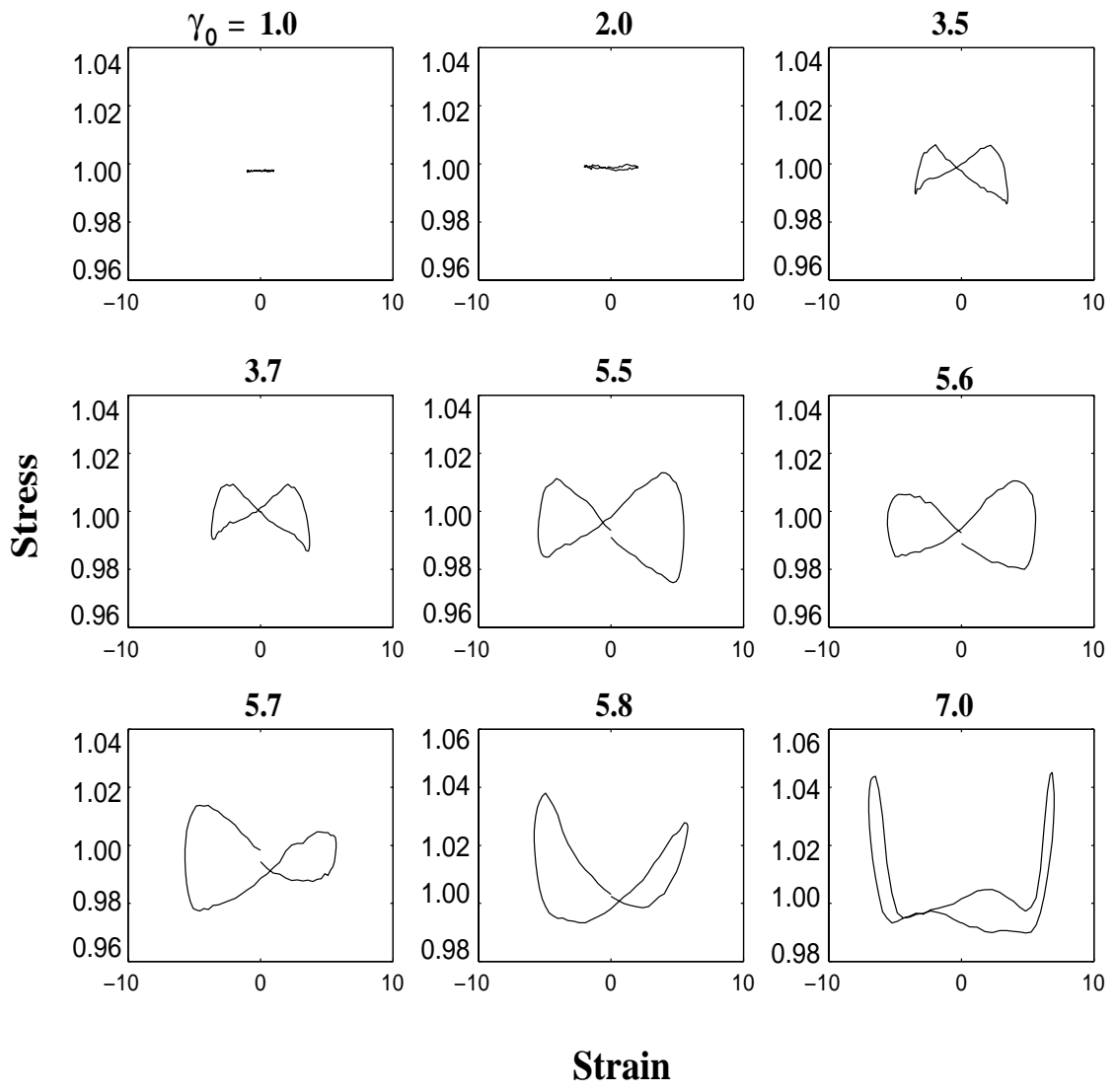


Figure 6.7: Stress-strain curves for ordered foam under periodic boundary shear with  $\mathcal{J}_{ij} = 3$ ,  $T = 0$  and  $\alpha = 1.7 \times 10^{-3}$ . Numbers above the figures are  $\gamma_0$ , the shear amplitude. Progressively increasing  $\gamma_0$  leads to transitions among three types of hysteresis:  $\gamma_0 = 1.0$  corresponds to elastic response,  $\gamma_0 = 3.5$  shows viscoelastic response (before any T1 event occurs),  $\gamma_0 = 7.0$  is a typical response when only one T1 event occurs during one cycle of strain loading. The intermediate steps show that the transition between these three types is smooth.

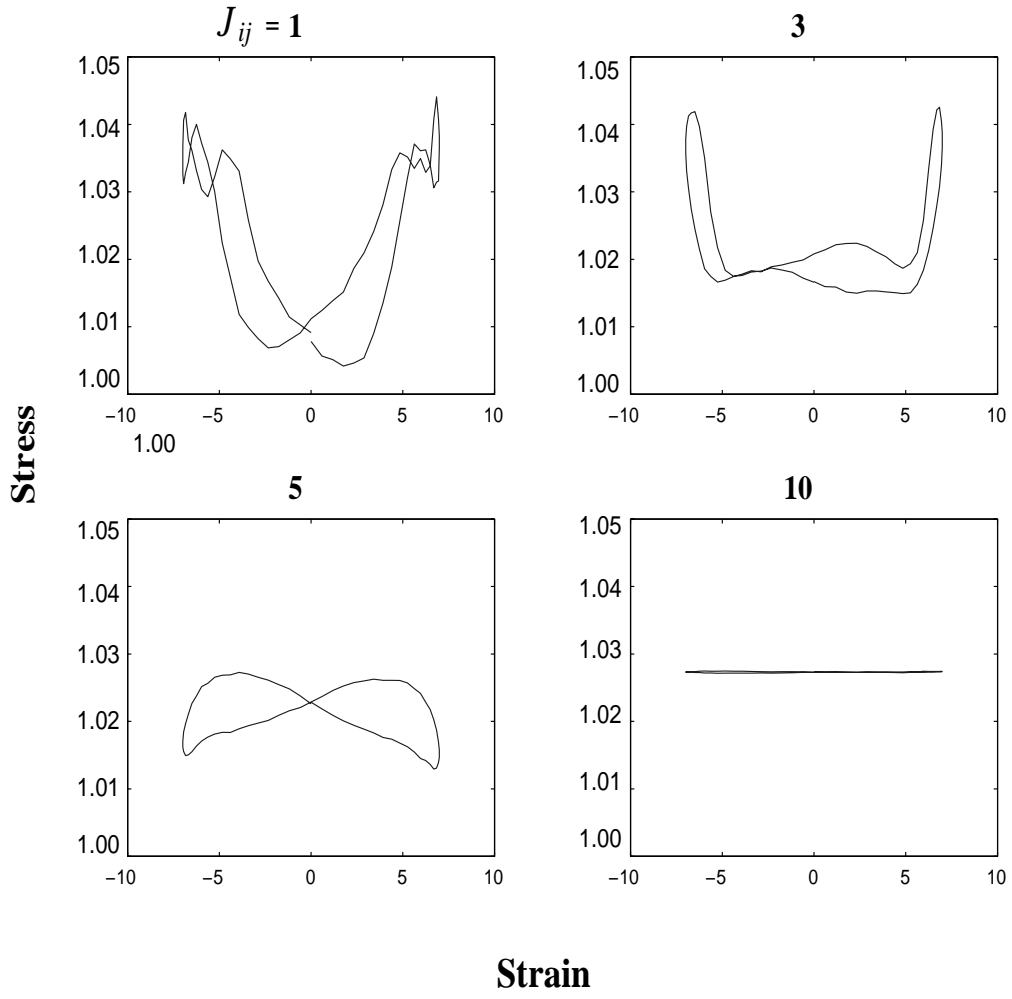


Figure 6.8: Stress-strain curves for ordered foam under periodic boundary shear with  $\gamma_0 = 7$ ,  $T = 0$  and  $\alpha = 1.7 \times 10^{-3}$ . Numbers above the figures are  $\mathcal{J}_{ij}$ , which is inversely related to liquid viscosity. Progressively decreasing  $\mathcal{J}_{ij}$  produces transitions from elastic ( $\mathcal{J}_{ij} = 10$ ), to viscoelastic ( $\mathcal{J}_{ij} = 5$ ) and to viscous flow due to T1 events. For  $\mathcal{J}_{ij} = 3$ , all the edge bubbles undergo one T1 during half a strain cycle. For  $\mathcal{J}_{ij} = 1$ , all the edge bubbles undergo three T1s during half a strain cycle.

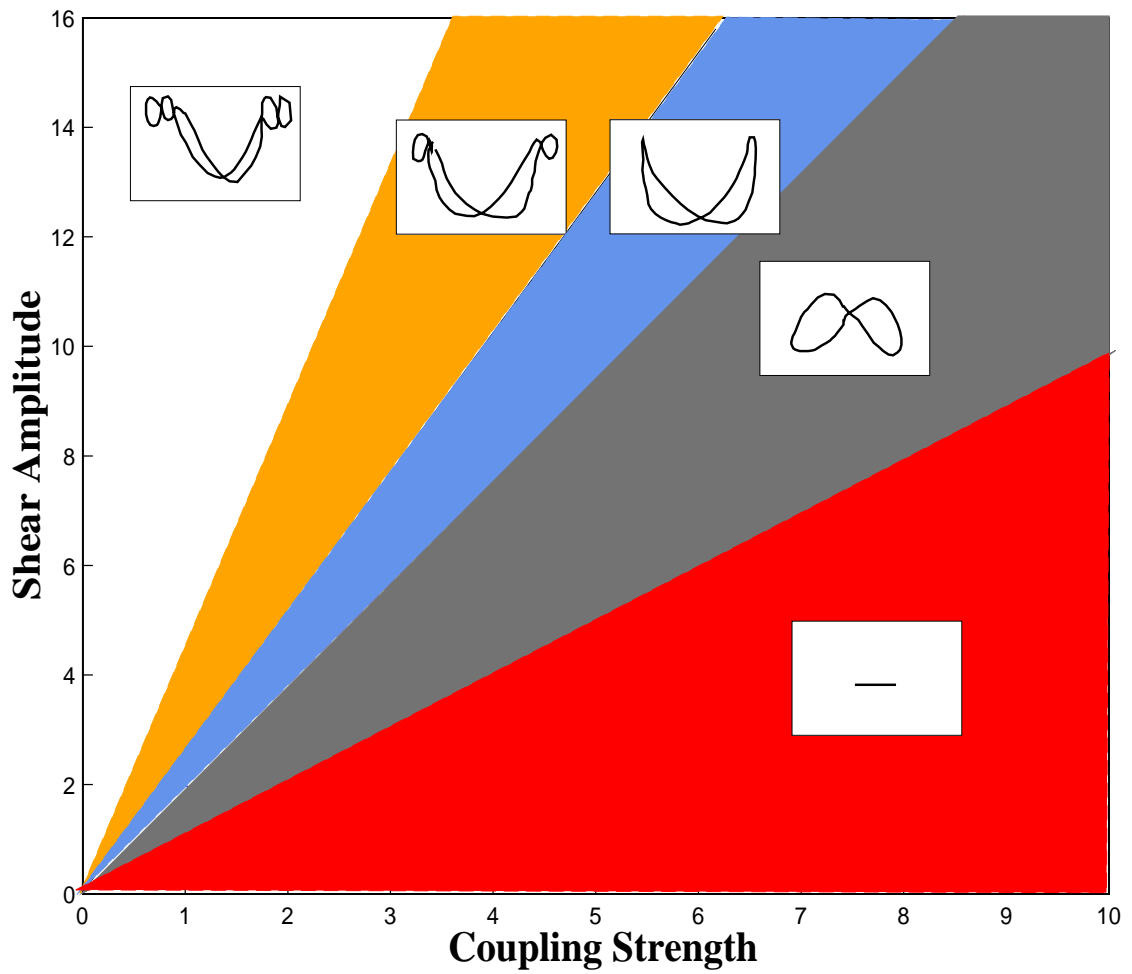


Figure 6.9: Phase diagram of hysteresis in the parameter space  $\gamma_0$  vs.  $J_{ij}$ , with  $T = 0$  and  $\alpha = 1.7 \times 10^{-3}$ .

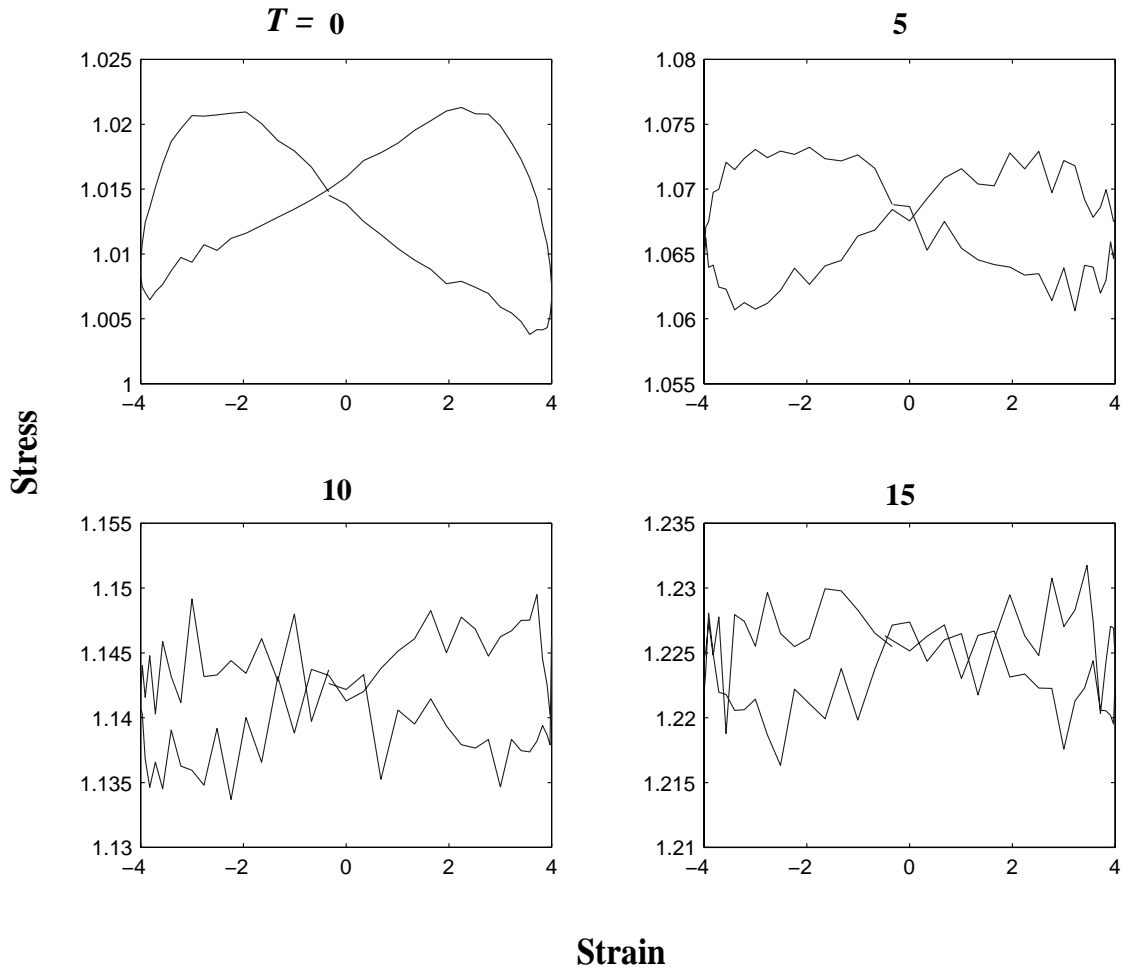


Figure 6.10: Effect of progressively increasing temperature,  $T$  ( $\mathcal{J}_{ij} = 3$ ,  $\gamma_0 = 4$ , and  $\alpha = 1.7 \times 10^{-3}$ ). All data shown are averages over 10 periods.

from  $\gamma_0$  at the top of the foam to  $-\gamma_0$  at the bottom. For an ordered foam, the stress-strain relationship has two distinct behaviors depending on the shear rate. For a small shear rate, a “sliding plane” develops in the middle of the foam. Figure 6.11 shows that defects (non-hexagonal bubbles) appear only at the center plane. The stress-strain curve, shown in Figure 6.8, therefore, is similar to that for boundary shear on an ordered foam. The periodicity is due to the periodic structure of the bubbles, reminiscent of the shear planes observed in metallic glasses in the inhomogeneous flow regime, where stress-induced rearrangement is the origin of plastic deformation [181].

At high shear rates, the T1 events are not localized in space [Figure 6.5(c)]. Non-hexagonal bubbles appear throughout the foam. The stress-strain curve, shown in Figure 6.9, is not periodic but rather smooth; the bubbles constantly move and do not have time to settle into a metastable configuration to sustain finite stress. The foam therefore shows a smaller yield strain. The transition between these two phenomena occurs when the shear rate is in the range  $1 \times 10^{-2} < |\beta| < 5 \times 10^{-2}$  (See Section 6.5 for a discussion of the effect of shear rate on yield strain.). This transition can be understood by looking at the relaxation time scale of the foam. In our simulations, the relaxation time for a single deformed bubble is a few MCS. In a foam, due to surface viscous drag and geometric confinement by other bubbles, the relaxation time for a single bubble becomes of the order of 10 MCS. For a shear rate  $\beta = 5 \times 10^{-2}$ ,  $\beta^{-1}$  is of the same order as the relaxation time. Thus for shear rates above the natural internal relaxation time scale, the macroscopic response changes from jagged and elastic to smooth and viscous response, as found in fingering experiments in foams [182].

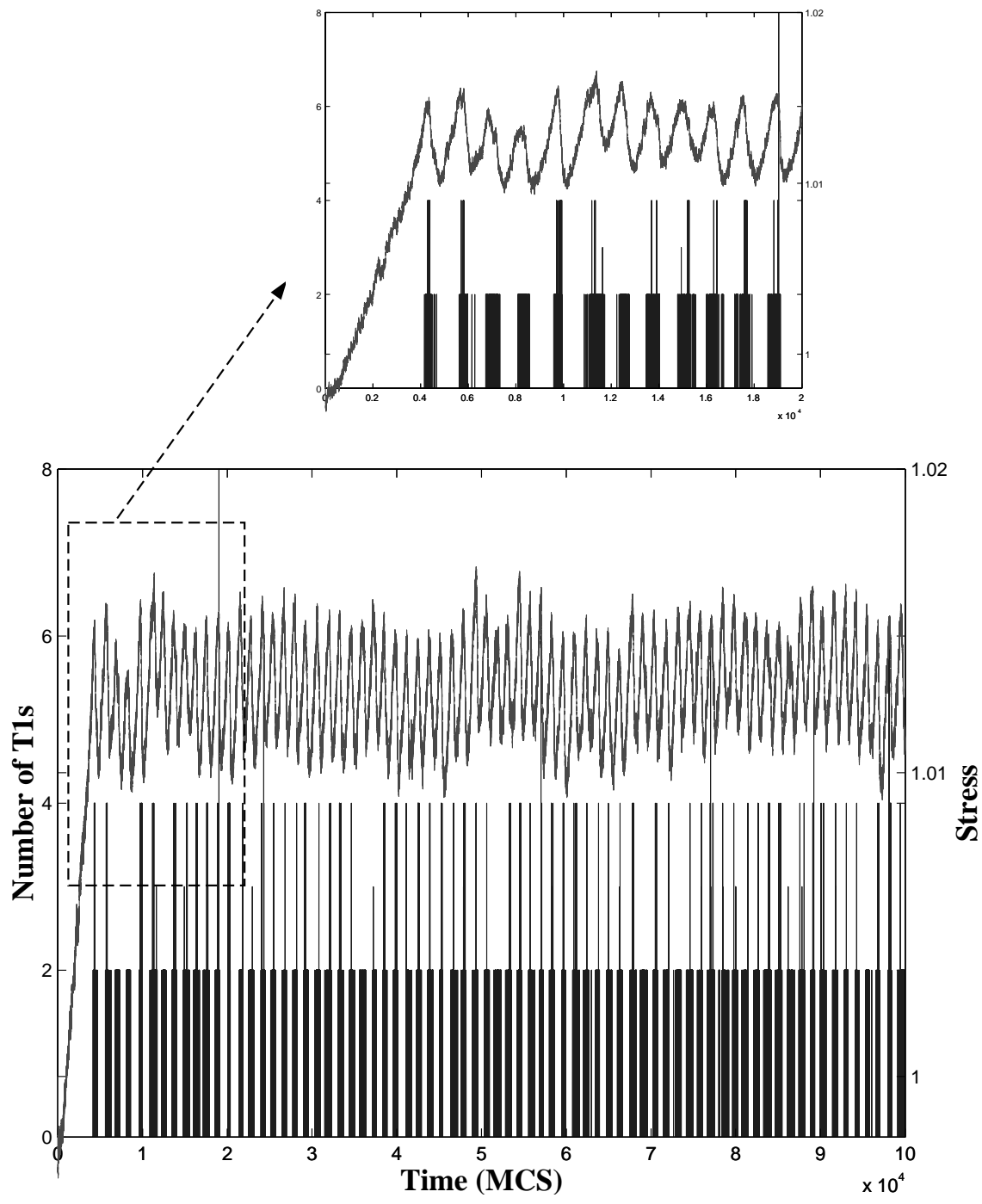


Figure 6.11: Stress-strain curve for an ordered foam under bulk shear at shear rate  $\beta = 0.01$ . The magnified view in the box shows the correlation between stress releases and individual avalanches of T1 events.

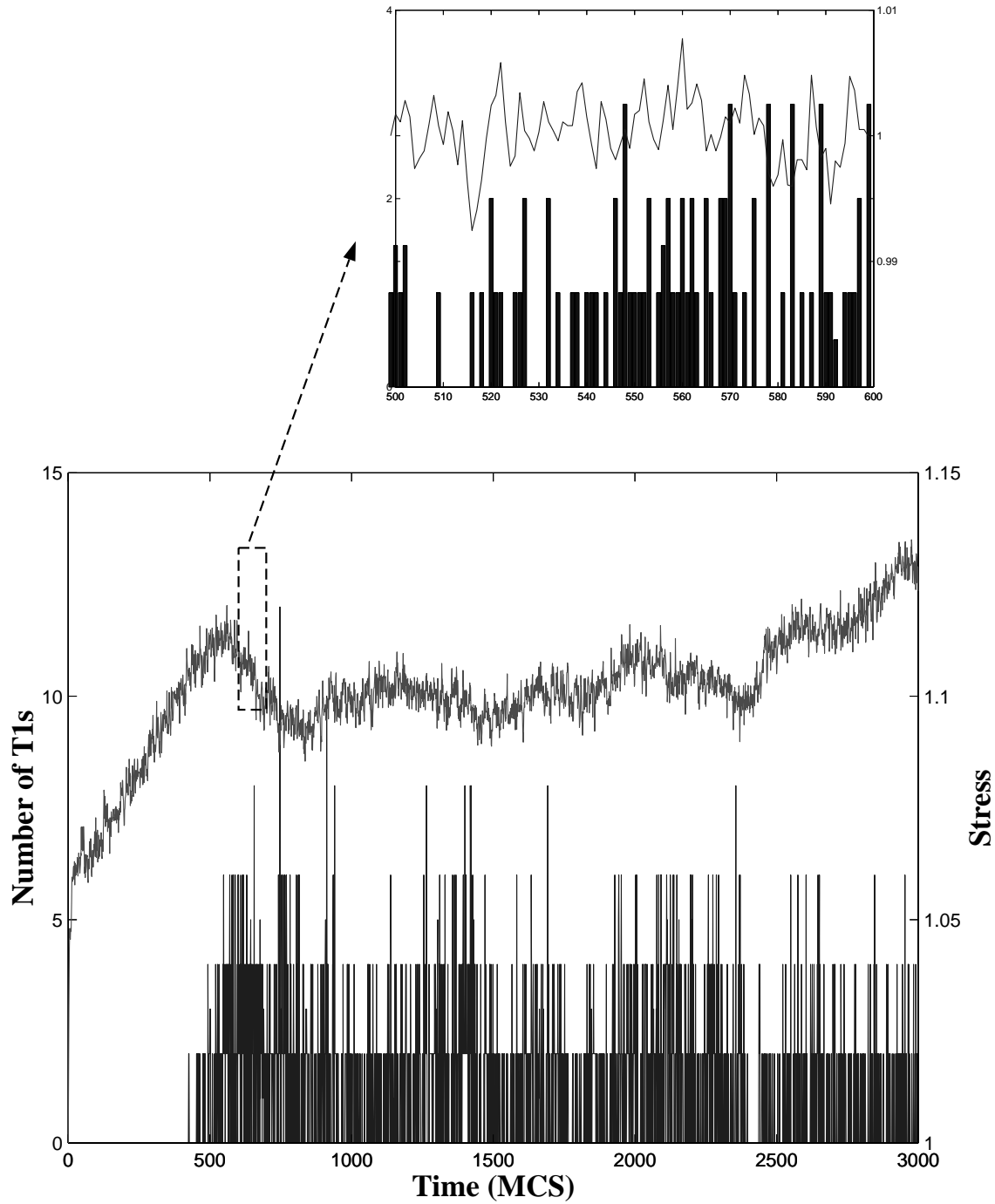


Figure 6.12: Stress-strain curve for an ordered foam under bulk shear at shear rate  $\beta = 0.05$ . The magnified view in the box shows the correlation between stress releases and overlapping avalanches of T1 events.

### 6.3.2 Disordered Foams

In a disordered foam, when boundary bubbles of different sizes undergo T1 events at different times, the boundary shear can no longer be confined to the edge layer; instead it propagates into the interior of the foam [Figure 6.13(a)]. The yield strain is much smaller. Figure 6.15 shows an example of such fluid-like behavior, where no stress can accumulate in the foam. Linear elasticity and linear viscoelasticity is not observed, since even a small deformation may lead to topological rearrangements for the small bubbles, when the size distribution of the foam is broad. The foam deforms and yields like a fluid upon application of the smallest strain. Note that when shear is first applied, the stress decreases to below 1, the initial value, before increasing to fluctuate around 1. This stress decrease occurs because the initial disordered pattern is not fully relaxed. We generate the disordered initial pattern by stopping coarsening of a foam at the desired  $\mu_2(n)$ . The initial pattern is thus likely to be in a metastable state. Shear induced rearrangement helps the bubbles to reach a packing configuration with lower surface energy.

A disordered foam under bulk shear, snapshots shown in Figure 6.13(b), behaves like an ordered foam if the shear rate is low. The rearrangements are discrete and avalanche-like, resembling a stick-slip process, or adding sand slowly to a sandpile. However, if the shear rate is high, all the avalanches overlap, and the deformation and rearrangements are more homogeneous and continuous, as in a simple viscous liquid.

Note that in all the hysteresis plots, the stress-strain curves cross at zero strain, indicating no residual stress at zero strain. This crossing is an artifact of the definition of stress, which ignores the angular measures of distortion, *i.e.* the total boundary length does not distinguish among the directions in which the bubbles

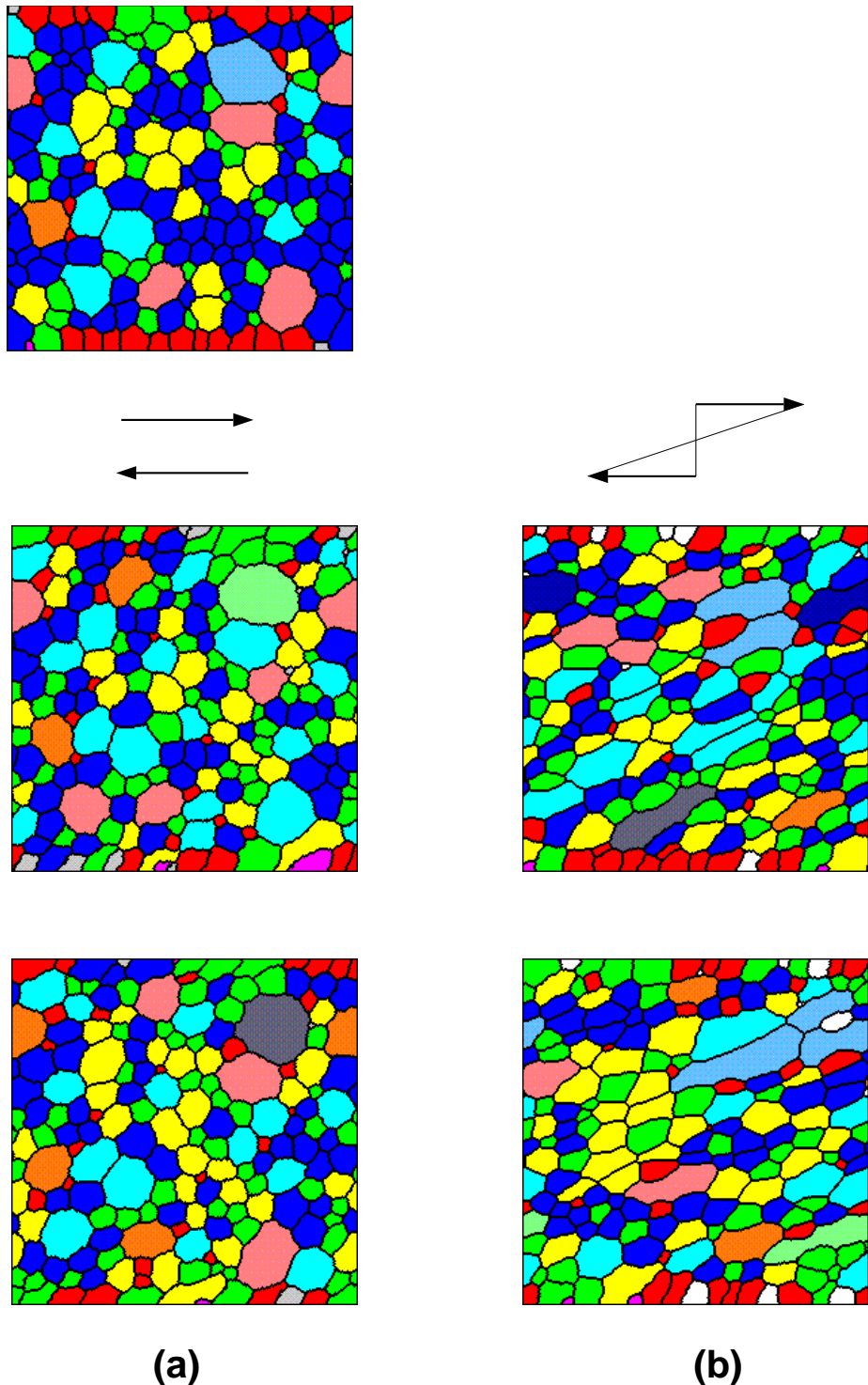


Figure 6.13: Snapshots of a disordered foam under shear. Colors encode bubble topologies (lattice size  $256 \times 256$ ): (a) boundary shear, (b) bulk shear.

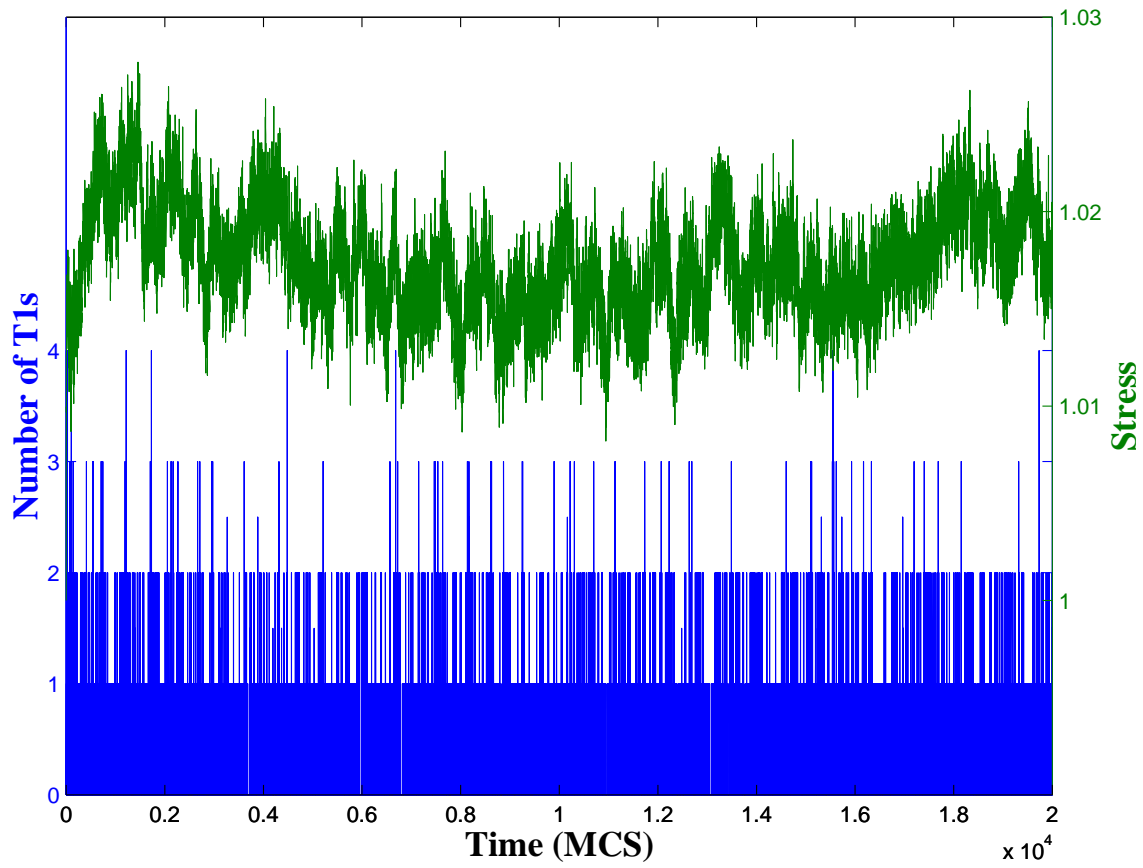


Figure 6.14: Stress-strain curves for a disordered foam under steady boundary shear, corresponding to Figure 6.13(a).

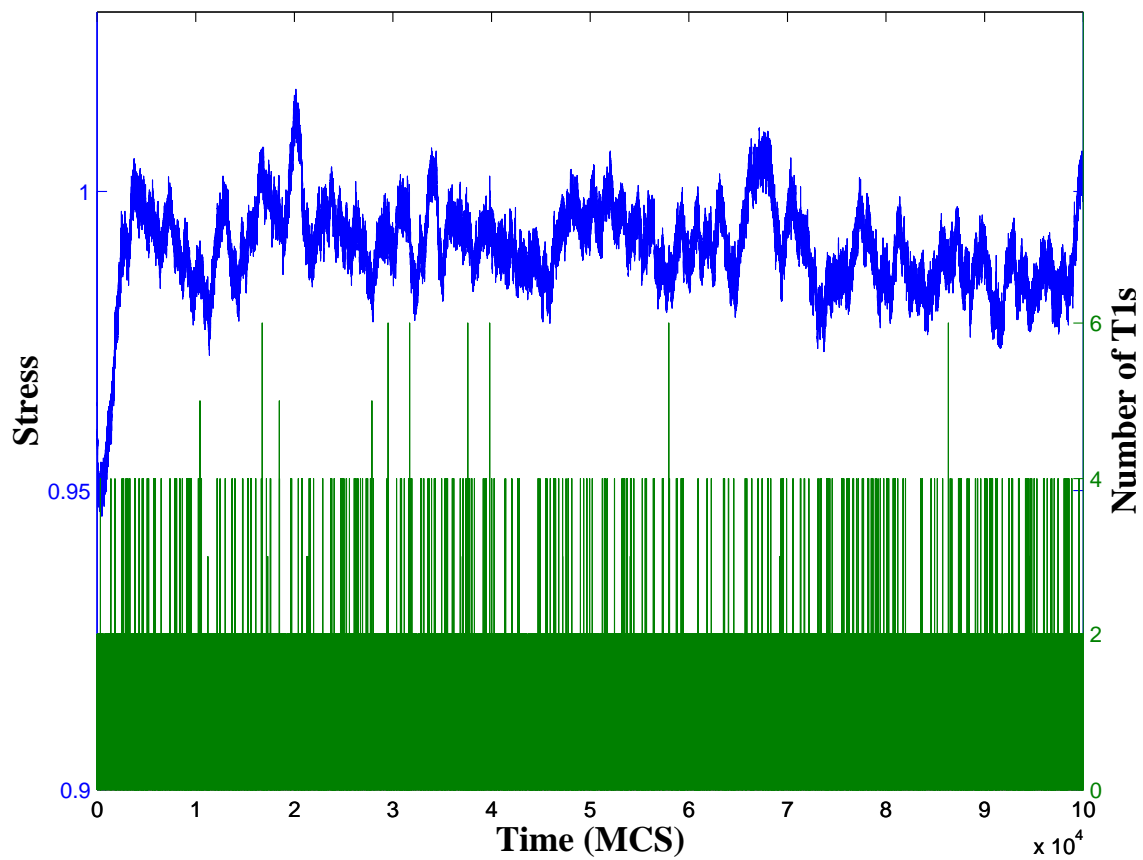


Figure 6.15: Stress-strain curves for a disordered foam under steady bulk shear at shear rate  $\beta = 0.01$ , corresponding to Figure 6.13(b).

tilt. A choice of stress definition which included phase information would show non-zero residual stress at zero strain, but would not otherwise affect the results reported here.

#### 6.4 T1 Avalanches

In both experiments [11, 17] and simulations, the contact angles of the vertices remain  $120^\circ$  until two vertices meet. The external strain determines the rate at which vertices meet. The new four-fold vertex rapidly splits into a vertex pair, recovering  $120^\circ$  contact angles, at a rate determined by the viscosity. This asymmetry of time scale in the T1 event contributes to the hysteresis.

In vertex model simulations, sudden releases of energy occur once the applied shear exceeds the yield strain [165]. The event size, *i.e.* the energy release per event in the dry foam limit, follows a power-law distribution:  $\rho(n) \sim n^{-\frac{3}{2}}$ , where  $n$  is the event size. A similar power-law distribution was found in Durian's bubble model [167], with an additional exponential cutoff for large events. Simulations of Weaire *et al.* [166, 179], however, suggest that power-law behavior only appears in the wet foam limit. Experiments, on the other hand, have never found system-wide events or long range correlations among events [177, 178]. One of our goals is to reconcile these different predictions.

These differences may result from the use of energy release, rather than enumeration of actual events, as well as the assumption of a linear relation between energy jumps and the number of T1 events, namely,

$$\frac{d\phi}{dt} = cN, \quad (6.6)$$

where  $N$  is the number of T1 events and  $c$  is a constant. A drastic drop in the total boundary length indicates a large number of T1 events. However, in a dis-

ordered foam, all T1 events are not equal, since they do not all release the same amount of stored elastic energy. Under the same strain, smaller bubbles flow more easily. When bubbles deform by the same amount,  $\Delta l$ , for smaller bubbles, the relative deformation  $\frac{\Delta l}{l}$  is much higher. Thus they are more likely to go through T1 events. Moreover, a T1 event is not strictly local, but results in a deformation over a certain finite range of its neighborhood, as demonstrated by T1 manipulations in ferro-fluid foam experiments [183]. Therefore, the number of T1 events is not necessarily directly proportional to the decrease in total boundary length. We cannot compare the energy dissipation and T1 events directly. Furthermore, the mechanisms of energy dissipation differ in these models. Kawasaki *et al.* [165] include the dissipation due to the flow of liquid out of the Plateau borders; Durian [167] considers only the viscous drag of the liquid, while the model of Weaire *et al.* [166] is an equilibrium calculation involving quasistatic steps in the strain that do not involve any dissipation. In the Potts model, the evolution minimizes the total free energy naturally.

The avalanche-like nature of rearrangements appears in the sudden decreases of the stress (as calculated from the total boundary length) and the total elastic energy as a function of time. Figure 6.11 shows the relation between stress and the number of T1 events in an ordered foam under steady simple shear for a small strain. The stored energy increases almost linearly until the yield strain is reached. The avalanches are separated nicely. Every cluster of T1 events corresponds to a drastic drop in the energy, and the periodicity is due to the ordered structure of the foam. At a higher shear rate, shown in Figure 6.12, the yield strain remains almost the same, but the avalanches start to overlap and the stress curve becomes smoother and less regular. In the sandpile analogy, instead of adding sand grains one at a time and waiting until one avalanche is over before dropping another grain, the grains

are added at a constant rate and the avalanches, large and small, overlap with each other. A disordered foam, however, may not have a yield strain [Figure 6.14]; T1 events occur for the smallest strain. The foam flows as a fluid without going through an intermediate elastic or viscoelastic regime.

To study the correlation between T1 events, we consider the power spectrum of  $N(t)$ , the number of T1 events at each time step,

$$p_N(f) = \int dt \int d\tau e^{-if\tau} N(t)N(t + \tau). \quad (6.7)$$

Figure 6.16 shows typical power spectra of the time series of T1 events in an ordered foam. At a shear rate  $\beta = 0.01$ , no power law exists for the T1 events. The peak at  $\sim 10^{-3}$  is due to the periodicity of bubble structure in an ordered foam when a “sliding plane” develops. At shear rate  $\beta = 0.02$ , the spectrum resembles white noise. As the shear rate increases to  $\beta = 0.05$ , the power spectrum develops a power law tail at the low frequency end, with an exponent very close to 1. In a disordered foam, with increasing shear rate, the spectra for the T1 events gradually change from completely uncorrelated white noise to  $1/f$  at higher shear rates. By  $1/f$ , we mean any noise of power spectrum  $S(f) \sim f^{-\alpha}$  where  $\alpha$  is near 1. Such noise is more erratic than Brownian noise,  $\alpha = 2$ , but more orderly than uncorrelated white noise,  $\alpha = 0$ .

These power spectra suggest that the experimental results for T1 events [177, 178] correspond to a low shear rate, with no long-range correlation among T1 events. Structural disorder introduces correlations among the events. Power-law avalanches do not occur in ordered polycrystalline lattices of hexagonal cells at low shear rate, where rearrangements occur simultaneously. At a high shear rate, when the value of  $\dot{\gamma}^{-1}$  is comparable to the duration of rearrangement events, the bubbles move constantly. The foam therefore behaves viscously, since rearrangements are induced

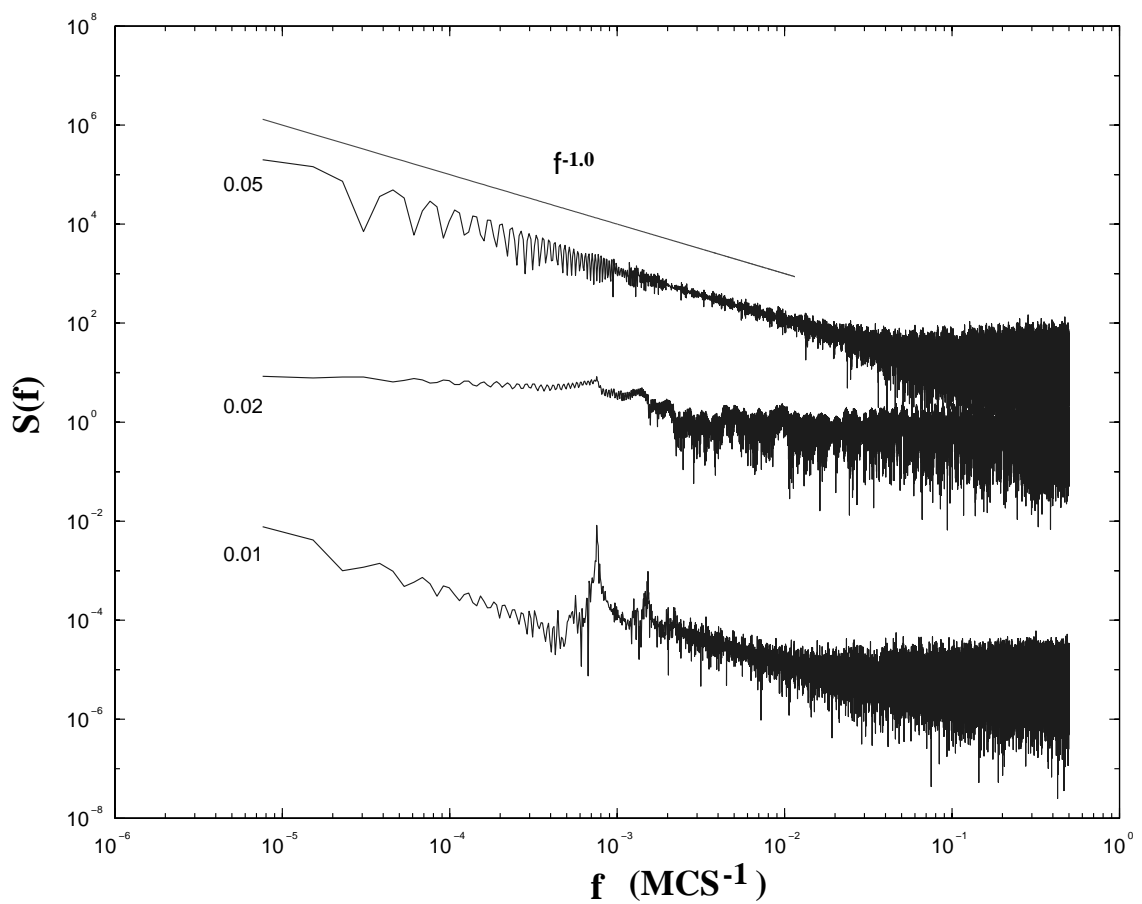


Figure 6.16: Power spectra of the time series of the number of T1 events in an ordered foam for three shear rates,  $\beta = 0.01, 0.02$  and  $0.05$ , respectively.

faster than bubbles can settle into metastable configurations which can support stress elastically. At these rates, even an ordered structure behaves like a disordered one, since its symmetry and periodicity are destroyed.

In a disordered foam, whenever one T1 event happens, the deformed bubbles release energy by viscous dissipation and also transfer stress to their neighboring bubbles, which in turn are more likely to undergo a T1. Thus, T1 events become more correlated. Shown in Figure 6.17, the power spectra change from that of white noise toward  $1/f$  noise. When the first sufficiently large region to accumulate stress undergoes T1 events, it releases stress and pushes most of the rest of the bubbles over the brink, causing an “infinite avalanche.” Some bubbles switch neighbors, triggering their neighbors to rearrange (and so on) until a finite fraction of the foam has changed configuration, causing a decrease in the total stored energy, mimicking the cooperative dynamic events in a random field Ising model [184].

On the other hand, in a highly disordered foam, the bubbles will essentially rearrange independently, if spatial correlations for area and topology are weak. Pairs of bubbles switch as strain exceeds their local yield points. Although more frequent, the avalanches will be small, without diverging correlation lengths. Figure 6.18 shows the power spectra for T1 events for a highly disordered structure with  $\mu_2(n) = 1.65$ . We observe no power law behavior, even at high shear rates. Thus a highly disordered foam resembles a homogeneous viscous fluid.

Over a range of structural disorder the topological rearrangements are strongly correlated. The question naturally arises whether the transition between these correlated and uncorrelated regimes is sharp or smooth, and what are the transition points. Detailed simulations involving different structural disorder should clarify these points.

Previous simulation [167] and experiments [178] measured  $\overline{N}$ , the average num-

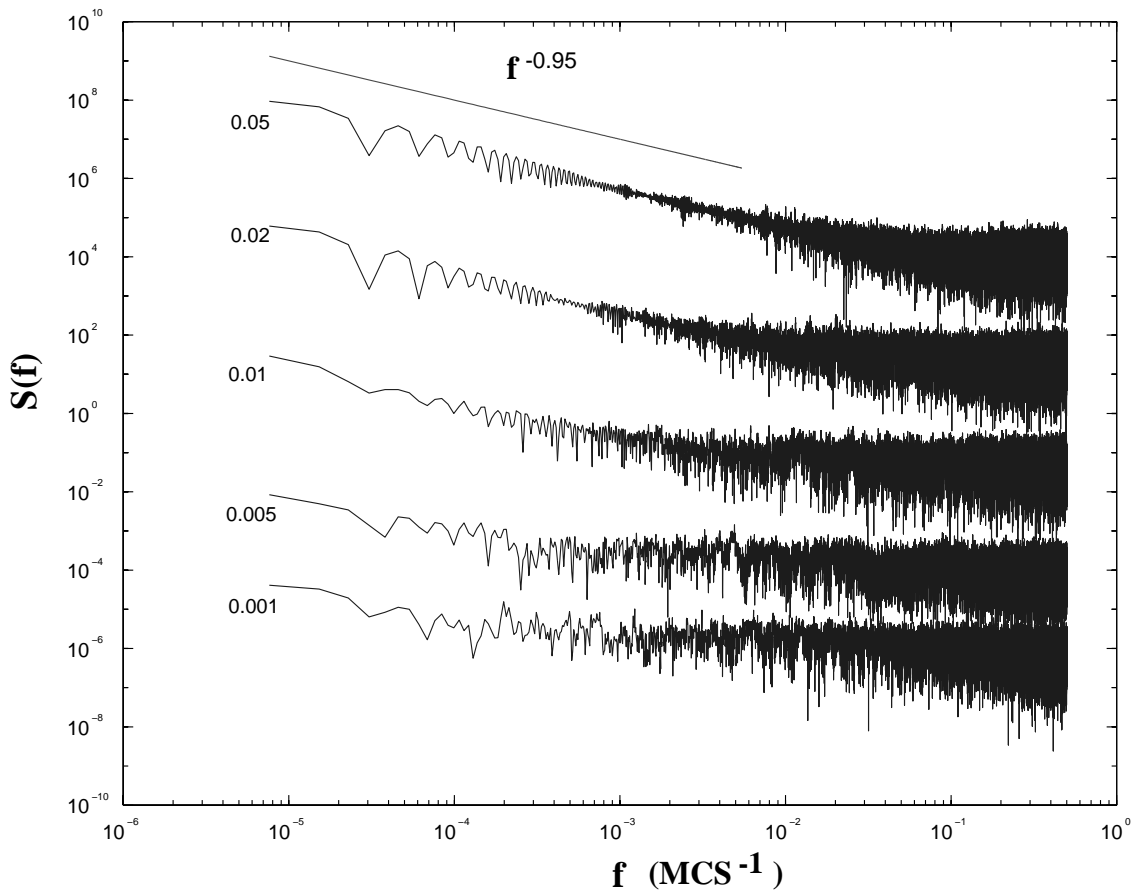


Figure 6.17: Power spectra of the time series of the number of T1 events in a disordered foam ( $\mu_2(n) = 0.81$ ,  $\mu_2(a) = 7.25$ ) for five shear rates  $\beta$  from 0.001 to 0.05.

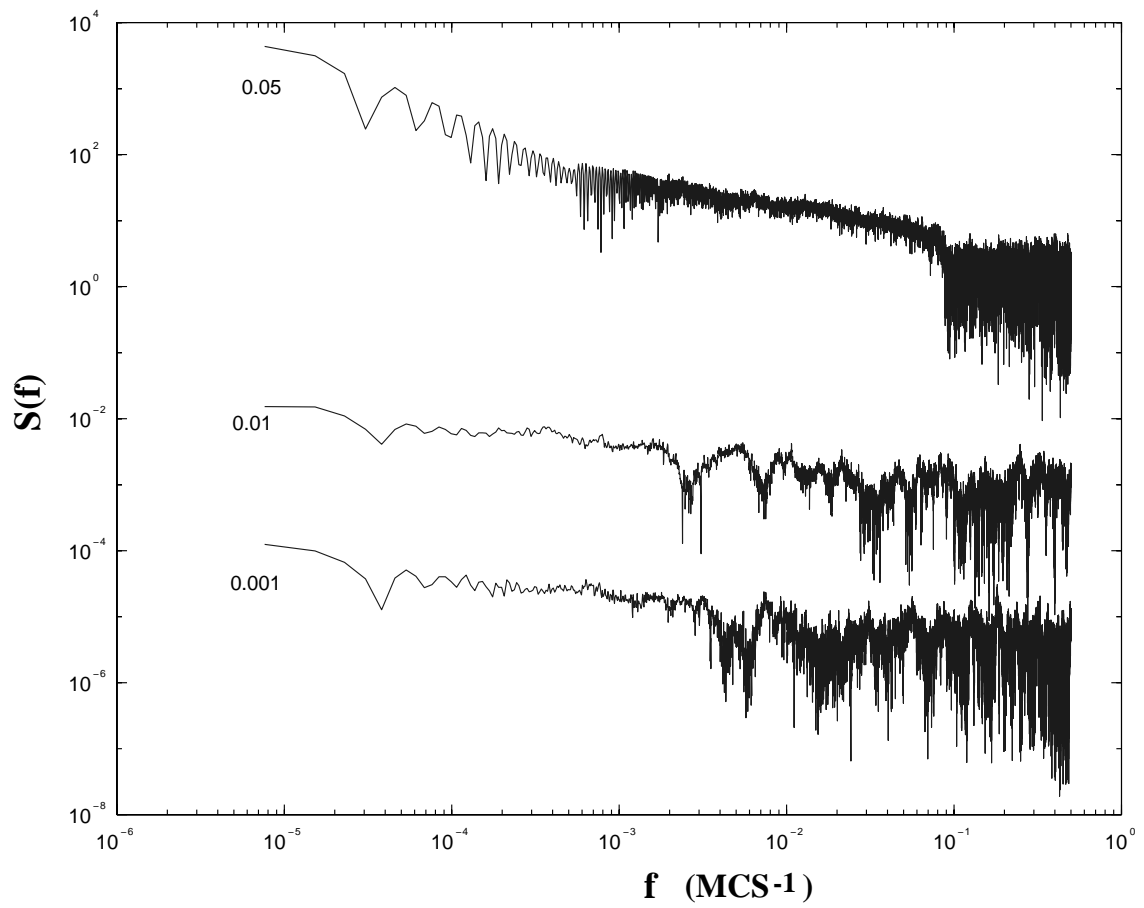


Figure 6.18: Power spectra of the time series of the number of T1 events in a very disordered foam ( $\mu_2(n) = 1.65, \mu_2(a) = 21.33$ ) for three shear rates.

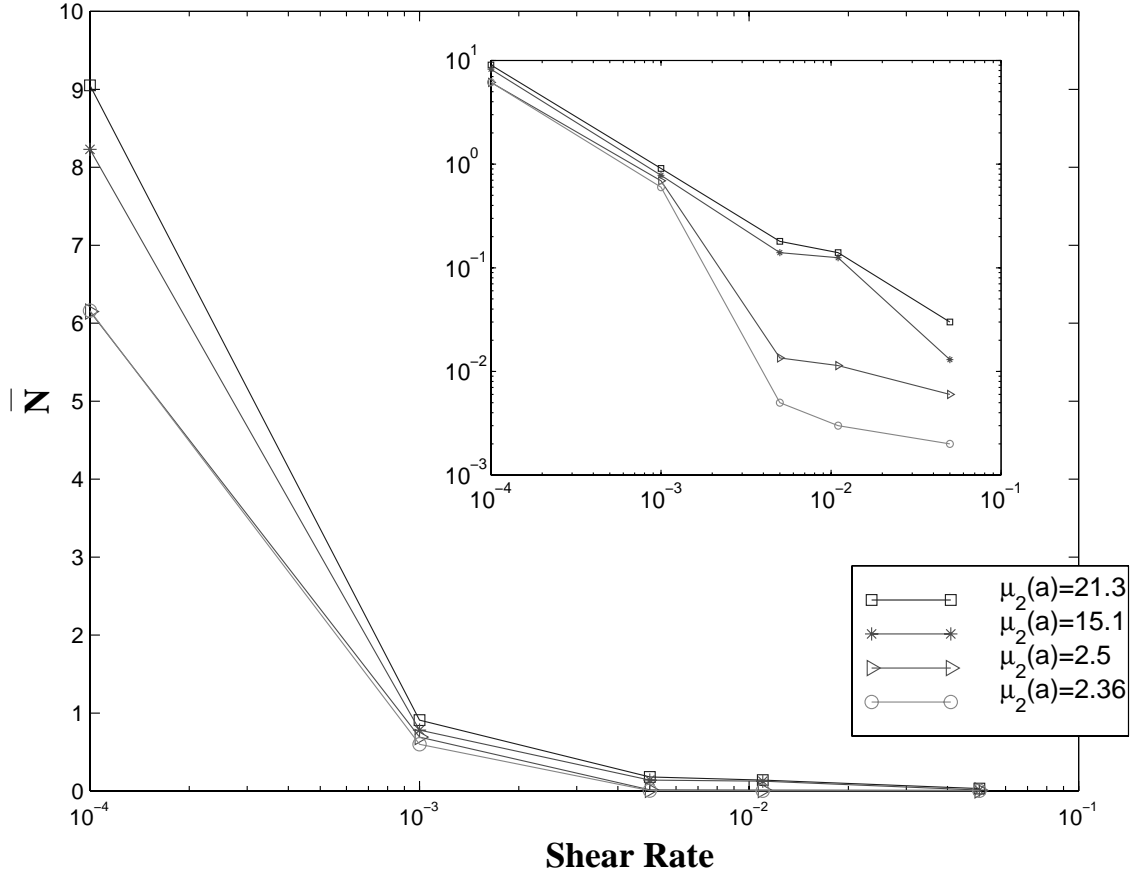


Figure 6.19: Number of T1 events per unit shear per bubble,  $\bar{N}$ , as a function of shear rate,  $\beta$ , for four samples. Squares correspond to a foam of 180 bubbles, with  $\mu_2(n) = 1.65$ ,  $\mu_2(a) = 21.33$ . Stars correspond to a foam of 246 bubbles with  $\mu_2(n) = 1.72$ ,  $\mu_2(a) = 15.1$ . Triangles correspond to a foam of 377 bubbles, with  $\mu_2(n) = 1.07$ ,  $\mu_2(a) = 2.50$ . Circles correspond to a foam of 380 bubbles, with  $\mu_2(n) = 0.95$ ,  $\mu_2(a) = 2.35$ . The inset shows on a log-log scale that the  $\bar{N}$  values differ by several orders of magnitude.

ber of T1 events per bubble per unit shear, and claimed that  $\bar{N}$  was independent of the shear rate. Our simulation results, based on three different sample foams and shear rates covering two orders of magnitude, however, disagree. As shown in Figure 6.19,  $\bar{N}$  depends sensitively on both the polydispersity of the foam and the shear rate. Only at large shear rates does  $\bar{N}$  seem to be independent of the shear rate, which might explain the above mentioned experimental data [178].

The avalanches and  $1/f$  power spectra are reminiscent of a number of examples

with many degrees of freedom and dissipative dynamics which self-organize into states that are barely stable [185]. Simple examples include stick-slip models, driven chains of nonlinear oscillators, and sandpile models. In sandpile models, both the energy dissipation rate (total number of transport events at each time step) and the output current (the number of sand grains leaving the pile) show power-law scaling in their distributions. In particular, if the avalanches do not overlap, then the power spectrum of the output current follows a power law with a finite size cutoff [186].  $1/f$ -type power spectra result from random superposition of individual avalanches [187].

If the analogy with sandpiles holds, we should expect the power spectra of the time derivative of energy to be  $1/f$ , and the power spectra of the energy to be  $f^{-2}$ . But Figures 6.20, 6.21 and 6.22, the corresponding power spectra for  $\phi$  from the same simulations as figures 6.16, 6.17, and 6.18, obviously do not show  $f^{-2}$ : *i.e.* the topological rearrangements are not in the same universality class as sandpiles.

In particular, Figure 6.22 shows a complicated trend: the slope of the power spectrum increases from a small value at shear rate  $\beta = 0.001$  to a power law  $f^{-0.8}$  spanning over 4 decades at  $\beta = 0.005$ . But as the shear rate  $\beta$  increases, the power law disappears. In addition, a flat tail develops at high frequencies due to Gaussian noise. Other different slopes appears over different regimes, indicating the existence of multiple timescales and lengthscales.

## 6.5 Structural Disorder

As structural disorder plays an important role in mechanical response, we study the effect of disorder on the yield strain and the evolution of disorder in foams under shear. We measure the yield strain, at which the first T1 avalanches occur, by the

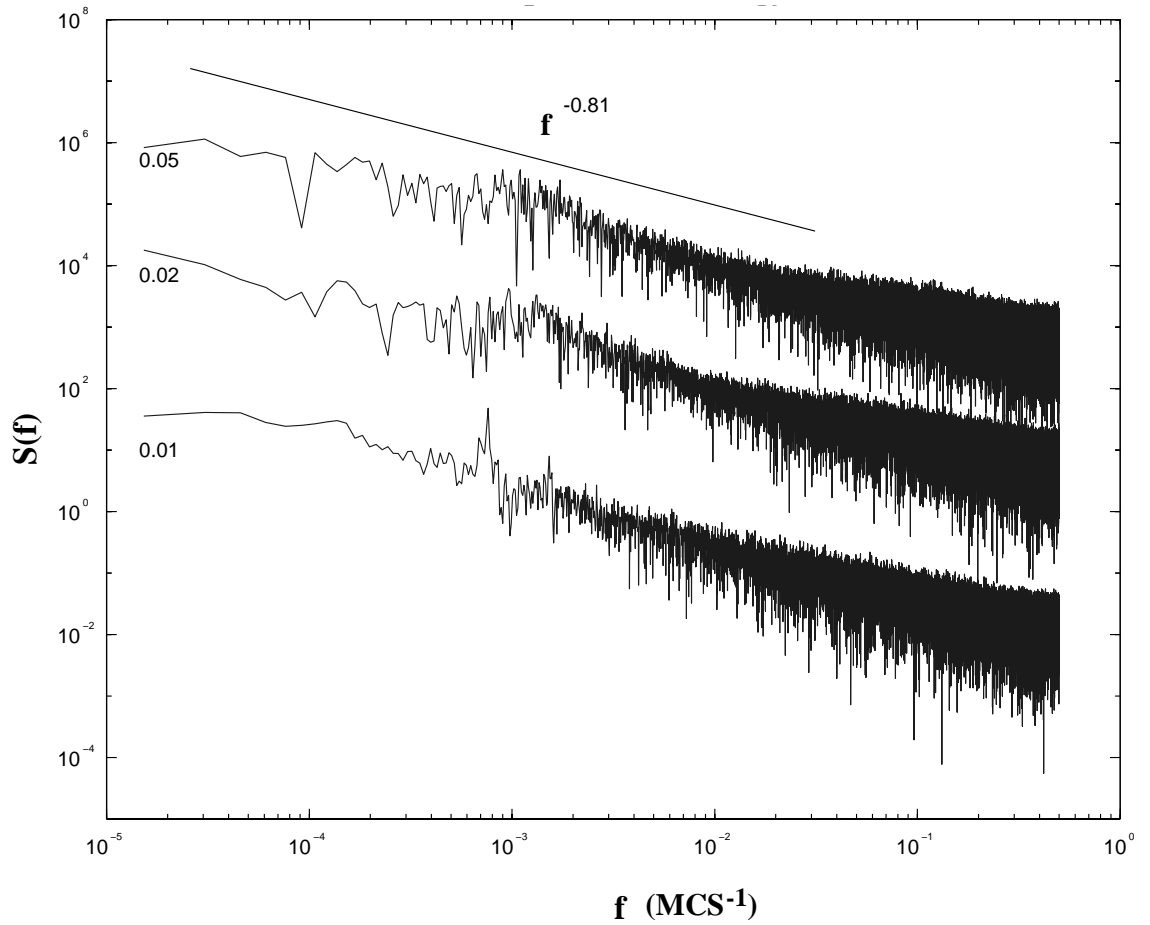


Figure 6.20: Power spectra of the energy for an ordered foam under steady bulk shear for three shear rates,  $\beta = 0.01, 0.02$ , and  $0.05$ .

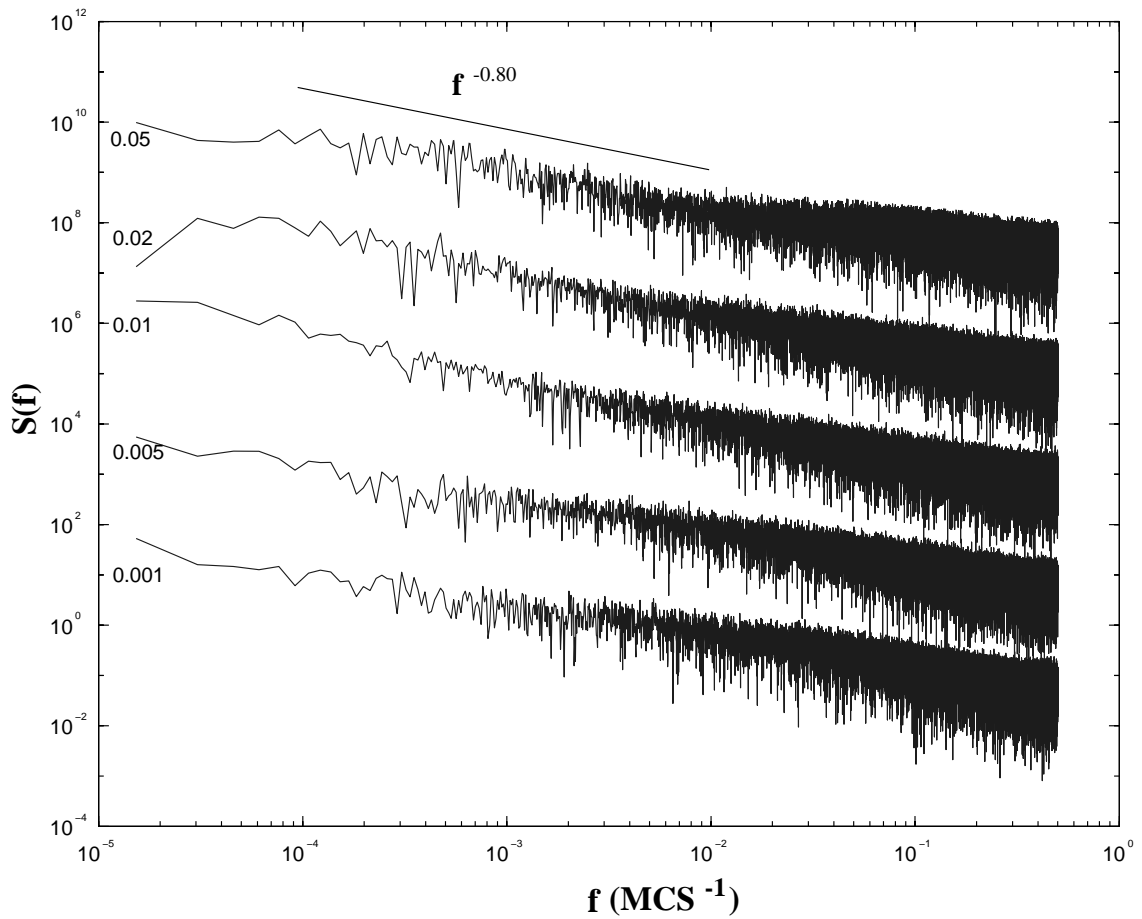


Figure 6.21: Power spectra of the energy for a disordered foam [ $\mu_2(n) = 0.81, \mu_2(a) = 7.25$ ] for five shear rates,  $\beta = 0.001, 0.005, 0.01, 0.02$ , and  $0.05$ .

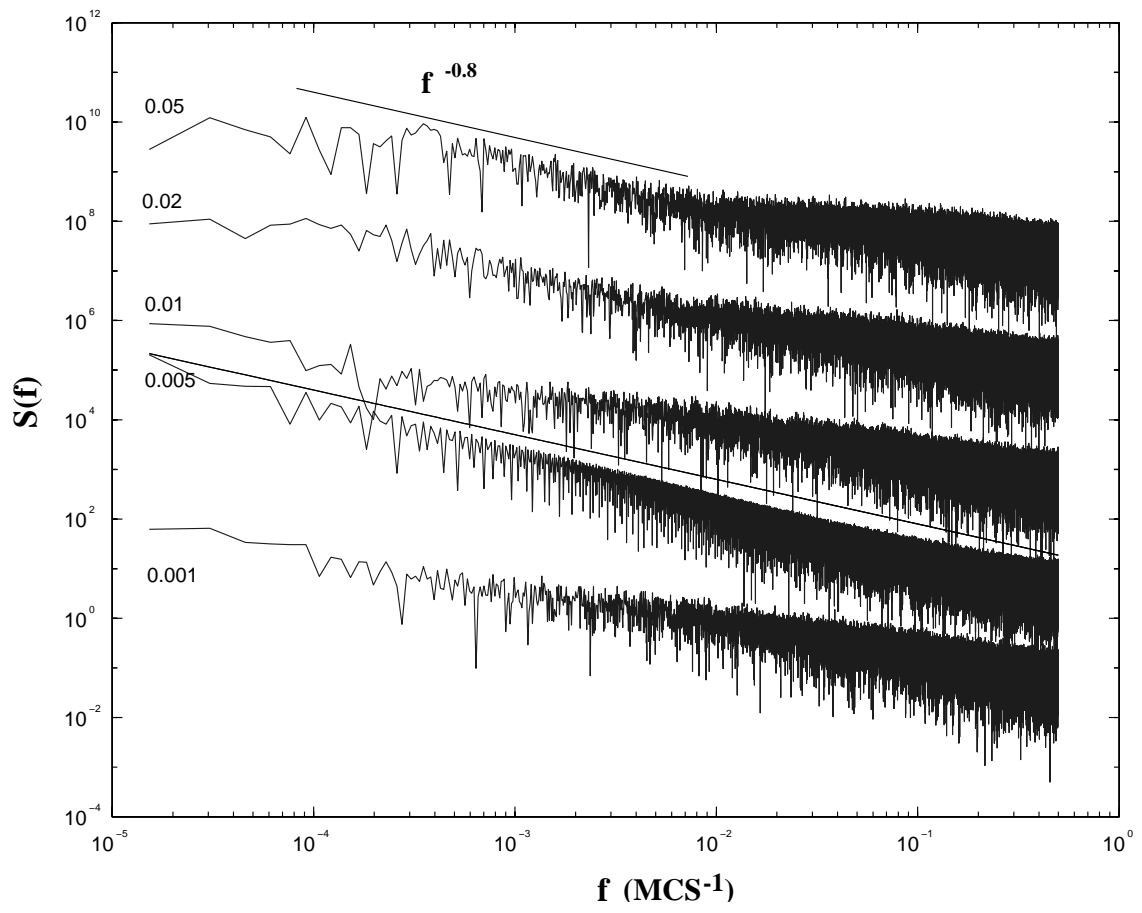


Figure 6.22: Power spectra of the energy for a very disordered foam [ $\mu_2(N) = 1.65, \mu_2(a) = 21.33$ ] for five shear rates,  $\beta = 0.001, 0.005, 0.01, 0.02$ , and  $0.05$ .

displacement at the top boundary of the foam divided by the half height of the foam (since the strain in the middle of the foam is zero) rescaled by the average bubble width.

Figure 6.23 shows the yield strain as a function of shear rate,  $\beta$ , for different foam disorders. For an ordered foam at low shear rates, when a sliding plane develops in the middle of the foam, the yield strain is the same for all shear rates. This equality is expected because T1 events occur almost simultaneously in the sliding plane, so the bubble size determines the yield strain. At high shear rates, T1 events distribute more homogeneously throughout the foam, which lowers the yield strain. The upper limit for the yield strain in an ordered foam is  $2/\sqrt{3}$ , when all the vertices in a hexagonal bubbles array simultaneously become four-fold under shear. The nucleation of defects (5-7 sided bubble pairs) and their propagation in real foams lower the yield strain. For disordered foams, the yield strain is lower for higher shear rate in the same foam; and at the same shear rate, the yield strain drastically decreases to zero as disorder increases, confirming that a higher shear rate has an effect similar to that of a higher disorder.

The most commonly used measure for topological disorder is the second moment of the topological distribution,  $\mu_2(n)$ . We used samples with initial  $\mu_2(n)$  ranging from 0.437 to 2.02, but have not observed any shear-induced ordering, *i.e.* reduction of  $\mu_2(n)$  with shearing, as reported in [166]. Instead,  $\mu_2(n)$  increases and never decreases back to its initial unstrained value, as shown in Figure 6.24 the evolution of  $\mu_2(n)$  in a few samples with different initial disorders. The difference between the simulations of Weaire *et al.* and the Potts model is not surprising. Weaire *et al.* applied step strain and observed the relaxed pattern. In our simulations, bubbles are constantly under shear. The foam is thus far from equilibrium. The topological disorder, as measured by  $\mu_2(n)$ , therefore does not necessarily settle to an equilibrium

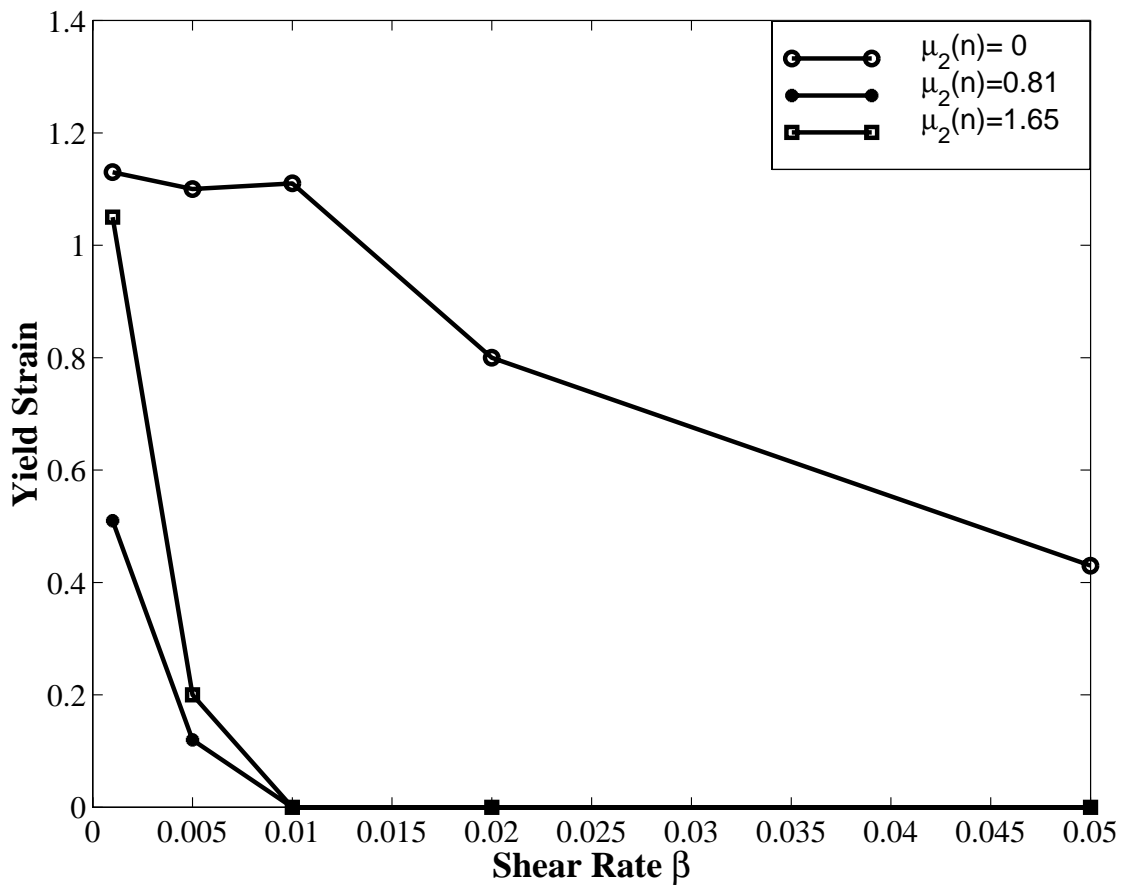


Figure 6.23: Yield strain as a function of shear rate.

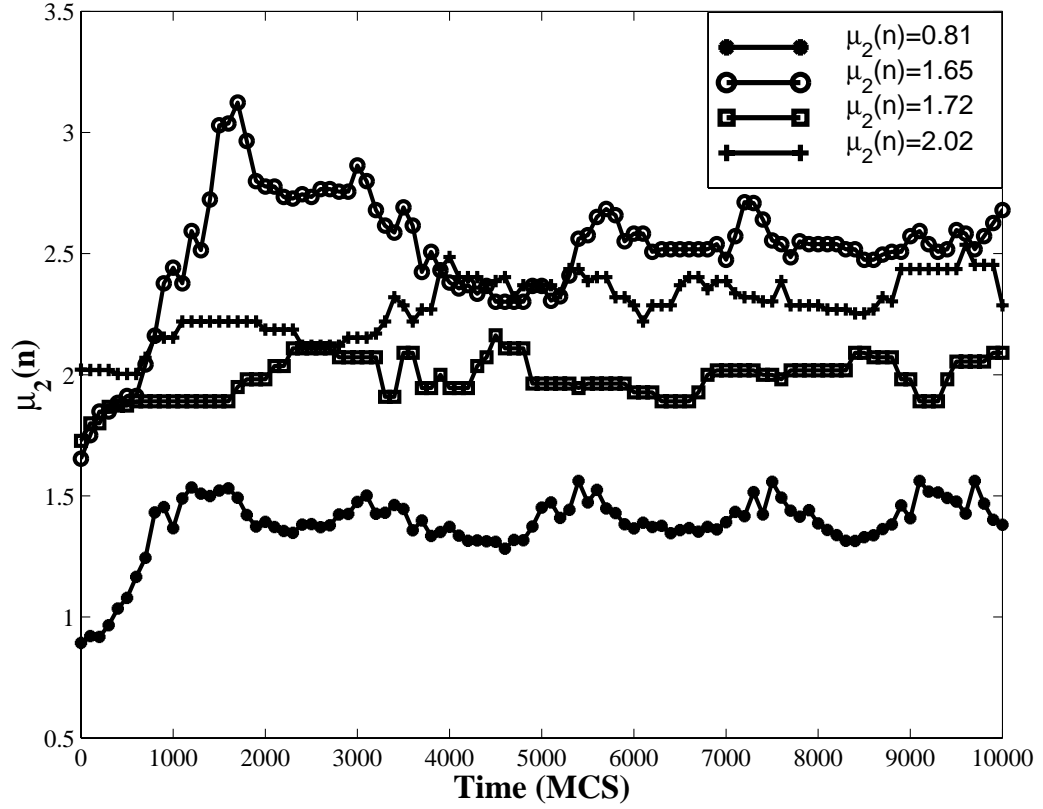


Figure 6.24: Evolution of  $\mu_2(n)$  under steady bulk shear. Legend denotes the initial  $\mu_2(n)$ .

value.

In an ordered foam at a small shear rate ( $\beta = 0.01$ ), with separated avalanches,  $\mu_2(n)$  fluctuates in synchrony with the decreases of stress, as shown in Figure 6.25. The amplitude of  $\mu_2(n)$  fluctuates from 0.437 to 0.500, as shown in Figure 6.25. During the period of stress increase,  $\mu_2(n)$  does not increase because the topology remains roughly constant. Instead  $\mu_2$  peaks at the beginning of avalanches, when the topological rearrangements broaden the topological distribution in ordered foams. Near the end of the avalanches of T1s,  $\mu_2(n)$  returns to its equilibrium value.

Notice that in the stress-time plots (Figures 6.6, 6.11, 6.12 and 6.14, 6.15), stress slowly increases at long times, because we continuously apply shear and the foam is

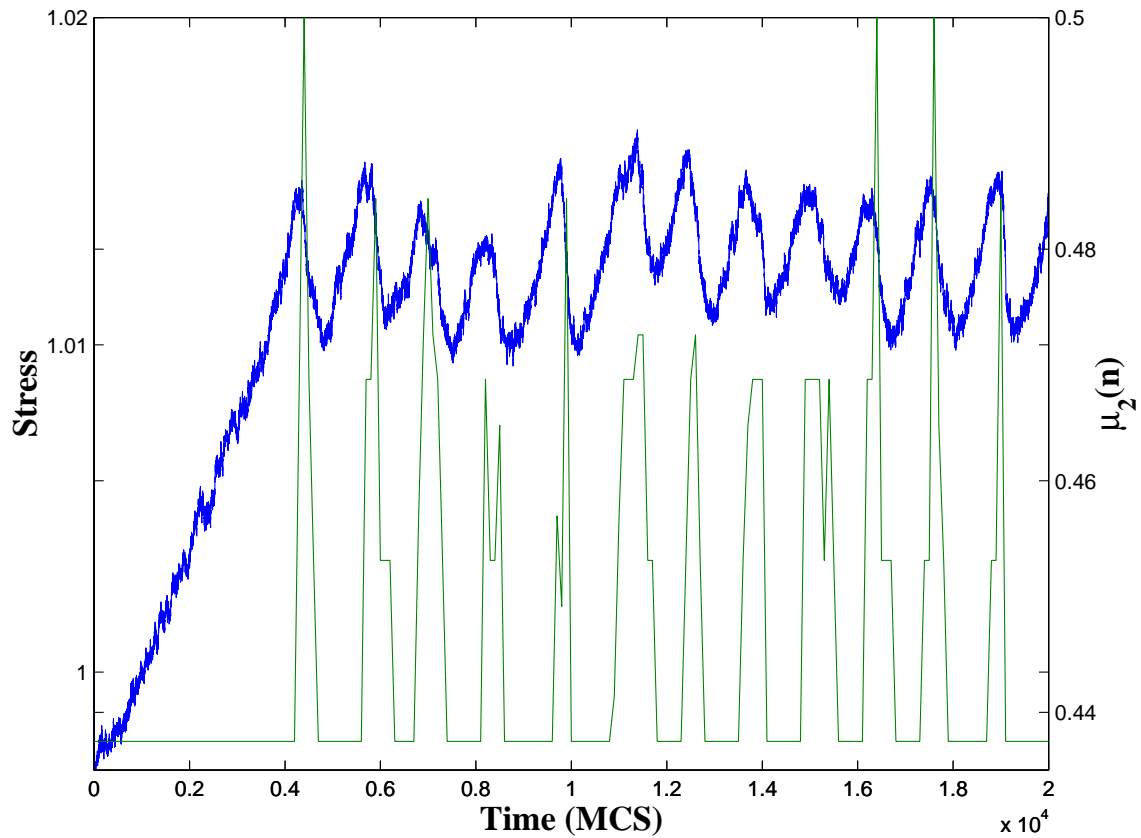


Figure 6.25: Evolution of  $\mu_2(n)$  under steady simple shear for an ordered foam, showing the correlation between the stress decreases and  $\mu_2(n)$ .

always out of equilibrium. Bubbles do not fully recover their original shapes. This deformation slowly accumulates at long times. In disordered foams, topological rearrangement may enhance the spatial correlation of bubbles, *i.e.* clustering of small bubbles in time. Results on spatial correlations for bubble topology,  $n$ , and area  $a$  should be investigated.

## 6.6 Effective Foam Viscosity

One of the greatest difficulties in applying the Potts model foam simulations to the analysis of experiments is our inability to derive the viscosity from the simulation parameters. We propose a few methods to measure the effective viscosity of simulated foams.

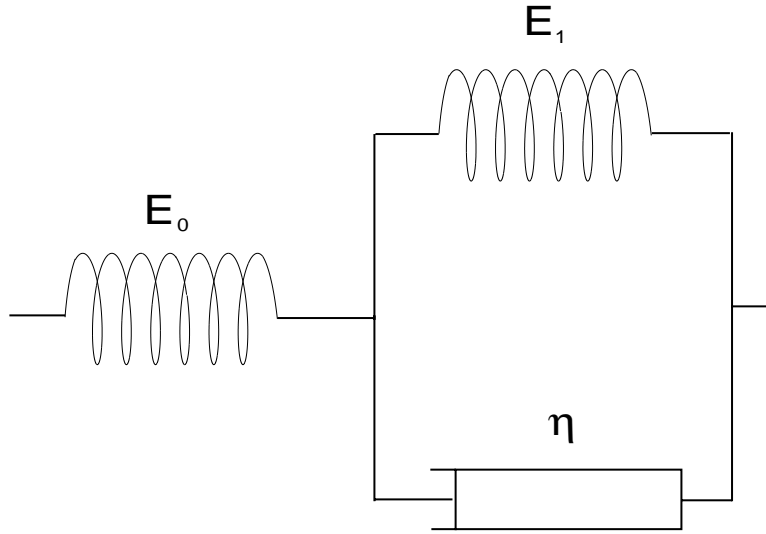


Figure 6.26: Schematic of the Kelvin Model for linear viscoelasticity.

Assuming that the viscoelastic behavior of foams arises from the viscoelastic nature of liquid films, we can apply the standard Kelvin model [170] (schematic shown in Figure 6.26), where a spring (elastic modulus  $E_0$ ) is connected in series with a dash-pot (viscosity  $\eta$ ) and another spring (elastic modulus  $E_1$ ) connected in parallel. For strain  $\epsilon$ ,

$$\epsilon = \epsilon^e + \epsilon^i = \frac{\sigma_0}{E_0} + \frac{1}{\eta} \int_{-\infty}^t e^{-(t-t')/\tau} \sigma(t') dt', \quad (6.8)$$

where  $\epsilon^e$  and  $\epsilon^i$  correspond to elastic and inelastic strain, respectively;  $\tau \equiv \eta/E_1$ .

For constant stress,  $\sigma(t) = 0, t \leq 0; \sigma(t) = \sigma_0, t > 0$ ,

$$\epsilon = \frac{\sigma_0}{E_0} + \frac{\sigma_0}{E_1} [1 - \exp(-t/\tau)]. \quad (6.9)$$

For a periodic stress  $\sigma(t) = 0, t \leq 0; \sigma(t) = \sigma_0 \sin(\omega t), t > 0$ , the strain would be,

$$\epsilon = \frac{\sigma_0}{E_0} + \frac{\sigma \tau}{\eta(1 + \omega^2 \tau^2)} [\omega \tau e^{-t/\tau} + \sin(\omega t) - \omega t \cos(\omega t)]. \quad (6.10)$$

Fitting this expression, Equation 6.10, to the stress-strain curve obtained in the viscoelastic regime, determines the effective viscosity of the foam for a given set of control parameters of the model (*i.e.* coupling strengths and shear rate). For simulations with parameter values  $\mathcal{J}_{ij} = 3, \Gamma = 1$  and three shear amplitudes  $\gamma_0 = 4.0, 5.0$  and  $5.5$ , we found  $E_0 = 4.01 \pm 0.25$ ,  $E_1 = 0.0027 \pm 0.0002$  and  $\eta = 1.80 \pm 0.03$ .

Note that the Kelvin model is only the zeroth order model for viscoelasticity. Due to the complexity of foam, it is not surprising that the response may have multiple time scales, requiring a generalized Kelvin model (schematic shown in Figure 6.27). A detailed study is needed to determine the dependence of viscosity  $\eta$  on model parameters by systematically varying  $\mathcal{J}_{ij}$  and shear rate.

Another way to estimate the effective foam viscosity is by analogy with viscous fluid. The traditional method of measuring fluid viscosity is to drop a heavy, hard sphere through the liquid and measure its terminal velocity. The hydrodynamic force derived from Stokes' law gives:

$$\frac{4}{3}\pi a^3 \Delta\rho g = 6\pi\eta U a, \quad (6.11)$$

where  $a$  is the radius of the sphere and  $\Delta\rho$  is the density difference between the sphere and the fluid,  $U$  is the terminal velocity and  $\eta$  is the viscosity of the fluid. Similarly, in the simulations, we can drop a “heavy bubble” through the foam by applying gravity to a single bubble only. The effective viscosity, in this analogy, is proportional to the ratio between gravity and terminal velocity. Figure 6.28 shows the terminal velocity as a function of the density of the “heavy bubble”.

We use an ordered hexagonal foam and drop a “heavy bubble” of the background bubble size through the pattern. We choose two directions for the gravitational field,  $\hat{x}$  and  $\hat{y}$ . Since the “heavy bubble” in the  $\hat{x}$ -gravity field meets more boundaries than in the  $\hat{y}$ -gravity field,  $v_x$  is smaller than  $v_y$ . But the slopes are the same for both cases, corresponding to the same viscosity of the foam.

This effective viscosity includes contributions from both films and topological rearrangements. This analysis may help to separate the effects of topological rearrangements and clarify how individual T1s contribute to the mechanical response [188].

## 6.7 Conclusions

Three different types of hysteresis occur in two-dimensional dry foams under periodic shear stress in the Potts model simulations. As the applied shear increases, foams change from elastic to viscoelastic to fluid-like. Glazier’s laboratory is currently testing this transition in an experiment similar to [180] by applying periodic boundary shear to a foam, measuring the total boundary length directly (instead of using DWS) to provide the stress, which, plotted against the applied strain, can be compared with the prediction of three distinct behaviors.

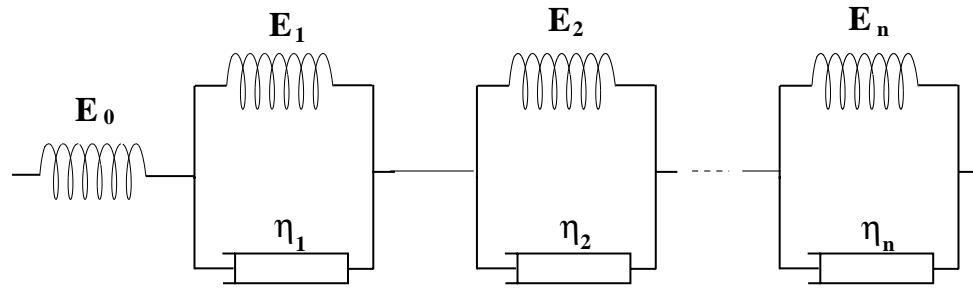


Figure 6.27: Schematic of the generalized Kelvin model.

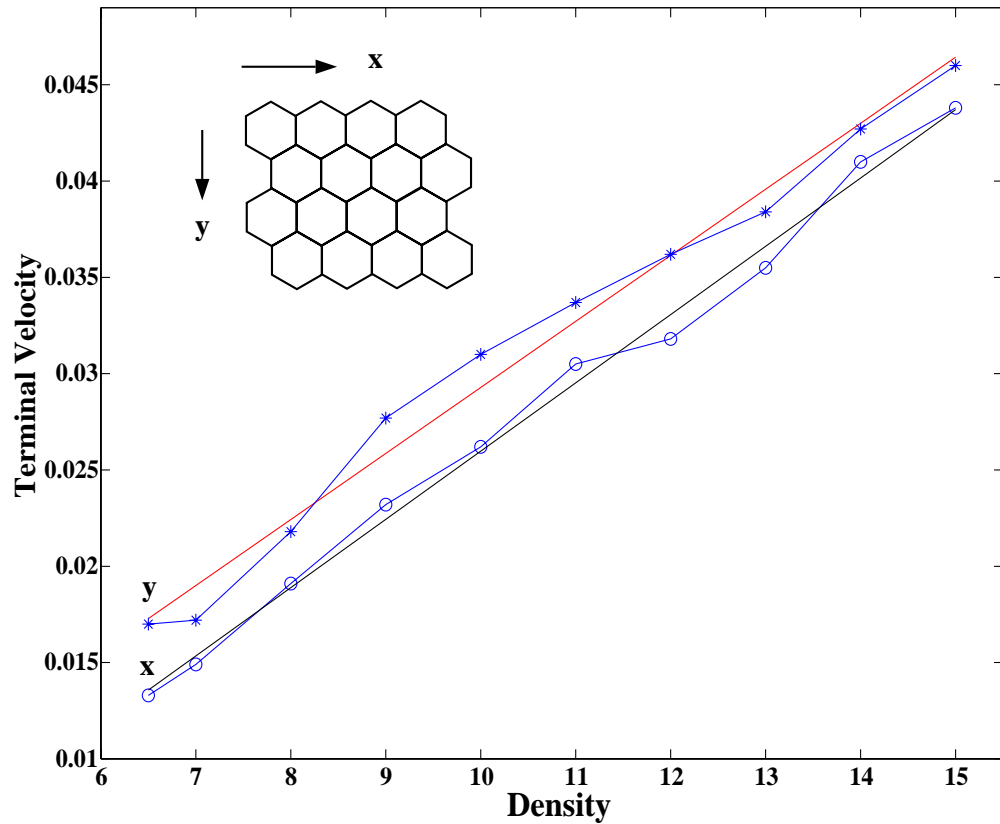


Figure 6.28: Terminal velocity as a function of density in simulations of dropping a “heavy bubble” through an ordered foam (lattice size  $256 \times 256$ ). Simulation parameters are  $T = 0$ ,  $\mathcal{J}_{ij} = 3$ , and  $\Gamma = 1$ . The stars (\*) and the circles (o) correspond to two different directions of the gravitational field with respect to the orientation of the hexagonal pattern. Straight lines are linear fits.

The comparison between the mechanical responses of ordered and disordered foams sheds some light on the relation between structure and mechanical properties. An ordered foam has a finite yield strain. As disorder increases, the yield strain decreases. For a random foam with a broad topology and area distribution, linear elasticity and viscoelasticity do not occur. Any finite stress can lead to topological rearrangements of small bubbles and thus to plastic yielding of the foam. More detailed simulations and experiments are needed to determine the dependence of the yield strain on the area and topological distributions of the foam, and shear rates.

High shear rates effectively introduce higher disorder into the foam, as seen in ordered foams driven at high shear rates. Local topological rearrangements (the appearance of non-hexagonal bubbles) occur throughout the foam, resulting in more homogeneous flow behavior, as in disordered foams. While previous studies claimed that  $\bar{N}$ , the average number of T1 events per bubble per unit shear, is independent of the foam structure and the applied strain rate, the simulation data show that  $\bar{N}$  is sensitive to the area distribution of the sample and the shear rate. Only for a small range of shear rates do samples having similar distributions show similar values of  $\bar{N}$ , which may be the range of the previous studies [167, 178]. Our results emphasize the importance of both structural disorder and metastability to the behavior of soft cellular materials.

In disordered foams, the number of T1 events is not directly proportional to the elastic energy release, because a T1 event is non-local and every T1 event releases a different amount of energy. Therefore, we must consider T1 events and energy release separately.

Avalanche-like topological rearrangements play a key role in foam rheology. In the Potts model simulations, T1 events do not have long-range temporal correla-

tions for ordered structures or slow shear rates, consistent with experimental observations. As the shear rate or structural disorder increases, the topological events become more correlated. Over a range of disorders, the power spectra are  $1/f$ . As Hwa and Kardar pointed out,  $1/f$  noise may arise from a random superposition of independent avalanches [187]. These  $1/f$  spectra suggest that avalanches of different sizes, although they overlap, are independent of each other. Both greater structural disorder and higher shear rate introduce a flat tail at the high frequency end, a signature of Gaussian noise, but do not change the exponent in the power law region.

However, unlike the sandpile model, a similar trend to  $1/f$  is found in the power spectra of the total energy, rather than in the energy dissipation. The difference between the T1 avalanches and the sand avalanches is that each sand grain carries the same energy while each T1 event has different energy. A better analogy is a “disordered sandpile” model, where the sand grains have different sizes or densities.

Avalanches of T1 events decrease the stored elastic energy, leading to foam flow. How do single T1 events contribute to the global response? Magnetic fluid foam experiments offer the unique opportunity to locally drive a vertex and force a single T1 event (or a T1 avalanche) by a well-controlled local magnetic field. We are currently investigating the effects of single T1 events using magnetic fluid foam experiments and the corresponding Potts model simulations [188]. This study may help to understand the connection between microscopic topological rearrangements and macroscopic mechanical response.

## CHAPTER 7

### CELL SORTING

#### 7.1 Introduction

Cell migration is a critical process for life. Cells move extensively as an embryo develops. In the adult, cells migrate to the site of an infection or wound. In cancer metastasis, invading cells move through a tissue. When cells of two or more types are randomly intermingled and aggregated, they are able to migrate over long distances compared to their diameter to re-establish homogeneous cell masses and sometimes to re-construct functional tissues (for a review, see [192]). Many embryos and living organisms, even a few adult animals such as *Hydra*, can regenerate from an aggregate of randomly mixed cells of different types [193, 194].

While a cell's molecular constitution, such as its cytoskeletal structure and the type and density of its surface adhesion molecules, are genetically controlled, its physical properties such as its mass, volume and surface tension restrict its possible motion.

Cell migration mechanisms falls in two categories: short range interactions where cells interact through direct contact, and long range interactions where cells interact through the external environment. The former includes differential adhesion, the direct cell-cell physical and chemical interactions depending on the cell types, and mechanical transduction. The latter includes (1) indirect physical and chemical interaction, *e.g.*, production of extracellular “wetting” fluid or extracellular matrix (ECM); and (2) chemotaxis (motion in response to gradients of chemical agents

which are emitted by the cells).

We now seek to understand how cells accomplish migration and sorting by studying these interactions in a simple organism, slime mold amoebae *Dictyostelium discoideum*. We focus our discussions on explaining cell sorting and patterning in the mound stage of *Dictyostelium*, based on direct (differential adhesion) and indirect (chemotactic) cell interactions. Section 7.2 introduces *Dictyostelium discoideum*. Section 7.3 describes differential adhesion. We compare our simulation results with experiments done with chicken embryo cells to validate the model. Section 7.4 introduces chemotaxis and evidence for its role in the development of *Dictyostelium*. Section 7.5 includes the experimental evidence on which the model is based, and the description of the extended large- $Q$  Potts model. Section 7.6 presents the simulation results on the effects of these two mechanisms on pattern formation in the *Dictyostelium* mound. Finally, we compare the Potts model to others, and point out some possible directions for future development of the model towards more realistic biological simulations.

## 7.2 *Dictyostelium*

One of the most widely used organisms to study relatively simple morphogenesis is the cellular slime mold *Dictyostelium discoideum*. *Dictyostelium* exhibits many general developmental processes including chemotaxis, complex behavior through self-organization, cell sorting and pattern formation.

Unicellular amoebae *Dictyostelium* inhabit soil and eat bacteria. When bacterial food becomes scarce, some cells, so called pace-maker cells, spontaneously emit diffusing chemical signals of 3'5' cyclic adenosine monophosphate (cAMP), thereby initiating an excitation wave which propagates outward as a concentric ring or a spiral wave, as the surrounding cells relay the signal [195]. Individual cells aggregate under the guidance of the cAMP waves by moving towards higher concentrations

of cAMP. The amoebae form streams when they touch each other and then form a multicellular mound, a hemispherical structure consisting of about  $10^5 - 10^6$  cells surrounded by a layer of slimy sheath which is chemically similar to extracellular matrix in the mound [196]. The cells in the mound then differentiate into two major types, pre-stalk (pst) cells (about 20% of the cells) and pre-spore (psp) cells (about 80%) [197, 198]. Subsequently, the initially randomly distributed pst cells move to the top of the mound and form a protruding tip. This tip controls all morphogenetic movements during later multicellular development[199]. The elongated mound bends over and migrates as a multicellular slug. The anterior consists of pst cells only and the posterior psp only. When the slug stops, the tip (the anterior part of slug) sits on a somewhat flattened mound consisting of psp cells (called a “Mexican hat” from its appearance). The tip retracts and the stalk (formerly pst) cells elongate and vacuolate, pushing down through the mass of spore (formerly psp) cells [200]. This motion hoists the mass of spore cells up along the long stalk. The mature fruiting body consists of spore cells sitting atop a slender tapering stalk. The whole life cycle, shown in Figure 7.1, normally takes about 24 hours.

We focus on the mound stage, when the cells have formed a compact aggregate with a layer of non-cellular sheath surrounding it so that no more cells can join the mound. Once the cells have differentiated into pst and psp cells in the correct proportion, how do the cells move and sort in the mound to form a protruding finger on the top of the mound which contains only pre-stalk cells?

Two possible mechanisms which could govern relative cell motion are differential adhesion based on the different surface adhesivities between psp and pst cells, and chemotactic motion of cells along a chemical gradient from persistence of the diffusible signals which play a crucial role during cell aggregation.

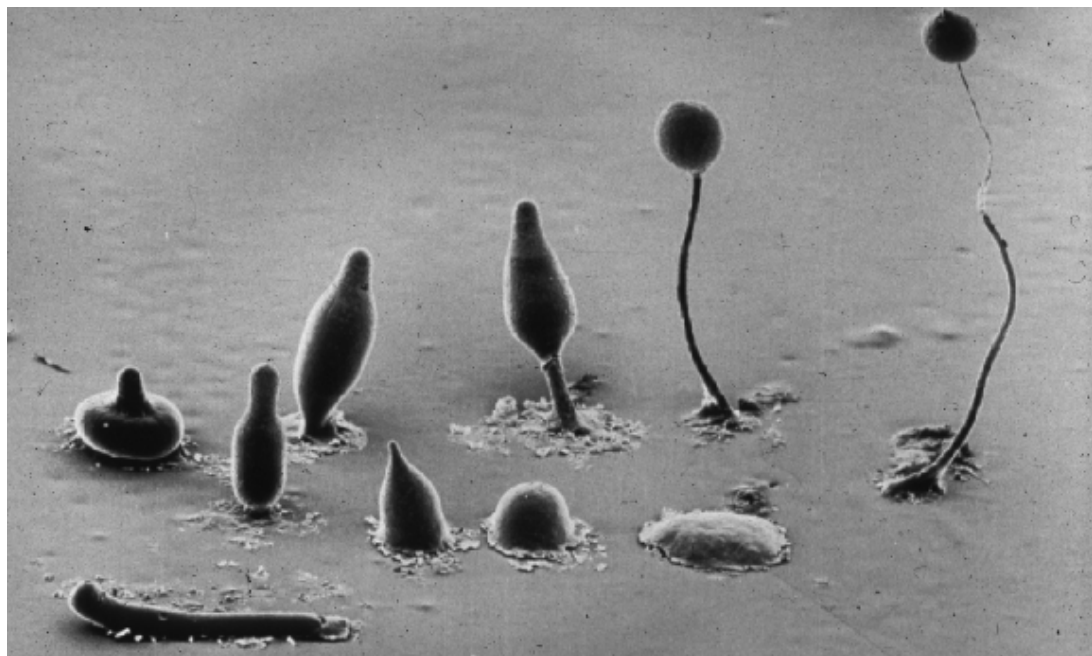


Figure 7.1: Life cycle of *Dictyostelium*. The individual cells are about  $10\mu m$  in diameter. The fruiting body is about  $3mm$  high. Aggregation starts  $6h$  after starvation; a tight mound forms at about  $10h$ ; tip formation finishes by  $12h$ ; culmination takes 6 hours from  $18h$  to  $24h$  [Courtesy of W. Loomis].

### 7.3 Differential Adhesion

Steinberg [201, 202, 203, 204] suggested that the interaction between two cells involved an adhesion surface energy which depended on the cell types through cell adhesion molecules on the cell membranes. His differential adhesion hypothesis (DAH) states that cells ergodically explore various configurations to arrive at the lowest-energy configuration. Additional energy comes from the surface tension between cells and the extracellular medium. This energetics biases the otherwise random movement of cells in aggregates, causing them to rearrange into patterns with minimal surface energy.

Experiments in *hydra* cell aggregates showed evidence that differential adhesion can dominate certain types of sorting [205]. Surface adhesivity is type-selective. During the regeneration of *hydra* aggregates, ectodermal cells surround endodermal cells which form a single cluster in the middle. The initial surface sorting is rapid and slows in time, apparently logarithmically [205], suggesting that sorting is an activated process. Glazier and Graner, using an extended large- $Q$  Potts model with differential adhesivity, showed that differential adhesion with fluctuations can explain a wide variety of experimental cell configurations [206]. Studies using chicken embryo cells showed that the cells indeed performed a biased random walk, caused by cytoskeletally driven membrane fluctuations [207, 208]. Both the chicken embryo cell experiments and simulations confirmed that sorting under DAH is a diffusion through a rugged free energy landscape.

#### 7.3.1 Experiments

Cell sorting is the classic behavior of mixed heterotypic aggregates. Figure 7.2 shows an experimental observation of cell sorting of neural (light) and pigmented (dark) retinal cells from chicken embryos [207]. This result resembles that reported

in [192]. Initially, the dark cells are randomly dispersed throughout the aggregate with some in contact with the medium [Figure 7.2(a), after 5h]. At a later time [Figure 7.2(b), after 10h], dark cells have formed large clusters and are separated from the medium by a monolayer of light cells. Later still, [Figure 7.2(c), after 72h] the dark cells form a single rounded mass inside each aggregate which may or may not be well centered.

A similar process occurs in a mixed aggregate of *Dictyostelium* cells. When cells from the anterior (pst) and posterior (psp) parts of a slug are dissociated and mixed in an aggregate in the right proportions, the two types of cells sort. Figure 7.3 reproduces the observations of Takeuchi *et al.* in [209]. Initially, Figure 7.3(a), at 2h, the dark (psp) and light (pst) cells are randomly mixed. Two hours later, Figure 7.3(b), at 4h, light cells form clusters in the aggregate. Then, a layer of non-cellular slime sheath forms around the aggregate which complicates the sorting. Instead of light cells forming a single cluster inside the aggregate, the sheath seems to attract the light cells to the surface, shown in Figure 7.3(c), at 6h. Sorting finishes when the light cells form a layer surrounding the aggregate, having maximum contact area with the slime sheath, and the dark cells form a single cluster in the middle of the aggregate, not necessarily in the center, as shown in Figure 7.3(d), at 8h.

### 7.3.2 Model

Simulations of cell sorting under differential adhesion started with cellular automaton models where each lattice site represents one cell which interacts with its neighbors [210]. Later improvements included the long-range effects of surface tension [211], the topology of the patterns [212] and cell geometries and molecular dynamics [213, 214].

Graner and Glazier [215, 206] extended the standard large- $Q$  Potts model to

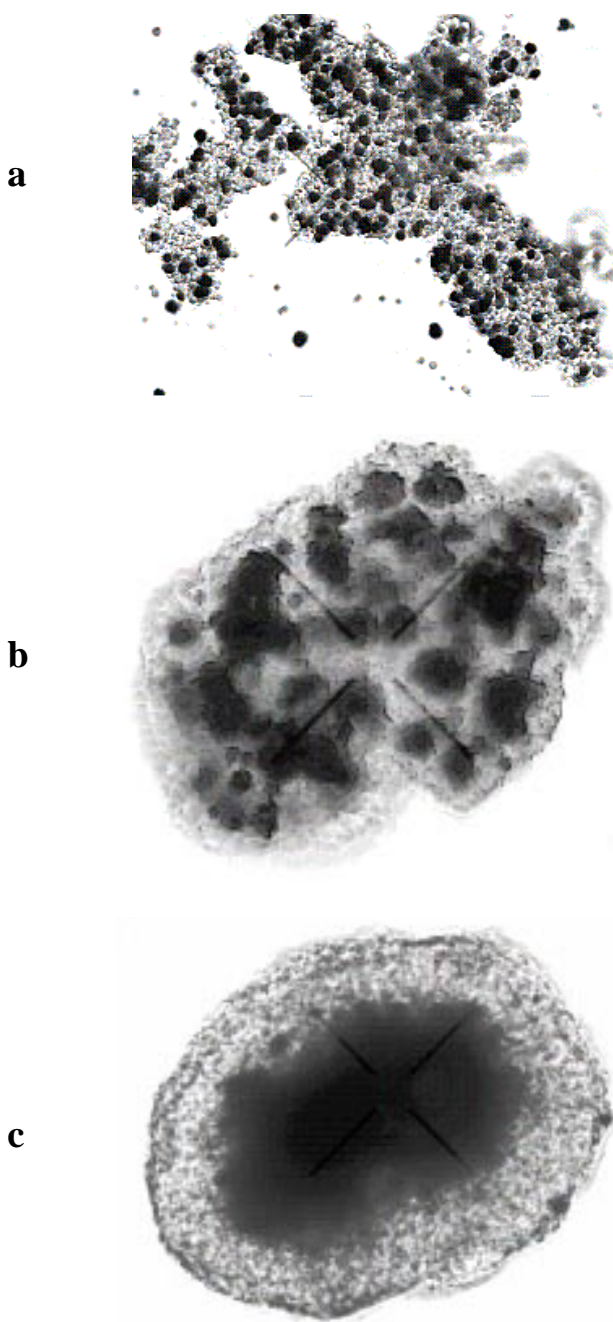


Figure 7.2: Sorting of an aggregate of neural retinal (light) and pigmented retinal cells (dark) obtained from 10-day old chick embryos. (a) Aggregate 5h after mixing of dissociated cells. (b) After 10h, the neural retinal cells form an external layer. (c) After 72h, the neural retinal cells surround an internal dark core of pigmented retinal cells. [After Mombach *et al.* [207]].

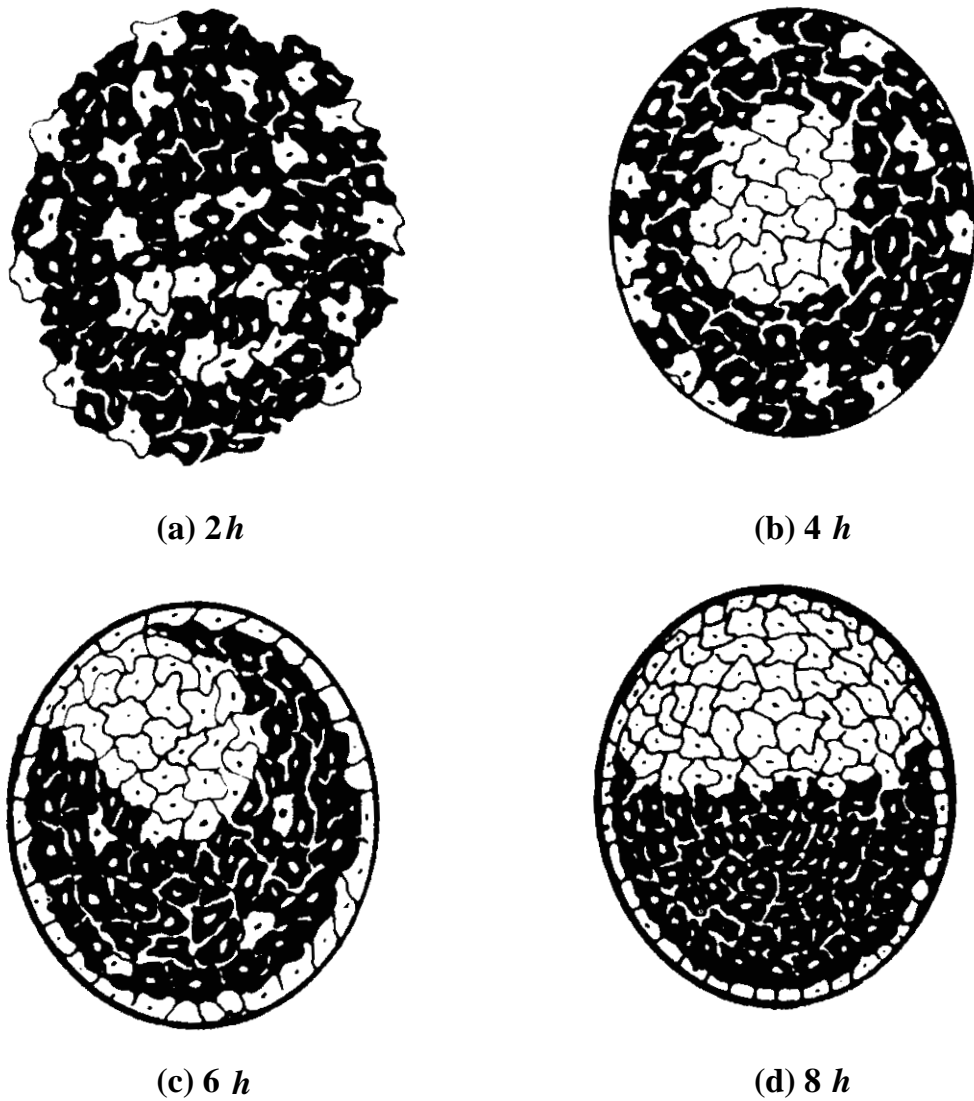


Figure 7.3: Reconstitution of *Dictyostelium* pre-stalk and pre-spore cell aggregates. Pre-stalk and pre-spore cells were dissociated from the slug stage. After indicated times, pre-stalk cells first formed a cluster inside pre-spore cells (dark), then moved to the surface of the aggregate. Except for the aggregate at 2h, the aggregates were encased by slime sheath. [After Takeuchi *et al.* [209]. Copyright ©1988 John Wiley & Sons Inc., used by permission of Wiley-Liss, a division of John Wiley & Sons, Inc.].

include area constraints and type-dependent boundary energies to study cell sorting under DAH. The finite cell size can be modeled with a volume-dependent (or area-dependent, in two-dimensional models) energy term [206]:

$$\mathcal{H}_{\text{general}} = \int_{\text{cellsurface}} \mathcal{J}(\tau_{\text{inside}}, \tau_{\text{outside}}) ds + \sum_{\text{cells } i} f_i(a_i), \quad (7.1)$$

where  $\mathcal{J}(\tau_{\text{inside}}, \tau_{\text{outside}})$  is the energy of a unit of cell membrane as a function of the cell types  $\tau_{\text{inside}}$  and  $\tau_{\text{outside}}$ .  $ds$  is a unit surface area.  $f_i$  encodes all information concerning bulk properties of a cell, *e.g.* membrane elasticity, cytoskeletal properties, *etc..* We choose  $f_i$  as a simple quadratic elastic function (see Equation 3.19), with all cells of a given type having the same volume or area. Additional simplifying assumptions include that the surface of each cell is isotropic, *i.e.*, the energy of a unit of cell membrane depends only on the types of the cells, and that the cell types and surface properties remain the same for all the cells during the simulated experiments. The configuration evolves by the standard finite temperature Monte Carlo dynamics, Equation 3.2.

The milestone work of Glazier and Graner [215, 206] studied two-dimensional cell aggregates: dark and light cell mixtures submerged in a fluid medium. Thus  $\tau$  assumes three values, for  $l$ ,  $d$  and  $M$ , respectively.

The surface tensions can be defined in terms of the boundary energies [214], as given in Equations `refgammadl`, `gammadm` and `gammalm`. These surface tensions are not equivalent to a biological membrane's internal tension, which appears as part of the membrane elasticity,  $\Lambda$ . They represent the difference in energy between heterotypic and homotypic interface per unit area of membrane [206].

$T$  does not correspond to the real experimental temperature. Rather, it indicates the amplitude of cell membrane fluctuations. Typically, in biological tissues, the cytoskeletally driven membrane fluctuations are much larger in amplitude than the

true thermal fluctuations. One simple example is that when a drug (cytochalasin-*B*) inhibits cytoskeletal fluctuations, the cell membranes appear essentially free from fluctuations. Defining  $T$  as the effective fluctuation temperature for cells makes the serious assumption that the cell surface moves as if it were driven by uncorrelated thermal noise. At the time this model was proposed [215], no experimental evidence supported this assumption. The model was based on its physical simplicity and its similarity to magnetic materials. Only recently have studies shown quantitative agreement between the simulation results from the extended Potts model and experimental results from chicken embryo cells [208, 216], supporting the idea that the cell membrane fluctuations are thermal. More detailed quantitative research must verify these assumptions and reveal the true underlying physics.

The model has two critical temperatures,  $T_{c1}$  and  $T_{c2}$ . The energy required to break a straight wall between cells determines  $T_{c1}$ . As illustrated in Figure 7.4, on a square lattice with fourth nearest neighbor interactions, the configuration energy difference before and after the spin flip is  $\Delta\mathcal{H} = 12\mathcal{J}_{12} - 8\mathcal{J}_{12} = 4\mathcal{J}_{12}$ . Therefore,  $T_{c1} \sim 4\mathcal{J}_{12}$ , such that this spin flip has a reasonable probability,  $\exp(-\Delta\mathcal{H}/T_{c1})$ , of occurring.  $\mathcal{J}_{12}$  here can be either homotypic or heterotypic coupling. Below  $T_{c1}$ , cell membranes are too rigid and cells have straight boundaries and cannot crumple enough to result in cell body movement. Each cell assumes shapes with boundaries aligned in the low energy orientation closest to the required minimal surfaces, but the pattern freezes in a metastable configuration. No sorting can occur. The second critical temperature is that at which individual cells dissociate. When a spin which is surrounded by only mismatched spins has a long expected lifetime, it can freely detach from the cell and the cell falls apart. Thus  $T_{c2}$  is  $N\mathcal{J}_{12}$ , with  $N$  the total number of neighbors for the spin. Approaching  $T_{c2}$ , the constraints that minimize the total surface area weaken and cell membranes can stretch and crumple until

individual spins can detach from the bulk cell body and cells melt.

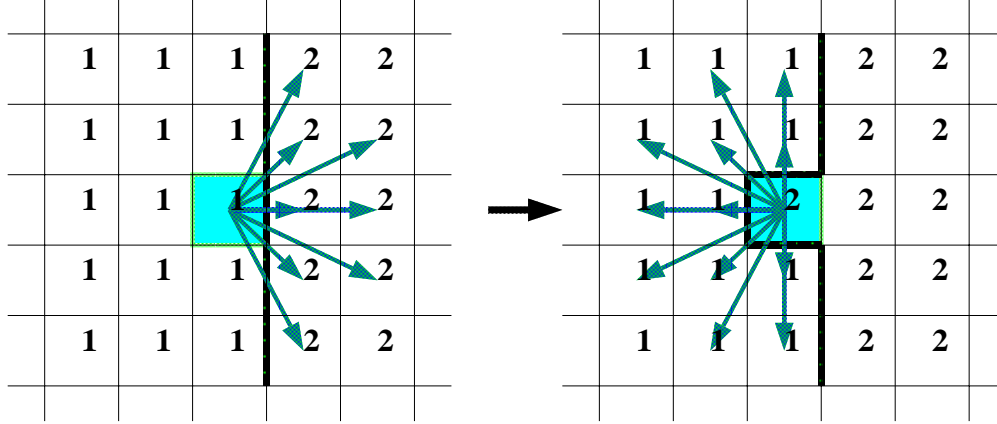


Figure 7.4: Schematic of spin change on a two-dimensional square lattice with fourth nearest neighbor interaction.

These critical temperatures differ for different cell types which have different surface energies. In practice, the simulations run at a temperature high enough that even the most rigid cell membranes (smallest coupling strength  $\mathcal{J}_{ij}$ ) can fluctuate, yet low enough that the weakest cell membranes (largest coupling strength  $\mathcal{J}_{ij}$ ) will not break apart. In other words,  $\max(T_{c1}) < T < \min(T_{c2})$ .

In principle, spinodal decomposition defines a third critical temperature [206] at which dark and light cells mix. The spinodal decomposition limit occurs when the entropy and energy are of the same order. Higher temperatures weaken area/volume constraints and the patterns coarsen. These limits, however, are above  $T_{c2}$ .

This simple model, which includes only differential surface energies and an area constraint, with isotropic cells and without detailed membrane or cytoskeletal properties, reproduces various observed biological phenomena, including complete and partial sorting, checker-board, position reversal, and dispersal [206]. Figure 7.5 shows an example of cell sorting with dark cells more adhesive than light cells.

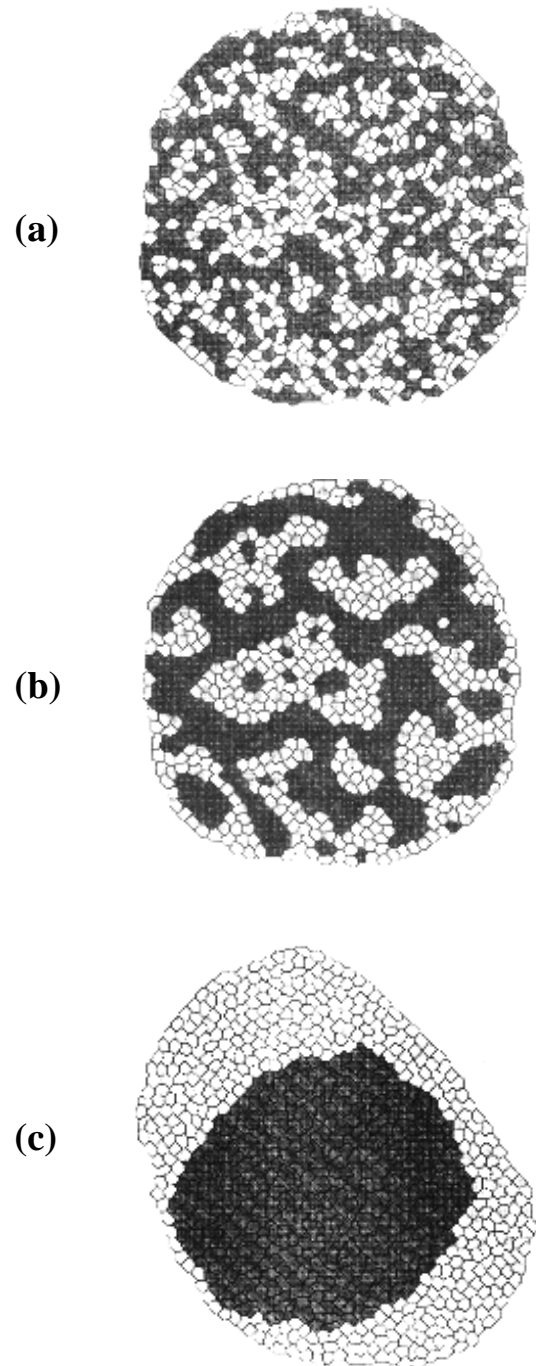


Figure 7.5: Potts model simulation of cell sorting with differential adhesion. Dark cells adhere to each other more strongly than light cells do: (a) 0 MCS, (b) 100 MCS, (c) 13500 MCS. [From Glazier and Graner [206]].

## 7.4 Chemotaxis

Chemotaxis is the motile response of cells or organisms to a gradient of a diffusible substance. It differs from chemokinesis in that the gradient alters probability of motion in one direction only, rather than changing the rate or frequency of random motion, as in bacterial motion.

During aggregation of *Dictyostelium*, some cells, so called pace-maker cells, spontaneously synthesize and secrete pulses of cAMP, creating a gradient of cAMP around themselves. A neighboring cell responds to such a gradient with several actions. It moves some micrometers up the gradient towards the source of cAMP (the exact pathway between the membrane cAMP receptors and cytoskeletal motion is not yet clear) [218, 219], and it synthesizes and releases its own pulse of cAMP, attracting neighboring cells. It then becomes refractory for a period of several minutes during which it cannot move or respond to cAMP signals. Under most natural conditions each cell amplifies the cAMP signal, which means that the cell synthesizes and releases more cAMP than was present in the original stimulus. This relaying results in cell-to-cell propagation of the cAMP signal [195]. Proper functioning of this response requires a number of macromolecules: surface receptors, adenylate cyclase to synthesize 3',5'-cAMP from ATP; and both secreted and surface phosphodiesterase to degrade cAMP to chemotactically inactive 5'-cAMP. The concentration of cAMP ranges from  $10^{-8}$  M to  $10^{-6}$  M at the peaks of waves [217]. The phosphodiesterase is essential to prevent the extracellular cAMP from building up to a level that swamps out any gradients.

Unlike differential adhesion, chemotactic cell motion is highly organized over a length scale significantly larger than the size of a single cell.

#### 7.4.1 Experiments

Chemotaxis has been studied extensively for aggregating *Dictyostelium* amoebae. Early experiments measured details of the spatial and temporal variations of cAMP concentrations among aggregating *Dictyostelium* cells, and the velocities and patterns of cell motion [217]. While cAMP is generally believed to be the chemoattractant that guides cell aggregation, attempts to prove its importance have failed. One problem is the difficulty of directly imaging chemical fields. The typical method is to infer concentration from other more easily observed phenomena. Dark-field imaging visualizes chemical waves indirectly from the changes in light scattering of cells during chemotactic cell movement. Figure 7.6 shows a dark-field image of aggregating *Dictyostelium* cells on an agar surface. When suddenly exposed to a cAMP gradient, cells first round up, then elongate towards the direction of higher cAMP concentration, causing a different light scattering index from unexcited cells. The white bands in the dark field image are the elongated cells, corresponding to the wave front of cAMP signals. This technique works well during aggregation, but poorly in the mound in which the cells pack tightly. Only recently has visualization within the mound using dark-field images become possible, showing that the waves propagate as concentric rings, spirals or multi-armed spirals depending on the variety of *Dictyostelium* and experimental conditions [220].

Instead of visualizing cell motion, one attempt to study the role of cAMP in cell sorting in the mound involved controlling the concentration of cAMP via the over-expression of secreted phosphodiesterase, lowering the cAMP concentration. No tip formed with the over-expression, implying that the cAMP level was too low to properly guide cells [221]; furthermore, exogenous cAMP could attract pre-stalk cells to the mound base, also suggesting that chemotaxis to cAMP determines tip formation. Supporting evidence comes from a mutant strain of *Dictyostelium* which



Figure 7.6: A dark field image of aggregating fields of *Dictyostelium* on an agar substrate. White bands are excited cells, corresponding to the wavefront of cAMP waves. Note the signaling spirals and the onset of streams at the aggregation edges. [Courtesy of H. Levine].

deletes a pre-stalk specific, low-affinity cAMP receptor (CAR2) and cannot form tips [222]. The idea that the cAMP wave detection by the cells switches from the usual high-affinity receptor (CAR1) to one with lower affinity is consistent with the phenomenology seen via the darkfield technique [223], with the crucial assumption that these waves are related to cAMP. However, chemotaxis to other diffusible chemicals remains possible.

#### 7.4.2 Models

Models of *Dictyostelium* chemotaxis have almost exclusively dealt with aggregation. These models form two major categories: those that treat the cells as discrete units and those which use a continuum description for the cell density. These models have given some insight into aggregation but none addressed the whole spectrum of problems.

The models developed by Parnas and Segel [224], MacKay [225] and Vasieva *et al.* [226] fall into the first category. The first two of these are similar in that they treat cells as black boxes which, when stimulated, release a fixed amount of cAMP. They incorporate no description of signal transduction, cAMP production, or adaptation, only diffusion of cAMP. The model of Parnas and Segel only deals with one space dimension and can only address how the cells decide when to move and, in a very simplistic manner, the direction of cell movement. MacKay's model is two-dimensional and can reproduce the observed streams, competition between two pacemakers and spiral waves. These models are a first step towards theoretical study of aggregation, but their rules are not based on a mechanistic description of signal detection, transduction, cAMP production and secretion. More recent modeling by Vasieva *et al.* omits the diffusion of cAMP. Instead, it used a cellular automaton with rules for neighbor activation to reproduce streams and self-sustaining sources of excitation. However, this purely formal model has little relevance to

*Dictyostelium* aggregation.

The models developed by Levine and Reynolds [227], Vasiev *et al.* [228] and Höfer *et al.* [229] fall into the second category. The Levine and Höfer models modified the Martiel and Goldbeter model [230] for cAMP production and signaling, whereas Vasiev *et al.* used a modified FitzHugh-Nagumo model for these processes. Several objections, however, can be raised for their local dynamics [231], especially when *ad hoc* assumptions are needed to incorporate cell's adaptation to chemical concentration for chemotactic movement. The attraction of continuum models is the ease of obtaining analytical insights with simplified local dynamics. The primary results of these models relate to the apparent instabilities which cause streams.

We have developed the extended large- $Q$  Potts model as a hybrid discrete-continuum model which treats the cells as individual units and describes the extra-cellular cAMP by a continuum chemodynamics equation. Such a model can describe signal transduction and adaptation and explore movement rules based on the intracellular dynamics. In this study, however, we focused on cell sorting during mound formation, and did not consider the detailed signal transduction dynamics [232].

## 7.5 *Dictyostelium* Mound Formation

### 7.5.1 Experiments

While intercellular adhesion is essential for *Dictyostelium* in the transition from unicellular amoebae to multicellular stage [233, 234], whether it is directly involved in the cell sorting in the mound is as yet unknown. Conceivably, intercellular adhesion only passively keeps cells together while diffusible signals morphoregulate. Alternatively, adhesive energy differences may drive cell motion while diffusible chemical gradients may be absent or may merely enhance the process. Or does proper tip formation require the collaboration of the two mechanisms?

The molecular basis of intercellular adhesion just before and during aggregation

has been intensively studied. The csA glycoprotein in particular, which mediates adhesion during aggregation, is one of the best defined cell adhesion molecules [233]. However, the cell surface components mediating cell adhesion during the mound and slug stages and the potential role of cell adhesion in tip formation and morphogenesis have not received as much attention, because of the inherently more complex nature of the multicellular stages. In addition, the prevailing notion is that pattern formation and morphogenetic movements in *Dictyostelium* depend mostly on diffusible chemical signals [221, 220].

However, some evidence suggests that pre-stalk and pre-spore cells types have different homotypic adhesivity. Tipped aggregates are more difficult to dissociate with EDTA than aggregation stage cells. When slugs form, pre-spore cells resist EDTA dissociation much more than pre-stalk cells [235], and in an aggregate with mixed pre-stalk and pre-spore cells, pre-stalk cells move to the periphery of the aggregate [236]. These results strongly suggest that pre-spore cells are more cohesive than pre-stalk cells. However, other lines of evidence suggest that pre-stalk cells are more cohesive than pre-spore cells [237, 209, 238]. The work of Takeuchi [209] (Figure 7.3) even suggested that the slime sheath may help pre-stalk cells to come to the surface of the aggregate.

*Dictyostelium* cells in the mound can respond chemotactically to chemical gradients and therefore such gradients may help control their relative motion. Dark-field imaging showed waves patterns in the mound [220] but failed to associate the images to three-dimensional distributions of putative chemical signals. Cell movement analysis, by tracking the positions and shapes of single cells, has shown that cell movement in mounds of the wild-type strain AX-3 is rotational, and measurements of single cell velocities and changes in cell shape and trajectories show that cells move faster in the mound than during aggregation [239]. The McNally group, using

three-dimensional optical sectioning microscopy, examined the distribution of movement in mounds of AX-2 [240]; no large scale rotation appeared, and cells moved in a variety of manners. Pre-stalk cells move about 50% faster than pre-spore cells but their paths are similar [241]. In the KAX-3 mutant, after some lag time, all cells move rotationally and pre-stalk cells move to the surface of the mound, but no tip forms [242].

As already mentioned, much current thinking assumes that the darkfield waves in the mound correspond to cAMP (as they do during aggregation) and cAMP chemotaxis dominates the measured motion. But, a recent report shows that *Dictyostelium* development can be independent of cAMP as long as the catalytic subunit of cAMP-dependent protein kinase is present [243]. In the acaA(PKA-C) mutant, *Dictyostelium* development seems “near-normal” without detectable accumulation of cAMP, suggesting that signals other than extracellular cAMP can coordinate morphogenesis. Since our simulation applies equally to any chemo-attractant, these findings do not affect our results as long as chemotaxis to some chemical exists. We did not investigate other possibilities, such as a chemo-repellent or a more complicated interaction with the slime sheath or the extracellular matrix.

### 7.5.2 A Model of *Dictyostelium*

Our model simplifies the biology, by assuming that:

- 1) All cells have differentiated to either pre-stalk cells (20% by volume) or pre-spore cells (80%). Cells have fixed surface properties that do not change during sorting and their volumes are constant.
- 2) The surface properties of cells are isotropic, neglecting cell polarity or membrane curvature dependence. Hence, cells have uniform energy per unit contact area.
- 3) As we do not explicitly consider extracellular matrix in the mound, cells

interact with their neighbors through direct contact. In principle, the different cell types might have different interaction energies with the outer boundary of the mound, although no data is available.

4) A layer of sheath, which may have different contact energies with different cell types, has formed around the mound before we start our simulations.

As described in Chapter 2, each lattice site contains a number  $\sigma$  corresponding to the unique index of a cell, which has a type  $\tau$  and a volume  $v$ . Adhesive energy resides on the membrane surfaces only, while cells have no internal adhesion energy. The sheath around the mound and the substrate supporting the mound are also represented as generalized cells, with particular properties and surface tensions. To keep the aggregate from falling apart, the cells adhere more to each other than to substrate or to sheath. As the cells do not grow or shrink during sorting, the target volume,  $V_\sigma$ , is constant and equal for both pre-spore and pre-stalk cells.

Savill and Hogeweg have used a similar model to describe the morphological changes in *Dictyostelium* from aggregation to migrating slug [244]. Figure 7.7 shows the time sequence of their simulated *Dictyostelium*. Pre-stalk cells are light and pre-spore cells are dark. Cells aggregate into a mound which then falls on the substrate and migrates like a slug. Notice that the mound and slug are random mixtures of two cell types. They did not study cell sorting and tip formation in the mound.

We can treat chemical concentration as an effective potential energy, although the chemo-attractant does not directly exert a force on the cell. Cells rectify traveling wave signals to move only opposite to wave propagation [245]; in the model the chemotactic response vanishes when the cells are in their (chemical) refractory state.

The total effective energy of the mound is:

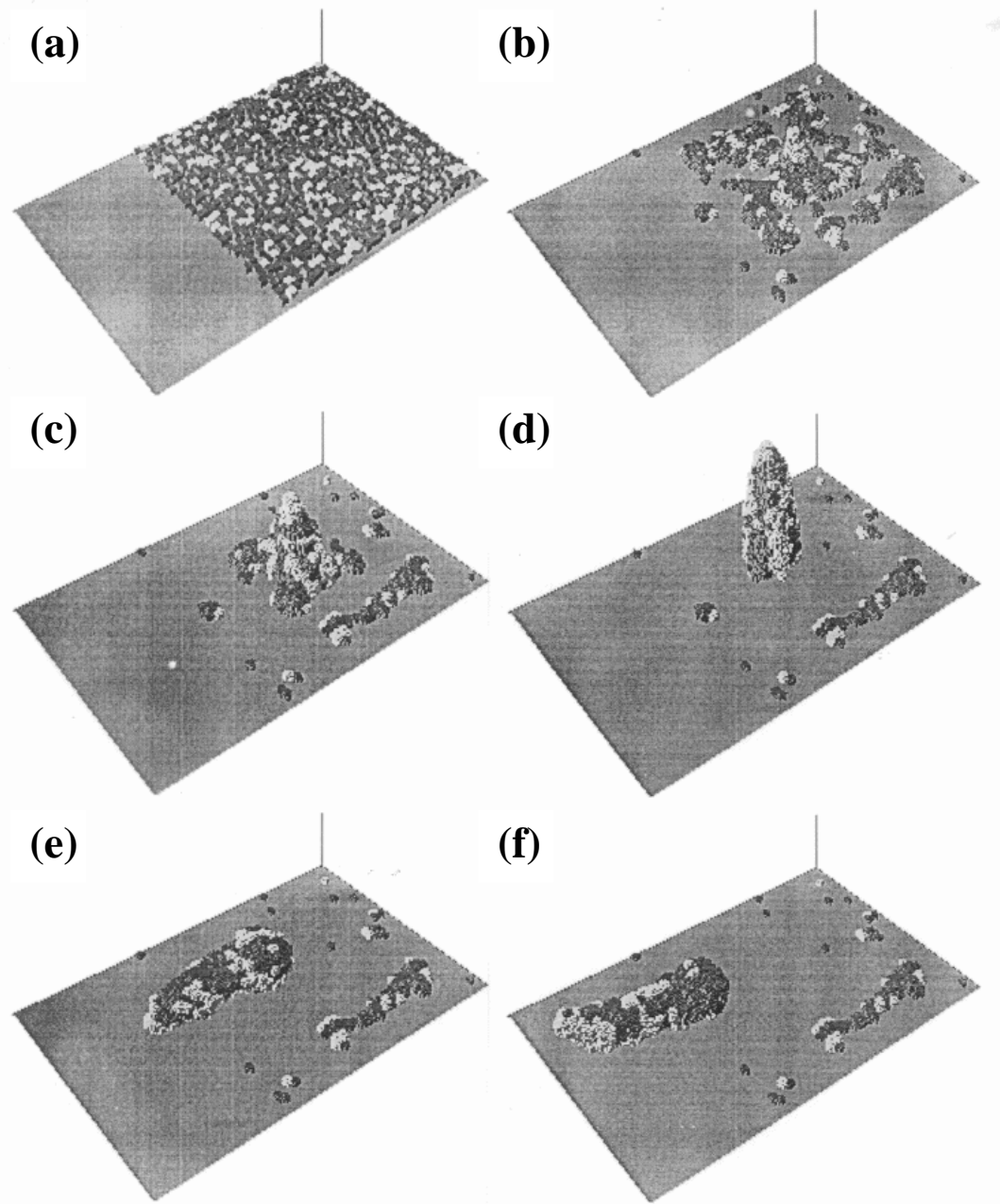


Figure 7.7: Time sequence of the aggregation, mound and slug phases of a simulation of *Dictyostelium*. (a) Initial random mixture of prestalk (light) and prespore (dark) cells on a substrate. (b) Cells start to stream into a mound. (c-d) Mound forms. (e) Mound falls to the ground. (f) Slug migrates. [From Savill *et al.* [244]].

$$\mathcal{H} = \sum_{\vec{i}} \sum_{\vec{j}} \mathcal{J}_{\tau(\sigma_{\vec{i}}), \tau(\sigma_{\vec{j}})} (1 - \delta_{\sigma_{\vec{i}}, \sigma_{\vec{j}}}) + \Lambda \sum_{\sigma} [v_{\sigma} - V_{\sigma}]^2 + \sum_{\vec{i}} \mu C(\vec{i}, t), \quad (7.2)$$

where  $\vec{i}$  is a neighbor of  $\vec{j}$  with the index  $\sigma$  ranging from 1 to  $N$ , the total number of cells in the simulation. Surface tensions in terms of the couplings between different cell types are:

$$\gamma_{\tau, \tau'} = \mathcal{J}_{\tau, \tau'} - \frac{\mathcal{J}_{\tau, \tau} + \mathcal{J}_{\tau', \tau'}}{2}, \quad (7.3)$$

$$\gamma_{\tau, M} = \mathcal{J}_{\tau, M} - \frac{\mathcal{J}_{\tau, \tau}}{2}, \quad (7.4)$$

where  $\gamma_{\tau, \tau'}$  refers to the heterotypic surface tension between any pair of cell types, and  $M$  refers to the medium (sheath or substrate).

The second term in the total energy (Equation 7.2) applies to the pre-stalk and pre-spore cells only, confining cell volumes near a fixed value  $V_{\sigma}$ . The last term is the effective chemical potential energy.  $C(\vec{i}, t)$  is the local concentration of the chemo-attractant, which is a function of time,  $t$ , and position,  $\vec{i}$ . The chemotactic response of cells derives from this term, in which  $\mu$  is the effective chemical potential. The local chemical gradient effectively exerts a force on the part of cell membrane that sees the gradient. If  $\mu > 0$ , a section of the cell membrane protrudes as a pseudopod towards higher chemical concentration and in time the cells move up the chemical gradient. If  $\mu < 0$ , cells move towards lower concentrations. Thus,  $\mu$  corresponds to the cell motility, which converts a chemical gradient into a velocity. Cell motility has been extensively studied in *Dictyostelium*. Fisher *et al.* [251] studied cell motility in a chemotaxis chamber which has stationary chemical gradients and found that the speed of AX-2 cells is  $3\mu\text{m}/\text{min}$  at a cAMP gradient of  $25\text{nM}/\text{mm}$  with a midpoint of  $25\text{nM}/\text{mm}$ . Soll *et al.* [252] developed a three-dimensional dynamic image analyzing system which produces detailed information about cell motility and

morphology based on the three-dimensional paths of the centroid and the three-dimensional contour of the cell. Their data show the cells moving at a velocity of  $12 - 15\mu m/min$  during natural aggregation, when the concentration of cAMP is rising from 10 to  $1000nM$ .

We define the control parameter, the relative strength of chemotaxis and differential adhesion, as:

$$\phi \equiv \mu / \gamma_{psp-pst}, \quad (7.5)$$

where  $\gamma_{psp-pst} = \mathcal{J}_{psp-pst} - (\mathcal{J}_{psp} + \mathcal{J}_{pst})/2$  is the heterotypic surface tension between pre-spore and pre-stalk cells.

The pattern evolves by the normal Potts model dynamics, Equation 3.2. In the results that follow,  $\mathcal{J}_{pst,substrate} = \mathcal{J}_{psp,substrate} = 20$ . Since the substrate does not participate in the spin reassessments, the value of  $\mathcal{J}_{cell,substrate}$  only sets the surface tensions between cells and substrate for correct contact angles. The behaviors of the cells are not sensitive to the exact value of  $\Lambda$  ranging from about 3 to 30 [206]. We use  $\Lambda = 10$  to keep the cells compact and close to the target volume. Without chemical dynamics, the amplitude of membrane fluctuations observed for chicken embryo retinal cells is about  $1\mu m$  for cells with a diameter of  $5 - 10\mu m$ . So we choose the amplitude of membrane fluctuation to be  $T = 10$ , which corresponds to a typical boundary fluctuation of 1 lattice site for a cell of size  $4 \times 4 \times 4$  in the absence of chemotaxis. Simulations, considering differential adhesion only, set the chemical potential  $\mu$  to be zero, *i.e.*, cells do not respond to chemical signals.

Due to the confusion in the literature on the relative adhesivity of pre-spore and pre-stalk cells and the lack of current experimental data, we simulated both possibilities: Figures 7.8(b) and (d) show the simulation with pre-stalk cells more cohesive than pre-spore cells ( $\mathcal{J}_{psp,psp} = 15, \mathcal{J}_{pst,pst} = 5$ , *i.e.*, prestalk cells are more cohesive

than prespore cells, corresponding to  $\gamma_{pst-sheath} : \gamma_{psp-sheath} = 0.38$ ), whereas Figures 7.8(c) and (e) have the pre-spore cells more cohesive ( $\mathcal{J}_{psp,psp} = 1.0$ ,  $\mathcal{J}_{pst,pst} = 3$ , corresponding to  $\gamma_{pst-sheath} : \gamma_{psp-sheath} = 2.6$ ). Experiments measuring the surface tensions of chicken embryo tissues found  $\gamma_{\text{liver}} : \gamma_{\text{heart}} = 4.3 \text{dyn/cm} : 8.3 \text{dyn/cm} = 0.52$  [246]. Our choices of surface tensions are biologically reasonable. We have also varied whether or not the pre-stalk cells have a preferential interaction with the sheath boundary to see the extent to which this hypothesized mechanism might be necessary to reproduce sorting patterns.

To incorporate chemotaxis, we set up an artificial two-dimensional chemical target pattern with a source located in the center column of the mound. The source (pace-maker cells) radiates chemical periodically outwards at a constant speed, giving rise to a concentration field:

$$C_p(r, t) = C_{p0} e^{[\sin(r+vt)-1]} / r, \quad (7.6)$$

where  $r$  is the distance from a site to the center of the horizontal plane where the site is located, and  $v$  is the traveling velocity of the chemical wave. The choice of chemical field is somewhat arbitrary, but it leads to waves which are consistent with the simplest interpretation of the circular darkfield waves seen in the AX-2 mound. We have tried to replace this pacing wave with a single pacemaker cell on the top of the mound; although we have not exhausted the parameter space, we have had no success in making a tip as yet. In the absence of experimental data about the three-dimensional distribution of chemo-attractant in the mound, this assumption is reasonable [247].

The cell's chemical cycle follows Kessler and Levine [248]. The cells may be quiescent, active or refractory (an enforced period following an active period when cells are immune to chemical signals). Once activated by a chemical signal (induced

by a temporal chemical gradient above a threshold), cells secrete a fixed amount of the same chemical (relay) and move chemotactically toward higher chemical concentration.

The chemical diffuses within the mound and on the surface of the substrate, decays due to proteolytic degradation (similar to that of cAMP by phosphodiesterase), and is secreted by the pacemaker and active cells. So the chemical dynamics is:

$$\frac{\partial C}{\partial t} = D \nabla^2 C - \beta C + C_0 + C_p, \quad (7.7)$$

where  $D$  is the diffusion constant and  $\beta$  is the rate of degradation.  $C_0$  is the secretion by active cells and  $C_p$  is the auto-catalytic pacing field given in Equation 7.6. All simulations used the following parameters for the chemical dynamics:  $D = 5$ ,  $\beta = 0.5$ ,  $C_0 = 50$ ,  $c_p = 0.6$ ,  $v = 1.05$ , most of which come from Kessler and Levine [248].

We simulate pure chemotactic motion by letting the surface tension for pre-spore and pre-stalk cells be the same, so the model does not distinguish between the cell types.

Some experiments suggest that pre-stalk cell respond more strongly to a chemoattractant than pre-spore cells [249]. Can differential chemotaxis to some agent play a significant role? We incorporated this observation by letting  $\mu$  have different values for different cell types. However, the simulation results were independent of this differential chemotactic response for relative  $\mu$  differing up to 50%. Therefore the experimentally observed difference in response is probably not significant for cell sorting in the mound.

### 7.5.3 Simulation Results

Figure 7.8(a-1) shows a vertical cross section of the hemispherical mound at time zero, sitting on the substrate, surrounded by the slime sheath. Figure 7.8(a-2) is the corresponding three-dimensional surface view. Prestalk cells are red and pre-

spore cells blue. Black represents the boundaries between cells (cell surface pixels). The mound contains about 500 cells. 20% of them are pre-stalk cells, randomly distributed in the mound. If both cell types interact equally with sheath, the more cohesive cell type should cluster inside the other cell type. Figure 7.8(b) shows that when pre-stalk cells are more cohesive, they form clusters inside the pre-spore aggregate. Figure 7.8(c) shows the opposite case when pre-spore cells are more cohesive: over long times, pre-stalk cells are “squeezed” to the surface as the pre-spore cells cluster to form a single aggregate, with small numbers of pre-stalk cells trapped inside. Because cells extend pseudopods when they move, their surface areas increase, increasing the number of black pixels in the cross section views. So, pre-stalk cells can sort to the surface without any preference for the surface, as long as pre-spore cells are more cohesive; the experimental signature of this mechanism would be clusters of pre-stalk cells at the surface which would not spread into a thin layer covering the whole mound. Neither case forms a tip.

If pre-stalk cells are much more adhesive to sheath than pre-spore cells, as Takeuchi *et al.* suggested [209], pre-stalk cells would move to the surface of the mound to minimize the contact area between pre-spore cells and sheath, regardless of whether they are more or less cohesive than pre-spore cells. For pre-stalk cells more cohesive (shown in Figures 7.8(d-1,2) at 2000 MCS), pre-stalk cells move slowly to the surface of the mound, leaving some small pre-stalk clusters behind; no tip forms. If the pre-spore cells are more cohesive than pre-stalk cells (shown in Figure 7.8(e) at 200 MCS), more pre-stalk cells appear on the surface, with some small clusters of pre-stalk cells left behind within the bulk of the mound, and again, no tip forms. The only difference we observed between the cases is that cells come to the surface more slowly in first case, which makes sense. If pre-stalk cells are more cohesive, they tend to cluster. Since membrane fluctuations drive the cell

motion, clusters diffuse more slowly than single cells. The difference between these possibilities could be studied experimentally by checking whether or not pre-stalk cells do in fact tend to form small clusters before they come to the surface.

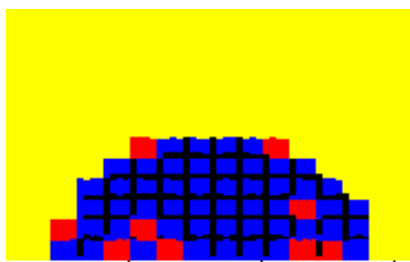
The results that follow assume that the best current guess about the true situation in *Dictyostelium* is the parameter set corresponding to Figure 7.8(e). That is, pre-spore cells are more cohesive and they weakly prefer the surface. This set of assumptions leads to the most rapid and most robust (in terms of varying the other parameters) sorting of the pre-stalk cells to the mound surface. Even in this case, though, no tip forms.

The simulated patterns which develop under differential adhesion resemble those seen in both carB [222] and tagB [250] null mutants, which are likely to have chemotactic defects. Pre-stalk cells form a thin surface layer on top of the mound but never form a protruding tip. If those mutants somehow interfere with chemotaxis (either by deleting a relevant receptor or, for tagB, by eliminating a subclass of cells which may be involved in initiating the chemical signal), these findings would be consistent with our model dynamics.

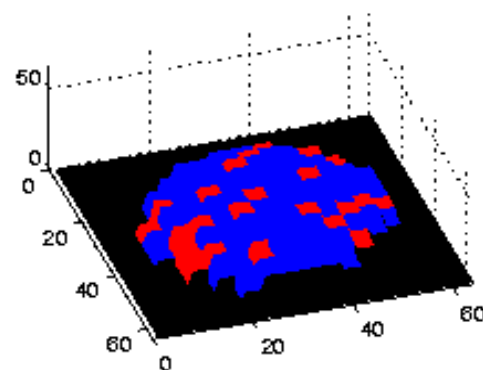
Including chemotaxis, an apical tip forms. Figure 7.9 shows a typical initial condition for simulations with chemotaxis: (a) shows the three-dimensional surface plot of the mound. Color codes indicate the different states of cells: green for quiescent, purple for active and yellow for refractory. At time zero, all cells are quiescent (green). (b) shows the cell type distribution on the surface of the mound: blue represents pre-spore cells and red, pre-stalk cells. (c) is a vertical cross section through the mound, red (pre-stalk) cells are randomly distributed. (d) shows the chemical concentration (viewed from the top) at the surface of the substrate, which is zero initially.

Figure 7.10 shows the pattern after 2000 MCS. A tip begins forming at the apex

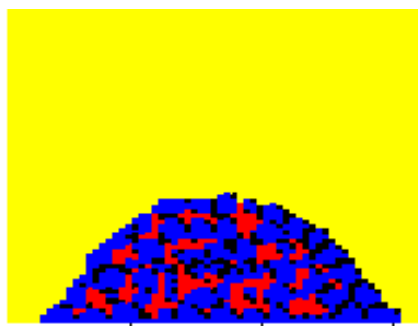
Figure 7.8: Sorting with differential adhesion only. (a-1) A vertical cross section view of the mound at time zero. About 20% pre-stalk cells (red) are randomly distributed among pre-spore cells (blue); cell surfaces are colored black. (a-2) A three-dimensional surface plot of the mound at time zero. (b) A vertical section view and a surface plot of the mound with pre-stalk cells more cohesive than pre-spore cells. Both cell types have the same adhesivity with sheath ( $\mathcal{J}_{psp,psp} = 15$ ,  $\mathcal{J}_{pst,pst} = 5$ , *i.e.* pre-stalk cells five times more cohesive than pre-spore cells,  $\mathcal{J}_{psp,sheath} = \mathcal{J}_{pst,sheath} = 10$ ), at 20000 Monte Carlo steps (MCS). (c) Same as (b) but with pre-stalk cells less cohesive than pre-spore cells ( $\mathcal{J}_{psp,psp} = 1$ ,  $\mathcal{J}_{pst,pst} = 3$ ,  $\mathcal{J}_{psp,sheath} = \mathcal{J}_{pst,sheath} = 10$ ), at 6000 MCS. (d) A vertical section view and a surface plot of the mound with pre-stalk cells more adhesive to sheath than pre-spore cells ( $\mathcal{J}_{pst,sheath} = 10$ ,  $\mathcal{J}_{psp,sheath} = 25$ , *i.e.* pre-stalk cells are 2.5 time more adhesive to sheath than pre-spore cells). Pre-stalk cells are more cohesive ( $\mathcal{J}_{psp,psp} = 15$ ,  $\mathcal{J}_{pst,pst} = 5$ , *i.e.* pre-stalk cells are three times more cohesive than pre-spore cells), at 2000 MCS: pre-stalk cells move to the surface of the mound, leaving some small clusters of pre-stalk cells in the bulk. (e) Same as (d) but with pre-spore cells more cohesive than pre-stalk cells ( $\mathcal{J}_{psp,psp} = 1.0$ ,  $\mathcal{J}_{pst,pst} = 3$ , *i.e.*, pre-spore cells are three times more cohesive than pre-stalk cells), at 200 MCS.



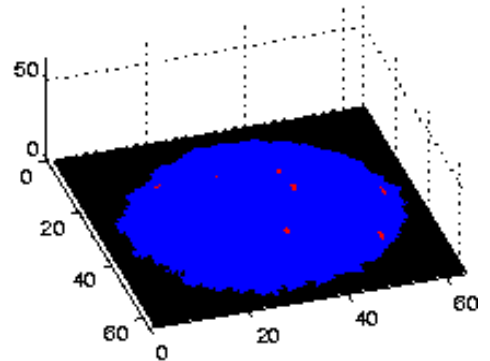
a-1



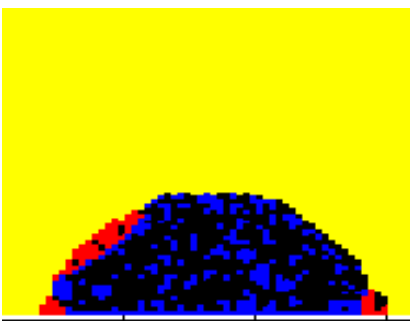
a-2



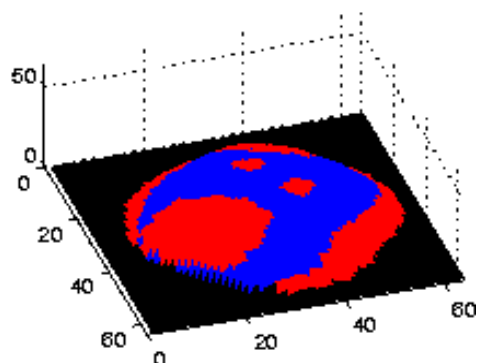
b-1



b-2

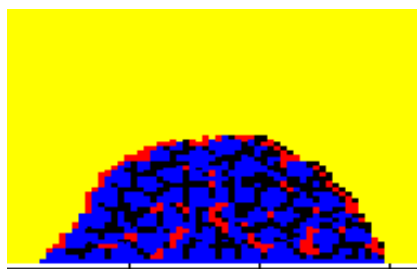


c-1

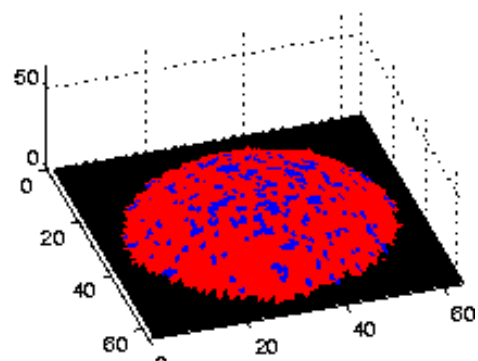


c-2

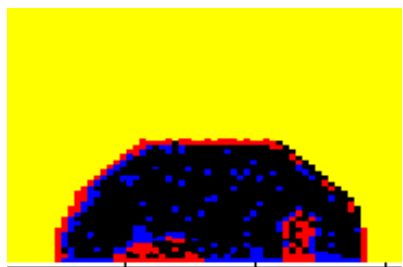
FIGURE 7.7: cont.



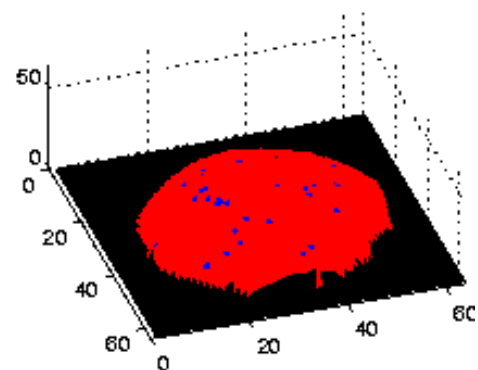
d-1



d-2



e-1



e-2

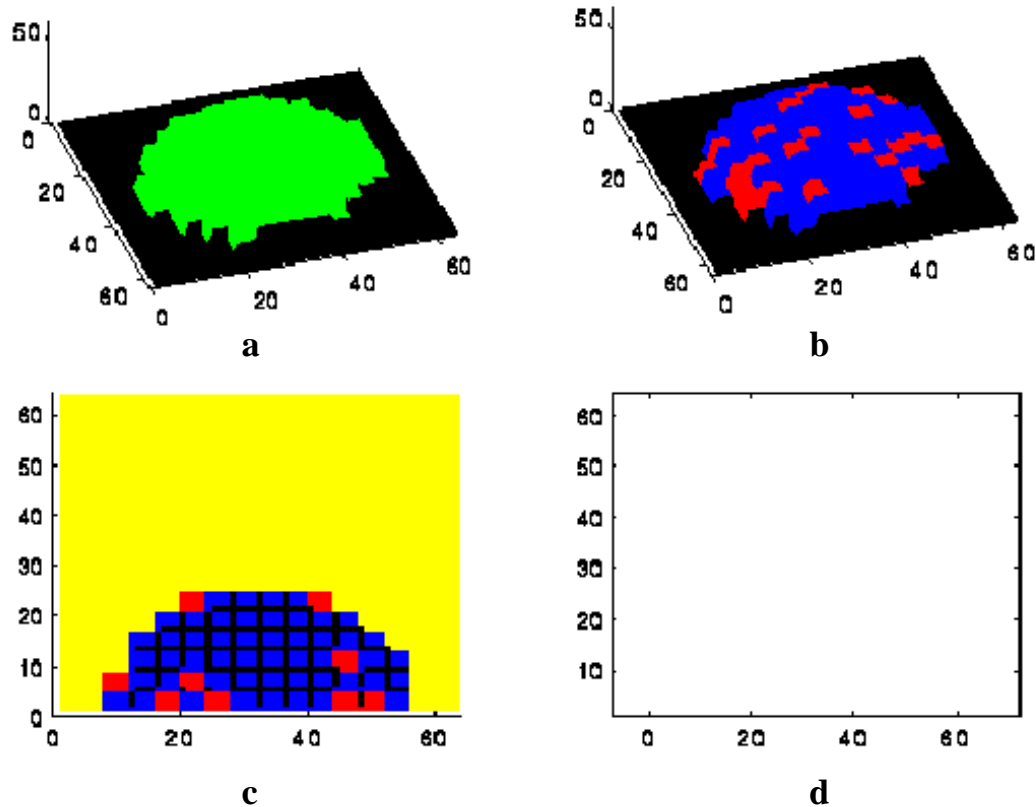


Figure 7.9: Initial configuration for simulations with both differential adhesion and chemotaxis ( $\mathcal{J}_{psp,psp} = 1.0$ ,  $\mathcal{J}_{pst,pst} = 3.0$ ,  $\mu = 20$ ). (a) A three-dimensional surface plot of the mound showing different states of the cells: green represents quiescent, purple active, and yellow refractory. (b) A three-dimensional surface plot of the mound showing cell type distribution: pre-spore cells are blue and pre-stalk cells red. (c) A vertical cross section of the mound showing cell type distribution: pre-spore cells are blue and pre-stalk cells red. Cell surface is black. (d) A projection from the top, of the chemical concentration on the surface of the substrate. The chemical field is zero at time zero.

of the mound and the pre-stalk cells move to the surface.

Figure 7.11 shows typical evolution in the mound with both mechanisms present. As time progresses, the tip grows taller and taller. Prestalk cells sort to the surface of the mound and in particular, make up the majority of cells in the protruding tip. This sequence is consistent with development in strains such as AX-2 for which our chemical dynamics is a possible caricature.

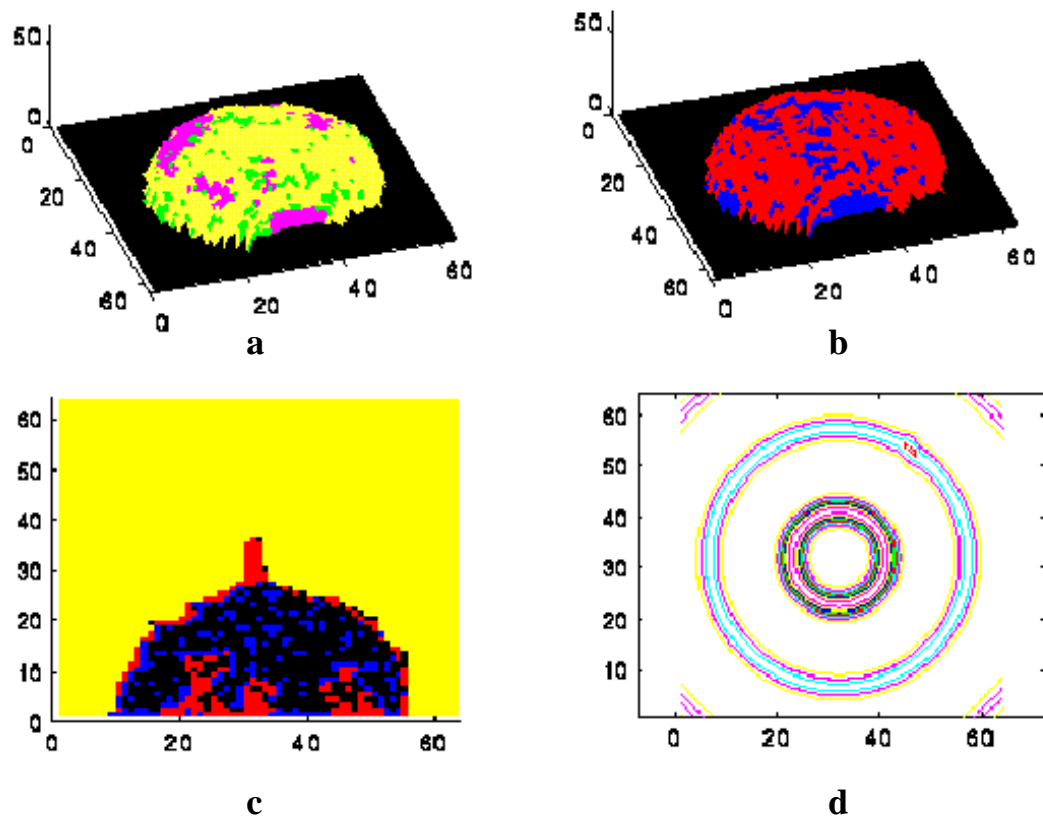


Figure 7.10: The same mound as in Figure 7.9 at 2000 MCS for simulations with both differential adhesion and chemotaxis.

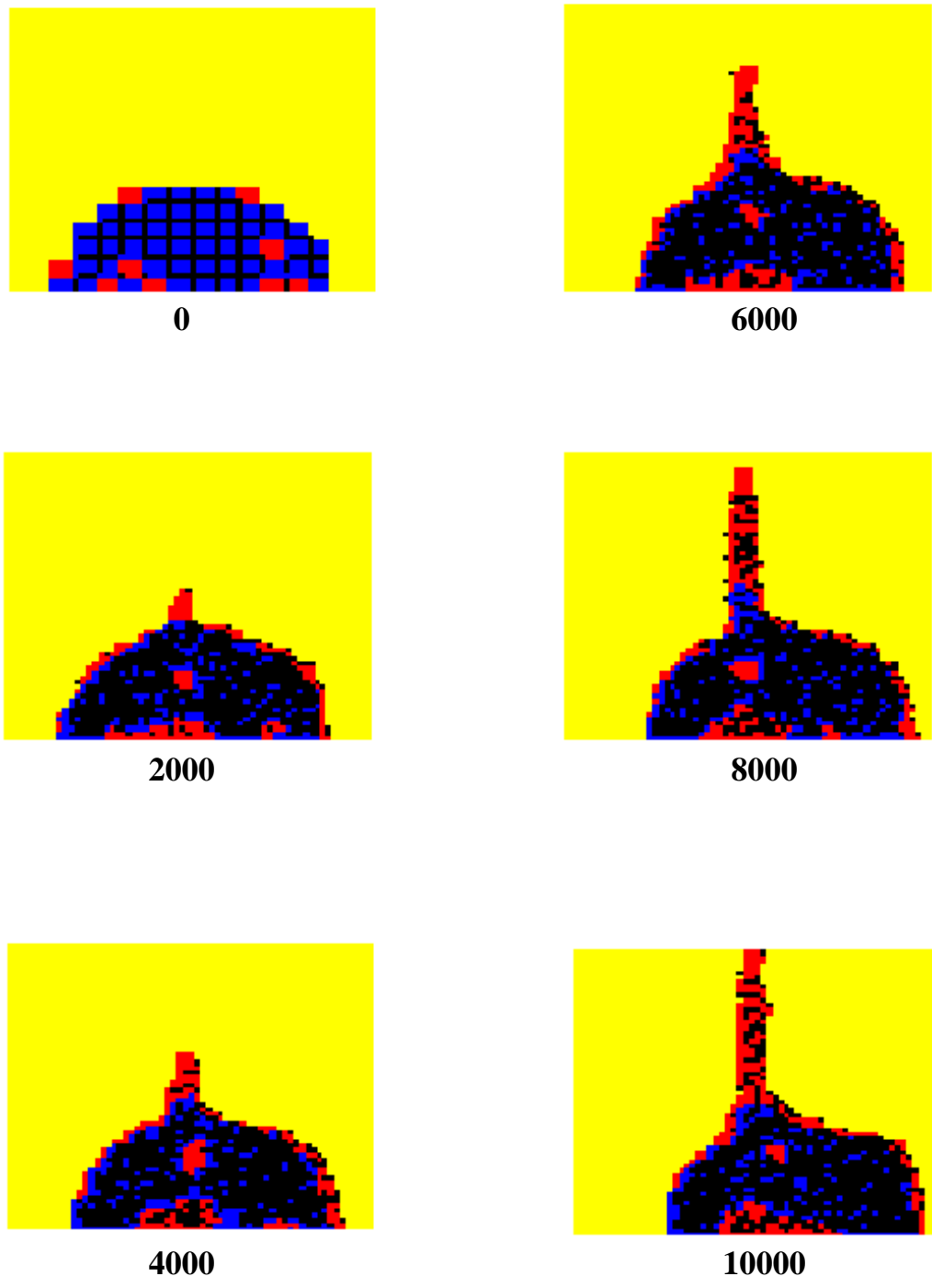


Figure 7.11: Vertical section views of the evolution of a mound ( $\mathcal{J}_{psp,psp} = 1$ ,  $\mathcal{J}_{pst,pst} = 3$ ,  $\mu = 20$ ). Numbers show time in MCS.

As we adjust the control parameter  $\phi$  to tune the relative strength of chemotaxis to differential adhesion, we see that the pattern formation (Figure 7.12) results from the competition between the minimization of adhesion energy (differential adhesion) and cell movement towards higher chemical concentration (chemotaxis). Stronger chemotaxis produces a large tip more rapidly, but the tip contains both pre-stalk and pre-spore cells, with no sorting of cell types. Chemotaxis only, when pre-stalk and pre-spore have the same adhesion energy, corresponds to  $\phi = \infty$ . Only within a certain range ( $5 < \phi < 8$ ) can we see a tip containing pre-stalk cells only. For  $\phi = 6.7$ , the maximum velocity of cell motion is about 1.5 lattice sites per MCS or 4 cell diameters per 10 MCS, measured from the center of mass of cells. If we equate 20 MCS to 1 minute in real time, the cell velocity corresponds to roughly  $16\mu\text{m}/\text{min}$ , as observed experimentally by Soll *et al.* [252]. This timescale in turn makes the sorting time about 100 minutes, which is realistic.

To provide experimentally verifiable quantitative results, we measured the size of the tip as a function of time for a series of relative strengths. Figure 7.13 shows that all the tips grow linearly in time, larger chemical potentials corresponding to faster tip growth. Next we measured the fraction of contacting surface between pre-stalk cells and sheath to indicate the degree of cell sorting to the surface. Shown in Figure 7.14, larger chemical potential results in somewhat faster but less complete sorting. When  $\phi = \infty$ , indicating pure chemotaxis, *i.e.* with pre-spore and pre-stalk cells having the same surface tensions, no sorting to the surface was observed. Notice that the slopes of the pst-sheath interface area are steeper for larger  $\phi$  before 1000 MCS, suggesting that, at short times at least, chemotaxis could enhance the speed of sorting. Again, the degree of surface sorting is easily measurable in experiments. Thus the experimentally determined rate of growth and degree of sorting will determine  $\phi$ . Of course, in real *Dictyostelium*, the tip does not grow indefinitely. We

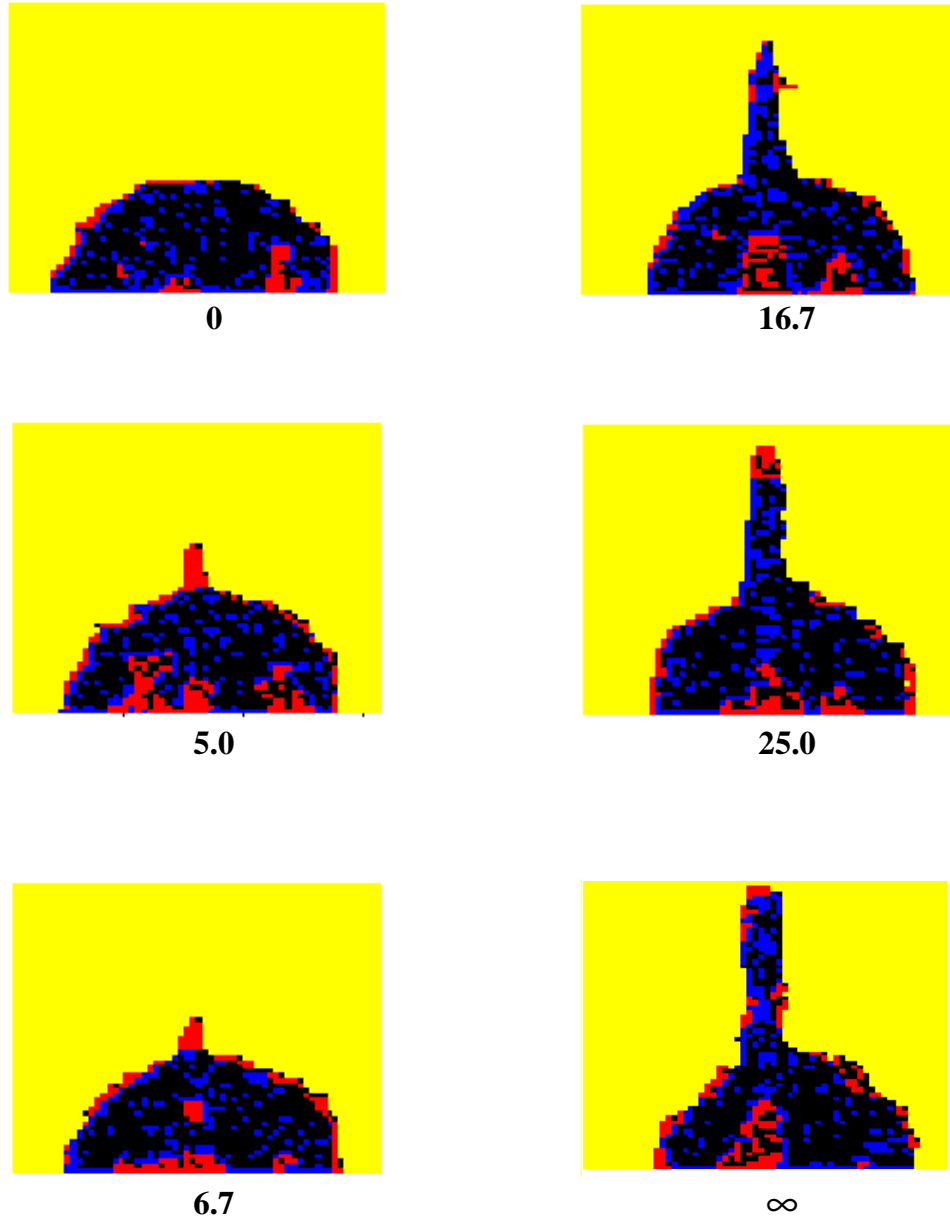


Figure 7.12: Vertical section views of the mounds at 2000 MCS for different relative strengths of chemotaxis and differential adhesion. Numbers show the values of the control parameter  $\phi$ .  $\phi = 0$  corresponds to pure differential adhesion,  $\phi = \infty$  to pure chemotaxis.

do not know when and how the growth stops. We focus on the sorting mechanisms only.

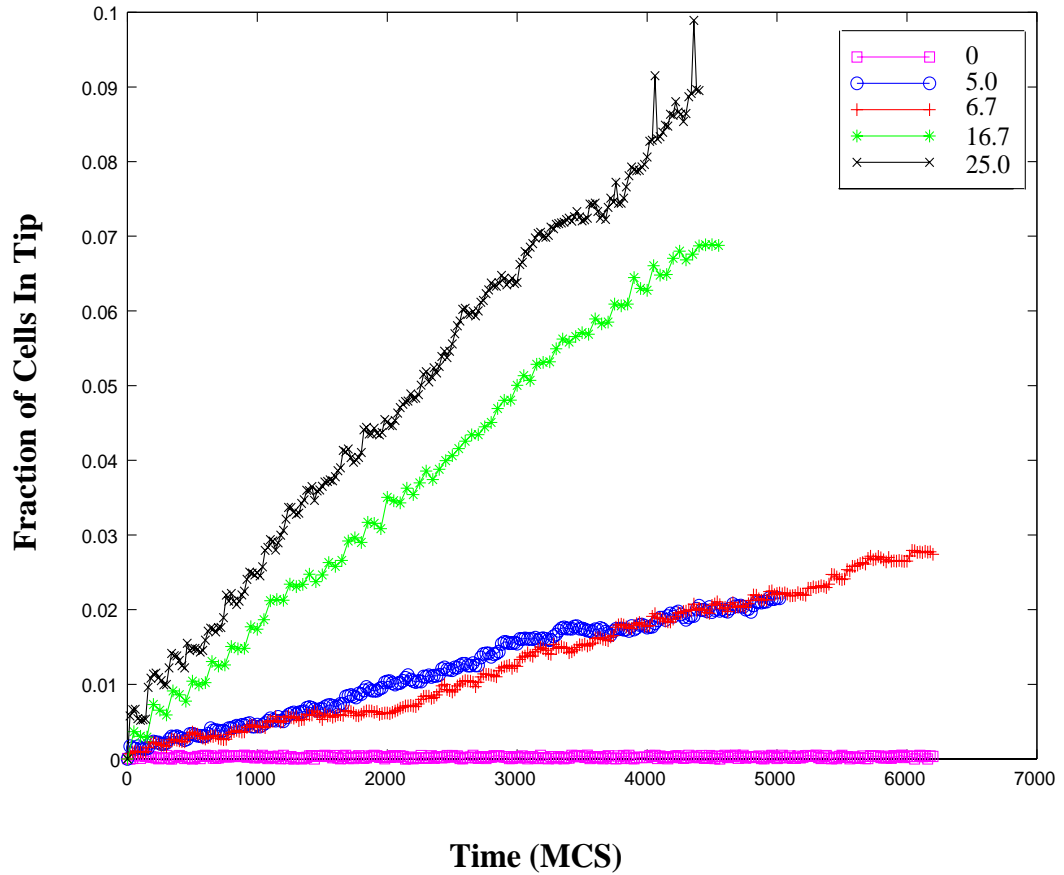


Figure 7.13: The evolution of tip size (fraction of cells in the tip) as a function of time for different  $\phi$ .

In conclusion, the simulation results suggest: In the mound stage, if only differential adhesion regulated cell sorting, pre-stalk cells would come to the surface of the mound but no tip would form. In other words, differential adhesion alone cannot explain the sorted tip in the mound. Chemotaxis of cells to a diffusible chemical can form a tip but the tip consists of both pre-stalk and pre-spore cells: no sorting can be accomplished by chemotaxis alone. Only the competition of both mechanisms

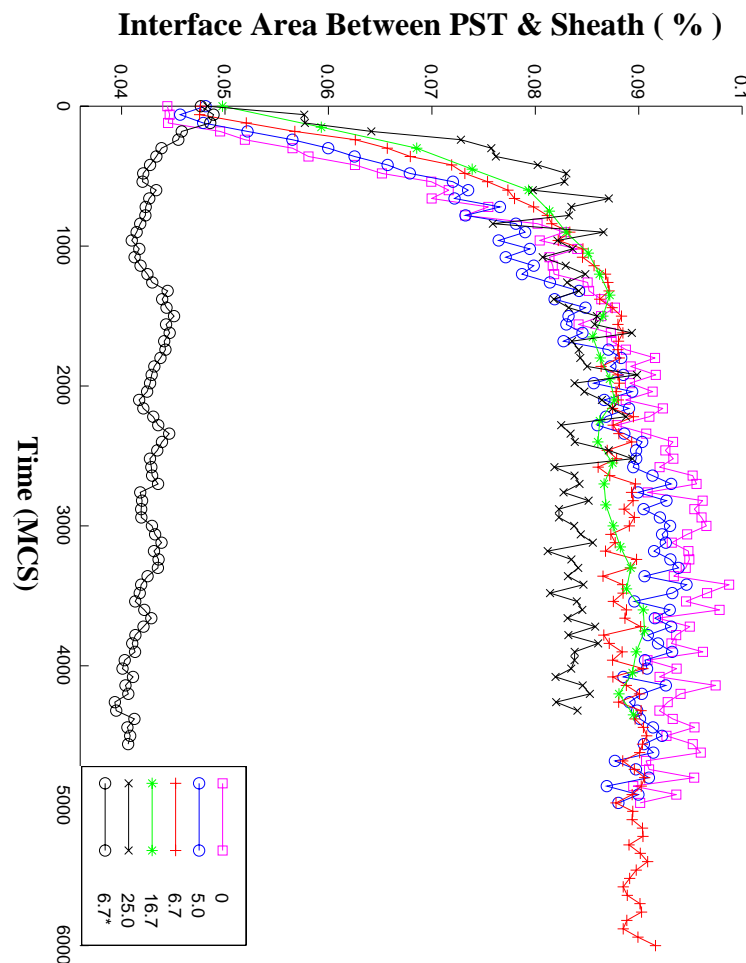


Figure 7.14: The fraction of pre-stalk cells in contact with sheath as a function of time for different  $\phi$ .  $\phi = \infty$  corresponds to the case of pure chemotaxis, with pre-stalk and pre-spore cells having the same surface tensions.

allows the cells to form a tip consisting of pre-stalk cells only. Similar methods can be used to study strains such as KAX-3 which have “pinwheel” waves, or to consider alternative mechanisms such as the possibility of a chemo-repellent emitted by the pre-spore cells.

## 7.6 Cellular Automata

Finally, we comment on the cellular automaton (CA) approach for modeling cell-cell interactions.

Cellular Automaton representations of biological cells typically employ one automaton per cell which interacts with the nearest and maybe some higher order neighbors under some local rules. This technique has several disadvantages, for example:

- Cells have a fixed size.
- Cells have no shape.
- Lattice effects can influence dynamics.
- All cells interact with a fixed number of neighbors.
- Time and space are highly discretized.

Not all of the above points will be important or affect a model’s dynamics but they might play a significant role in the observed behavior.

A single-automaton cell model can model collective cell motions and global patterning, but can not model behaviors that require information on cell shape, size or cell membrane motion. A multi-automaton cell model is necessary to model cellular level activities, such as cell membrane fluctuations or cell growth.

Agarwal [254, 255] recently introduced a “cell programming language” in which a collection of connected squares represents a “cell.” The cells can perform global

functions such as growing, dividing, rounding, *etc.*. However, an inelegant aspect of this model is that before a cell can perform any function it must recompute its neighborhood to take into account of any changes that have taken place since it was last updated.

The extended large- $Q$  Potts model is more elegant. Starting from cell sorting through differential cellular adhesion, the model can be easily extended to include growth, cell division *etc.* on the subcellular level. It then becomes a useful tool for modeling cell-cell interactions and possibly self-organized complex behaviors. Simply varying the values of the adhesion energy can simulate many different types of behaviors, including engulfment, cell dispersal and cell sorting.

Cell growth can be modeled by slowly increasing the target volume,  $V$ , of a cell of volume,  $v$ , (for example when a cell consumes some nutrient). Because  $v$  remains close to  $V$ , the cell's volume will slowly increase. Cell division occurs when a cell's volume (or surface to volume ratio) reaches a threshold. Then the sites in one half of the cell are assigned to an, as yet, unused identification number (spin). Mombach *et al.* [256] simulated two-dimensional tissue growth and mitosis using the large- $Q$  Potts model. Instead of controlling the target areas, they allowed the cells to grow as in normal diffusional coarsening, and then divided the cells whose area/perimeter ratio exceeded a critical value by introducing a new wall along the least diameter. As discussed in Chapter 3, target-volume (or area, in two dimensions) mediated growth can separate the diffusion and relaxation timescales. For biological cells, growth is much slower than relaxation, and is determined by more complex mechanisms than the pressure-difference driven diffusion of soap froth. Therefore, target-volume-mediated growth is more appropriate for biological cell growth. After cell mitosis, the daughter cells can inherit the parent's properties with or without mutation.

Gravity or chemotaxis can be modeled as a positive bias in the probability of

cell motion in a given direction. Chemodynamics can be modeled by a set of differential equation for the diffusion and production of a chemical (*e.g.* cAMP in *Dictyostelium*), which can be coupled with the cell's motility to make the cell migrate along chemical gradients towards higher or lower concentrations.

As an example of growth and division rules, we can look at two-dimensional diffusion limited growth of bacterial cells. Bacteria can be modeled as cells of a single cell type that adhere to each other and do not move chemotactically. Starting with only one bacterium and a sparse distribution of nutrients represented as independent particles, the bacterium target area,  $A$ , increases by a certain amount each time the bacterium consumes a nutrient particle. When the bacterial area  $a$  reaches a threshold value the bacterium divides in half along its axis of smallest moment of inertia. For low growth rate per unit nutrient we expect fractal structures, resembling diffusion limited aggregation (DLA); for higher rates we should find more compact structures. Other extensions could include random walks and chemokinesis [257] and mutations for selection of growth strategies [258]. Varying cell motility and nutrient concentration may reproduce a morphology diagram like that first observed by Mastushita *et al.* [259].

Coupling cell growth, division and death to nutrient diffusion can model the concentric shell structure of spherical avascular tumors [59]. Cells in the outer shell receive sufficient nutrient to grow and divide normally. Limited nutrient supply results in quiescent cells in the middle shell which are alive but do not grow or divide. The center of the tumor, where the nutrient concentration is below the critical level to sustain life, consists a core of dead cells.

If we couple the growth, division and death of cells with chemotaxis to randomly appearing patches of food sources which secrete a diffusible chemoattractant, we can examine which cell strategies are selected in this environment. If we evolve the

strength of the adherence/repulsion between cell species, we can model selection favoring those cell types that repel themselves from other cell types. By dispersing, a small population of repelling cells cover more area than an adhering population and hence are more likely to encounter chemoattractant or nutrients.

The Potts model also makes some experimentally testable predictions: cells in aggregates move faster than when alone [244]; cells do not sort without differential adhesion even with differential chemotaxis [232]. The sorting of cell types can be partially or completely due to differential adhesion between the cell types.

The elegance of the Potts model comes from its simplicity: all interactions and constraints are formulated in terms of effective free energies. It performs localized minute adjustments to cell membranes to minimize the total free energy. We believe that this modeling approach may be useful in examining and explaining behavior in many cellular structures where cell-cell adhesion plays a critical role in the formation of patterns.

## CHAPTER 8

### CONCLUSIONS AND OUTLOOK

We have extended the large- $Q$  Potts model and applied it to cellular pattern formation in foams and living organisms.

#### 8.1 Grain Growth

In two-dimensional coarsening, the growth of a single topological defect in a homogeneous isotropic lattice reaches a special scaling state with time invariant statistics but no length scale change. The deep question: is there a unique stable scaling state, however, remains open. A promising advance may lie in the recent interest in persistence, *i.e.* the fraction of the system frozen in its initial state. An experiment on soap froth [260] and a mean field model [261] have shown that the area of regions that do not change during coarsening (survivors) shows power law scaling in time. The source of this new scaling is not yet clear, but it may shed some light on the universality of the scaling state.

Widely spaced topological defects can cause abnormal grain growth, without strong surface energy anisotropy. Experiments and other models have confirmed this result [262, 264, 263, 101, 102]. We know that a disordered cluster evolved from one single defect has a diverging topological distribution. Competition among more topological defects should confine the distribution. As the density of topological defects increases, the topological distribution at long times tends towards the same scaling distribution as normal coarsening. At what density of defects does abnormal

coarsening becomes normal? In the dry limit, two-dimensional coarsening scales as  $\langle r \rangle \sim t^{1/2}$ . In the wet limit, the growth law is  $\langle r \rangle \sim t^{1/3}$  (Ostwald ripening). Is the transition between these two scalings smooth; *i.e.* what is the growth kinetics for intermediate wetness? These two questions can be answered with detailed Potts model simulations.

We have only considered coarsening due to gas diffusion without wall breakage (or film rupture). Wall breakage causes bubble coalescence and complicated wall and vertex motion, resulting in different scaling behaviors which are only described by “semi-empirical” rules [55, 263].

It is worth noting that linear problems like two-dimensional coarsening involving energy minimization subject to constraints can result in notably complex patterns and behaviors, for which we have no fundamental theory yet.

All the above questions can be asked in case of three-dimensional foams. Both theoretical and experimental studies for three-dimensional coarsening are still preliminary. We need large scale simulations, and experiments offering full three-dimensional information over long evolution times to provide convincing answers.

## 8.2 Foam Drainage

In three-dimensional wet foams, liquid flows through the Plateau border network of bubble film junctions until gravity balances capillary effects, resulting in a spontaneous tendency for the foam to separate into two distinct bulk phases.

Our model reproduces this behavior. In ordered foams, liquid profiles for free drainage and forced drainage agree with both experimental data and analytical calculations. For pulsed drainage, the lattice size limited simulations. We used a sample that was only 1/20 the length of the experiment, thus the simulation only covered the initial stage of the experiment; the simulated pulse velocity was constant while experiments show a velocity proportional to  $t^{-1/2}$ . This defect can be easily

taken care of by running on a much larger lattice. Moreover, the simulations can study regimes beyond current experiments and theory and predict new phenomena. In disordered foams or when coarsening takes place over the same time scales as drainage, the interface between wet and dry foam is no longer sharp. The onset of wetting front instability calls for further study. The flow of the liquid then resembles flow in porous media, only with the random network evolving in time.

Current segmented-ac-capacitance measurement is essentially one dimensional, only resolving the averaged liquid fraction at different vertical positions in the foam. MRI can provide averaged one-dimensional profiles, two-dimensional sections and full three-dimensional images to study the shape and stability of the wetting front.

The drainage equation assumes non-slip boundary conditions for the micro-channel flow in the Plateau borders, which justify the assumption of Poiseuille flow. Kraynik [142] argued that in most cases this assumption is true because the inequality:

$$\eta_s > 10\eta\Phi_l^{1/2}r \quad (8.1)$$

holds. Here  $\eta$  and  $\eta_s$  are the bulk and surface viscosities,  $r$  is the radius of curvature of the Plateau border and  $\Phi = \Phi(x, t)$  is the liquid fraction. This inequality is reasonable on dimensional grounds but requires more analysis. Experiments with foams of different bulk and surface viscosities would be valuable.

Experiment, theory and simulation have all focused on fairly dry foams. Wet foams need attention. Experiments suggested a departure from the expected  $\Phi \propto \sqrt{V}$  behavior for high flow rate,  $V$ , which was attributed to the accumulation of liquid in the expanded Plateau borders [129]. Is drainage in the wet limit significantly different from the predicted behavior?

The Potts model simulations have not only pointed out a new direction in the

theoretical study of foam drainage, but potentially can extend to problems involving many interacting mechanisms and complex boundary conditions, in particular, biochemical reactions coupled with flow in porous media.

### 8.3 Foam Rheology

We have studied the dynamics of local topological rearrangement in two-dimensional foams. Since topological rearrangements (T1 events) are non-local and in disordered structures T1 events are not the same, we have considered the stored energy and T1 events separately. We predicted three different types of hysteresis in the mechanical response of foams under periodic shear, corresponding to elastic, viscoelastic and viscous-fluid-like behavior.

The unique rheology of foam is essentially independent of the properties of the foam's liquid composition except for its viscosity but sensitively depends on the polydispersity of the foam structure. We have related the macroscopic mechanical response to the microscopic topological rearrangement at the bubble level. We have shown that as the structural disorder increases, the yield strain decreases from a finite value for an ordered foam to zero for a very disordered foam; also the topological rearrangements become more correlated in time, with their power spectra changing from white noise towards  $1/f$  noise. The spatial correlation of the topological rearrangements remains to be studied.

Avalanches of topological rearrangements release stored energy and stress, but single T1 events only locally reduce bubble elongation. Also, instead of energy dissipation (the derivative of the total energy), the power spectra of the total stored energy exhibit the same  $1/f$  trend as the T1 events. Though we have tried to draw analogies with more familiar models with  $1/f$  power law behaviors, we do not yet understand the reason for the  $1/f$  spectrum for the stored energy.

While we have not yet derived the explicit dependence of foam viscosity on

the Potts model parameters, we have proposed several methods to determine the effective foam viscosity. Separating the effects of topological rearrangement and film visco-elasticity in the simulations may help link the model parameters with the viscosity coefficient. We have focused on the dry foam limit. Experiments have found that the liquid concentration changes the rheological properties of foams dramatically. Including different liquid fractions in the current model would be valuable.

#### 8.4 Cell Sorting

For biological cells, we have developed a cellular level model to study the mechanisms of cell migration and sorting during tip formation in the *Dictyostelium* mound. Certain evidence in the literature points to differential adhesion as the mechanism for sorting pre-spore and pre-stalk cells, while other observations suggest that chemotaxis plays an important role. We have shown that differential adhesion is sufficient for segregation of the two cell types, but tip formation requires chemotaxis. Only when both mechanisms work in concert can the tip form with only one type of cells. The significance of these results, however, hinges on whether the parameter values are physiologically relevant. We can relate parameters to physical parameters that are in principle measurable in experiments. But since no experimental results are available for some of the parameters, *e.g.* the surface tensions of the different cell types, we can only claim that the values we have chosen are biologically reasonable by comparing them to those of chicken embryo tissues, where such measurements have been done. We have suggested a series of new experiments and eagerly wait experimental verification.

Finally, the large- $Q$  Potts model and its extensions have proven to be very powerful and flexible in modeling cellular structures where surface energy minimization is important. Nevertheless, the basic assumption of the model is that the kinetics

can be described by Boltzmann thermodynamics. In some situations the assumption may not be true.

## List of References

- [1] M. C. Cross and P. C. Hohenberg, Rev. Mod. Phys. **65**, 851 (1993).
- [2] R. Boyle, *New Experiments, Physico-Mechanical, Touching the Spring of Air* (Oxford: Oxford, 1660).
- [3] Sir R. Bulkley, Phil. Trans. Roy. Soc. London **17**, 708 (1693).
- [4] A. Aydin and J. M. DeGraff, Science **239**, 471 (1988).
- [5] W. B. Krantz, K. J. Gleason and N. Caine, Sci. Am. **259**, 68 (1988).
- [6] K. J. Dormer, *Fundamental Tissue Geometry for Biologists* (Cambridge University Press: Cambridge, 1980).
- [7] G. Reiter, Phys. Rev. Lett. **68**, 75 (1992).
- [8] R. J. Bray and R. E. Loughhead, *Sunspots* (Dover, New York 1979).
- [9] J. R. A. Pearson, J. Fluid Mech. **4**, 489 (1958).
- [10] D. Weaire and N. Rivier, Contemp. Phys. **25**, 59 (1984).
- [11] J. A. Glazier, Dynamics of Cellular Patterns, Ph.D. Thesis, The University of Chicago, 1989 (unpublished).
- [12] J. Stavans, Rep. Prog. Phys. **56**, 733 (1993).
- [13] D'Arcy W. Thompson, *On Growth and Form*, (Cambridge University Press: Cambridge, 1942).
- [14] C. S. Smith, in *Metal Interfaces*, ed. C. Herring, American Society for Metals: Cleveland, 65 (1952).
- [15] J. von Neumann, in *Metal Interfaces*, ed. C. Herring, American Society for Metals: Cleveland, 108 (1952).
- [16] J. A. Glazier, S. P. Gross, and J. Stavans, Phys. Rev. A **36**, 306 (1987).
- [17] J. Stavans and J. A. Glazier, Phys. Rev. Lett. **62**, 1318 (1989).
- [18] J. A. Glazier and J. Stavans, Phys. Rev. A **40**, 7398 (1989).

- [19] K. L. Babcock and R. M. Westervelt, Phys Rev. A **40**, 2022 (1989).
- [20] K. L. Babcock and R. M. Westervelt, Phys. Rev. Lett. **64**, 2168 (1990).
- [21] K. L. Babcock, R. Seshadri, and R. M. Westervelt, Phys. Rev. A **41**, 1952 (1990).
- [22] K. J. Stine, S. A. Rauseo, B. G. More, J. A. Wise, and C. M. Knobler, Phys. Rev. A **41**, 6884 (1990).
- [23] B. Berge, A. J. Simon, and A. Libchaber, Phys. Rev. A **41**, 6893 (1989).
- [24] M. O. Magnasco, Phil. Mag. B **65**, 895 (1992).
- [25] F. Elias, C. Flament, J.-C Bacri, O. Cardoso, and F. Graner, Phys. Rev. E **56**, 3310 (1997).
- [26] V. E. Fradkov, L. S. Shvindlerman, and D. G. Udler, Scripta Met. **19**, 1285 (1985); *ibid*, 1291 (1985).
- [27] M. O. Magnasco, Phil. Mag. B **69**, 397 (1994).
- [28] J. Plateau, *Statique Expérimentale et Théorique des Liquides Soumis aux Seules Forces Moléculaires*. (Gauthier-Villars: Ghent, 1873).
- [29] S. Hildebrandt and A. Tromba, *The Parsimonious Universe: Shape and Form in the Natural World*, (Springer-Verlag, New York, 1996).
- [30] See, *e.g.*, M. R. Garey, R. L. Graham, and D. S. Johnson, SIAM J. Appl. Math. **32**, 835 (1977).
- [31] F. K. Hwang and D. S. Richards, Networks **22**, 55 (1992).
- [32] R. B. Potts, Proc. Camb. Phil. Soc. **48**, 106 (1952).
- [33] J. Ashkin and E. Teller, Phys. Rev. **64**, 178 (1943).
- [34] C. Domb, J. Phys. A **7**, 1335 (1974).
- [35] F. Y. Wu, Rev. Mod. Phys. **54**, 235 (1982).
- [36] See, *e.g.*, A. Pelizzola, Phys. Rev. E **54**, R5585 (1996).
- [37] N. Goldenfeld, *Lectures on Phase Transitions and the Renormalization Group*, (Addison-Wesley: US, 1992).
- [38] P. S. Sahni, G. S. Grest, M. P. Anderson, and D. J. Srolovitz, Phys. Rev. Lett. **50**, 263 (1983).
- [39] D. J. Srolovitz, M. P. Anderson, G. S. Grest, and P. S. Sahni, Scripta Met. **17**, 241 (1983).

- [40] D. J. Srolovitz, M. P. Anderson, G. S. Grest, and P. S. Sahni, *Acta Met.* **32**, 793 (1984).
- [41] D. J. Srolovitz, M. P. Anderson, G. S. Grest, and P. S. Sahni, *Acta Met.* **32**, 1429 (1984).
- [42] D. J. Srolovitz, G. S. Grest, and M. P. Anderson, *Acta Met.* **33**, 2233 (1985).
- [43] D. J. Srolovitz, *J. Vac. Sci. Technol.* **A4**, 2925 (1986).
- [44] M. P. Anderson, D. J. Srolovitz, G. S. Grest, and P. S. Sahni, *Acta Met.* **B59**, 293 (1984).
- [45] M. P. Anderson, G. S. Grest and D. J. Srolovitz, *Scripta Met.* **19**, 225 (1985).
- [46] M. P. Anderson, G. S. Grest and D. J. Srolovitz, in *Computer Simulation of Microstructural Evolution*, The Metallurgical Society: Warrendale, 77 (1986).
- [47] M. P. Anderson, in *Annealing Processes – Recovery, Recrystallization and Grain Growth*, eds. N. Hansen, D. J. Jensen, T. Leffers, and B. Ralph, Risø National Laboratory: Roskilde, Denmark, 15 (1986).
- [48] M. P. Anderson, G. S. Grest, and D. J. Srolovitz, *Phil. Mag. B* **59**, 283 (1989).
- [49] A. D. Rollett, D. J. Srolovitz and M. P. Anderson, *Acta Met.* **37**, 1227 (1989).
- [50] G. S. Grest and M. P. Anderson, *Phys. Rev. B* **38**, 4752 (1988).
- [51] G. S. Grest, M. P. Anderson, D. J. Srolovitz and A. D. Rollett, *Scripta Met.* **24**, 661 (1990).
- [52] N. Metropolis, A. W. Rosenbluth, M. N. Rosenbluth, A. H. Teller, and E. Teller, *J. Chem. Phys.* **21**, 1087 (1953).
- [53] B. Radharkishnan and T. Zacharia, *Metal. and Mat. Trans.* **26A**, 167 (1995).
- [54] F. Haessner and S. Hofmann, in *Recrystallization of Metallic Materials*, ed. F. Haessner, Riederer Verlag: Stuttgart, (1978).
- [55] G. D. Burnett, J. J. Chae, W. Y. Tam, R. M. C. de Almeida, and M. Tabor, *Phys. Rev. E* **51**, 5788 (1995).
- [56] E. Holm, J. A. Glazier, D. J. Srolovitz, and G. S. Grest, *Phys. Rev. A* **43**, 2262 (1991).
- [57] M. Zajac, private communication.
- [58] J. Wejchert, D. Weaire, and J. P. Kermode, *Phil. Mag. B* **53**, 15 (1986).
- [59] E. L. Stott, N. F. Britton, J. A. Glazier, and M. Zajac, *Mathematical and Computer Modelling*, in press (1998).

- [60] Y. Jiang and J. A. Glazier, unpublished.
- [61] P. Peczak, G. Grest, and D. Levine, Phys. Rev. E **48**, 4470 (1993).
- [62] J. E. Avron and D. Levine, Phys. Rev. Lett. **69**, 208 (1992).
- [63] P. Cotterill and P. R. Mould, *Recrystallization and Grain Growth in Metals*, (John Wiley & Sons: New York, 1976).
- [64] K. Detert, in *Recrystallization of Metallic Materials*, ed. F. Haessner, Riederer Verlag: Stuttgart, (1978).
- [65] H. J. Frost, C. V. Thompson and D. T. Walton, Mat. Sci. Forum **94**, 2 (1992)
- [66] H. J. Frost, C. V. Thompson and D. T. Walton, Acta Met. **38**, 1455 (1990).
- [67] H. J. Frost, C. V. Thompson and D. T. Walton, Acta Met. **40**, 779 (1992).
- [68] C. S. Smith, Rev. Mod. Phys. **36**, 524 (1964).
- [69] C. S. Smith, Metal. Rev. **9**, 1 (1964).
- [70] T. Nagai, K. Kawasaki, and K. Nakamura, J. Jpn. Phys. Soc. **43**, 437 (1988).
- [71] D. Weaire and H. Lei, Phil. Mag. Lett. **62**, 427 (1990).
- [72] W. W. Mullin, Scr. Metal. **22**, 1441 (1988).
- [73] F. T. Lewis, Anat. Rec. **38**, 341 (1928).
- [74] F. T. Lewis, Am. J. Botany **30**, 74 (1934).
- [75] J. M. C. Mombach, Rita M. C. de Almeida, and J. R. Iglesias, J. Phys. D **23**, 600 (1990).
- [76] N. Rivier and A. Lissowski, J. Phys. A **15**, L143 (1982).
- [77] J. A. Glazier and D. Weaire, J. Phys.: Condens. Matter **4**, 1867 (1992).
- [78] J. R. Iglesias and Rita M. C. de Almeida, Phys. Rev. A **43**, 2763 (1991).
- [79] T. Herdtle and H. Aref, J. Fluid Mech. **241**, 233 (1992).
- [80] H. Flyvbjerg, Phys. Rev. E **47**, 4037 (1993).
- [81] D. A. Aboav, Metallography **3**, 383 (1970).
- [82] D. Weaire, Metallography **7**, 157 (1974).
- [83] D. A. Aboav, Metallography **13**, 43 (1980).
- [84] J. A. Glazier, M. P. Anderson and G. S. Grest, Phil. Mag. B **62**, 615 (1990).

- [85] M. Marder, Phys. Rev. A **36**, 438 (1987).
- [86] V. E. Fradkov, Phil. Mag. Lett. **58**, 271 (1988).
- [87] V. E. Fradkov, D. G. Udler, and R. E. Kris, Phil. Mag. Lett. **58**, 277 (1988).
- [88] C. W. J. Beenakker, Phys. Rev. A **37**, 1697 (1988).
- [89] H. Flyvbjerg and C. Jeppesen, Phys. Scr. T **38**, 49 (1991).
- [90] J. Stavans, E. Domany, and D. Mukamel, Europhys. Lett. **15**, 419 (1991).
- [91] D. Segel, D. Mukamel, O. Krichevsky, and J. Stavans, Phys. Rev. E **47**, 812 (1993).
- [92] M. Palmer, K. Rajan, M. Glicksman, V. Fradkov, and J. Nordberg, Metal. Mat. Trans. A **26**, 1061 (1995).
- [93] D. G. Dunn and J. L. Walter, in *Recrystallization, Grain Growth and Textures*. Am. Soc. Metall.: Ohio, 461 (1966).
- [94] V. Randle, B. Ralph, and M. Hansen, in *Annealing Process - Recovery, Recrystallization and Grain Growth*, eds. N. Hansen, D. J. Jensen, T. Leffers, and B. Ralph, Risø National Laboratory: Roskilde, Denmark, 123 (1986).
- [95] S. Yabushita, N. Hatta, S. Kikuchi, and J. Kokado, Scr. Met. **19**, 853 (1985).
- [96] M. Hillert, Acta Met. **13**, 227 (1965).
- [97] B. Levitan, Phys. Rev. Lett. **72**, 4057 (1994).
- [98] D. Weaire, Phys. Rev. Lett. **74**, 3710 (1995).
- [99] C. Sire, Phys. Rev. Lett. **74**, 3708 (1995).
- [100] Y. Jiang, J. C. M. Mombach, and J. A. Glazier, Phys. Rev. E **52**, R3333 (1995).
- [101] M. F. Vaz and M. A. Fortes, J. Phys: Condens. Matter **9**, 8971 (1997).
- [102] A. A. E. Kader and J. C. Earnshaw, Phys. Rev. E **56**, 3251 (1997).
- [103] S. Vaidya, T. T. Sheng, and A. K. Sinha, Appl. Phys. Lett. **36**, 464 (1980).
- [104] D. T. Walton, H. J. Frost, and C. V. Thompson, in *Grain Growth in Polycrystalline Materials*, Mat. Sci. Forum **94-96**, 531 (1992).
- [105] D. T. Walton, H. J. Frost, and C. V. Thompson, Appl. Phys. Lett. **61**, 40 (1992).
- [106] W. W. Mullins, J. Appl. Phys. **27**, 900 (1956).

- [107] H. J. Frost, C. V. Thompson, C. L. Howe, and J. Whang, *Scripta Met.* **22**, 65 (1988).
- [108] H. J. Frost and C. V. Thompson, *J. Elec. Materials* **17**, 447 (1988).
- [109] C. V. Thompson, H. J. Frost, and F. Spaepen, *Acta Met.* **35**, 887 (1987).
- [110] M. A. Fortes, M. E. Rosa, S. Findlay, and M. Guedes, *Phil. Mag. A* **77**, 257 (1998).
- [111] M. E. Rosa, and M. A. Fortes, *Europhys. Lett.* **41**, 577 (1998).
- [112] M. Asipauskas and J. A. Glazier, in preparation (1998).
- [113] J. A. Glazier, *Phys. Rev. Lett.* **70**, 2170 (1993).
- [114] C. Sire, *Phys. Rev. Lett.* **72**, 420 (1994).
- [115] D. J. Durian, D. A. Weitz, and D. J. Pine, *Science* **252**, 686 (1991).
- [116] D. J. Durian, D. A. Weitz, and D. J. Pine, *Phys. Rev. A* **44**, R7902 (1992).
- [117] C. P. Gonatas, J. S. Leigh, A. G. Yodh, J. A. Glazier, and B. Prause, *Phys. Rev. Lett.* **75**, 573 (1995).
- [118] B. A. Prause, J. A. Glazier, S. A. Gravina, and C. D. Montemagno, *J. Phys. Condens. Matter* **7**, L511 (1995).
- [119] C. Monnereau and M. Vignes-Adler, *Phys. Rev. Lett.* **80**, 5228 (1998).
- [120] K. Kawasaki, T. Nagai, and K. Nakashima, *Phil. Mag. B* **60**, 399 (1989).
- [121] T. Nagai, S. Ohta, K. Kawasaki, and T. Okuzono, *Phase Trans.* **28**, 177 (1990).
- [122] D. Weaire and J. A. Glazier, *Phil. Mag. Lett.* **68**, 6 (1993); *ibid*, 363 (1993).
- [123] R. M. C. de Almeida and J. C. M. Mombach, *Physica A* **236**, 268 (1997).
- [124] C. G. J. Bisperink, J. C. Akkerman, A. Prins, and A. D. Ronteltap, *Food Struct.* **11**, 101 (1992).
- [125] K. Brakke, *Exp. Math.* **1**, 2 (1992); *ibid*, 141 (1992).
- [126] C. V. Boys, *Soap Bubbles: Their colors and forces which mold them* (Dover: New York, 1958).
- [127] J. J. Bikerman, *Foams: Theory and Industrial Applications* (Reinhold: New York, 1953).
- [128] K. J. Mysels, K. Shinoda, and S. Frankel, *Soap Films: Studies of Their Thinning and a Bibliography* (Pergamon Press: Oxford, 1959).

- [129] D. Weaire, S. Hutzler, G. Verbist, and E. Peters, *Adv. Chem. Phys.* **102**, 315 (1997).
- [130] G. Verbist, and D. Weaire, *Euro. Phys. Lett.* **26**, 631 (1994).
- [131] G. Verbist, D. Weaire, and A. M. Kraynik, *J. Phys: Condens. Matter* **8**, 3715 (1996).
- [132] Y. Jiang and J. A. Glazier, *Phil. Mag. Lett.* **74**, 119 (1996).
- [133] Y. Jiang and J. A. Glazier, *Mat. Res. Soc. Symp. Proc.* **463**, 307 (1997).
- [134] A. Bhakta and E. Ruckenstein, *Adv. Colloid Interface Sci.* **70**, 1 (1997).
- [135] D. Weaire, N. Pittet, S. Hutzler, and D. Pardal, *Phys. Rev. Lett.* **71**, 2670 (1993).
- [136] D. Weaire, S. Findlay and G. Verbist, *J. Phys: Condens. Matter* **7**, L217 (1995).
- [137] A. D. Rudin, *J. Institute Brewing* **63**, 506 (1957).
- [138] E. R. Brierley, P. J. Wilde, A. Onishi, P. S. Hughes, W. J. Simpson and D. C. Clark, *J. Sci. Food Agric.* **70**, 531 (1996).
- [139] S. Hutzler, G. Verbist, D. Weaire and K. A. van der Steen, *Europhys. Lett.* **31**, 497 (1995).
- [140] J. B. German and M. J. McCarthy, *J. Agric. Food Chem.* **37**, 1321 (1989); M. J. McCarthy and E. Perez, *Biotechnol. Prog.* **7**, 540 (1991).
- [141] I. I. Gol'dfarb, K. B. Kann, and I. R . Sreiber, *J. Fluid Dyn.* **23**, 244 (1988).
- [142] A. M. Kraynik, Sandia Report, Sand83-0844 (1983).
- [143] K. B. Kann, *J. Fluid Dynamics*, **22**, 420 (1986); *ibid*, **25**, 236 (1990).
- [144] V. Goldstein, I. Gol'dfarb, and I. Shreiber, *Int. J. Multiphase Flow* **22**, 991 (1996).
- [145] P. A. Hass and H. F. Johnson, *Ind. Eng. Chem. Fund.* **6**, 225 (1967).
- [146] M. V. Ramani, R. Kumar and K. S. Gandhi, *Chem. Eng. Sci.* **48**, 455 (1993).
- [147] A. Bhakta and K.C. Khilar, *Langmuir* **7**, 1827 (1991).
- [148] G. Narsimhan, *J. Food Eng.* **14**, 139 (1991).
- [149] M. A. Fortes and S. Coughlan, *J. Appl. Phys.* **76**, 4029 (1994).
- [150] F. S. Shih and R. Lemlich, *AIChEJ* **11**, 18 (1965).

- [151] D. Weaire, N. Pittet, S. Hutzler and D. Pardal, Phys. Rev. Lett. **71**, 2670 (1993).
- [152] A. Bhakta and E. Ruchenstein, Langmuir **11**, 1486 (1995).
- [153] F. Sebba, *Foams and biliquid foams* (John Wiley & Sons: Aphrons, 1987).
- [154] G. Narsimhan and E. Ruckenstein, in *Foams: Theory, Measurements and Applications*, eds. R. K Prud'homme and S. A Khan, Marcel Dekker: New York, 99 (1995).
- [155] E. Ruckenstein and F. Sun, Ind. Eng. Chem. Res. **34**, 3581 (1995).
- [156] J. S. Park and E. Ruckenstein, J. Appl. Polym. Sci. **38**, 452 (1989).
- [157] A. R. Bhakta and E. Ruckenstein, Langmuir **11**, 1486 (1995).
- [158] A. R. Bhakta and E. Ruckenstein, Langmuir **11**, 4642 (1995).
- [159] A. R. Bhakta and E. Ruckenstein, Langmuir **12**, 3089 (1996).
- [160] E. Ruckenstein and A. R. Bhakta, Langmuir **12**, 4134 (1996).
- [161] P. Sollich, F. Lequeux, P. Hebraud, and M. E. Cates, Phys. Rev. Lett. **78**, 2020 (1997).
- [162] R. K. Prud'homme, Ann. Meet. Soc. Rheol., Lexington, KY (1981).
- [163] H. M. Princen, J. Colloid Interface Sci. **91**, 160 (1983).
- [164] S. A. Khan and R. C. Armstrong, J. Non-Newtonian Fluid Mech. **22**, 1 (1986); S. A. Khan and R. C. Armstrong, *ibid*, **25**, 61 (1987).
- [165] T. Okuzono and K. Kawasaki, Phys. Rev. E **51**, 1246 (1995).
- [166] D. Weaire, F. Bolton, T. Herdtle, and H. Aref, Phil. Mag. Lett. **66**, 293 (1992).
- [167] D. J. Durian, Phys. Rev. E **55**, 1739 (1997).
- [168] Y. Jiang, P. J. Swart, A. Saxena, M. Asipauskas, and J. A. Glazier, Phys. Rev. E, submitted (1998).
- [169] A. M. Kraynik, Ann. Rev. Fluid Mech. **20**, 325 (1988).
- [170] J. Lubliner, *Plasticity Theory* (Macmillan: New York, 1990).
- [171] D. A. Reinelt and A. M. Kraynik, J. Fluid Mech. **215**, 431 (1990).
- [172] S. A. Langer and A. J. Liu, J. Phys. Chem. B **101**, 8667 (1997).
- [173] S. A. Khan, C. A. Schnepper, and R. C. Armstrong, J. Rheol. **31**, 69 (1988).

- [174] L. W. Schwartz and H. M. Princen, J. Colloid Interface Sci. **118**, 201 (1987).
- [175] D. Weaire and M. A. Fortes, Adv. Phys. **43**, 685 (1994).
- [176] H. M. Princen and A. D. Kiss, J. Colloid Interface Sci. **112**, 427 (1986).
- [177] A. D. Gopal and D. J. Durian, Phys. Rev. Lett. **75**, 2610 (1995).
- [178] M. Dennin and C. M . Knobler, Phys. Rev. Lett. **78**, 2485 (1997).
- [179] S. Hutzler, D. Weaire, and H. Bolton, Phil. Mag. B **71**, 277 (1995).
- [180] R. Höhler, S. Cohen-Addad, and H. Hoballah, Phys. Rev. Lett. **79**, 1154 (1997).
- [181] F. Spaepen, Acta Met. **25**, 407 (1997).
- [182] S. S. Park and D. J. Durian, Phys. Rev. Lett. **72**, 3347 (1994).
- [183] F. Elias, C. Flament, J.-C. Bacri, and F. Graner, in *Foams and Emulsions*, eds. J.-F. Sadoc and N. Rivier, (Kluwer: Amsterdam, 1998).
- [184] J. P. Sethna, K. Dahmen, S. Kartha, J. Krumhansl, B. W. Roberts, and J. D. Shore, Phys. Rev. Lett. **70**, 3347 (1993).
- [185] P. Bak, C. Tang, and K. Wiesenfeld, Phys. Rev. Lett. **59**, 381 (1987); Phys. Rev. A **38**, 364 (1988).
- [186] H. J. Jensen, K. Christensen, and H. C. Fogedby, Phys. Rev. B **40**, 7425 (1989); K. Christensen, H. C. Fogedby, and H. J. Jensen, J. Stat. Phys. **63**, 653 (1991).
- [187] T. Hwa and M. Kardar, Phys. Rev. A **45**, 7002 (1992).
- [188] F. Elias, C. Flament, J. A. Glazier, F. Graner, and Y. Jiang, in preparation (1998).
- [189] T. G. Mason and D. A. Weitz, Phys. Rev. Lett. **74**, 1250 (1995).
- [190] A. J. Liu, S. Ramaswanmy, T. G. Mason, H. Gang, and D. A. Weitz, Phys. Rev. Lett. **76**, 3017 (1996).
- [191] P. Hébraud, F. Lequeux, J. P. Munch, and D. J. Pine, Phys. Rev. Lett. **78**, 4657 (1997).
- [192] P. Armstrong, Crit. Rev. Biochem. Molec. Biol. **24**, 119 (1989).
- [193] A. Gierer, S. Berking, H. Bode, C. N. David, G. Hansmann, H. Schaller, and E. Trenkner, Nature New Biol. **239**, 98 (1972).

- [194] F. Glick and H. Bode, in *Hydra: Research Methods*, ed. H. Lenhoff (Plenum: New York, 1983).
- [195] M. J. Caterina and P. M. Devreotes, *FASEB J.* **5**, 3078 (1991).
- [196] W. F. Loomis, private communication (1996).
- [197] J. G. Williams, *Curr. Opin. Genet. Dev.* **1**, 338 (1991).
- [198] W. F. Loomis, *Curr. Top. Dev. Biol.* **28**, 1 (1995).
- [199] J. Rubin and A. Robertson, *J. Embryol. Exp. Morphol.* **33**, 227 (1975).
- [200] J. Darnell, H. Lodish, and D. Baltimore, *Molecular Cell Biology*, (Scientific American Books: New York, 1986).
- [201] M. Steinberg, *Proc. Nat. Acad. Sci. USA* **48**, 1577 (1962).
- [202] M. Steinberg, *Proc. Nat. Acad. Sci. USA* **28**, 1769 (1962).
- [203] M. Steinberg, *Science* **137**, 762 (1962).
- [204] M. Steinberg, *Science* **141**, 410 (1963).
- [205] U. Technau and T. W. Holstein, *Devel. Biol.* **151**, 117 (1992).
- [206] J. A. Glazier and F. Graner, *Phys. Rev. E* **47**, 2128 (1993).
- [207] J. C. M. Mombach, J. A. Glazier, R. C. Raphael, and M. Zajac, *Phys. Rev. Lett.* **75**, 2244 (1995).
- [208] J. C. M. Mombach and J. A. Glazier, *Phys. Rev. Lett.* **76**, 3032 (1996)
- [209] I. Takeuchi, T. Kakutani, and M. Tasaka, *Devel. Genetics* **9**, 607 (1988).
- [210] M. Steinberg, *J. Theor. Biol.* **55**, 431 (1975).
- [211] T. Roigars and J. Sampson, *J. Biol. Med. Comp.* **8**, 45 (1977).
- [212] T. Matela and R. Fletterick, *J. Theor. Biol.* **76**, 403 (1979); *ibid.* **84**, 673 (1980).
- [213] D. Greenspan, *J. Math. Biol.* **12**, 227 (1981).
- [214] F. Graner, *J. Theor. Biol.* **164**, 455 (1993).
- [215] F. Graner and J. A. Glazier, *Phys. Rev. Lett.* **69**, 2013 (1992).
- [216] A. Upadhyaya and J. A. Glazier, in preparation (1998).
- [217] W. F. Loomis, *The Development of Dictyostelium Discoideum*, (Academic Press: New York, 1982).

- [218] B. Varnum, K. B. Edwards, and D. R. Soll, *Dev. Biol.* **113**, 218 (1986).
- [219] D. Wessels, J. Murray, and D. R. Soll, *Cell Motil. Cytoskel.* **23**, 145 (1992).
- [220] F. Siegert and C. J. Weijer, *Current Biology*, **5**, 937 (1995).
- [221] D. Traynor, R. H. Kessin, and J. G. Williams, *Proc. Natl. Acad. Sci. USA* **89**, 8303 (1992).
- [222] C. L. Saxe 3d, G. T. Ginsburg, J. M. Louis, R. Johnson, P. N. Devreotes, and A. R. Kimmel, *Genes and Development* **7**, 262 (1993).
- [223] B. Vasiev, F. Siegert, and C. Weijer, *Phys. Rev. Lett.* **78**, 2489 (1997).
- [224] H. Parnas, and L. A. Segel, *J. Cell Sci.* **25**, 191 (1977).
- [225] S. MacKay, *J. Cell Sci.* **33**, 1 (1978).
- [226] O. O. Vasieva, B. N. Vasiev, V. A. Karpov, and A. N. Zaikin, *J. Theor. Biol.* **171**, 361-367 (1994).
- [227] H. Levine and W. Reynolds, *Phys. Rev. Lett.* **66**, 2400 (1991).
- [228] B. N. Vasiev, P. Hogeweg, and A. V. Panfilov, *73*, 3173 (1994).
- [229] T. Höfer, J. A. Sherratt, and P. K. Maini, *Proc. Roy. Soc. Lond. B* **259**, 249 (1995).
- [230] J. L. Martiel and J. Goldbeter, *C. R. Acad. Sci. Paris III* **298**, 549 (1984).
- [231] J. D. Dallon and H. G. Othmer, *Phil. Trans. Roy. Soc. Lond. B* **352**, 391-417 (1997).
- [232] Y. Jiang, H. Levine, and J. A. Glazier, *Biophys. J.*, in press (1998).
- [233] S. Bozzaro, and E. Ponte, *Experientia* **51**, 1175 (1995).
- [234] H. Levine, L. Tsimring, and D. Kessler, *Physica D* **106**, 375 (1997).
- [235] T. Y. Lam, G. Pickering, J. Geltosky, and C. H. Siu, *Differentiation* **20**, 22 (1981).
- [236] C. Siu, B. D. Roches, and T. Y. Lam, *Proc. Natl. Acad. Sci. USA* **80**, 6596 (1983).
- [237] M. Tasaka, and I. Takeuchi, *Differentiation* **18**, 191 (1981).
- [238] D. Traynor, M. Rasaka, I. Takeuchi, and J. Williams, *Development* **120**, 591 (1994).
- [239] J. Rietdorf, F. Siegert, and C. J. Weijer, *Dev. Biol.* **177**, 427 (1996).

- [240] K. W. Doolittle, I. Reddy, and J. G. McNally, Dev. Biol. **167**, 118 (1995)
- [241] K. A. Kellerman and J. G. McNally, International Dictyostelium Conference abstract (1997).
- [242] K. A. Kellerman and J. G. McNally, preprint (1998).
- [243] B. Wang and A. Kuspa, Science **277**, 251 (1997).
- [244] N. Savill, and P. Hogeweg, J. Theor. Biol. **184**, 229 (1997).
- [245] R. E. Goldstein, Phys. Rev. Lett. **77**, 775 (1995).
- [246] R. A. Foty, C. M. Pfleger, G. Forgacs, and M. S. Steinberg, Development **122**, 1611 (1996).
- [247] J. G. McNally, private communication.
- [248] D. Kessler and H. Levine, Phys. Rev. E **48**, 4801 (1993).
- [249] J. Sternfeld and C. N. David, Differentiation **20**, 10 (1981).
- [250] G. Shaulsky, A. Kuspa, and W. F. Loomis, Genes and Development **9**, 1111 (1995).
- [251] P. R. Fisher, R. Merkl, and G. Gerisch. J. Cell Bio. **108**, 973 (1989).
- [252] D. Soll, D. Wessels, and A. Sylvester, in *Experimental and theoretical advances in biological pattern formation*, eds. H. G. Othmer, P. K. Maini and J. D. Murray, Plenum: London, 325 (1993).
- [253] M. S. Steinberg, Science **141**, 401 (1963).
- [254] P. Agarwal, Comput. Appl. Biosci. **10**, 647 (1994).
- [255] P. Agarwal, Artificial Life **2**, 37 (1995).
- [256] J. C. M. Mombach, R. M. C. de Almeida, and J. R. Iglesias, Phys. Rev. E. **48**, 598 (1993).
- [257] E. Ben-Jacob, A. Tenenbaum, and O. Shochet, Physica A **187**, 378 (1992).
- [258] E. Ben-Jacob, A. Tenenbaum, O. Shochet, and O. Ovidan, Physica A **202**, 1 (1994).
- [259] M. Matsushita, M. Ohgiwari, and T. Matsuyama, in *Growth patterns in physical sciences and biology* (Plenum Press: New York, 1993).
- [260] W. Y. Tam, R. Zeitak, K. Y. Szeto, and J. Stavans, Phys. Rev. Lett. **78**, 1588 (1997).

- [261] B. Levitan and E. Domany, *Europhys. Lett.* **38**, 485 (1997).
- [262] H. J. Ruskin and Y. Feng, *Physica A* **20**, 230 (1996).
- [263] J. J. Chae and M. Tabor, *Phys. Rev E* **55**, 598 (1997).
- [264] B. Levitan and E. Domany, *Phys. Rev. E* **54**, 2766 (1994).
- [265] B. Levitan, E. Slepian, O. Krichevsky, J. Stavans, and E. Domany, *Phys. Rev. Lett.* **73**, 756 (1994).

## BIBLIOGRAPHY

- Abbruzzese, G. (1985). *Computer Simulated Grain Growth Stagnation*. Acta Met. 33: 1329-1337.
- Abbruzzese, G. and K. Lüke (1986). *A Theory of Texture Controlled Grain Growth—I. Derivation and General Discussion of the Model*. Acta Met. 34: 905-914.
- Abbruzzese, G. (1986). *Computer Simulated Stagnation and Abnormal Grain Growth*. Computer Simulation of Microstructural Evolution. Warrendale, The Metallurgical Society: 61-76.
- Abbruzzese, G. and K. Lüke (1986). *A Statistical Theory of Grain Growth Including Texture and Drag Effects and Its Application to Texture Controlled Grain Growth*. Annealing Processes—Recovery, Recrystallization and Grain Growth, Proceedings of the 7th Risø International Symposium on Metallurgy and Materials Science. N. Hansen, D. J. Jensen, T. Leffers and R. B. Roskilde, Risø National Laboratory: 1-14.
- Abbruzzese, G. and K. Lüke (1992). *Theory of Grain Growth in the Presence of Second Phase Particles*. Materials Sci. Forum 94-96: 597-604.
- Abbruzzese, G., I. Heckelmann, and K. Lucke (1992). *Statistical Theory of Two-Dimensional Grain Growth – I. The Topological Foundation*. Acta Met. 40: 519-532.
- Aboav, D. A. and T. G. Langdon (1969). *The Shape of Grains in a Polycrystal*. Metallography 13: 43-58.
- Aboav, D. A. (1970). *The Arrangement of Grains in a Polycrystal*. Metallography 3: 383-390.

- Aboav, D. A. (1971). *The Stability of Grains in a Polycrystal*. Metallography 4: 425-441.
- Aboav, D. A. (1980). *The Arrangement of Cells in a Net*. Metallography 13: 43-58.
- Aboav, D. A. (1992). *The Topology of a Polycrystal in Three Dimensions*. Materials Sci. Forum 94-96: 275-280.
- Adams, C. D., D. J. Srolovitz, and M. Atzmon (1993). *Monte-Carlo Simulation of Phase-separation During Thin-film Codeposition*. J. Appl. Phys. 74: 1707-1715.
- Agishtein, M. E. and A. A. Migdal (1990). *Recursive Sampling of Planar Graphs and Fractal Properties of a Two-dimensional Quantum Gravity*. Int. J. Mod. Phys. C 1: 165-179.
- Agishtein, M. E. and A. A. Migdal (1991). *Geometry of a Two-Dimensional Quantum Gravity: Numerical Study*. Nuc. Phys. B 350: 690-728.
- Agishtein, M. E. and A. A. Migdal (1992). *Numerical Simulations of a Three-Dimensional Quantum Gravity*. Nuc. Phys. B (Proc. Suppl.) 25A: 1-7.
- Agishtein, M. E. and A. A. Migdal (1992). *Simulations of Four-Dimensional Simplicial Quantum Gravity as Dynamical Triangulation*. Mod. Phys. Lett. A 7: 1039-1061.
- Alberts, B., D. Bray, *et al.* (1989). *Molecular Biology of the Cell*. New York, Garland Publishing.
- Almgren, F., W. Browder, and E. H. Lieb (1988). *Co-Area, Liquid- Crystals, and Minimal Surfaces*. Lecture Notes in Mathematics 1306: 1-22.

- Almgren, F., J. E. Taylor, and L. Wang (1993). *Curvature-Driven Flows: A Variational Approach*. SIAM Journal on Control & Optimization 31: 387-437.
- Almgren, F., and J. E. Taylor (1995). *Optimal Geometry in Equilibrium and Growth*. Fractal 3: 713-723.
- Ambjrn, J., B. Durhuus, *et al.* (1985). *Diseases of Triangulated Random Surface Models, and Possible Cures*. Nuc. Phys. B 257: 433-449.
- Andelman, D., F. Brochard, J. F. Joanny (1987). *Phase-Transitions in Langmuir Monolayers of Polar-Molecules*. J. Chem. Phys. 86: 3673-3681.
- Andelman, D., F. Brochard, J. F. Joanny (1987). *Modulated Structures and Competing Interactions in Amphiphilic Monolayers*. Proc. Nat. Acad. Sci. USA 84: 4717-4718.
- Andelman, D., M. E. Cates, D. Roux, and S. A. Safran (1987). *Structure and phase-equilibria of microemulsions*. J. Chem. Phys. 87: 7229-7241.
- Anderson, M. P., D. J. Srolovitz, *et al.* (1984). *Computer Simulation of Grain Growth – I. Kinetics*. Acta Met. 32: 783-791.
- Anderson, M. P., G. S. Grest, and D. J. Srolovitz (1985). *Grain Growth in Three Dimensions: A Lattice Model*. Scripta Met. 19: 225-230.
- Anderson, M. P. (1986). *Simulation of Grain Growth in Two and Three Dimensions*. Annealing Processes– Recovery, Recrystallization and Grain Growth, Proceedings of the 7th Risø International Symposium on Metallurgy and materials Science. N. Hansen, D. J. Jensen, T. Leffers and B. B. Ralph. Roskilde, Risø National Laboratory: 15-34.

- Anderson, M. P., G. S. Grest, *et al.* (1986). *The Microstructural Dynamics of Primary and Secondary Recrystallization*. Computer Simulation of Microstructural Evolution. Warrendale, The Metallurgical Society: 77-93.
- Anderson, M. P., G. S. Grest, *et al.* (1989). *Computer Simulation of Normal Grain Growth in Three Dimensions*. Phil. Mag. B 59: 293-329.
- Andrade, E. N. d. C. and D. A. Aboav (1966). *Grain Growth in Metals of Close Packed Hexagonal Structure*. Proc. Roy. Soc. London 291A: 18-40.
- Andrade, E. N. d. C. and D. A. Aboav (1966). *Grain Growth in Metals of Close-Packed Hexagonal Structure*. Proc. Roy. Soc. London 291A: 18-40.
- Andrade, P. N. and M. A. Fortes (1988). *Distribution of Cell Volumes in a Voronoi Partition*. Phil. Mag. B 58: 671-674.
- Andrienko, Y. A., N. V. Brilliantov, and P. L. Krapivsky (1994). *Pattern-Formation by Growing Droplets : The Touch-and-Stop Model of Growth*. J. Stat. Phys. 75: 507-523.
- anon. (1871). *The Royal Society's Soirée*. Nature 3: 395-396.
- Argon, A. S. and L. T. Shi (1982). *Analysis of Plastic Flow in an Amorphous Soap Bubble Raft by the Use of an Inter-Bubble Potential*. Phil. Mag. A 46: 275-294.
- Arndt, K. and C. Redies (1996). *Restricted Expression of R-Cadherin by Brain Nuclei and Neural Circuits of the Developing Chicken Brain*. J. Comparative Neurology. 373: 373-399.
- Ashby, M. F. and Verrall (1973). *Diffusion-Accommodated Flow and Superplasticity*. Acta Met. 21: 149-163.

- Assink, R. A. A. Caprihan, and E. Fukushima (1988). *Density Profiles of a Draining Foam by Nuclear Magnetic Resonance Imaging*. *AiChE J.* 34: 2077-2079.
- Aste, T. (1995). *Equilibrium and Evolution of Froths Under Topological Constraints*. *Phil. Mag. B* 71: 967-979.
- Aste, T., D. Boose, and N. Rivier (1996). *From One-Cell to the Whole Froth : A Dynamical Map*. *Phys. Rev. E* 53: 6181-6191.
- Aste, T., K. Y. Szato, and W. Y. Tam (1996). *Statistical Properties and Shell Analysis in Random Cellular Structures*. *Phys. Rev. E* 54: 5482-5492.
- Atkinson, H. V. (1988). *Theories of Normal grain Growth in Pure Single Phase Systems*. *Acta Met.* 36: 469-491.
- Atwater, H. A., C. V. Thompson, and H. I. Smith (1988). *Mechanisms for Crystallographic Orientation in the Crystallization of Thin Silicon Films From the Melt*. *J. Mat. Res.* 3: 1232-1237.
- Atwater, H. A. and C. V. Thompson (1988). *Point-Defect Enhanced Grain-Growth in Silicon Thin-Films: The Role of Ion-Bombardment and Dopants*. *Appl. Phys. Lett.* 53: 2155-2157.
- Aubert, J. H., A. M. Kraynik, *et al.* (1986). *Aqueous Foams*. *Sci. Am.* 254: 74-82.
- Avron, J. E. and D. Levine (1992). *Geometry and Foams: 2D Dynamics and 3D Statics*. *Phys. Rev. Lett.* 69: 208-211.
- Aydin, A. and J. M. DeGraff (1988). *Evolution of Polygonal Fracture Patterns in Lava Flows*. *Science* 239: 471-476.

- Babcock, K. L. and R. M. Westervelt (1989). *Topological “Melting” of Cellular Domain Lattices in Magnetic Garnet Films*. Phys. Rev. Lett. 63: 175-178.
- Babcock, K. L. and R. M. Westervelt (1989). *Elements of Cellular Domain Patterns in Magnetic Garnet Films*. Phys. Rev. A 40: 2022-2037.
- Babcock, K. L. and R. M. Westervelt (1990). *Avalanches and Self-Organization in Cellular Magnetic-Domain Patterns*. Phys. Rev. Lett. 64: 2168-2171.
- Babcock, K. L., R. Seshadri, and R. M. Westervelt (1990). *Coarsening of Cellular Domain Patterns in Magnetic Garnet Films*. Phys. Rev. A 41: 1952-1962.
- Bacri, L.-C., A. Cebers, J.-C. Dabadie, S. Neveu, and R. Perzynski (1994). *Threshold and Marginal Curve of Magnetic Faraday Instability*. Europhys. Lett. 27: 437-443.
- Bak, P. and H. Flyvbjerg (1992). *Self-Organization of Cellular Magnetic-Domain Patterns*. Phys. Rev. A 45: 2192-2200.
- Bak, P. and H. Flyvbjerg (1992). *Self-Organization of Magnetic Domain Patterns*. Physica A 185: 3-10.
- Bay, B. and N. Hansen (1986). *Deformed and Recovered Microstructures in Pure Aluminum*. Annealing Processes & Recovery, Recrystallization and Grain Growth, Proceedings of the 7th Risø International Symposium on Metallurgy and Materials Science. N. Hansen, D. J. Jensen, T. Leffers and B. Ralph. Roskilde, Risø National Laboratory: 215-220.
- Beck, P. A. (1954). *Annealing of Cold Worked Metals*. Adv. Phys. 3: 245-324.

- Beenakker, C. W. J. (1986). *Evolution of Two-Dimensional Soap-Film Networks*. Phys. Rev. Lett. 57: 2454-2457.
- Beenakker, C. W. J. (1987). *Two-Dimensional Soap Froths and Polycrystalline Networks: Why are Large Cells Many-Sided?* Physica A 147: 256-267.
- Beenakker, C. W. J. (1988). *Numerical Simulation of Grain Growth in a Two-Dimensional Network*. Phys. Rev. A 37: 1697-1702.
- Beenakker, C. W. J. (1988). *Evolution of Two-Dimensional Soap-Film Networks*. Phys. Rev. A 37: 1697-1704.
- Belanger D. P. and A. P. Young (1991). *The Random Field Ising Model*. J. Magnetism and Mag. Mat. 100: 272-291.
- Bell, G. (1978). *Models For the Specific Adhesion of Cells to Cells*. Science 200: 618-627.
- Bell, G. (1988). *Models of Cell Adhesion Involving Specific Binding: Physical Basis of Cell-Cell Adhesion*. P. Bongrand. Boca Raton, CRC Press: Chap. 10.
- Berg, H. C. (1983). *Random Walks in Biology*. Princeton University Press, New Jersey.
- Berge, B., A. J. Simon, and A. Libchaber (1990). *Dynamics of Sas Bubbles in Monolayers*. Phys. Rev A 41: 6893-6900.
- Berret J. F., D. C. Roux, and G. Porte (1994). *Istropic-to-Nematic Transition in Wormlike Micelles Under Shear*. J. Physique II 4: 1261-1279.
- Bhakta, A. and E. Ruckenstein (1995). *Drainage of a Standing Foam*. Langmuir 11: 1486-1492.

- Bhakta, A. and E. Ruckenstein (1997). *Drainage and Coalescence in Standing Foams*. J. Colloid & Interface Sci. 191: 184.
- Bhakta, A. and E. Ruckenstein (1997). *Decay of Standing Foams: Drainage, Coalescence and Collapse*. Adv. Colloid & Interface Sci. 70: 1-124.
- Billoire, A. and F. David (1986). *Scaling Properties of Randomly Triangulated Planar Random Surfaces*. Nuc. Phys. B 275: 617-640.
- Binder, K. (1977). *Theory for the Dynamics of "Clusters". II. Critical Diffusion in Binary Systems and the Kinetics of Phase Separation*. Phys. Rev. B 15: 4425-4447.
- Blanc, M. and A. Mocellin (1979). *Grain Coordination in Plain Sections of Polycrystals*. Acta Met. 27: 1231-1237.
- Bobeck, A. H. (1967). *Properties and Device Applications of Magnetic Domains in Orthoferrites*. Bell Tech. J. 46: 1901-1925.
- Bode, P. and H. Bode (1984). *Formation of Pattern in Regenerating Tissue Pieces of Hydra Attenuata. III. The Shaping of the Body Column*. Dev. Biol. 106: 315-325.
- Bokstein, B. S., C. V. Kopeczki, et al. (1980). *Thermodynamics and Kinetics of Grain Boundaries in Metals*. Moscow.
- Bokstein, B. S., V. E. Fradkov, and D. L. Beke (1992). *Grain-Boundary Segregation and Grain-Boundary Heterodiffusion*. Phil. Mag. A 65: 277-286.
- Bolling, G. F. and W. C. Winegard (1958). *Grain Growth in Zone-Refined Lead*. Acta Met. 6: 283-287.

- Bolling, G. F. and W. C. Winegard (1958). *Some Effects of Impurities on Grain Growth in Zone-Refined Lead*. Acta Met. 6: 288-292.
- Bolton, F. and D. Weaire (1990). *Rigidity Loss Transition in a Disordered 2D Froth*. Phys. Rev. lett. 65: 3449-3451.
- Bolton, F. and D. Weaire (1991). *The Effects of Plateau Borders in the Two-Dimensional Soap Froth. I. Decoration Lemma and Diffusion Theorem*. Phil. Mag. B 63: 795-809.
- Bolton, F. and D. Weaire (1992). *The Effects of Plateau Borders in the Two-Dimensional Soap Froth. II. General Simulation and Analysis of Rigidity Loss Transition*. Phil. Mag. B 65: 473-478.
- Bons, P. D. and J. L. Urai (1992). *Syndeformational Grain-Growth : Microstructures and Kinetics*. J. Struc. Geo. 14: 1101-1109.
- Bongrand, P., C. Capo, et al. (1979). *Evaluation of Intercellular Adhesion With a Very Simple Technique*. J. Immunol. Meth. 28: 133-141.
- Bongrand, P. and P. Goldstein (1983). *Reproducible Dissociation of Cellular Aggregates With a Wide Range of Calibrated Shear Forces*. J. Immunol. Meth. 58: 209-224.
- Bongrand, P., ed. (1988). *Physical Basis of Cell-Cell Adhesion*. Boca Raton, CRC Press.
- Boots, B. N. (1982). *The Arrangement of Cells in "Random" Networks*. Metallurgy 15: 53-62.
- Boyle, R. (1660). *New Experiments, Physico-Mechanical, Touching the Spring of Air*. Oxford, Oxford.

- Boys, C. V. (1959). *Soap Bubbles: Their Colours and the Forces which Mold Them*. New York, Dover Press.
- Bozzaro, S. and E. Ponte (1995). *Cell Adhesion in the Life Cycle of Dictyostelium*. Experientia 51: 1175-1188.
- Bragg, S. L. (1942). *A Model Illustrating Intercrystalline Boundaries and Plastic Flow in Metals*. J. Sci. Instr. 19: 148-159.
- Bragg, S. L. B. and J. F. Nye (1947). *A Dynamical Model of Crystal Structure*. Proc. Roy. Soc. London A 190: 474-481.
- Brody, D. and N. Rivier (1995). *Geometrical Aspects of Statistical-Mechanics*. Phys. Rev. E 51: 1006-1011.
- Bronsard, L. and F. Reitich (1993). *On 3-Phase Boundary Motion and the Singular Limit of a Vector-Valued Ginzburg-Landau Equation*. Archive For Rational Mechanics and Analysis 124: 355-379.
- Bronsard L, and B. T. R. Wetton (1995). *A Numerical-Method for Tracking Curve Networks Moving With Curvature Motion*. J. Comp. Phys. 120: 66-87.
- Brook, R. J. (1976). *Controlled Grain Growth*. Ceramic Fabrication Processes. eds. F. F. Y. Wang. New York, Academic Press 9: 331-364.
- Browne, M. W. (1990). *Humble Froth Offers Clues to New Materials*. New York Times, New York.
- Bulaevskii, L. N. and S. V. Panjukov (1985). *Domain-Wall Structure and the Properties of the Coexistence Phase in Ferromagnetic Superconductors  $Homo_6S_8$  And  $Homo_6Se_8$* . Solid State Comm. 53: 243-247.

- Bulkley, S. R. (1693). *Concerning the Giant's Causeway,...* Phil. Trans. Roy. Soc. London 17: 708-711.
- Bunge, H. J. and E. Dahlem (1986). *Texture Changes and Growth Anomalies During Continuous Grain Growth.* Annealing Processes– Recovery, Recrystallization and Grain Growth, Proceedings of the 7th Risø International Symposium on Metallurgy and materials Science. N. Hansen, D. J. Jensen, T. Leffers and B. Ralph. Roskilde, Risø National Laboratory: 255-260.
- Burke, J. E. and D. Turnbull (1952). *Recrystallization and Grain Growth.* Prog. Met. Phys. 3: 220-292.
- Burnett G. D, J. J. Chae, W. Y. Tam. R. M. C. de Almeida and M. Tabor (1995). *Structure and Dynamics of Breaking Foams.* Phys. Rev. E 51: 5788-5796.
- Cahn, J. W. (1965). *On Hillert's Grain Growth Catalyst.* Acta Met. 13: 1091-1092.
- Cahn, J. W. (1974). *Topology of Crystal Grains.* Nature 250: 702-703.
- Cahn, J. W. (1989). *Interfacial Free-Energy and Interfacial Stress: The Case of an Internal Interface in a Solid.* Acta Met. 37: 773-854.
- Cahn, J. W. (1991). *Stability, Microstructural Evolution, Grain Growth, and Coarsening in a Two-Dimensional Two-Phase Microstructure.* Acta Met. 39: 2189-2199.
- Cahn, J. W. and E. S. Vanvleck (1996). *Quadrijunctions Do Not Stop 2-Dimensional Grain-Growth.* Acta Met. 34: 909-912.

- Callaghan, P. T. (1993). *Principles of Nuclear Magnetic Resonance Microscopy*. Oxford University Press, New York.
- Calvert, J. R. (1990). *Pressure Drop For Foam Flow Through Pipes*. Int. J. Heat & Fluid Flow 11: 236-241.
- Cape, J. A. and G. W. Lehman (1971). *Magnetic Domain Structures in Thin Uniaxial Plates with Perpendicular Easy Axis*. J. Appl. Phys. 43: 5732-5756.
- Carnal, E. and A. Mocellin (1981). *A Topological Model for Plane Sections of Polycrystals*. Acta Met. 29: 135-143.
- Cashman K. V. and M. T. Mangan (1994). *Physical Aspects of Magmatic Degassing .2. Constraints on Vesiculation Processes From Textural Studies of Eruptive Products*. Rev. Mineralogy. 30: 447-478.
- Caterina, M. J. and P. M. Devreotes. (1991). *Molecular Insights Into Eukaryotic Chemotaxis*, FASEB J. 5: 3078-3085.
- Ceppi, E. A. and O. B. Nasello (1984). *Computer Simulation of Bidimensional Grain Growth*. Scripta Met. 18: 1221-1225.
- Ceppi, E. A. and O. B. Nasello (1986). *Computer Simulation of Grain Boundary Migration (I): The Algorithm*. Computer Simulation of Microstructural Evolution. Warrendale, The Metallurgical Society: 77-93.
- Cerisier, P., S. Rahal, and N. Rivier (1996). *Topological correlations in benard-marangoni convective structures*. Phys. Rev. E 54: 5086-5094.
- Chae, J. J. and M. Tabor (1997). *Dynamics of Foams With and Without Wall Rupture*. Phys. Rev. E 55: 598-610.

- Chen, C. H., J. C. Phillips, *et al.* (1981). *Domain Microscopy in Chalcogenide Alloy Glass Thin Films*. Sol. State Comm. 38: 657-661.
- Childress, S. and K. Percus (1981). *Nonlinear Aspects of Chemotaxis*. Math. Biosci. 56: 217-237.
- Childress, S. (1983). *Models of Cell-Interaction Based on Differential Adhesion*. Ann. Biomedical Eng. 11: 64-65.
- Childress, S. (1984). *Models of Cell-Interaction Based on Differential Adhesion*. J. Biomechanical Eng. 106: 36-41.
- Choy, M., S. Oltjen, D. Ratcliff, M. Armstrong, and P. Armstrong (1993). *Fibroblast Behavior in the Embryonic Chick Heart*. Dev. Dynamics 198: 97-107.
- Cohen-Addad, S., H. Hoballah, and R. Höhler (1998). *Viscoelastic Response of a Coarsening Foam*. Phys. Rev. E 57: 6897-6901.
- Collins, R. and A. Wragg (1977). *Maximum Entropy Histograms*. J. Phys. A 10: 1441-1464.
- Condic, M. L., D. Fristrom, *et al.* (1991). *Apical Cell Shape Changes During Drosophila Imaginal Leg Disc Elongation: A Novel Morphogenetic Mechanism*. Development 111: 22-33.
- Coughlan, S. D. and M. A. Fortes (1993). *Self-Similar Size Distributions in Particle Coarsening*. Scripta Met. 28: 1471-1476.
- Coxeter, H. S. M. (1969). *Introduction to Geometry*. New York, John Wiley and Sons.

- Crain, I. K. (1978). *The Monte-Carlo Generation of Random Polygons*. Comp. and Geosci. 4: 131-141.
- Cross, M. C. and P. C. Hohenberg (1993). *Pattern Formation Outside of Equilibrium*. Rev. Mod. Phys. 65: 851-1112.
- Curtis, A. and C. Wilkinson (1988). *Ambiguities in the Evidence About Cell-Adhesion : Problems With Activation Events and With the Structure of the Cell Contact*. Studiobiophysica 127: 75-82.
- Curtis, A. and J. Lackie, eds. (1991). *Measuring Cell Adhesion*. London, Wiley.
- Cwajna, J., A. Maciejny, *et al.* (1986). *Stereological Criteria of Grain Size Homogeneity*. Annealing Processes– Recovery, Recrystallization and Grain Growth, Proceedings of the 7th Risø International Symposium on Metallurgy and Materials Science, eds. N. Hansen, D. J. Jensen, T. Leffers and B. Ralph. Roskilde, Risø National Laboratory: 273-278.
- Danan, F. and L. Q. Chen (1997). *Computer-Simulation of Grain-Growth and Ostwald Ripening in Alumina-Zirconia 2-Phase Composites*. J. Am. Ceramic Soc. 80: 1773-1780.
- Dan-Sohkawa, M., H. Yamanaka, *et al.* (1986). *Reconstruction of Bipinnaria Larvae From Dissociated Embryonic Cells of the Starfish, Asterina Pectinifera*. J. Embryol. exp. Morph. 94: 47.
- David, F. (1985). *Planar Diagrams, Two-Dimensional Lattice Gravity and Surface Models*. Nuc. Phys. B 257: 45-58.
- David, F. (1985). *A Model of Random Surfaces With Non-Trivial Critical Behaviour*. Nuc. Phys. B 257: 543-576.

- Davis, R. H. (1996). *Hydrodynamic Diffusion of Suspended Particles: A Symposium*. J. Fluid Mech. 310: 325-335.
- de Albuquerque, M. P. and P. Molho (1992). *Memory Effect in a Labyrinth Domain-Structure in Bubble Materials*. J. Magnetism and Magnetic Mat. 113: 132-136.
- de Albuquerque, M. P. and P. Molho (1995). *Evolution of a Magnetic Cellular-Pattern Under Field Cycles*. J. Magnetism and Magnetic Mat. 140: 1869-1870.
- de Almeida, R. M. C. and J. R. Iglesias (1988). *Towards Statistical Mechanics of a 2-D Random Cellular Structure*. J. Phys. A 21: 3365-3377.
- de Almeida, R. M. C. and J. R. Iglesias (1989). *Equilibrium States of 2d Cellular Structures*. Phys. Lett. A. 138: 253-257.
- de Almeida, R. M. C. and J. C. M. Mombach (1997). *Scaling Properties of 3-Dimensional Foams*. Physica A 236: 268-278.
- Deicaza, M., A. Jimenezceniceros, and V. M. Castano (1994). *Statistical Distribution-Functions in 2d Foams*. J. Appl. Phys. 76: 7317-7321.
- Deicazaherrera, M. and V. M. Castano (1995). *Scaling State in Froths Deduced From a Corrected von Neumanns Law*. Physica A 217: 140-145.
- Delannay, R., G. Le Caér, et al. (1992). *Random Cellular Structures Generated From a 2D Ising Ferromagnet*. J. Phys. A: Math. Gen. 25: 6193-6210.
- Delannay, R. and G. Le Caér (1994). *Topological Characteristics of 2D Cellular Structures Generated by Fragmentation*. Phys. Rev. Lett. 73: 1553-1556.

- Delannay, R. and G. Le Caér (1994). *Exact 2-Cell Correlations in Random Cellular Structures Generated From a 2d Ising Ferromagnet*. Physica A 212: 1-11.
- Dennin, M. and C. M. Knobler (1997). *Experimental Studies of Bubble Dynamics in a Slowly Driven Monolayer Foam*. Phys. Rev. Lett. 78: 2485-2488.
- Derrida, B., P. M. C. Deoliveira, and D. Stauffer (1996). *Stable Spins in the Zero-Temperature Spinodal Decomposition of 2d Potts Models*. Physica A 224: 604-612.
- Derrida, B. (1997). *Nontrivial Exponents in Coarsening Phenomena*. Physica D 103: 466-477.
- Desch, C. H. (1919). *The Solidification of Metals from the Liquid State*. J. Inst. Metals 22: 241-263.
- Desmarest, M. (1771). *Mémoire Sur l'Origine & la Nature du Basalte à Grandes Colonnes Polygones, Déterminées par l'Histoire Naturelle de Cette Pierre Observé en Auvergne*. Mem. Acad. Roy. Sci. (Paris) 87: 705-774.
- Dewar, J. (1917). *Soap Bubbles of Long Duration*. Proc. Roy. Inst. Gt. Brit. 22: 179-185.
- Dewar, J. (1923). *Soap Films as Detectors: Stream Lines and Sound*. Proc. Roy. Inst. (London) 24: 197-204.
- Deymire, P. A., J. O. Vasseur, and L. Dobrzknski (1997). *Anomalous Exponent in the Kinetics of Grain-Growth With Anisotropic Interfacial Energy*. Phys. Rev. B 55: 205-211.

- di Meglio, J.-M. and P. Baglioni (1994). *Local Dynamics of Foam Drainage Investigated by ESR*. J. Phys: Condens. Matter 6: A375-A380.
- Doherty, R. D. (1975). *Discussion of ‘Mechanism of Steady State Grain Growth in Aluminum’*. Met. Trans. 6A: 588-589.
- Doherty, R. D., D. J. Srolovitz, *et al.* (1987). *On the Volume Fraction Dependence of Particle Limited Grain Growth*. Scripta Met. 21: 675-679.
- Doherty, R. D., Kang Li, *et al.* (1990). *Modelling of Recrystallization Kinetics and Particle Limited Grain Boundary Motion*. Recrystallization '90. T. Chandra. Warrendale, The Metallurgical Society: 129-150.
- Donald, A. M. (1994). *Physics of Foodstuffs*. Rep. Prog. Phys. 57: 1081-1135.
- Doolittle, K. W., I. Reddy, and J. G. McNally. (1995). *3-D Analysis of Cell Movement During Normal and Myosin-II-null Cell Morphogenesis In Dictyostelium*. Dev. Biol. 167: 118-129.
- Dormer, K. J. (1980). *Foundamental Tissue Geometry for Biologists* Cambridge, Cambridge University Press.
- Drollet, J. P. and A. Galabois (1968). *The Impurity-Drag Effect on Grain Growth*. Acta Met. 16: 1387-1399.
- Druyvesteyn, W. F. and J. W. F. Derleijn (1971). *Calculations on Some Periodic Magnetic Domain Structures; Consequences for Bubble Devices*. Philips Res. Repts. 26: 11-28.
- Dubertret, B. and N. Rivier (1997). *The Renewal of the Epidermis : A Topological Mechanism*. Biophys. J. 73: 38-44.

- Dubertret, B., N. Rivier, and M. A. Peshkin (1998). *Long-Range Geometrical Correlations in 2-Dimensional Foams*. J. Phys. A 31: 879-900.
- Dudek, M. R., J. F. Gouyet, and M. Kolb (1998). *Q+1 State Potts-Model o Late-Stage Sintering*. Surf. Sci. 401: 220-226.
- Dunn, C. G. and J. L. Walter (1966). *Secondary Recrystallization*. Chapter 10 in Recrystallization, Grain Growth and Textures. Metals Park, OH, ASM: 461-521.
- Dunn, C. G. (1966). *Some Implications of Mullins' Steady State Solution for Grain Boundary Migration in Sheet Material*. Acta Met. 14: 221-222.
- Durian, D. J., K. Abeywuriya, S. K. Watson, and C. Franck (1990). *Capillary Behavior of Binary-Liquid Mixtures Near Criticality : Rise and Kinetics*. Phys. Rev. A 42: 4724-4734.
- Durian, D. J., D. A. Weitz, and D. J. Pine (1990). *Dynamics and Coarsening in Three-Dimensional Foams*. J. Phys.: Condensed Matter 2: SA433-SA436.
- Durian, D. J., D. A. Weitz, and D. J. Pine (1991). *Multiple Light-Scattering Probes of Foam Structure and Dynamics*. Science 252: 686-688.
- Durian, D. J., D. A. Weitz, and D. J. Pine (1991). *Scaling Behavior in Shaving Cream*. Phys. Rev. A 44: R7902-R7905.
- Durian, D. J. (1994). *Relaxation in Aqueous Foams*. MRS Bulletin. 19: 20-23.
- Durian, D. J. (1995). *Accuracy of Diffusing-Wave Spectroscopy Theories*. Phys. Rev. E 51: 3350-3358.
- Durian, D. J. (1995). *Foam Mechanics at the Bubble Scale*. Phys. Rev. Lett. 75: 4780-4783.

- Durian, D. J. (1997). *Fast, Nonevolutionary Dynamics in Foams*. Curr. Opinion in Colloid & Interface Sci. 2: 615-621.
- Durian, D. J. (1997). *Bubble-Scale Model of Foam Mechanics : Melting, Non-linear Behavior, and Avalanches*. Phys. Rev. E 55: 1739-1751.
- Earnshaw, J. C. and A. H. Jaafar (1994). *Diffusing-Wave Spectroscopy of a Flowing Foam*. Phys. Rev. E 49: 5408-5411.
- Earnshaw, J. C. and D. J. Robinson (1995). *Inter-Cluster Scaling in Two-Dimensional Colloidal Aggregation*. Physica A 214: 23-51.
- Edelman, G. and J.-P. Thiery, eds. (1985). *The Cell in Contact*. New York, Wiley.
- Edwards, S. F. and K. D. Pithia (1994). *The Evolution of Liquid Foams*. Physica A 205: 548-564.
- Edelman, G. M., B. A. Murray, *et al.* (1987). *Cellular Expression of Liver and Neural Cell Adhesion Molecules After Transfection With Their cDNAs Results in Specific Cell-Cell Binding*. Proc. Natl. Acad. Sci. USA 84: 8502-8506.
- Edelman, G. (1988). *Morphoregulatory Molecules*. Biochemistry 27: 3533-3543.
- Eichelkraut, H., K. Lücke, *et al.* (1986). *Texture Controlled Grain Growth in Cu-Zn and Al-Mg Alloys*. Annealing Processes– Recovery, Recrystallization and Grain Growth, Proceedings of the 7th Risø International Symposium on Metallurgy and Materials Science. N. Hansen, D. J. Jensen, T. Leffers and B. Ralph. Roskilde, Risø National Laboratory: 303-308.

- Elias, F., C. Flament, J.-C. Bacri, O. Cardoso, and F. Graner (1997). *2-Dimensional Magnetic Liquid Froth: Coarsening and Topological Correlations*. Phys. Rev. E 56: 3310-3318.
- Elias, F., C. Flament, J.-C. Bacri, and S. Neveu (1997). *Macro-Organized Patterns in Ferrofluid Layer: Experimental Studies*. J. Physique I 7: 711-728.
- Elias, F., C. Flament, J.-C. Bacri, and F. Graner (1998). *Two Dimensional Magnetic Liquid Froth*, in Foams and Emulsions. eds. J. F. Sadco and N. Rivier. Netherlands, Kluwer.
- Enomoto, Y., K. Kawasaki, *et al.* (1989). *Two Dimensional Vertex Model with Local Friction Coefficient*. Int. J. Mod. Phys. B 3: 163-169.
- Enomoto, Y. and R. Kato (1989). *Pattern Evolutions in Quenched Systems With a Complex Scalar Order Parameter*. Phys. Letts. A 142: 256-260.
- Enomoto, Y. and R. Kato (1990). *A Model Simulation Study of Domain Growth in a System With Multiply Degenerate Ordered States*. J. of Phys. Condense. Matter 2: 9215-9220.
- Enomoto, Y. and R. Kato (1990). *Scaling Behavior of 2-Dimensional Vertex Model For Normal Grain-Growth*. Acta Met. 38: 765-769.
- Epp, L., I Smid, and P. Tardent (1985). *THE Mesoglea of Hydra is Synthesized by Both Ectoderm and Endoderm*. Am. Zool. 25: A100-A100.
- Epp, L., I. Smid, and P. Tardent (1986). *Synthesis of the Mesoglea by Ectoderm and Endoderm in Reassembled Hydra*. J. Morphol. 189: 271-279.
- Eschenfelder, A. H. (1980). *Magnetic Bubble Technology*. Berlin, Springer Verlag.

- Ettensohn, C. A. (1984). *Primary Invagination of the Vegetal Plate During Sea Urchin Gastrulation*. Am. Zool 24: 571-588.
- Ettensohn, C. A. (1985). *Mechanisms of Epithelial Invagination*. Q. Rev. Biol. 60: 289-307.
- Ettensohn, C. A. and D. R. McClay (1986). *The Regulation of Primary Mesenchyme Cell-Migration in the Sea-Urchin Embryo: Transplantations of Cells and Latex Beads*. Dev. Biol. 117: 380-391.
- Ettensohn C. A. and D. R. McClay (1988). *Cell Lineage Conversion in the Sea-Urchin Embryo*. Dev. Biol. 125: 396-409.
- Fan, D. A, and L. Q. Chen (1997). *Diffuse-Interface Description of Grain-Boundary Motion*. Phil. Mag. Lett. 75: 187-196.
- Fan, D. N., L. Q. Chen, and S. P. Chen (1997). *Effect of Grain-Boundary Width on Grain-Growth in a Diffuse-Interface Field Model*. Mat. Sci. Eng. A 238: 78-84.
- Fan, D. N. and L. Q. Chen (1997). *Topological Evolution During Coupled Grain-Growth and Ostwald Ripening in Volume-Conserved 2-D 2-Phase Polycrystals*. Acta Mat. 45: 4145-4154.
- Fan, D. N. C. W. Geng, and L. Q. Chen (1997). *Computer-Simulation of Topological Evolution in 2-D Grain-Growth Using a Continuum Diffuse-Interface Field Model*. Acta Mat. 45: 1115-1126.
- Feltham, F. (1957). *Grain Growth in Metals*. Acta Met. 5:97-105.
- Ferro, A. C. and M. A. Fortes (1997). *The Elimination of Grains and Grain-Boundaries in Grain-Growth*. Interface Sci. 5: 263-278.

- Findlay, S. (1997). *Experimental Probes of Liquid Foams*. Ph.D. thesis, University of Dublin.
- Fisher, P. R., R. Merkl, and G. Gerisch (1989). *Quantitative Analysis of Cell Motility and Chemotaxis in Dictyostelium Discoideum by Using an Image Processing System and a Novel Chemotaxis Chamber Providing Stationary Chemical Gradients*. J. Cell Bio. 108: 973-984.
- Flam, F. (1989). *Frothy Physics*. Science News 136: 72-75.
- Flesselles, J.-M., M. O. Magnasco, and A. Libchaber (1991). *From Disks to Hexagons and Beyond: A Study in Two Dimensions*. Phys. Rev. lett. 67: 2489-2492.
- Flyvbjerg, H. and C. Jeppesen (1991). *A Solvable Model for Coarsening Soap Froths and Other Domain Boundary Networks in 2 Dimensions*. Physica Scripta T38: 49-54.
- Flyvbjerg, H. (1993). *Dynamics of Soap Froth*. Physica A 194: 298-306.
- Flyvbjerg, H. (1993). *Model for Coarsening Froths and Foams*. Phys. Rev. E 47: 4037-4054.
- Foley, S. (1694). *An Account of the Giants Causeway in the North of Ireland*. Phil. Trans. Roy. Soc. London 18: 169-182.
- Fontanari, J. F. and W. K. Theumann (1986). *Effects of Trilinear Symmetry Breaking on the Potts-Model Transition of Uniaxially Stressed  $SrTiO_3$* . Phys. Rev. B 33: 3530-3533.
- Fortes, M. A. and A. C. Ferro (1985). *Topology and Transformation in Cellular Structures*. Acta Met. 33: 1697-1708.

- Fortes, M. A. and A. C. Ferro (1985). *Trivalent Polyhedra: Properties, Representation and Enumeration*. Acta Met. 33: 1683-1696.
- Fortes, M. A. (1986). *The Average Rate of Growth of Individual Cells in a Cellular Structure: Effect of the Number of Topological Elements*. J. Mat. Sci. 21: 2509-2513.
- Fortes, M. A. and M. T. Nogueira (1989). *The Poisson Effect in Cork*. Mat. Sci. Eng. A 122: 227-232.
- Fortes, M. A. and P. N. Andrade (1989). *The Arrangement of Cells in 3- and 4-Regular Planar Networks Formed by Random Straight Lines*. J. de physique 50: 717-724.
- Fortes, M. A. and P. N. Andrade (1989). *Topological Properties of Cellular Structures Based on the Staggered Packing of Prisms*. J. de physique 50: 725-731.
- Fortes, M. A., J. J. Fernandes, I. Serralheiro, and M. E. Rosa (1989). *Experimental Determination of Hydrostatic Compression Versus Volume Change Curves for Cellular Solids*. Journal of Testing and Evaluation 17: 67-71.
- Fortes, M. A. and M. E. Rosa (1992). *Growth Stresses and Strains in Cork*. Wood Sci. Techn. 26: 241-258.
- Fortes, M. A. (1993). *Applicability of Aboav's rule to a three-dimensional Voronoi partition*. Phil. Mag. Lett. 68: 69-71.
- Fortes, M. A. and P. Pina (1993). *Average topological properties of successive neighbors of cells in random networks*. Phil. Mag. B 67: 263-276.

- Fortes, M. A. and P. Pina (1993). *Average Topological Properties of Successive Neighbors of Cells in Random Networks*. Phil. Mag. B 67: 263-276.
- Fortes, M. A. and S. Coughlan (1994). *Simple-Model of Foam Drainage*. J. Appl. Phys. 76: 4029-4035.
- Fortes, M. A. (1994). *On the Existence of a Scaling Relation in the Evolution of Cellular Systems*. Acta Met. 42: 1643-1651.
- Fortes, M. A. (1994). *Applicability of Aboav Rule to a 3-Dimensional Voronoi Partition*. Phil. Mag. Lett. 68: 69-71.
- Fortes, M. A. (1995). *Applicability of Lewis' and Aboav-Weaire Laws to 2D and 3D Cellular Structures Based on Poisson Partitions*. J. Phys. A 28: 1055-1068.
- Fortes, M. A. (1995). *The Thermal Expansion of Liquid Foam*. Langmuir 11:639-642.
- Fortes, M. A. and A. M. Deus (1995). *Expansion of a Foam Due to Absorption of an Outside Gas*. J. Colloid Interface Sci. 176: 248-255.
- Fortes, M. A. (1997). *The Kinetics of Grain-Growth in the Scaling and Transient Regimes*. Scripta Met. 37: 679-684.
- Fortes, M. A., M. E. Rosa, S. Findlay, and M. Guedes (1998). *Development of Bamboo Structure in a Foam: The Kinetics of Foam Coarsening*. Phil. Mag. A 77: 257-265.
- Foty, R. A., C. M. Pfleger, G. Forgacs and M. S. Steinberg. (1996). *Surface Tensions of Embryonic Tissues Predict Their Mutual Development Behavior*. Development 122: 1611-1620.

- Fradkov, V. E., A. S. Kravchenko, *et al.* (1985). *Experimental Investigation of Normal Grain Growth in Terms of Area and Topological Class.* Scripta Met. 19: 1291-1296.
- Fradkov, V. E., L. S. Shvindlerman, *et al.* (1985). *Computer Simulation of Grain Growth in Two Dimensions.* Scripta Met. 19: 1285-1290.
- Fradkov, V. E., L. S. Shvindlerman, *et al.* (1987). *Short Range Order in the Arrangement of Grains in a Two-Dimensional Polycrystal.* Phil. Mag. Lett. 55: 289-294.
- Fradkov, V. E. (1988). *A Theoretical Investigation of Two-Dimensional Grain Growth in the “Gas” Approximation.* Phil. Mag. Let. 58: 271-275.
- Fradkov, V. E., D. G. Udler, and R. E. Kris (1988). *Computer Simulation of Two-Dimensional Normal Grain Growth (the “Gas” Approximation).* Phil. Mag. Lett. 58: 277-283.
- Fradkov, V. E. and D. G. Udler (1989). *Normal Grain Growth in 2-D Polycrystals.* Academy of Sciences of the USSR, the Institute of Solid State Physics, Chernogolovka.
- Fradkov, V. E. and D. Udler (1990). *Uniform Boundary Model for Two-Dimensional Grain Growth.* Simulation and Theory of Evolving Microstructure. eds. M. P. Anderson and A. D. Rollett. Warrendale, The Metallurgical Society: 15-30.
- Fradkov, V. E. (1992). *Main Regularities of 2-D Grain Growth.* Mat. Sci. Forum 94-96: 269-274.
- Fradkov, V. E., M. E. Glicksman, *et al.* (1992). *Topological Stability of 2-D*

*Vanishing Grains.* Computational Methods in Materials Science, San Francisco, California, MRS.

- Fradkov, V. E., M. E. Glicksman, M. Palmer, J. Nordberg, and K. Rajan (1993). *Topological Rearrangements During 2d Normal Grain-Growth.* Physica D 66: 50-60.
- Fradkov, V. E., M. O. Magnasco, D. Ulller, and D. Weaire (1993). *Determinism and Stochasticity in Ideal 2-Dimensional Soap Froths.* Phil. Mag. Lett. 67: 203-211.
- Fradkov, V. E. and D. Ulller (1994). *2-Dimensional Normal Grain-Growth : Topological Aspects.* Adv. Phys. 43: 739-789.
- Fradkov, V. E., S. S. Mani, M. E. Glicksman, J. R. Rogers, J. P. Downey, W. K. Witherow, B. R. Facemire, and D. O. Frazier (1994). *Coarsening of 3-Dimensional Droplets by 2-Dimensional Diffusion .2. Theory.* J. Elec. Mat. 23: 1007-1013.
- Fradkov, V. E. (1994). *Rapid Liquid-Metal Corrosion Along Grain-Boundaries.* Scripta Met. 30: 1599-1603.
- Fradkov, V. E., M. E. Glicksman, M. Palmer, and K. Rajan (1994). *Topological Events in 2-Dimensional Grain-Growth: Experiments and Simulations.* Acta Met. 42: 2719-2727.
- Fradkov, V. E., M. E. Glicksman, and S. P. Marsh (1996). *Coarsening Kinetics in Finite Clusters.* Phys. Rev. E 53: 3925-3932.
- Francis, G., L. Fischer, *et al.* (1987). *Direct Measurement of Cell Detachment Force on Single Cells Using a New Electro-Mechanical Method.* J. Cell Sci. 87: 519-523.

- Friedlander, D. R., R.-M. Mége, *et al.* (1989). *Sorting Out is Modulated by Both the Specificity and Amount of Different Cell Adhesion Molecules (CAMs) Expressed on Cell Surfaces*. Proc. Natl. Acad. Sci. USA 86: 7043-7047.
- Fristrom, D. (1976). *The Mechanism of Evagination of Imaginal Discs of Drosophila Melanogaster. III Evidence for Cell Rearrangement*. Dev. Biol. 54: 163-171.
- Fristrom, D. and J. W. Fristrom (1982). *Cell-Surface Binding-Sites for Peanut Agglutinin in the Differentiating Eye Disk of Drosophila*. Dev. Biol. 92: 418-427.
- Fristrom, D. (1982). *Septate Junctions in Imaginal Discs of Drosophila: a Model for the Redistribution of Septa During Cell Rearrangement*. J. Cell Biol. 94: 77-87.
- Fristrom, D. (1988). *The Cellular Basis of Epithelial Morphogenesis. A Review*. Tissue & Cell 20: 645-690.
- Frost, H. J. and F. Spaepen (1982). *Hard-Sphere Models for the Structure of Grain-Boundaries*. J. Physique I 43: 73-82.
- Frost, H. J. (1982). *The geometry of Cavities in Dense Random Packings*. J. Met. 34: 10-10.
- Frost, H. J. (1982). *Cavities in Dense Random Packings*. Acta Met. 30: 889-904.
- Frost, H. J., J. Whang, *et al.* (1986). *Modeling of Grain Growth in Thin Films*. Annealing Processes— Recovery, Recrystallization and Grain Growth,

Proceedings of the 7th Risø International Symposium on Metallurgy and Materials Science. N. Hansen, D. J. Jensen, T. Leffers and B. Ralph. Roskilde, Risø National Laboratory: 315-320.

- Frost, H. J. and C. V. Thompson (1986). *Microstructural Evolution in Thin Films*. Computer Simulation of Microstructural Evolution. Warrendale, The Metallurgical Society: 33-47.
- Frost, H. J. and C. V. Thompson (1987). *The Effect of Nucleation Conditions on the Topology and Geometry of Two-Dimensional Grain Structures*. Acta Met. 35: 529-540.
- Frost, H. J. (1987). *Grain Boundary Ordering Configurations in the  $LI_2$  or  $Ni_3Al$  Structure*. Acta Met. 35: 519-527.
- Frost, H. J. and C. V. Thompson (1987). *Development of Microstructure in Thin Films*. S.P.I.E. 821: 77-87.
- Frost, H. J., C. V. Thompson (1988). *Computer-Simulation of Microstructural Evolution in Thin-Films*. J. Elec. Mat. 17: 447-458.
- Frost, H. J. (1988). *Grain Boundary Structure and the Effect of Boron in  $Ni_3Al$* . Acta Met. 36: 2199-2211.
- Frost, H. J., C. V. Thompson, C. L. Howe, and J. H. Whang (1988). *A Two-Dimensional Computer Simulation of Capillaity Driven Grain Growth: Preliminary Results*. Scripta Met. 22: 65-70.
- Frost, H. J., C. V. Thompson, and D. T. Walton (1990). *Simulation of Thin-Film Grain Structures .1. Grain-Growth Stagnation*. Acta Met. 38: 1455-1462.

- Frost, H. J., C. V. Thompson, and D. T. Walton (1991). *Grain Growth Stagnation and Abnormal Grain Growth in Thin Films*. Simulation and Theory of Evolving Microstructures, eds. M. P. Anderson and A. D. Rollet. Warrendale, The Metallurgical Society: 31-39.
- Frost, H. J. (1992). *Abnormal Grain Growth in Thin Films Due to Anisotropy of Free-Surface Energies*. Mat. Sci. Forum 94-96: 543-550.
- Frost, H. J., C. V. Thompson, and D. T. Walton (1992). *Simulation of Thin Film Grain Structures: II. Abnormal Grain Growth*. Acta Met. 40: 779.
- Frost, H. J. (1994). *Microstructural Evolution in Thin-Films*. Materials Charaterization. 32: 257-273.
- Frost, H. J. and C. V. Thompson (1996). *Computer-Simulation of Grain-Growth*. Curr. Opinion in Solid State & Mat. Sci. 1: 361-368.
- Fu, T. (1988). *A Study of Two-Dimensional Soap Froths*, M.S. Thesis, Trinity College, Dublin.
- Fuchizaki, K. and K. Sawasaki (1995). *Time Evolution of 3-Dimensional Cellular-Systems: Computer Modeling Based on Vertex-Type Models*. Physica A 221: 202-215.
- Fuchizaki, K., T. Kusaba, and K. Sawasaki (1995). *Computer Modeling of 3-Dimensional Cellular-Pattern Growth*. Phil. Mag. B 71: 333-357.
- Fuchizaki, K., and K. kawasaki (1996). *3-Dimensional Computer Modeling of Grain-Growth: A Vertex Model Approach*. Mat. Sci. Forum 204: 267-278.
- Fukushima, E. and A. Ookawa (1953). *Observation of the Grain Boundary in Soap Bubble Raft Part I. Static Feature of the Grain Boundary*. J. Phys. Soc.

Jap. 8: 609-614.

- Fukushima, E. and A. Ookawa (1953). *On the Dynamical Behavior of the Grain Boundary in Soap Bubble Raft Under Shear Stress*. J. Phys. Soc. Jap. 8: 280-282.
- Fukushima, E. and A. Ookawa (1953). *The Transition Structure of the Grain Boundary Observed in Soap Bubble Raft*. J. Phys. Soc. Jap. 8: 129-130.
- Fukushima, E. and A. Ookawa (1954). *Observation of the Grain Boundary in Soap Bubble Raft Part II. Dynamical Behaviour of the Grain Boundary*. J. Phys. Soc. Jap. 9: 44-51.
- Fukushima, E. and A. Ookawa (1955). *Some Characters of the Soap Bubble Raft in a Vibrating State*. J. Phys. Soc. Jap. 10: 970-981.
- Fukushima, E. and A. Ookawa (1957). *Observation of the Grain Boundary in Soap Bubble Raft Part III. The Grain Boundary in Vibrating State*. J. Phys. Soc. Jap. 10: 139-146.
- Fullman, R. L. (1952). *Boundary Migration During Grain Growth*. Metal Interfaces. Cleveland, American Society for Metals: 179-207.
- Gaines, G. L. (1966). *Insoluble Monolayers at Liquid-Gas Interfaces*. New York, Interscience.
- Galina, A. V., V. E. Fradkov, et al. (1987). *Influence of Grain Ternary Joint Mobility on Boundary Migration*. Phys. Met. Metall. 63: 165-168.
- Gardner, M. (1986). *Mathematical Games*. Sci. Am. 254: 16-23.

- Gaultier, L. (1813). *Mémoire Sur les Moyens Généraux de Construire Graphiquement un Cercle Déterminé par Trois Conditions, et une Sphère Déterminée par Quatre Conditions*. Journal de l'Ecole Polytechnique 16: 124-214.
- German, J. B. and M. J. McCarthy (1989). *Stability of Aqueous Foams: Analysis Using Magnetic Resonance Imaging*. J. Agric. Food Chem. 37: 1321-1324.
- Getis, A. and B. Boots (1978). *Models of Spatial Processes: An Approach to the Study of Point, Line and Area Patterns*. Cambridge, Cambridge University Press.
- Gibson, L. and M. F. Ashby (1988). *Cellular Solids: Structure and Properties*. Cambridge, Cambridge University Press.
- Gibson, L. and M. F. Ashby (1997). *Cellular Solids: Structure and Properties - 2nd ed.*. Cambridge, Cambridge University Press.
- Gierer, A., S. Berking, *et al.* (1972). *Regeneration of Hydra From Reaggregated Cells*. Nature New Biol. 239: 98-101.
- Gilbert, E. N. (1962). *Random Subdivisions of Space into Crystals*. Ann. Math. Stat. 33: 958-972.
- Gill, S. P. A. and A. C. F. Cocks (1996). *A variational approach to 2-dimensional grain-growth. 2. numerical results*. Acta Mat. 44: 4777-4789.
- Gladstone (1857). *Notes on Froth*. Phil. Mag. 14: 314-315.
- Glazier, J. A., S. P. Gross, *et al.* (1987). *Dynamics of Two-Dimensional Soap Froth*. Phys. Rev. A 36: 306-312.
- Glazier, J. A. and J. Stavans (1989). *Non-Ideal Effects in the Two Dimensional Soap Froth*. Phys. Rev. A 40: 7398-7401.

- Glazier, J. A. (1989). *The Dynamics of Two Dimensional Cellular Patterns*, Ph.D. Thesis, University of Chicago.
- Glazier, J. A., M. P. Anderson, and G. S. Grest (1990). *Coarsening in the Two Dimensional Soap Froth and the Large-Q Potts Model: A Detailed Comparison*. Phil. Mag. B 62: 615-645.
- Glazier, J. A., G. S. Grest, (1990). “Ideal” Two Dimensional Grain Growth. Simulation and Theory of Evolving Microstructures. eds. M. P. Anderson and A. D. Rollet. Warrendale, The Metallurgical Society: 41-55.
- Glazier, J. A. and D. Weaire (1992). *The Kinetics of Cellular Patterns*. J. Phys. Condens. Matter 4: 1867-1894.
- Glazier, J. A. (1993). *Cellular Patterns*. Bussei Kenkyu 58: 608-612.
- Glazier, J. A. and F. Graner (1993). *Simulation of the Differential-Adhesion Driven Rearrangement of Biological Cells*. Phys. Rev. E 47: 2128-2154.
- Glazier, J. A. (1993). *Grain Growth in Three Dimensions Depends on Grain Topology*. Phys. Rev. Lett. 70: 2170-2173.
- Glazier, J. A. and D. Weaire (1994). *Construction of Candidate Minimal Surface Area Space Filling Partitions*. Phil. Mag. Lett. 70: 351-356.
- Glicksman, M. E. and S. P. Marsh (1986). *Microstructural Coarsening in 2- and 3-Dimensions—Applications of Multiparticle Diffusion Algorithms*. Computer Simulation of Microstructural Evolution. Warrendale, The Metallurgical Society: 109-124.
- Glicksman, M. E., K. Rajan, *et al.* (1992). *Experimental and Theoretical Study of 2D Grain Growth in Succinonitrile*. Mat. Sci. Forum 94-96: 909-914.

- Glicksman, M. E., M. B. Koss, V. E. Fradkov, M. E. Rettenmayr, and S. S. Mani (1994). *Quantification of crystal morphology*. J. Crystal Growth. 137: 1-11.
- Godfrey, A. W. and J. W. Martin (1995). *Some Monte-Carlo Studies of Grain-Growth in a Temperature-Gradient*. Phil. Mag. A 72: 737-749.
- Goel, N. and A. Leith (1970). *Self-sorting of Anisotropic Cells*. J. Theor. Biol. 28: 469-482.
- Goel, N., R. Campbell, *et al.* (1970). *Self-Sorting of Isotropic Cells*. J. Theor. Biol. 28: 423-468.
- Goel, N. and G. Rogers (1978). *Computer Simulation of Engulfment and Other Movements of Embryonic Tissues*. J. Theor. Biol. 71: 103-140.
- Goicoechea, J. and J. Ortin (1995). *A Random-Field 3-State Spin Model to Simulate Hysteresis and Avalanches in Martensitic Transformations*. J. Physique IV 5: 71-76.
- Gol'dfarb, I. I., K. B. Kann, and I. R. Shreiber (1988). *Liquid Flow in Foams*. Fluid dynamics. 23: 224-249.
- Goldschein, V., I. Gol'dfarb, and I. Shreiber (1996). *Drainge Waves Structure in Gas-Liquid Foam*. Int. J. Multiphase Flow. 22: 991-1003.
- Goldstein, R. E. (1995). *Traveling-Wave Chemotaxis*. Phys. Rev. Lett. 77: 775-778.
- Gonatas, C. P., J. S. Leigh, A. G. Yodh, J. A. Glazier and B. Prause (1995). *Magnetic Resonance Images of Coarsening Inside a Foam*. Phys. Rev. Lett. 75: 573-576.

- Goodrich, K., A. Yoshimura, and R. K. Prod'homme (1989). *Measurement of the Mudulus and Yield Strength of Soft Gels: Experiments and Numerical Simulation*. J. Rheol. 33: 317-327.
- Gopal, A. D. and D. J. Durian (1995). *Nonlinear Bubble Dynamics in a Slowly Driven Foam*. Phys. Rev. Lett. 75: 2610-2613.
- Gopal, A. D. and D. J. Durian (1997). *Fast Thermal Dynamics in Aqueous Foams*. J. Opt. Soc. Am. A 14: 150-155.
- Gordon, R., N. S. Goel, *et al.* (1972). *A Rheological Model Sufficient to Explain the Kinetics of Cell-Sorting*. J. Theor. Biol. 37: 43-73.
- Goryachev, S. B. (1997). *Kinetics, Hydrodynamics and Stochastodynamics of Cellular Structure Coarsening*. Mod. Phys. Lett. 11: 949-961.
- Graf, L. and A. Gierer (1980). *Size, Shape and Orientation of Cells in Budding Hydra and Regulation of Regeneration of Cell Aggregates*. Wilhelm Roux Arch. Dev. Biol. 188: 141-151.
- Graham, D. J. P. Magdalinos, and D. Pimentel (1997). *Detergent Foam Images as Analogue/Digital Model Fluids: 1. Phase-Behavior and Effective Pair Potentials*. J. Phys. Chem. B 101: 11204-11211.
- Graner, F. and J. A. Glazier (1992). *Simulation of Biological Cell Sorting Using a Two-Dimensional Extended Potts Model*. Phys. Rev. Lett. 69: 2013-2016.
- Graner, F. (1993). *Can Surface Adhesion Drive Cell-rearrangement? Part I: Biological Cell-sorting*. J. Theor. Biol. 164: 455-476.

- Graner, F. and Y. Sawada (1993). *Can Surface Adhesion Drive Cell Rearrangement? Part II: A Geometrical Model.* J. Theor. Biol. 164: 477-506.
- Graustein, W. C. (1931). *On the Average Number of Sides of Polygons of a Net.* Ann. of Math. 32: 149-153.
- Greenspan, D. (1981). *A Classical Molecular Approach to Computer Simulation of Biological Sorting.* J. Math. Biol. 12: 227-235.
- Grest, G. S., D. J. Srolovitz, and M. P. Anderson (1985). *Computer Simulation of Grain Growth-IV. Anisotropic Grain Boundary Energies.* Acta Met. 33: 509-520.
- Grest, G. S., M. P. Anderson, *et al.* (1986). *Computer Simulation of Microstructural Dynamics.* Computer Simulation of Microstructural Evolution. Warrendale, The Metallurgical Society: 21-32.
- Grest, G. S., D. J. Srolovitz, and D. J. Srolovitz (1988). *Domain-Growth Kinetics for the Q-State Potts Model in Two and Three Dimensions.* Phys. Rev. B 38: 4752-4760.
- Grey, E. A. and G. T. Higgins (1972). *A Velocity Independent Drag During Grain Boundary Migration.* Scripta Met. 6: 253-258.
- Grey, E. A. and G. T. Higgins (1973). *Solute Limited Grain Boundary Migration: A Rationalization of Grain Growth.* Acta Met. 21: 309-321.
- Gromov, M. (1986). *Partial Differential Relations.* Berlin, Springer Verlag.
- Guazzelli, E. (1986). *Deux Etudes Experimentales du Desordre en Hydrodynamique Physique.* Ph.D. Thesis, L'Universite de Provence.

- Gururaj, M., R. Kumar, and K. S. Gandhi (1995). *A Network Model of Static Foam Drainage*. Langmuir 11: 1381-1391.
- Hardin, J. D. and L. Y. Cheng (1986). *The Mechanisms and Mechanics of Archenteron Elongation During Sea Urchin Gastrulation*. Dev. Biol. 115: 490-501.
- Hardin, J. D. (1987). *Archenteron Elongation in the Sea Urchin is a Micro-Tubules Independent Process*. Dev. Biol. 121: 253-262.
- Hasegawa, M. and M. Tanemura (1976). *On the Pattern of Space Division by Territories*. Ann. Inst. Stat. Math. 28: 509-516.
- Hassold, G. N., E. A. Holm, and D. J. Srolovitz (1990). *Effects of Particle-Size on Inhibited Grain-Growth*. Scripta Met. 24: 101-106.
- Hayakawa, H. and F. Family (1990). *Many-Body Effects in Two-Dimensional Ostwald Ripening*. Physica A 163: 491-500.
- Hébraud, P., F. Lequeux, J. P. Munch and D. J. Pine (1997). *Yielding and Rearrangements in Disordered Emulsions*. Phys. Rev. Lett. 78: 4657-4660.
- Heil, J. R., K. L. McCarthy, J. B. German, and M. J. McCarthy. (1990). *Use of Magnetic Resonance Imaging for Evaluation of Beer Foam Characteristics*. J. American Society of Brewing Chemists 48: 119-122.
- Heil, J. R., M. Özilgen, and M. McCarthy (1993). *Magnetic Resonance Imaging Analysis of Water Migration and Void Formation in Baking Biscuits*. Food Dehydration, AIChE Symposium Series 89: 39-45.
- Heimfeld, S. and H. R. Bode (1984). *Interstitial Cell-Migration in Hydrattenuata. 1. Quantitative Description of Cell Movements*. Dev. Biol. 106:

1-9.

- Heimfeld, S. and H. R. Bode (1984). *Interstitial Cell-Migration in Hydra-Attenuata. 2. Selective Migration Of Nerve-Cell Precursors as the Basis for Position-Dependent Nerve-Cell Differentiation*. Dev. Biol. 106: 10-17.
- Held, L. (1979). *A High-Resolution Morphogenetic Map of the Second-Leg Basitarsus in Drosophila Melanogaster*. Wilhelm Roux Arch. Dev. Biol. 187: 129-150.
- Hennecke, M (1997). *Survivors in the 2-Dimensional Potts-Model: Zero-Temperature Dynamics of  $q=$ Infinity*. Physica A 246: 519-528.
- Hennecke, M (1998). *Universality of Derrida Coarsening in the Triangular Potts-Model*. Int. J. Mod. Phys. C. 9: 325-330.
- Herdtle, T. and H. Aref (1991). *Relaxation of Fractal Foams*. Phil. Mag. Lett. 64: 335-340.
- Herdtle, T. and H. Aref (1991). *On the Geometry of Composite Bubbles*. Proc. Roy. Soc. Lond. A 434: 441-447.
- Herdtle, T. and H. Aref (1992). *Numerical Experiments on Two-Dimensional Foams*. J. Fluid Mech. 241: 233-260.
- Herrera, O., A. Olguin, M. Ortiz, and C. H. Worner (1997). *Pinned State in a 2-Dimensional Soap Froth*. Phys. Rev. E 55: 4475-4477.
- Hildebrandt, S and A. Tromba (1996). *The Parsimonious Universe: Shape and Form in the Natural World*. New York, Springer-Verlag.
- Hillert, M. (1965). *On the Theory of Normal and Abnormal Grain Growth*. Acta Met. 13: 227-238.

- Hoballah, H., R. Höhler, and S. Cohen-Addad (1997). *Time Evolution of the Elastic Properties of Aqueous Foam*. J. Physique II 7: 1215-1224.
- Hoff, H. A., C. J. Craigie, E. Dantsker, and C. S. Pande (1991). *Columnar Growth in Combustion Deposited Diamond Thin-Films*. Appl. Phys. Lett. 59: 1693-1695.
- Höhler, R., S. Cohen-Addad, and H. Hoballah (1997). *Periodic Nonlinear Bubble Motion in Aqueous Foam Under Oscillating Shear Strain*. Phys. Rev. Lett. 79: 1154-1157.
- Holm, E. A., G. N. Hassold, *et al.* (1990). *Effects of Inert Particle Morphology on Two-Dimensional Grain Growth*. Simulation and Theory of Evolving Microstructures. eds. M. P. Anderson and A. D. Rollett. Warrendale, The Metallurgical Society: 57-64.
- Holm, E. A., J. A. Glazier, D. J. Srolovitz, and G. S. Grest (1991). *The Effect of Lattice Anisotropy and Temperature on Grain Growth in the Two-Dimensional Potts Model*. Phys. Rev. A 43: 2662-2668.
- Holm, E. A., D. J. Srolovitz, and J. W. Kahn (1993). *Microstructural Evolution in Two-Dimensional Two-Phase Polycrystals*. Acta Met. 41: 1119-1136.
- Holm, E. A., N. Zacharopoulos, and D. J. Srolovitz (1998). *Nonuniform and Directional Grain-Growth Caused by Grain-Boundary Mobility Variations*. Acta Met. 46: 953-964.
- Holm, E. A. (1998). *Surface Formation Energy for Intergranular Fracture in 2-Dimensional Polycrystals*. J. Am. Ceramic Soc. 81: 455-459.
- Holmes, E. L. and W. C. Winegard (1959). *Grain Growth in Zone-Refined Tin*. Acta Met. 7: 411-414.

- Holtfreter, J. (1944). *Experimental Studies on the Development of the Pronephros*. Rev. Can. Biol. 3: 220-250.
- Holtfreter, J. (1947). *Observation of the Migration, Aggregation and Phagocytosis of Embryonic Cells*. J. Morph. 80: 25-55.
- Honda, H. (1978). *Description of Cellular Patterns by Dirichlet Domains: the Two-Dimensional Case*. J. Theor. Biol. 72: 523-543.
- Honda, H. and G. Eguchi (1980). *How Much Does the Cell Boundary Contract in a Monolayered Cell Sheet?* J. Theor. Biol. 84: 575-588.
- Honda, H., Y. Ogita, et al. (1982). *Cell Movements in a Living Mammalian Tissue: Long Term Observation of Individual Cells in Wounded Corneal Endothelia of Cats*. J. Morph. 174: 25-39.
- Honda, H. (1983). *Geometrical Models for Cells in Tissue*. Int. Rev. Cytol. 81: 191-248.
- Honda, H., H. Yamanaka, et al. (1986). *Transformation of a Polygonal Cellular Pattern During Sexual Maturation of the Avian Oviduct Epithelium: Computer Simulation*. J. Embryol. exp. Morph. 98: 1-19.
- Hosking, F. M., F. G. Yost, E. A. Holm, and J. R. Michael (1996). *Solder Flow on Narrow Copper Strips*. J. Elec. Mat. 25: 1099-1107.
- Howe, A. M., A. Clarke, and T. H. Whitesides (1997). *Viscosity of Emulsions of Polydisperse Droplets With a Thick Adsorbed Layer*. Langmuir 13: 2617-2626.
- Howe, C. L. (1987). *Computer Simulation of Grain Growth in Two Dimensions*. M.S. Thesis, Dartmouth College.

- Hsu, H. and B. B. Rath (1970). *On the Time Exponent in Isothermal Grain Growth.* Met. Trans. 1: 3181-3184.
- Huang, T., M. R. Kamal, and A. D. Rey (1995). *Experimental-Study of Topological Organization and Scaling of Polygrains in a Solidified Polymer Film.* J. Mat. Sci. Lett. 14: 220-223.
- Hull, B. and L. A. Staehelin (1976). *Functional Significance of the Variations in Geometrical Organization of Tight Junctions Networks.* J. Cell Biol. 68: 688-704.
- Hunderi, O. (1979). *Steady State Grain Growth, A Note on the Kinetics.* Acta Met. 27: 167-169.
- Hunderi, O., N. Ryum, *et al.* (1979). *Computer Simulation of Grain Growth.* Acta Met. 27: 161-165.
- Hunderi, O. and N. Ryum (1980). *The Kinetics of Normal Grain Growth.* J. Mater. Sci. 15: 1104-1108.
- Hunderi, O. and N. Ryum (1981). *Computer Simulation of Stagnation in Grain Growth.* Acta Met. 29: 1737-1745.
- Hutzler, S., G. Verbist, D. Weaire, and J. A. van der Steen (1995). *Measurement of Foam Density Profiles Using AC Capacitance.* Europhys. Lett. 31: 497-502.
- Hutzler, S., D. Weaire, and F. Bolton (1995). *The Effects of Plateau Borders in the Two-Dimensional Soap Froth III. Further Results.* Phil. Mag. B 71: 277-289.

- Hutzler, S. (1997). *The Physics of Foams*. Ph.D. Thesis, The University of Dublin.
- Hynes, R. and K. Yamada (1982). *Fibronectins: Multifunctional Modular Glycoproteins*. J. Cell Biol. 95: 369-377.
- Iglesias, J. R. and R. M. C. de Almeida (1991). *Statistical Thermodynamics of a 2-Dimensional Cellular-System*. Phys. Rev. A 43: 2763-2770.
- Imai, M., T. Kato, and D. Schneider (1998). *Coarsening of Cubic Lattice Domains Observed in a Nonionic Surfactant System*. J. Chem. Phys. 108: 1710-1714.
- Ispolatov, I, P. L. Krapivsky, and S. Redner (1996). *War: the Dynamics of Vicious Civilizations*. Phys. Rev. E 54: 1274-1289.
- Jacobs, W. P. (1994). *Caulerpa*. Sci. Am. 271: 100-105.
- Jacobson, A. G. and R. Gordon (1976). *Changes in the Shape of the Developing Vertebrate Nervous System Analyzed Experimentally, Mathematically and by Computer Simulation*. J. Exp. Zool. 197: 191-246.
- Jacobson, A. G., G. F. Oster, et al. (1986). *Neurulation and the Cortical Tractor Model for Epithelial Folding*. J. Embryol. exp. Morph. 96: 19-49.
- Jaynes, E. T. (1957). *Information Theory and Statistical Mechanics*. Phys. Rev. 106: 620-630.
- Jaynes, E. T. (1957). *Information Theory and Statistical Mechanics. II*. Phys. Rev. 108: 171-190.

- Jeppesen, C., H. Flyvbjerg, and O. G. Mouritsen (1989). *Dynamics of Ordering in Highly Degenerate Models With Anisotropic Grain-Boundary Potential: Effects of Temperature and Vortex Formation*. Phys. Rev. B 40: 9070-9079.
- Jeppesen, C., O. G. Mouritsen, and H. Flyvbjerg (1990). *Computer-Simulation of Vortex Formation During Domain Growth*. Physica Scripta T 33: 180-184.
- Jiang, Y., J. C. M. Mombach, and J. A. Glazier (1995). *Grain Growth From Homogeneous Initial Conditions: Anomalous Grain Growth and Special Scaling States*. Phys. Rev. E 52: R3333-R3336.
- Jiang, Y. and J. A. Glazier (1996). *Extended Large-Q Potts Model Simulation of Foam Drainage*. Phil. Mag. Lett. 74: 119-128.
- Jiang, Y. and J. A. Glazier (1997). *Foam Drainage: Extended Large-Q Potts Model Simulation and a Mean Field Theory*. Proceedings of MRS 463: 307-312.
- Jiang, Y., H. Levine, and J. A. Glazier (1998). *Possible Collaboration of Differential Adhesion and Chemotaxis Cooperate in Mound Formation of Dictyostelium*, Biophys. J., in press.
- Jimenezceniceros, A, G. Vazquezpolo, C. Renero, and V. M. Castano (1994). *Mechanical Model for 2-Dimensional Coarsening Foams*. Mat. Lett. 19: 317-323.
- Joye, J.-L., G. J. Hirasaki, and L. A. Miller (1994). *Asymmetric Drainage in Foam Films*. Langmuir 10: 3174-3179.
- Kader, A. A. E. and J. C. Earnshaw (1997). *Evolution of a 2-Dimensional Foam Containing a Single Topological Defect: an Experimental Study*. Phys. Rev. E 56: 3251-3255.

- Kamal, M. R., T. Huang, and A. D. Rey (1997). *Topological Properties of Polymer Spherulitic Grain Patterns From Simultaneous Nucleation*. J. Mat. Sci. 32: 4085-4099.
- Kang, S-Y. and A. S. Sangani (1997). *Rheology of Dense Bubble Suspensions*. Phys. Fluids 9: 1540-1561.
- Kawasaki, K. and Y. Enomoto (1988). *Statistical Theory of Ostwald Ripening With Elastic Field Interaction*. Physica A 150: 462-498.
- Kawasaki, K., T. Nagai, and K. Nakashima (1989). *Vertex Models for Two-Dimensional Grain-Growth*. Phil. Mag. B 60: 399-421.
- Kawasaki, K (1990). *Aspects of Late-Stage Dynamics of Ordering Processes*. Physica A 163: 59-70.
- Keller, R. E. (1978). *Time-Lapse Cinemicrographic Analysis of Superficial Cell Behavior During and Prior to Gastrulation in Xenopus Laevis*. J. Morph. 157: 223-248.
- Keller, R. E. and J. P. Trinkaus (1987). *Rearrangement of Enveloping Layer Cells Without Disruption of the Epithelial Permeability Barrier as a Factor in Fundulus Epiboly*. Dev. Biol. 120: 12-24.
- Keller, R. E. and J. P. Hardin (1987). *Cell Behavior During Active Cell Rearrangement: Evidence and Speculation*. J. Cell Sci. Suppl.: Cell Behavior: Shape, Adhesion and Motility 8s: 369-393.
- Kelvin (1887). *On the Division of Space with Minimal Partition Area*. Phil. Mag. 24: 503-515.

- Kermode, J. P. and D. Weaire (1990). *2D-Froth: A Program for the Investigation of 2-Dimensional Froths*. Comp. Phys. Comm. 60: 75-109.
- Kessler, D. and H. Levine. 1993. *Pattern Formation in Dictyostelium Via the Dynamics of Cooperative Biological Entities*. Phys. Rev. E 48: 4801-4804.
- Khan, S. A. and R. C. Armstrong (1986). *Rheology of Foams: I. Theory for Dry Foams*. J. Non-Newtonian Fluid Mech. 22: 1-22.
- Khan, S. A. (1987). *Foam Rheology: Relation Between Extensional and Shear Deformations in High Gas Fraction Foams*. Rheol. Acta 26: 78-84.
- Khan, S. A. and R. C. Armstrong (1987). *Rheology of Foams: II. Effects of Polydispersity and Liquid Viscosity for Foams Having Gas Fractional Approaching Unity*. J. Non-Newtonian Fluid Mech. 25: 61-92.
- Khan, S. A., C. A. Schnepper, and R. C. Armstrong (1988). *Foam Rheology: III. Measurement of Shear Flow Properties*. J. Rheol. 32: 69-92.
- Khan, S. A. and R. C. Armstrong (1989). *Rheology of Foams: IV. Effect of Gas Volume Fraction*. J. Rheol. 33: 881-911.
- Kikuchi, R. (1956). *Shape Distribution of Two Dimensional Soap Froths*. J. Chem. Phys. 24: 861-867.
- Kim, H.-J. and C. V. Thompson (1990). *The Effect of Dopants on Surface Energy Driven Secondary Grain Growth in Silicon Films*. J. Appl. Phys. 67: 757-767.
- Kirchner, H. O. K. (1971). *Coarsening of Grain-Boundary Precipitates*. Met. Trans. 2: 2861-2864.

- Klinger, L. M, E. E. Glickman, V. E. Fradkov, W. W. Mullins and C. L. Bauer (1995). *Extensions of Thermal Grooving for Arbitrary Grain-Boundary Flux*. J. Appl. Phys. 78: 3833-3838.
- Knobler, C. M. (1990). *Seeing Phenomena in Faltland: Studies of Monolayers by Fluorescence Microscopy*. Science 249: 870-874.
- Kolega, J. (1986). *Effects of Mechanical Tension on Protrusive Activity and Microfilament and Intermediate Filament Organization in an Epidermal Epithelium Moving in Culture*. J. Cell Biol. 102: 1400-1411.
- Konig, G. and W. Blum (1980). *Comparison Between the Cell Structures Produced in Aluminum by Cycling and by Monotonic Creep*. Acta Met. 28: 519-537.
- Kooy, C. and U. Enz (1960). *Experimental and Theoretical Study of the Domain Configuration in Thin Layers of BaFe<sub>12</sub>O<sub>19</sub>*. Philips Res. Repts. 15: 7-29.
- Korneta, W., S. K. Mendiratta, and J. Menteiro (1998). *Topological and Geometrical Properties of Crack Patterns Produced by the Thermal-Shock in Ceramics*. Phys. Rev. E 57: 3142-3152.
- Krantz, W. B., K. J. Gleason, and N. Caine (1988). *Patterned Ground*. Sci. Am. 259: 68-76.
- Krapivsky, P. L and E. Ben-Naim (1997). *Domain Statistics in Coarsening Systems*. Phys. Rev. E 56: 3788-3798.
- Kravchenko, A. S., D. G. Udler, *et al.* (1987). *Correlations in Two-Dimensional Grain Structures*. Phys. Met. Metall. 63: 103-108.

- Kraynik, A. M. and M. G. Hansen (1986). *Foam and Emulsion Rheology: A Quasistatic Model for Large Deformations of Spatially-Periodic Cells.* J. Rheology 30: 409-439.
- Kraynik, A. M. (1988). *Foam Flows.* Ann. Rev. Fluid. Mech. 20: 325-357.
- Kraynik, A. M., D. A. Reinelt, H. M. Princen (1991). *The Nonlinear Elastic Behavior of Polydisperse Hexagonal Foams and Concentrated Emulsions.* J. Rheol. 35: 1235-1253.
- Kreines, A. I. and V. E. Fradkov (1986). *Automatizirvannie Analiz Iotcheis-tech Struktur.* Experimental problems and techniques 5: 62-64.
- Krichevsky, O, and J. Stavans (1992). *Coarsening of 2-Dimensional Soap Froths in the Presence of Pinning Centers.* Phys. Rev. B 46: 10579-10582.
- Krichevsky, O. and J. Stavans (1993). *Surfactant-Polymer Interactions in Soap Films.* Physica A 200: 743-750.
- Krichevsky, O. and J. Stavans (1993). *Correlated Ostwald Ripening in Two Dimensions.* Phys. Rev. Lett. 70: 1473-1476.
- Krichevsky, O. and J. Stavans (1995). *Ostwald Ripening in a 2-Dimensional System: Correlation-Effects.* Phys. Rev. Lett. 52: 1818-1827.
- Krichevsky, O. and J. Stavans (1995). *Micellar Stratification in Soap Films: a Light-Scattering Study.* Phys. Rev. Lett. 74: 2752-2755.
- Krichevsky, O. and J. Stavans (1997). *Confined Fluid Between 2 Walls : The Case of Micelles Inside a Soap Film.* Phys. Rev. E 55: 7260-7266.
- Kumar S, S. K. Kurtz (1993). *Properties of a 2-Dimensional Poisson-Voronoi Tesselation: A Monte-Carlo Study.* Materials Characterization. 31: 55-68.

- Kumar, S., S. K. Kurtz, and D. Weaire (1994). *Average Number of Sides for the Neighbors in a Poisson-Voronoi Tesselation*. Phil. Mag. B 69: 431-435.
- Kumar, S., S. K. Kurtz and M. Cieplak (1997). *Topological Disorder in Cellular Microstructures*. Phil. Mag. B 75: 669-679.
- Kurtz, S. K. and F. M. A. Carpay (1980). *Microstructure and Normal Grain Growth in Metals and Ceramics. Part I. Theory*. J. Appl. Phys. 51: 5725-5744.
- Kurtz, S. K. and F. M. A. Carpay (1980). *Microstructure and Normal Grain Growth in Metals and Ceramics. Part II. Experiment*. J. Appl. Phys. 51: 5745-5754.
- Kuz, V. A. (1992). *Dynamics of Bubbles in a Liped Monolayer*. Phys. Rev. A 45: 8975-8976.
- Lacasse, M.-D., G. S. Grest, D. Levine, T. G. Mason, and D. A. Weitz (1996). *Model for the Elasticity of Compressed Emulsions*. Phys. Rev. Lett. 76: 3448-3451.
- Lacasse, M.-D., G. S. Grest, and D. Levine (1996). *Deformation of Small Compressed Droplets*. Phys. Rev. E 54: 5436-5446.
- Lacomabe, J. C., M. B. Koss, V. E. Fradkov, and M. E. Glicksman (1995). *3-Dimensional Dendrite-Tip Morphology*. Phys. Rev. E 52: 2778-2786.
- Lajzerowicz, J. and J. J. Niez (1979). *Phase Transition in a Domain Wall*. J. Physique Lett. 40: L165-L169.
- Lam, T. Y, G. Pickering, J. Geltosky, and C. H. Siu. (1981). *Differential Cell Cohesiveness Expressed by Pre-spore and Pre-stalk Cells of Dictyostelium*

*Discoideum*. Differentiation 20: 22-28.

- Lambert, C. J. and D. Weaire (1981). *Theory of the Arrangement of Cells in a Network*. Metallography 14: 307-318.
- Lambert, C. J. and D. Weaire (1983). *Order and Disorder in Two-Dimensional Random Networks*. Phil. Mag. B 47: 445-450.
- Langer, J. S. (1981). *Pattern Formation During Crystal Growth: Theory. Nonlinear Phenomena at Phase Transitions and Instabilities*. T. Riste. New York, Plenum Press: 309-336.
- Langer, S. A. and A. J. Liu. *Effect of Random Packing on Stress Relaxtion in Foams*. J. Phys. Chem. B 101: 8667-8671.
- Lantuejoul, C. (1978). *Computation of the Histograms of the Number of Edges and Neighbors of Cells in a Tesselation*. Geometrical Probability and Biological Structure: Buffon's 200th Anniversary. R. E. Miles and J. Serra. Berlin, Springer-Verlag: 323-329.
- Le Caer, G (1991). *Topological Models of 2D Cellular Structures .2. Z-Greater-Than-or-Equal-to-5*. J. Phys. A 24: 4655-4675.
- Le Caer, G. and R. Delannay (1993). *Correlations in Topological Models of 2D Random Cellular Structures*. J. Phys. A 26: 3931-3954.
- Le Caer, G. and R. Delannay (1993). *The Administrative Divisions of Mainland France as 2D Random Cellular Structures*. J. Phys. I France 3: 1777-1800.
- Leeuwenhoek, A. v. (1692). *On the Formation of Rushes*. Arcana Naturae: Epistola 74.

- Lehn, H. (1953). *Die histologischen Vorgänge bei der Reparation von Hydren aus Aggregaten kleiner Fragmente*. Roux Archives für Entwicklungsmechanik 146: 371-402.
- Leith, A. and N. Goel (1971). *Simulation of Movements of Cells During Self-sorting*. J. Theor. Biol. 33: 171-188.
- Lemaitre, J. A. Gervois, D. Bideau, J. P. Troadec, and M. Ammi (1992). *Distribution of Cell Edges in 2-Dimensional Mosaics*. C. R. Acad. Sci. II 315: 35-38.
- Levine, R. D. and M. Tribus (1979). *The Maximum Entropy Formalism*. Cambridge, USA, M.I.T. Press.
- Levine, H., L. Tsimring, and D. Kessler. (1997). *Computational Modeling of Mound Development in Dictyostelium*. Physica D 106: 375-388.
- Levitan, B., E. Slepian, O. Krischvsky, J. Stavans, and E. Domany. (1994). *Topological Distribution of Survivors in an Evolving Cellular Structure*. Phys. Rev. Lett. 73: 756-759.
- Levitan, B. (1994). *Evolution of Two-Dimensional Soap Froth with a Single Defect*. Phys. Rev. Lett. 72: 4057-4061.
- Levitan, B. and E. Domany (1995). *Topological Model of Soap Froth Evolution With Deterministic T2 Processes*. Europhys. Lett. 32: 543-548.
- Levitan, B. (1995). *Evolution of 2-Dimensional Soap Froth With a Single Defect: Reply*. Phys. Rev. Lett. 74: 3711-3711.
- Levitan, B. and E. Domany (1996). *Topological Simulations of Dynamical Features in Coarsening Soap Froth*. Phys. Rev. E 54: 2766-2772.

- Levitan, B. and E. Domany (1996). *Dynamical Features in Coarsening Soap Froth : Topological Approach*. Int. J. Mod. Phys. B 10: 3765-3805.
- Levitan, B. and E. Domany (1997). *Long-Time Behavior of the Survivors Areas*. Europhys. Lett. 38: 485-490.
- Levitan, B. (1997). *Randomness and Determinism in Soap Froth Dynamics*. Phys. Rev. E 55: 1205-1208.
- LEVY, L. P. and H. Bouchiat (1988). *Asymmetric Hysteresis Cycles as a Probe of Local-Fields in Metallic Spin-Glasses*. J. Appl. Phys. 63: 4358-4358.
- Levy, L. P. (1993). *Reptation and Hysteresis in Disordered Magnets*. J. Physique I 3: 533-557.
- Lewis, F. T. (1925). *A Further Study of the Polyhedral Shapes of Cells*. Proc. Amer. Acad. Arts and Sci. 61: 1-34.
- Lewis, F. T. (1928). *Mathematically Precise Features of Epithelial Mosaics: Observations on the Endothelium of Capillaries*. Anat. Rec. 55: 323-341.
- Lewis, F. T. (1928). *The Correlation Between Cell Division and the Shape and Sizes of Prismatic cells in the Epidermis of Cucumis*. Anat. Rec. 38: 341-362.
- Lewis, F. T. (1931). *A Comparison Between the Mosaic of Polygons in a Film of Artificial Emulsion and the Pattern of Simple Epithelium in Surface View (Cucumber Epidermis and Human Amnion)*. Anat. Rec. 50: 235-265.
- Lewis, F. T. (1943). *A Geometric Accounting for Diverse Shapes of 14-hedral Cells: the Transition from Dodecahedra to Tetrakaidekahedra*. Am. J. Bot. 30: 74-81.

- Lewis, F. T. (1944). *The Geometry of Growth and Cell Division in Columnar Parenchyma*. Am. J. Bot. 31: 619-629.
- Lewis, F. T. (1944). *The Geometry of Growth and Cell Division in Epithelial Mosaics*. Am. J. Bot. 30: 766-776.
- Lewis, F. T. (1948). *The Analogous Shapes of Cells and Bubbles*. Proc. A.A.A.S. 77: 147-186.
- Li, W.-B. and K. E. Easterling (1990). *The Influence of Particle Shape on Zener Drag*. Acta Met. 38: 1045-1052.
- Lifschitz, I. M. and V. V. Slyozov (1959). *Kinetics of Diffusive Decomposition of Supersaturates Solid Solutions*. Soviet JETP 35: 331-339.
- Lifschitz, I. M. and V. V. Slyozov (1961). *The Kinetics of Precipitation From Supersaturated Solid Solutions*. J. Phys. Chem. Solids 19: 35-50.
- Ling, S. and M. P. Anderson (1992). *Monte-Carlo Simulation of Grain-Growth and Recrystallization in Polycrystalline Materials*. J. TMMMS. 44: 30-36.
- Liu, A. J., S. Ramaswamy, T. G. Mason, H. Gang. and D. A. Weitz (1996). *Anomalous Viscous Loss in Emulsions*. Phys. Rev. Lett. 76: 3017-3020.
- Liu, J. M. (1996). *Scaling of Size Distribution for Normal Domain Growth Mode*. Mat. Lett. 26: 327-332.
- Loomis, W. F. (1995). *Lateral Inhibition and Pattern Formation in *Dicystostelium**. Curr. Top. Dev. Biol. 28: 1-46.
- Lotwick, H. W. (1982). *Simulation of Some Spatial Hard Core Models, and the Complete Packing Problem*. J. Statist. Comput. Simul. 15: 295-314.

- Louat, N. P. (1974). *On the Theory of Normal Grain Growth*. Acta Met. 22: 721-724.
- Lösche, M. and H. Möhwald (1984). *Fluorescence Microscope to Observe Dynamical Processes in Monomolecular Layers at the Air/Water Interface*. Rev. Sci. Instrum. 55: 1968-1972.
- Lubliner, J. (1990). *Plasticity Theory*. New York, Macmillan.
- Lucassen, J., S. Akamatsu, and F. Rondelez (1991). *Formation, Evolution, and Rheology of 2-Dimensional Foams in Spread Monolayers at the Air-Water-Interface*. J. Colloid Interface Sci. 144: 434-448.
- Maddox, J. (1989). *Soap Bubbles Make Serious Physics*. Nature 338: 293.
- Maggs, A. C, D. Mukamel, and C. A. Pillet (1994). *Selection of Length Distributions in Living Polymers*. Phys. Rev. E 50: 774-77.
- Magnasco, M. O. (1992). *2-Dimensional Bubble Rafts*. Phil. Mag. B 65: 895-920.
- Magnasco, M. O. (1994). *Correlations in Cellular Patterns*. Phil. Mag. B 69: 397-429.
- Maillard, J. M. and R. Rammal (1983). *Some Analytical Consequences of the Inverse Relation for the Potts Model*. J. Phys. A 16: 353-367.
- Majors, P. D., R. C. Givler, *et al.* (1989). *Velocity and Concentration Measurements in Multiphase Flows by NMR*. J. Magnetic Resonance 85: 235-243.
- Mallet, R. (1875). *On the Origin and Mechanism of Production of the Prismatic (or Columnar) Structure of Basalt*. Phil. Mag. 50: 122-135 & 201-227.

- Malozemoff, A. P. and J. C. Slonczewski (1979). *Magnetic Domain Walls in Bubble Materials*. New York, Academic Press.
- Mangan M. T. and K. V. Cashman (1996). *The Structure of Basaltic Scoria and Reticulite and Inferences for Vesiculation, Foam Formation, and Fragmentation in Lava Fountains*. J. Volcanology and Geothermal Res. 73: 1-18.
- Marder, M. (1987). *Soap Bubble Growth*. Phys. Rev. A 36: 438-440.
- Marthinsen, K., O. Hunderi, and N. Ryum (1996). *The Influence of Spatial Grain-Size Correlation and Topology on Normal Grain-Growth in 2 Dimensions*. Acta Met. 44: 1681-1689.
- Marvin, J. W. (1939). *The Shape of Compressed Lead Shot and Its Relation to Cell Shape*. Am. J. Bot. 26: 280-288.
- Mason, T. G. and D. A. Weitz (1995). *Optical Measurements of Frequency-Dependent Linear Viscoelastic Moduli of Complex Fluids*. Phys. Rev. Lett. 74: 1250-1253.
- Mason, T. G., J. Bibette, and D. A. Weitz (1995). *Elasticity of Compressed Emulsions*. Phys. Rev. Lett. 75: 2051-2054.
- Mason, T. G., M.-D. Lacasse, G. S. Grest, D. Levine, J. Bibette, and D. A. Weitz (1997). *Osmotic Pressure and Viscoelastic Shear Moduli of Concentrated Emulsions*. Phys. Rev. E 56: 3150-3166.
- Matos, J. and J. Laine (1998). *A Carbon Macro-Network From the Controlled Pyrolysis of Saccharose*. J. Mat. Sci. Lett. 17: 649-651.
- Matsubara, H. and R. J. Brook (197). *Computer Modling of Sintering Process in Ceramics*. Key Eng. Mat. 132-136: 710-713.

- Matsubara, H., S. Kitaoka, and H. Nomura (1997). *Computaional Modeling of Sintering and Grain Growth for Microstructural Design*. Int. Symp. Ceramic Materials and Components for Engines. 654-767.
- Matzke, E. B. (1939). *Volume-Shape Relationships in Lead Shot and Their Bearing on Cell Shapes*. Am. J. Bot. 26: 288-293.
- Matzke, E. B. (1946). *The Three Dimensional Shape of Bubbles in Foam—an Analysis of the Role of Surface Forces in Three Dimensional Cell Shape Determination*. Am. J. Bot. 33: 58-80.
- Matzke, E. B. and J. Nestler (1946). *Volume-Shape Relationships in Variant Foams. A Further Study of Role of Surface Forces in Three Dimensional Cell Shape Determination*. Am. J. Bot. 33: 130-144.
- McCarthy, K. L., M. J. McCarthy, and J. B. German. (1989). *Modeling of Foam Drainage and Collapse: Incorporation of Vertical Mass Distribution*. in Physical Properties and Process Control. eds. W. E. L. Spiess and H. Schubert. London, Elsevier Applied Science 1: 225-234.
- McCarthy, M. J. and J. R. Heil. *Mobility of Water in Foams Determined by Magnetic Resonance Sopectroscopy* in Food Emulsion and Foams; Theory and Practice, AIChE Symposium Series # 277. eds. P. J. Wan, J. L. Cavallo, F. Z. Saleeb and M. J. McCarthy. New York, AIChE. 86: 102-110.
- McCarthy, M. J., K. L. McCarthy, *et al. Foam and Emulsion Stability: Measurements by Magnetic Resonance Imaging* in Physical Properties and Process Control. eds. W. E. L. Spiess and H. Schubert. London, Elsevier Applied Science 1: 235-244.

- McCarthy, M. J., E. Perez, and M. Özilgen. (1991). *Model for Transient Moisture Profiles of a Drying Apple Slab Using the Data Obtained with Magnetic Resonance Imaging*. Biotechnol. Prog. 7: 540-543.
- McClay, D. R. and C. A. Ettenson (1987). *Cell Adhesion in Morphogenesis*. Ann. Rev. Cell Biol. 3: 319-345.
- McConnell, H. M., L. K. Tamm, *et al.* (1984). *Periodic Structures in Lipid Monolayer Phase Transitions*. Proc. Natl. Acad. Sci. USA 81: 3249-3253.
- Meijering, J. L. (1953). *Interface Area, Edge Length, and Number of Vertices in Crystal Aggregates with Random Nucleation*. Philips Res. Repts. 8: 270-290.
- Meller, A. and J. Stavans (1992). *Glass-Transition and Phase-Diagrams of Strongly Interacting Binary Colloidal Mixtures*. Phys. Rev. Lett. 68: 3646-3649.
- Mertig M., U. Thiele, J. Bradt, G. Leibiger, W. Pompe, and H. Wendrock. *Scanning Force Microscopy and Geometric Analysis Of 2-Dimensional Collagen Network Formation*. Surface & Interface Analysis. 25: 514-521.
- Messier, R. and R. C. Ross (1982). *Evolution of Microstructure in Amorphous Hydrogenated Silicon*. J. Appl. Phys. 53: 6220-6225.
- Mège, J.-L., C. Capo, *et al.* (1986). *Determination of Binding Strength and Kinetics of Binding Initiation: A Model Study Made on the Adhesive Properties of P388D1 Macrophage-Like Cells*. Cell Biophys. 8: 141-160.
- Mège, R.-M. (1991). *Les Molécules D'adhérence Cellulaire: Molécules Morphogénétiques*. Médecine Sciences 7: 544-552.

- Miles, R. E. (1974). *Stochastic Geometry*. New York, John Wiley.
- Min, K. Y., J. Stavans, R. Piazza, and W. I. Goldburg (1989). *Steady-State Nucleation in a Binary Mixture : the Effect of Stirring*. Phys. Rev. Lett. 63: 1070-1073.
- Miodownik, M. A. and J. W. Martin (1996). *Monte-Carlo Simulations of Particle/Boundary Interactions*. Mat. Sci. Forum 207: 529-532.
- Miranda, R. M. and M. A. Fortes (1989). *Austenite Grain Growth, Microstructure and Hardness in the Heat-Affected Zone of a 2.25Cr-1Mo Steel*. Mat. Sci. Eng. A 108: 1-8.
- Mochizuki, A., N. Wada, H. Ide, and Y. Iwasa (1998). *Cell-Cell Adhesion in Limb-Formation, Estimated From Photographs of Cell Sorting Experiments Based on a Spatial Stochastic-Model*. Dev. Dynamics 211: 204-214.
- Molho, P., J. Gouzerh, et al. (1986). *Topological Hysteresis in Stripe Domain Structures*. J. Mag. & Mag. Mat. 54-57: 857-858.
- Molho, P., J. L. Porteseil, et al. (1987). *Irreversible Evolution in the Topology of Magnetic Domains*. J. Appl. Phys. 61: 4188.
- Molodov, D. A., V. E. Fradkov, et al. (1984). *Analysis of Diffusion Impurity Drag on Grain Boundaries*. Sov. Phys. Solid State 26: 1285-1290.
- Mombach, J. C. M., M. A. Z. Vasconcellos, et al. (1990). *Arrangement of Cells in Vegetable Tissues*. J. Phys. D 23: 600-606.
- Mombach, J. C. M., R. M. C. de Almeida, and J. R. Iglesias (1993). *Mitosis and Growth in Biological Tissues*. Phys. Rev. E 48: 598-602.

- Mombach, J. C. M., R. M. C. de Almeida, and J. R. Iglesias (1993). *Two-Cell Correlations in Biological Tissues*. Phys. Rev. E 47: 3712-3716.
- Mombach, J. C. M. and J. A. Glazier. (1996). *Single Cell Motion in Aggregates of Embryonic Cells*. Phys. Rev. Lett. 76: 3032-3035.
- Monnereau, C. and M. Vignesadler (1998). *Optical Tomography of Real 3-Dimensional Foams*. J. Colloid Interface Sci. 202: 45-53.
- Moore, B., C. M. Knobler, *et al.* (1986). *Studies in Phase Transitions in Langmuir Monolayers by Fluorescence Microscopy*. J. Chem. Soc. Faraday. Trans. 282: 1753-1761.
- Moritsen, O. G. (1986). *Universal Aspects of Domain-Growth Kinetics*, in Annealing Processes— Recovery, Recrystallization and Grain Growth, Proceedings of the 7th Risø International Symposium on Metallurgy and Materials Science. N. Hansen, D. J. Jensen, T. Leffers and B. Ralph. Roskilde, Risø National Laboratory: 457-462.
- Morral, J. E. and M. F. Ashby (1974). *Dislocated cellular structures*. Acta Met. 22: 567-575.
- Morris, P, G. (1986). *Nuclear Magnetic Resonance in Medicine and Biology*. New York, Oxford University Press.
- Moukarzel, C. (1993). *Voronoi Foams*. Physica A 199: 19-30.
- Moukarzel, C. (1997). *Geometrical Consequences of Foam Equilibrium*. Phys. Rev. E 55: 6866-6880.
- Moulin, S. and A. M. Bonnot (1994). *Thin-Film Growth*. Diamond and Related Materials 3: 577-580.

- Mulheran, P. A. (1994). *The scaling state in 2-dimensional grain-growth*. Acta Met. 42: 3589-3593.
- Mulheran, P. A. (1995). *Theory of the Size Distribution in 3-Dimensional Grain-Growth*. Phys. Rev. E 51: R3803-R3806.
- Mullins, W. W. (1956). *Two-Dimensional Motion of Idealized Grain Boundaries*. J. Appl. Phys. 27: 900-904.
- Mullins, W. W. and R. F. Sekerka (1963). *Morphological Stability of a Particle Growing by Diffusion or Heat Flow*. J. Appl. Phys. 34: 323-329.
- Mullins, W. W. (1986). *The Statistical Self-Similarity Hypothesis in Grain Growth and particle Coarsening*. J. Appl. Phys. 59: 1341-1349.
- Mullins, W. W. (1988). *On Idealized Two Dimensional Grain Growth*. Scripta Met. 22: 1441-1451.
- Mysels, K. J., K. Shinoda, et al. (1959). *Soap Films: Studies of their Thinning and a Bibliography*. New York, Pergamon Press.
- Nabarro, F. R. N. (1967). *Theory of Crystal Dislocations*. London, Oxford University Press.
- Nagai, T., K. Kawasaki, et al. (1988). *Dynamics of Two Dimensional Cell Patterns*. Nihon Butsuri Gakkaishi 43: 437-444.
- Nagai, T., K. Kawasaki, and K. Nakamura (1988). *Vertex Dynamics of Two-Dimensional Cellular-Patterns*. J. Phys. Soc. Jpn. 57: 2221-2224.
- Nagai, T., S. Ohta, K. Kawasaki, and T. Okuzono (1990). *Computer-Simulation of Cellular-Pattern Growth in 2 and 3 Dimensions*. Phase Transitions. 28: 177-211.

- Nagai, T., K. Fuchizaki, and K. Kawasaki (1994). *Orientation Effect on Grain-Growth*. Physica A 204: 450-463.
- Nakashima, K., T. Nagai, and K. Kawasaki (1989). *Scaling Behavior of 2-Dimensional Domain Growth : Computer-Simulation of Vertex Models*. J. Stat. Phys. 57: 759-787.
- Nardi, J. and F. Kafatos (1976). *Polarity and Gradients in Lepidopteran Wing Epidermis. II The Differential Adhesiveness Model: Gradient of a Non-Diffusible Cell Surface Parameter*. J. Embryol. exp. Morph. 36: 489-512.
- Nardi, J. and M. Magee-Adams (1986). *Formation of Scale Spacing Patterns in Moth Wing*. Dev. Biol. 116: 278-290.
- Nasello, O. B. and E. A. Ceppi (1986). *Computer Simulation of Bidimensional Grain Boundary Migration (II): An Application to Grain Growth*. Computer Simulation of Microstructural Evolution. Warrendale, The Metallurgical Society: 13-20.
- Neubert L. and M. Schreckenberg (1997). *Numerical-Simulation of 2-Dimensional Soap Froth*. Physica A 240: 491-502.
- Newman, S. A. and W. D. Comper (1990). *“Generic” Physical Mechanisms of Morphogenesis and Pattern Formation*. Development 110: 1-18.
- Newton, I. (1672). *Answer to Some Considerations Upon His Doctrine of Light and Colours*. Phil. Trans. Roy. Soc. London 7: 5084-5103.
- Nicol, A. and D. R. Garrod (1979). *The Sorting Out of Embryonic Cells in Monolayer, the Differential Adhesion Hypothesis and the Non-Specificity of Cell Adhesion*. J. Cell Sci. 38: 249-266.

- Nicol, A. and D. R. Garrod (1982). *Fibronectin, Intercellular Junctions and the Sorting Out of Chick Embryonic Tissue Cells in Monolayer*. J. Cell Sci. 54: 357-372.
- Nichols C. S, C. M. Mansuri, S. J. Townsend, and D. A. Smith (1993). *In situ Studies of Grain-Growth in Thin Metal-Films*. Acta Met. 41: 1861-1868.
- Niemark, A. V. and M. Vignes-Adler (1995). *Variations From the Plateau Law in Foams*. Phys. Rev. E 51: 788-791.
- Noda, K. (1971). *Hidora No Kairi Saibo Kara No Saikosei*. Zool. Mag. 80: 99-101.
- Noever, D. A. (1991). *Statistics of Premixed Flame Cells*. Phys. Rev. A 44: 968-974.
- Noever, D. A. and H. C. Matsos (1991). *A Bioassay for Monitoring Cadmium Based on Bioconvective Patterns*. J. Env. Sci. & Health A 26: 273-286.
- Noever, D. A. (1991). *Evolution of Bioconvective Patterns in Variable Gravity*. Phys. Rev. A 44: 5279-5291.
- Noever, D. A. (1992). *Statistics of Expanding Gel Surface Patterns*. J. Macromolecular Science - Phys. B 31: 357-364.
- Noever, D. A. (1992). *Statistical Crystallography of Surface Micelle Spacing*. Langmuir 8: 1036-1038.
- Noever, D. A. (1992). *Statistics of Emulsion Lattice*. Colloids & Surfaces 62: 243-247.

- Noever, D. A. (1994). *Solar Granulation and Statistical Crystallography : A Modeling Approach Using Size-Shape Relations*. Astro. Astrophys. 282: 252-261.
- Noever, D. A. (1994). *Statistics of Low-Density Microcellular Materials*. J. Mat. Res. 9: 515-522.
- Noever, D. A. and R. J. Cronise (1994). *Weightless Bubble Lattices : A Case of Froth Wicking*. Phys. Fluid 6: 2493-2500.
- Noever, D. A. (1994). *Crystallography of Rare Galactic Honeycomb Structure Near Supernova 1987A*. Astrophys. Space Sci. 220: 65-74.
- Noever, D. A., H. c. Matsos, R. J. Cronise, L. L. Looger, R. A. Relvani, and V. I. Nikora. *Ocean-Atmosphere Co<sub>2</sub> Exchange : An Accessible Lab Simulation for Considering Biological Effects*. Climatic Changes 27: 299-320.
- Noever, D. A. and R. J. Cronise (1994). *Froth Instability in Small-Over-Large Bubble Lattices*. Physica D 71: 452-459.
- Noever, D. A. (1995). *Order and Statistical Crystallography of Patterned Breath Figures*. J. Colloid Interface Sci. 174: 92-96.
- Nogueire, M. T. and M. A. Fortes (1988). *Strain Profiles in Tensile Specimens Exhibiting Periodic Load Serrations*. Scripta Met. 22: 1459-1464.
- Novikov, V. Y. (1978). *Computer Simulation of Normal Grain Growth*. Acta Met. 26: 1739-1744.
- Novikov, V. Y. (1979). *On Computer Simulation of Texture Development in Normal Grain Growth*. Acta Met. 27: 1461-1466.

- Nübler-Jung , K. and B. Mardini (1990). *Insect Epidermis: Polarity Patterns After Grafting Result From Divergent Cell Adhesion Between Host and Graft Tissues.* Development 110: 1071-1079.
- Öbrink, B. (1986). *Epithelial Cell Adhesion Molecules.* Exp. Cell Res. 163: 1-21.
- O'Dell, T. H. (1973). *The Dynamics of Magnetic Bubble Domain Arrays.* Phil. Mag. 27: 595-606.
- O'Dell, T. H. (1986). *Magnetic Bubble Domain Devices.* Rep. Prog. Phys. 49: 589-620.
- Occelli, R., E. Guazzelli, *et al.* (1983). *Order in Convective Structures.* J. Phys. Lett. (Paris) 44: L567-L580.
- Odell, G. M., G. Oster, *et al.* (1981). *The Mechanical Basis of Morphogenesis. I. Epithelial Folding and Invagination.* Dev. Biol. 85: 446-462.
- Oger, L., A. Gervois, J. P. Troadec, and N. Rivier (1996). *Voronoi Tessellation of Packings of Spheres : Topological Correlation and Statistics.* Phil. Mag. B 74: 177-197.
- Okuzono, T., K. Kawasaki, and T. Nagai (1993). *Rheology of Random Foams.* J. Rheol. 37: 571-586.
- Okuzono, T. and K. Kawasaki (1995). *Intermittent Flow Behavior of Random Foams: A Computer Experiment on Foam Rheology.* Phys. Rev. E 51: 1246-1253.
- Ondarcuhu, T., G. B. Mindlin, H. L. Mancini, and C. P. Garcia (1993). *Dynamic Patterns in Bénard-Marangoni Convection in a Square Container.*

Phys. Rev. Lett. 70: 3892-3895.

- Oster, G., J. D. Murray, *et al.* (1983). *Mechanical Aspects of Mesenchymal Morphogenesis*. J. Embryol. exp. Morph. 78: 83-125.
- Palmer, J. E., C. V. Thompson, and H. I. Smith (1987). *Grain Growth and Grain Size Distributions in Thin Germanium Films*. J. Appl. Phys. 62: 2492-2497.
- Palmer, J. E., V. E. Fradkov, M. E. Glicksman, and K. Rajan (1994). *Experimental Assessment of the Mullins-von Neumann Grain-Growth Law*. Scripta Met. 30: 633-637.
- Palmer, J. E., K. Rajan, M. Glicksman, V. E. Fradkov, and J. Nordberg (1995). *2-Dimensional Grain-Growth in Rapidly Solidified Succinonitrile Films*. J. Met. Mat. Transactions A 26: 1061-1066.
- Pande, C. S. and E. Dantsker (1990). *On a Stochastic Theory of Grain Growth-II*. Acta Met. 38: 945-951.
- Pande, C. S. and E. Dantsker (1991). *On a Stochastic Theory of Grain Growth - III*. Acta Met. 39: 1359-1365.
- Pande, C. S. (1992). *A Stochastic Theory of Grain Growth*. Mat. Sci. Forum 94-96: 351-357.
- Pande, C. S. and E. Dantsker (1994). On a Stochastic Theory of Grain Growth - IV. Acta Met. 42: 2899-2903.
- Park, S. S. and D. J. Durian (1994). *Viscous and Elastic Fingering Instabilities in Foam*. Phys. Rev. Lett. 72: 3347-3350.

- Peczak, P., G. S. Grest and D. Levine (1993). *Monte-Carlo Studies of Grain-Growth on Curved Surfaces*, Phys. Rev. E 48: 4470-4482.
- Peczak, P. (1995). *A Monte-Carlo Study of Influence of Deformation Temperature on Dynamic Recrystallization*. Acta Met. 43: 1279-1291.
- Pelizzola, A. (1996). *Low-Temperature Phase of the Three-State Antiferromagnetic Potts Model on the Simple-Cubic Lattice*. Phys. Rev. E 54: R5885-R5888.
- Pereira, H., M. E. Rosa and M. A. Fortes (1987). *The1 Cellular Structure of Cork From Quercus-Suber L*. IAWA Bulletin 8: 213-218.
- Peshkin, M. A., K. J. Strandburg, and N. Rivier (1991). *Entropic Predictions for Cellular Networks*. Phys. Rev. Lett. 67: 1803-1806.
- Peters, R. and K. Beck (1983). *Translational Diffusion in Phospholipid Monolayers Measured by Fluorescence Micropolymerysis*. Proc. Natl. Acad. Sci. USA 80: 7183-7187.
- Petersen, N., W. McConaughey, *et al.* (1982). *Dependence of Locally Measured Cell Deformability on Position of the Cell, Temperature, and Cytochlasin B*. Proc. Natl. Acad. Sci. USA 79: 5327-5331.
- Petit, P. A., M. P. de Albuquerque, V. Cabuil, and P. Molho. *Evolution of the Domain-Like Pattern in a Film of Ferrofluid in Normal Fields*. J. Magnetism & Magnetic Mat. 113: 127-131.
- Phaneuf, R. J., N. C. Bartelt, E. D. Williams, W. Swiech, and E. Bauer (1992). Surf. Sci. 268: 227-237.

- Phelan, R., D. Weaire, E. A. J. F. Peterse, and G. Verbist (1996). *The Conductivity of a Foam*. J. Phys: Condens. Matter 8: L475-L482.
- Phillips, H. M. and M. S. Steinberg (1978). *Embryonic Tissues as Elastoviscous Liquids. I. Rapid and Slow Shape Changes in Centrifugated Cell Aggregates*. J. Cell Sci. 30: 1-20.
- Phillips, H. M. and G. S. Davis (1978). *Liquid-Tissue Mechanics in Amphibian Gastrulation: Germ-Layer Assembly in Rana Pipiens*. Am. Zool. 18: 81-93.
- Piazza, R., J. Stavans, T. Bellini, and V. Degiorgio (1989). *Light-Scattering Study of Crystalline Latex-Particles*. Optics Comm. 73: 263-267.
- Piazza, R., V. Degiorgio, M. Corti, and J. Stavans (1990). *Rotational and Translational Self-Diffusion of Interacting Spherical Brownian Particles*. Phys. Rev. B 42: 4885-4888.
- Pieri, D. C. (1981). *Lineament and Polygon Patterns on Europa*. Nature 289: 17-21.
- Pina, P. and M. A. Fortes (1996). *Characterization of Cells in Cork*. J. Phys. D 29: 2507-2514.
- Pithia, K. d. and S. F. Edwards (1994). *Rheology of Liquid Foams*. Physica A 205: 565-576.
- Pithia, K. D. and S. F. Edwards (1995). *Dislocations in 2-Dimensional Liquid Foams*. Physica A 215: 277-282.
- Pittet, N., P. Boltenhagen, N. Rivier, and D. Weaire (1996). *Structural Transitions in Ordered, Cylindrical Foams*. Europhys. Lett. 35: 547-552.

- Plateau, J. (1843). *Memoir on the Phenomena Presented by a Mass of Liquid Free and Removed from the Action of Gravity*. Mem. Acad. R. Belg. 16.
- Plateau, J. (1873). *Statique Experiméntale et Théorique des Liquides Soumis aux Seulles Forces Moléculaires*. Paris, Gauthier-Villars.
- Prakash O., H. Sang, and J. D. Embury (1995). *Structure and Properties of Al-SiC Foam*. Mat. Sci. Eng. A. 199:195-203.
- Prause, B. A., J. A. Glazier, S. J. Gravina, and C. D. Montemagno (1995). *Three-dimensional Magnetic Resonance Imaging of a Liquid Foam*. J. Phys.: Condens. Matter 7: L511-L516.
- Preparata, F. and M. I. Shamos (1985). *Computational Geometry: An Introduction*. Berlin, Springer Verlag.
- Princen, H. M. and S. G. Mason (1965). *The Permeability of Soap Films to Gases*. J. Colloid Sci. 20: 353-375.
- Princen, H. M. (1986). *Osmotic Pressure of Foams and Highly Concentrated Emulsions: 1. Theoretical Considerations*. Langmuir 2: 519-524.
- Princen, H. M. and A. D. Kiss (1989). *Rheology of Foams and Highly Concentrated Emulsions: IV. An Experimental Study of the Shear Viscosity and Yield Stress of Concentrated Emulsions*. J. Colloid Interface Sci. 128: 176-187.
- Prost, J. and F. Rondelez (1991). *Structures in Colloidal Physical-Chemistry*. Nature 350: 11-23.
- Prusinkiewicz, P. and A. Lindenmayer (1990). *The Algorithmic Beauty of Plants*. New York, Springer-Verlag.
- Purcell, E. (1977). *Life at Low Reynolds Number*. Am. J. Phys. 45: 3-11.

- Qiu, X., J. Ruizgarcia, K. J. Stine, C. M. Knobler, and J. V. Selinger (1991). *Direct Observation of Domain-Structure in Condensed Monolayer Phases*. Phys. Rev. Lett. 67: 703-706.
- Radhakrishnan, B. and T. Zacharia (1995). *Simulation of Curvature-Driven Grain Growth by Using a Modified Monte Carlo Algorithm*. Met. Mat. Transactions A 26: 167-180.
- Randle, V., D. Ralph, and M. Hansen (1986). *Grain Growth in Crystalline Materials*. Annealing Processes— Recovery, Recrystallization and Grain Growth, Proceedings of the 7th Risø International Symposium on Metallurgy and Materials Science. N. Hansen, D. J. Jensen, T. Leffers and B. Ralph. Roskilde, Risø National Laboratory: 123-142.
- Rayleigh, L. (1890). *On the Theory of Surface Forces I*. Phil. Mag. 30: 285-299.
- Rammal, R. and J. M. Maillard (1983). *Q-State Potts Model on the Checkerboard Lattice*. J. Phys. A 16: 1073-1081.
- Rayleigh, L. (1890). *On the Theory of Surface Forces II*. Phil. Mag. 30: 456-475.
- Reed, M. G., C. V. Howard, and C. G. Shelton (1997). *Confocal Imaging and 2nd-Order Stereological Analysis of a Liquid Foam*. J. Microscopy-Oxford 185: 313-320.
- Reinelt, D. A. and A. M. Kraynik (1990). *On the Shearing Flow of Foams and Concentrated Emulsions*. J. Fluid Mech. 215: 431-455.
- Reinelt, D. A. and A. M. Kraynik (1996). *Simple Shearing Flow of a Dry Kelvin Soap Foam*. J. Fluid Mech. 311: 327-343.

- Rhines, F. N., K. R. Craig. (1974). *Mechanism of Steady State Grain Growth in Aluminum*. Met. Trans. 5: 413-425.
- Rhines, F. N. and K. R. Craig (1975). *Author's Reply*. Met. Trans. 6A: 590-591.
- Rhines, F. N. and B. R. Patterson (1982). *Effect of the Degree of Cold Work on the Grain Volume Distribution and Rate of Grain Growth of Recrystallized Aluminum*. Met. Trans. 13A: 985-993.
- Rietdorf, J., F. Siegert, and C. J. Weijer (1996). *Analysis of Optical Density Wave Propagation and Cell Movement During Mound Formation in Dictyostelium Discoideum*. Dev. Biol. 177: 427-438.
- Rivier, N. (1979). *Disclination Lines in Glasses*. Phil. Mag. A 40: 859-868.
- Rivier, N. and A. Lissowski (1982). *On the Correlation Between Sizes and Shapes of Cells in Epithelial Mosaics*. J. Phys. A 15: L143-L148.
- Rivier, N. (1983). *On the Structure of Random Tissues or Froths and Their Evolution*. Phil. Mag. B 47: L45-L49.
- Rivier, N. (1985). *Statistical Crystallography: Structure of Random Cellular Networks*. Phil. Mag. B 52: 795-819.
- Rivier, N. (1987). *Continuous Random Networks From Graphs to Glasses*. Adv. in Phys. 36: 95-134.
- Rivier, N., D. Weaire, and R. Deromer (1988). *Tetrahedrally Bonded Random Networks Without Odd Rings*. J. Non-Crystalline Solids 105: 287-291.
- Rivier, N. and J. F. Sadoc (1988). *The Local Geometry of Disorder*. J. Non-Crystalline Solids 106: 282-285.

- Rivier, N. (1988). *Statistical Geometry of Tissues*, in Thermodynamics and Pattern Formation in Biology. Berlin, Walter de Gruyter: 415-445.
- Rivier, N. (1988). *Topology and Ring Statistics in Covalent Glasses*. J. Non-Crystalline Solids 106: 278-281.
- Rivier, N. (1992). *The Structure and Dynamics of Patterns of Bénard Convection Cells*. J. Phys. Condens. Matter 4: 931-943.
- Rivier, N. (1993). *Nonstick Quasi-Crystalline Coatings*. J. Non-Crystalline Solids 153: 458-462.
- Rivier, N. (1994). *Aboav's Law for an Assembly of Discs of Different Sizes*. J. Physique I 4: 127-131.
- Rivier, N. (1994). Blowing Bubbles for Fun and Profit. Phys. World 7: 22-23.
- Rivier, N. (1994). *Kelvin's Conjecture on Minimal Froths and the Counter-Example of Weaire and Phelan*. Phil. Mag. Let. 69: 297-303.
- Rogers, T. and J. Sampson (1977). *Computer Simulations of Surface Tensions in Cellular Aggregates*. Int. J. Biomed. Comp. 8: 45-60.
- Rogers, G. and N. Goel (1978). *Computer Simulation of Cell Movements: Cell-Sorting, Cellular Migration Through a Mass of Cells and Contact Inhibition*. J. Theor. Biol. 71: 141-166.
- Rogers, J. R., J. P. Downey, W. K. Witherow, B. R. Facemire, D. O. Frazier, V. E. Fradkov, S. S. Mani, and M. E. Glicksman (1994). *Coarsening Of 3-Dimensional Droplets By 2-Dimensional Diffusion. 1. Experiment*. J. Elec. Mat. 23: 999-1006.

- Rollett, A. D., D. J. Srolovitz, and M. P. Anderson (1989). *Simulation and Theory of Abnormal Grain Growth - Anisotropic G. B. Energies and Mobilities*. Acta Met. 37: 1227-1240.
- Rollett, A. D. (1997). *Overview of Modeling and Simulation of Recrystallization*. Prog. Mat. Sci. 42: 79-99.
- Rosa, M. E. and M. A. Fortes (1988). *Temperature-Induced Alterations of the Structure and Mechanical-Properties of Cork*. Mat. Sci. Eng. 100: 69-78.
- Rosa, M. E. and M. A. Fortes (1988). *Stress-Relaxation and Creep of Cork*. J. Mat. Sci. 23: 35-42.
- Rosa, M. E. and M. A. Fortes (1988). *Rate Effects on the Compression and Recovery of Dimensions of Cork*. J. Mat. Sci. 23: 879-885.
- Rosa, M. E., Pereira H, and M. A. Fortes (1990). *Effects of Hot Water-Treatment on the Structure and Properties of Cork*. Wood and Fiber Sci. 22: 149-164.
- Rosa, M. E. and M. A. Fortes (1991). *Deformation and Fracture of Cork in Tension*. J. Mat. Sci. 26: 341-348.
- Rosa, M. E. and M. A. Fortes (1993). *Water-Absorbtion by Cork*. Wood and Fiber Sci. 25: 339-348.
- Rosa, M. E., A. C. Diogo, and M. A. Fortes (1995). *Measurement of Foam Viscosity by Indentation*. Langmuir 11: 2329-2333.
- Rosa, M. E. and M. A. Fortes (1998). *Development of Bamboo Structure in a 2D Liquid Foam*. Europhys. Lett. 41: 577-582.

- Rosa, M. E. and M. A. Fortes (1998). *Nucleation and Glide of Dislocations in a Monodisperse 2-Dimensional Foam Under Uniaxial Deformation*. Phil. Mag. A 77: 1423-1446.
- Rubin, J. and A. Robertson. 1975. *The Tip of the Dictyostelium Discoideum Plasmodium as an Organizer*. J. Embryol. Exp. Morphol. 33: 227-241.
- Ruizgarcia, J., R. Gamezcorrales, and B. I. Ivlev (1997). *Foam and Cluster Structure Formation by Latex-Particles at the Air/Water Interface*. Physica A 236: 97-104.
- Ruskin, H. J. and Y. Feng (1995). *The Evolution of a 2-Dimensional Soap Froth With a Single Defect*. J. Phys. Condens. Matter 7: L553-L559.
- Ruskin, H. J. and Y. Feng (1996). *Scaling Properties for Ordered/Disordered 2-D Dry Froths*. Physica A 230: 455-466.
- Ruskin, H. J. and Y. Feng (1997). *A Note on Stages of Evolution in a 2d Froth*. Physica A 247: 153-158.
- Ruskin, H. J. and Y. Feng (1997). *Self-Organized Criticality in Some Dissipative Sandpile Models*. Physica A 245: 453-460.
- Rutenberg, A. D. (1996). *Stress-Free Spatial Anisotropy in Phase Ordering*. Phys. Rev. E 54: R2181-R2184.
- Sahni, P. S., G. S. Grest, *et al.* (1983). *Kinetics of the Q-State Potts Model in Two Dimensions*. Phys. Rev. Lett. 50: 263-266.
- Saltykov, S. A. (1970). *Stereometric Metallography*. Moscow, Matallurgizdat.

- Sato-Maeda, M., M. Uchida, F. Graner, and H. Tashiro (1994). *Quantitative Evaluation of Tissue-Specific Cell Adhesion at the Level of a Single Cell Pair.* Dev. Biol. 162: 77-84.
- Savill, N. and P. Hogeweg. (1997). *Modeling morphogenesis: from single cells to crawling slugs.* J. Theo. Biol. 184: 229-235.
- Saxe C. L. III, G. T. Ginsburg, J. M. Louis, R. Johnson, P. N. Devreotes and A. R. Kimmel. (1993). *CAR2, a prestalk cAMP receptor required for normal tip formation and late development of Dictyostelium discoideum.* Genes and Dev. 7: 262-272.
- Scavuzzo, C. M., M. A. Ré, and E. A. Ceppi, (1988). *A Numerical Model for Three-Dimensional Grain Boundary Migration in Bicrystals.* Scripta Met. 24: 1901-1906.
- Schulson, E. M., T. P. Weihs, I. Baker and H. J. Frost, and J. A. Horton (1986). *Grain boundary accommodation of slip in Ni<sub>3</sub>Al.* Acta Met. 34: 1395-1399.
- Schulze, G. E. W. and H.-P. Wilbert (1989). *Chord Intercepts in a Two-Dimensional Cell Growth Model. Part I.* J. Mat. Sci. 24: 3101-3106.
- Schulze, G. E. W. and H.-P. Wilbert (1989). *Chord Intercepts in a Two-Dimensional Cell Growth Model. Part II.* J. Mat. Sci. 24: 3107-3112.
- Segel, D., D. Mukamel, O. Krichevsky, J. Stavans (1993). *Selection Mechanisms and Area Distribution in Two-Dimensional Cellular Structures.* Phys. Rev. E 47: 812-819.
- Segel, D., D. Mukamel, O. Krichevsky, and J. Stavans (1993). *Selection Mechanism and Area Distribution in 2-Dimensional Cellular Structures.* Phil. Mag.

Lett. 67: 203-211.

- Selleck, M., K. Rajan, *et al.* (1990). *Organic Materials as an Experimental Model System for Grain Growth Study*. Simulation and Theory of Evolving Microstructures. eds. M. P. Anderson and A. D. Rollett. Warrendale, The Metallurgical Society: 79-86.
- Senuma, T. and H. Yada (1986). *Microstructural Evolution of Plain Carbon Steels in Multiple Hot Working*, in Annealing Processes - Recovery, Recrystallization and Grain Growth, Proceedings of the 7th Risø International Symposium on Metallurgy and Materials Science. N. Hansen, D. J. Jensen, T. Leffers and B. Ralph. Roskilde, Risø National Laboratory: 547-552.
- Seul, M. and M. J. Sammon (1990). *Competing Interactions and Domain-Shape Instabilities in a Monomolecular Film at an Air-Water-Interface*. Phys. Rev. Lett. 64: 1903-1906.
- Seul, M. and R. Wolfe (1992). *Evolution of Disorder in Magnetic Stripe Domains .1. Transverse Instabilities and Disclination Unbinding in Lamellar Patterns*. Phys. Rev. A 46: 7519-7533.
- Seul, M and C. A. Murray (1993). *Scale Transformation of Magnetic “Bubble” Arrays: Coupling of Topological Disorder and Polydispersity*. Science 262: 558-560.
- Seul, M. (1994). *Dislocation-Mediated Period Adaptation in Magnetic-Bubble Arrays*. J. Physique I 4: 319-334.
- Shackleford, J. F. (1982). *Triangle Rafts-Extended Zachariasen Schematics for Structure Modeling*. J. Non-Crystalline Solids 49: 19-28.

- Shaulsky, G., A. Kuspa and W. F. Loomis. (1995). *A Multidrug Resistance Transporter/Serine Protease Gene is Required for Prestalk Specialization in Dictyostelium*. Genes & Dev. 9: 1111-1122.
- Siegert, F. and C. J. Weijer. (1995). *Spiral and Concentric Waves Organize Multicellular Dictyostelium Discoideum*. Curr. Biol. 5: 937-943.
- Simpson, C. J., K. T. Aust, et al. (1971). *Activation Energies for Normal Grain Growth in Lead and Cadmium Base Alloy*. Met. Trans. 2: 993-997.
- Sire, C. (1994). *Growth Laws for 3D Soap Bubbles*. Phys. Rev. Lett. 72: 420-423.
- Sire C. and S. N. Majumdar (1995). *Correlations and Coarsening in the q-State Potts-Model*. Phys. Rev. Lett. 74:4321-4324.
- Sire C. and S. N. Majumdar (1995). *Coarsening in the q-State Potts-Model and the Ising-Model With Globally Conserved Magnetization*. Phys. Rev. E 52: 244-254.
- Siu, C., B. D. Roches, and T. Y. Lam. (1983). Involvement of a Cell-Surface Glycoprotein in the Cell-Sorting Process of *Dictyostelium Discoideum*. Proc. Natl. Acad. Sci. 80: 6596-6600.
- Smith, C. S. (1952). *Grain Shapes and Other Metallurgical Applications of Topology*. Metal Interfaces. Cleveland, American Society for Metals: 65-108.
- Smith, C. S. (1954). *The Shape of Things*. Sci. Am. 190: 58-64.
- Smith, C. S. (1964). *Structure, Substructure and Superstructure*. Rev. Mod. Phys. 36: 524-532.

- Smith, C. S. (1964). *Some Elementary Principle of Polycrystalline Microstructure*. Met. Rev. 9: 1-48.
- Soares, A., A. C. Ferro, et al. (1985). *Computer Simulation of Grain Growth in a Bidimensional Polycrystal*. Scripta Met. 19: 1491-1496.
- Soliman, S. E., N. Hansen, et al. (1986). *Isothermal Grain-Growth Kinetics in UO<sub>2</sub>*, in Annealing Processes - Recovery, Recrystallization and Grain Growth, Proceedings of the 7th Risø International Symposium on Metallurgy and Materials Science. N. Hansen, D. J. Jensen, T. Leffers and B. Ralph, Risø National Laboratory. Roskilde: 553-560.
- Soll, D., D. Wessels, and A. Sylvester. 1993. *The Motile Behavior of Amoebae in the Aggregation Wave in Dictyostelium Discoideum*, in *Experimental and Theoretical Advances in Biological Pattern Formation*, ed. H. G. Othmer, P. K. Maini and J. D. Murray. London, Plenum: 325-338.
- Sollich, P. F. Lequeux, P. Hébraud, and M. E. Cates (1997). *Rheology of Soft Glassy Materials*. Phys. Rev. Lett. 78: 2020-2023.
- Sornette, D. (1987). *Undulational Instability in Stripe Domain Structures of "Bubble" Material*. J. Phys. (Paris) 48: 151-165.
- Souèges, R. (1923). *Embryogénie des Géraniacées. Développement de l'embryon chez le Geranium molle L.* C. R. Acad. Sci. 177: 556-558.
- Sperry, R. (1963). *Chemoaffinity in the Orderly Growth of Nerve Fiber Patterns and Connections*. Proc. Natl. Acad. Sci. USA 50: 703-710.
- Springer, T. (1990). *Adhesion Receptors of the Immune System*. Nature 346: 425-434.

- Spry, A. (1961). *The Origin of Columnar Jointing, Particularly in Basalt Flows*. J. Geol. Soc. Australia 8: 191-216.
- Srolovitz, D. J., M. P. Anderson, *et al.* (1983). *Grain Growth in Two Dimensions*. Scripta Met. 17: 241-246.
- Srolovitz, D. J., M. P. Anderson, *et al.* (1984). *Computer Simulation of Grain Growth-III. Influence of Particle Dispersion*. Acta Met. 32: 1429-1438.
- Srolovitz, D. J., M. P. Anderson, *et al.* (1984). *Computer Simulation of Grain Growth-II. Grain Size Distribution, Topology and Local Dynamics*. Acta Met. 32: 793-802.
- Srolovitz, D. J., G. S. Grest, and M. P. Anderson (1985). *Computer Simulation of Grain Growth-V. Abnormal Grain Growth*. Acta Met. 33: 2233-2247.
- Srolovitz, D. J. (1986). *Grain Growth Phenomena in Films: A Monte Carlo Approach*. J. Vac. Sci. Technol. A 4: 2925-2931.
- Stavans, J. and J. A. Glazier (1989). *The Soap Froth Revisited: Dynamic Scaling in the Two-Dimensional Froth*. Phys. Rev. Lett. 62: 1318-1321.
- Stavans, J. (1990). *Coarsening in the 2-Dimensional Soap Froth and the Large- $q$  Potts-Model : A Temporal Evolution of 2-Dimensional Drained Soap Froths*. Phys. Rev. A 42: 5049-5051.
- Stavans, J., E. Domany, and D. Mukamel (1991). *Universality and Pattern Selection in 2-Dimensional Cellular Structures*. Europhys. Lett. 15: 479-484.
- Stavans, J. (1993). *Evolution of 2-Dimensional Cellular Structures : the Soap Froth*. Physica A 194: 307-314.

- Stavans, J. (1993). *The Evolution of Cellular Structures*. Rep. Prog. Phys. 56: 733-789.
- Steiner, U., A. Meller, and J. Stavans (1995). *Entropy-Driven Phase-Separation in Binary Emulsions*. Phys. Rev. Lett. 74: 4750-4753.
- Steinberg, M. S. (1962). *On the Mechanisms of Tissue Reconstruction by Dissociated Cells. I. Population Kinetics, Differential Adhesiveness, and the Absence of Directed Migration*. Proc. Nat. Acad. Sci. USA 48: 1577-1582.
- Steinberg, M. S. (1963). *Reconstruction of Tissues by Dissociated Cells*. Science 141: 401-408.
- Steinberg, M. S. (1964). *The Problem of Adhesive Selectivity in Cellular Interactions. Cellular Membranes in Development*. ed. M. Locke. New York, Academic Press: 321-366.
- Steinberg, M. S. (1970). *Does Differential Adhesion Govern Self-Assembly Processes in Histogenesis? Equilibrium Configurations and the Emergence of a Hierarchy Among Populations of Embryonic Cells*. J. Exp. Zool. 173: 395-434.
- Steinberg, M. S. (1975). *Adhesion-Guided Multicellular Assembly: A Commentary Upon the Postulates, Real and Imagined, of the Differential Adhesion Hypothesis, With Special Attention to Computer Simulations of Cell-Sorting*. J. Theor. Biol. 55: 431-443.
- Steinberg, M. S. and D. R. Garrod (1975). *Observations on the Sorting-Out of Embryonic Cells in Monolayer Culture*. J. Cell Sci. 18: 385-403.
- Sternfeld, J. and C. N. David. 1981. *Cell sorting during pattern formation in Dictyostelium*. Differentiation 20: 10-21.

- Stevens, P. S. (1974). *Patterns in Nature*. Boston, Atlantic Monthly Press.
- Stewart, I. (1998). *Mathematical Recreations*. Sci. Am. (Jan.): 104-104.
- Stine, K. J., S. A. Rauseo, and B. G. Moore (1990). *Evolution of Foam Structures in Langmuir Monolayers of Pentadecanoic Acid*. Phys. Rev. A 41: 6884-6892.
- Stine, K. J., C. M. Knobler, and R. C. Desai (1991). *Buckling Instability In Monolayer Network Structures*. Phys. Rev. Lett. 65: 1004-1007.
- Sudo, S. H. Hashimoto, and K. Katagiri (1990). *Dynamics of Magnetic Fluid Foam*. J. Magnetism & Magnetic Mat. 85: 159-162.
- Sulsky, D., S. Childress, and J. Percus (1984). *A Model of Cell Sorting*. J. Theor. Biol. 106: 275-301.
- Swiler, T. P., V. Tikare, and E. A. Holm (1997). *Heterogeneous Diffusion Effects in Polycrystalline Microstructures*. Mat. Sci. & Eng. A. 238: 85-93.
- Szekely, J. (1993). *The Smart Way to Make Materials*. Technology Rev. 96: 39-44.
- Szeto, K. Y. and W. Y. Tam (1995). *Lewis Law Versus Felthams Law in Soap Froth*. Physica A 221: 256-262.
- Szeto, K. Y. and W. Y. Tam (1996). *Universal Topological Properties of Shells in Soap Froth*. Phys. Rev. E 53: 4213-4216.
- Szymczak, R., K. Piotrowski, and A. Szewczyk (1982). *Domain Structure in Garnet Films Near the Phase Transition From the Homogeneous State to the Domain State*. Physica B 113: 113-117.

- Tajika, M., H. Matsubara, and W. Rafaniello (1997). *Experimental and Computational Study of Grain Growth in AlN Based Ceramics*. J. Ceramic Soc. Jpn. 105: 928-933.
- Takeichi, M. (1990). *Cadherins: A Molecular Family Important in Selective Cell-Cell Adhesion*. Ann. Rev. Biochem. 59: 237-252.
- Takeichi, M. (1991). *Cadherin Cell Adhesion Receptors as a Morphogenetic Regulator*. Science 251: 1451-1455.
- Takeuchi, I., T. Kakutani, and M. Tasaka. 1988. *Cell Behavior During Formation of Prestalk/Prespore Pattern in Submerged Agglomerates of Dictyostelium Discoideum*. Devel. Genetics 9: 607-614.
- Talbot, C. J. and M. D. A. Jackson (1987). *Salt Tectonics*. Sci. Am. 257: 70-79.
- Tam, W. Y. and K. Y. Szeto (1996). *Evolution of Soap Froth Under Temperature Effects*. Phys. Rev. E 53: 877-880.
- Tam, W. Y., R. Zeitak, K. Y. Szeto, and J. Stavas (1997). *First-Passage Exponent in 2-Dimensional Soap Froth*. Phys. Rev. Lett. 78: 1588-1591.
- Tanemura, M., T. Ogawa, et al. (1983). *A New Algorithm for Three-Dimensional Voronoi Tessellation*. J. Comput. Phys. 51: 191-207.
- Tasaka, M. and I. Takeuchi. 1981. *Role of Cell Sorting in Pattern Formation in Dictyostelium Discoideum*. Differentiation 18: 191-196.
- Taylor, J. E., J. W. Cahn, and C. A. Handwerker (1992). *Geometric 1. Models of Crystal-Growth*. Acta Met. 40: 1443-1474.

- Tolley, H., T. M. Leibling, *et al.* (1986). *Simulation of Grain Growth in 2-Dimensions: Influence of the Energy Expression for the Grain Boundary Network*. Annealing Processes— Recovery, Recrystallization and Grain Growth, Proceedings of the 7th Risø International Symposium on Metallurgy and Materials Science. N. Hansen, D. J. Jensen, T. Leffers and B. Ralph. Roskilde, Risø National Laboratory: 573-578.
- Tolley, H., T. M. Liebling, and A. Mocellin (1996). *The Laguerre Model of Grain-Growth in 2 Dimensions .1. Cellular Structures Viewed as Dynamical Laguerre Tessellations*. Phil. Mag. B 73: 395-408.
- Thiele, A. A. (1969). *The Theory of Cylindrical Magnetic Domains*. Bell Tech. J. 48: 3287-3335.
- Thiele, A. A., A. H. Bobeck, *et al.* (1971). *The Energy and General Translation Force of Cylindrical Magnetic Domains*. Bell Tech. J. 50: 711-724.
- Thiele, A. A. (1971). *Device Implications of the Theory of Cylindrical Magnetic Domains*. Bell Tech. J. 50: 725-773.
- Thomas, W. A. and J. Yancey (1988). *Can Retinal Adhesion Mechanisms Determine Cell-Sorting Patterns: A Test of the Differential Adhesion Hypothesis*. Development 103: 37-48.
- Thomas, P. D., R. C. Darton, and P. B. Whalley (1998). *Resolving the Structure of Cellular Foams by the use of Optical Tomography*. Industrial & Eng. Chem. Res. 37: 710-717.
- Thompson, C. V. (1985). *Secondary Grain Growth in Thin Films of Semiconductors: Theoretical Aspects*. J. Appl. Phys. 58: 763-772.

- Thompson, C. V., H. J. Frost, F. Spaepen (1987). *The Relative Rates of Secondary and Normal Grain Growth*. Acta Met. 35: 887-890.
- Thompson, C. V., J. Floro, and H. I. Smith (1990). *Epitaxial Grain Growth in Thin Metal Films*. J. Appl. Phys. 67: 4099-4104.
- Thompson, C. V. (1992). *Experimental and Theoretical Aspects of Grain Growth in Thin Films*. Mat. Sci. Forum 94-96: 245-256.
- Thompson, G. S., J. M. Rickman, M. P. Harmer, and E. A. Holm (1996). *The Effects of Particle-Size Distribution and Induced Unpinning During Grain-Growth*. J. Mat. Res. 11: 1520-1527.
- Thompson, S. W. (1987). *On the Division of Space With Minimum Partitional Area*. Phil. Mag. 24: 503-514.
- Thompson, S. D. W. (1942). *On Growth and Form*. Cambridge, England, Cambridge University Press.
- Tikare, V. and J. D. Cawley (1998). *Numerical-Simulation of Grain-Growth in Liquid-Phase Sintered Materials : I : Model*. Acta Met. 46: 1333-1342.
- Tikare, V. and E. A. Holm (1998). *Simulation of Grain-Growth and Pore Migration in a Thermal-Gradient*. J. Am. Ceramic Soc. 81: 480-484.
- Traynor, D., M. Rasaka, I. Rakeuchi, and J. Williams. 1994. *Aberrant Pattern Formation in Myosin Heavy Chain Mutants of Dictyostelium*. Development 120: 591-601.
- Trembley, A. (1744). *Memoires Pour Servir l'Histoire Naturelle d'un Genre de Polypes D'eau Douce*. Leyden, Bras en Forme de Cornes.

- Trinkaus, J. P., M. Trinkaus, *et al.* (1992). *On the Convergent Cell Movements of Gastrulation in Fundulus*. *J. Exp. Zool.* 261: 40-61.
- Tseng, C. H., S. Peled, L. Nascimben, E. Oteiza, R. L. Walsworth, and F. A. Jolesz (1997). *NMR of Laser-Polarized Xe-129 in Blood Foam*. *J. Mag. Res.* 126: 79-86.
- Turing, A. (1952). *The Chemical Basis of Morphogenesis*. *Phil. Trans. Roy. Soc. Lond. B* 237: 37-72.
- Underwood, E. E. (1970). *Quantitative Stereology*. Reading, MA, Addison-Wesley.
- Varnum, B., K. B. Edwards, and D. R. Soll. 1986. *The developmental Regulation of Single-Cell Mobility in Dictyostelium Discoideum*. *Dev. Biol.* 113: 218-227.
- Vasiev, B., F. Siegert, and C. Weijer. 1997. *Multiarmed Spirals in Excitable Media*. *Phys. Rev. Lett.* 78: 2489-2492.
- Vaz, M. F., and M. A. Fortes (1988). *Grain-Size Distribution: The Lognormal and the Gamma-Distribution Functions*. *Scripta Met.* 22: 35-40.
- Vaz, M. F., A. Soures, *et al.* (1990). *Computer Simulation of Grain Growth in Non-Equiaxed Polycrystal*. *Scripta Met.* 24: 2453-2458.
- Vaz, M. F. and M. A. Fortes (1990). *The Effect of Recrystallization and Grain Growth on the Shape of Non-equiaxed Grains*. *Zeitschrift fur Metallkunde* 81: 576-580.
- Vaz, M. F. and M. A. Fortes (1993). *Characterization of Deformation Bands in the Compression of Cellular Materials*. *J. Mat. Sci. Lett.* 12: 1408-1410.

- Vaz, M. F., L. Faria, and M. A. Fortes (1995). *Initiation and Propagation of Cell Collapse in Dynamic Compression of Cellular Materials*. Int. J. Impact Eng. 16: 253-271.
- Vaz, M. F. and M. A. Fortes (1997). *Experiments on Defect Spreading in Hexagonal Foams*. J. Phys. Condens. Matter 9: 8921-8935.
- Vaz, M. F. and M. A. Fortes (1998). *Friction Properties of Cork*. J. Mat. Sci. 33: 2087-2093.
- Verbist, G. and D. Weaire (1994). *A Soluble Model for Foam Drainage*. Europhys. Lett. 26: 631-636.
- Verbist, G., D. Weaire, and A. M. Kraynik (1996). *The Foam Drainage Equation*. J. Phys. Condens. Matter 8: 3715-3731.
- Voevodskii, V. A. and G. B. Shabat (1989). *Equilateral Triangulations of Riemann Surfaces, and Curves Over Algebraic Number Fields*. Soviet Math. Dokl. 39: 38-41.
- von Neumann, J. (1952). Discussion in Metal Interfaces. Cleveland, American Society for Metals: 108-110.
- Voorhees, P. W. (1985). *The Theory of Ostwald Ripening*. J. Stat. Phys. 38: 231-252.
- Wang, B. and A. Kuspa. 1997. *Dictyostelium Development in the Absence of cAMP*. Science 277: 251-254.
- Warner, M. and R. M. Hornreich (1985). *The Stability of Quasi 2D Lattices of Magnetic Holes*. J. Phys. A 18: 2325-2341.

- Wasan, D. T., A. D. Nikolov, L. A. Lobo, K. Loczo, and D. A. Edwards. (1992). *Foams, Thin Films and Surface Rheological Properties*. Progress in Surface Science 39: 119-154.
- Weaire, D. (1974). *Some Remarks on the Arrangement of Grains in a Poly-crystal*. Metallography 7: 157-160.
- Weaire, D. and J. P. Kermode (1983). *The Evolution of the Structure of a Two-Dimensional Soap Froth*. Phil. Mag. B 47: L29-L31.
- Weaire, D. and J. P. Kermode (1983). *Computer Simulation of a Two-Dimensional Soap Froth: I. Method and Motivation*. Phil. Mag. B 48: 245-259.
- Weaire, D. and C. O'Carroll (1983). *A New Model for the Giant's Causeway*. Nature 302: 240-241.
- Weaire, D. and J. P. Kermode (1984). *Computer Simulations of a Two-Dimensional Soap Froth: II. Analysis and Results*. Phil. Mag. B 50: 379-395.
- Weaire, D. and N. Rivier (1984). *Soap, Cells and Statistics-Random Patterns in Two Dimensions*. Contemp. Phys. 25: 59-99.
- Weaire, D., J. P. Kermode, and J. Wejchert (1986). *On the Distribution of Cell Areas in a Voronoi Network*. Phil. Mag. B 53: L101-L105.
- Weaire, D. (1987). *Fizz and Froth: How the Bubbles Take the Strain*. New Scientist 116: 33-33.
- Weaire, D. (1989). *A Note on the Elastic Behavior of Ordered Hexagonal Froth*. Phil. Mag. Lett. 60: 27-30.

- Weaire, D. and H. Lei (1990). *A Note on the Statistics of the Mature 2-Dimensional Soap Froth.* Phil. Mag. Lett. 62: 427-430.
- Weaire, D. (1990). *Soap Froth Revisited : Dynamic Scaling in the 2-Dimensional Froth : Comment.* Phys. Rev. Lett. 64: 3202-3202.
- Weaire, D. and V. Pacheron (1990). *Frustrated Froth : Evolution of Foam Inhibited by an Insoluble Gaseous Component.* Phil. Mag. Lett. 62: 417-421.
- Weaire, D., F. Bolton, et al. (1991). *Investigation of an Elementary Model for Magnetic Froth.* J. Phys. Condens. Matter 3: 2101.
- Weaire, D. and J. A. Glazier (1992). *Modelling Grain Growth and Soap Froth Coarsening: Past, Present and Future.* Mat. Sci. Forum 94-96: 27-51.
- Weaire, D. (1992). *Some Lessons From Soap Froth for the Physics of Soft Condensed Matter.* Physica Scripta T45: 29-33.
- Weaire, D., S. Hutzler, and N. Pittet (1992). *Cylindrical Packing of Foam Cells.* Forma. 7: 259-263.
- Weaire, D., f. Bolton, T. Herdtle, and H. Aref (1992). *The Effect of Strain Upon the Topology of a Soap Froth.* Phil. Mag. Lett. 66: 293-299.
- Weaire, D. (1993). *On the Motion of Vertices in 2-Dimensional Grain-Growth.* Phil. Mag. Lett. 68: 93-98.
- Weaire, D. and J. A. Glazier (1993). *Relation Between Volume, Number of Faces and Three Dimensional Growth Laws in Coarsening Cellular Patterns.* Phil. Mag. Lett. 68: 363-365.
- Weaire, D., N. Pittet, and S. Hutzler (1993). *Steady-State Drainage of an Aqueous Foam.* Phys. Rev. Lett. 71: 2670-2673.

- Weaire, D. and R. Phelan (1994). *The Structure of Monodisperse Foam*. Phil. Mag. Lett. 70: 345-350.
- Weaire, D. and R. Phelan (1994). *A Counter-Example to Kelvin's Conjecture on Minimal Surfaces*. Phil. Mag. Lett. 69: 107-110.
- Weaire, D. and M. A. Fortes (1994). *Stress and Strain in Liquid and Solid Foams*. Adv. Phys. 43: 685-738.
- Weaire, D. (1995). *Evolution of 2-Dimensional Soap Froth With a Single Defect : Comment*. Phys. Rev. Lett. 74: 3710-3710.
- Weaire, D., S. Findlay, and G. Verbist (1995). *Measurement of Foam Drainage Using Ac Conductivity*. J. Phys. Condens. Matter 7: L217-222.
- Weaire, D., S. Coughlan, and A. M. Fortes (1995). *The Modeling of Liquid and Solid Foams*. J. Mat. Processing Tech. 55: 178-185.
- Weaire, D. and S. McMurry (1996). *Grain-Boundary Motion in Idealized Models*. Mat. Sci. Forum 207: 569-572.
- Weaire, D. and R. Phelan (1996). *Vertex Instabilities in Foams and Emulsions*. J. Phys. Condens. Matter 8: L37-L43.
- Weaire, D. and R. Phelan (1996). *The Physics of Foams*. J. Phys. Condens. Matter 8: 9519-9524.
- Weaire, D. and S. McMurry (1997). *Some Fundamentals of Grain-Growth*. Solid State Phys. 50: 1-36.
- Weitz, D. A., J. X. Zhu, D. J. Durian, H. Gang, and D. J. Durian (1993). *Diffusing-Wave Spectroscopy : The Technique and Some Applications*. Physica Scripta T49: 610-621.

- Wejchert, J., D. Weaire, and J. P. Kermode (1986). *Monte Carlo Simulation of the Evolution of a Two-Dimensional Soap Froth*. Phil. Mag. B 53: 15-24.
- Weliky, M. and G. Oster (1990). *The Mechanical Basis of Cell Rearrangement. I. Epithelial Morphogenesis During Fundulus Epiboly*. Development 109: 373-386.
- Weliky, M., S. Minsuk, *et al.* (1991). *Notochord morphogenesis in Xenopus laevis: simulation of cell behavior underlying tissue convergence and extension*. Development 113: 1231-1244.
- Weliky, M., S. Minsuk, *et al.* (1991). *The mechanical basis of cell rearrangement. II. Notochord morphogenesis in Xenopus laevis: simulation of cell behavior underlying tissue convergence and extension*. Development 113: 1231-1244.
- Wessels, D., H. Vawter-Hugart, J. Murray, and D. R. Soll. (1994). *Three-Dimensional Dynamics of Pseudopod Formation and the Regulation of Turning During the Motility Cycle of Dictyostelium*, Cell Motil. Cytoskel. 27: 1-12.
- Westervelt, R. M., K. L. Babcock, M. Vu, and R. Seshadri (1991). *Avalanches and Self-Organization in the Dynamics of Cellular Magnetic Domain Patterns*. J. Appl. Phys. 69: 5436-5440.
- White, P. L. and L. H. Van Vlack (1970). *A Comparison of Two- and Three-Dimensional Size Distributions in a Cellular Material*. Metallography 3: 241-258.
- Williams, J. G. (1991). *Regulation of Cellular Differentiation During Dictyostelium Morphogenesis*. Curr. Opin. Genet. Dev. 1: 338-362.

- Williams, W. M. and C. S. Smith (1952). *A Study of Grain Shape in an Aluminum Alloy and Other Applications of Stereographic Microradiography*. J. Metals 194: 755-765.
- Wilson, A. J. ed. (1989). *Foams: Physics, Chemistry and Structure* New York, Springer-Verlag.
- Wolfe, R. and J. C. North (1974). *Planar Domains in Ion-Implanted Magnetic-Bubble Garnets Revealed by Ferrofluid*. Appl. Phys. Lett. 25: 122-124.
- Wong, C. C. H. I. Smith, and C. V. Thompson (1986). *Surface Energy Driven Secondary Grain Growth in Thin Au Films*. J. Appl. Phys. 48: 335-337.
- Woolhouse, G. R. and P. Chaudhari (1974). *Two-Dimensional Lattice Simulation by Magnetic Bubbles*. Phil. Mag. 28: 161-172.
- Wray, P. J., O. Richmond, *et al.* (1983). *Use of the Dirichlet Tessellation for Characterizing and Modeling Nonregular Dispersions of Second-Phase Particles*. Metallography 16: 39-58.
- Wright, A. C., G. A. N. Connell, *et al.* (1980). *Amorphography and the Modeling of Amorphous Solid Structures by Geometric Transformations*. J. Non-Crystalline Solids 42: 69-86.
- Wright, A. C. (1982). *Basic amorphography. Coherence and Energy Transfer in Glasses*. P. A. Fleury and B. B. Golding. New York, Plenum Press: 1-38.
- Wu, F. Y. (1982). *The Potts Model*. Rev. Mod. Phys. 54: 235-267.
- Yoshimura, A. and R. K. Prud'homme (1988). *Wall Slip Corrections for Couette and Parallel Disk Viscometers*. J. Rheol. 32: 53-67.

- Yoshimura, A. and R. K. Prud'homme (1988). *Wall Slip Effects on Dynamics Oscillatory Measurements*. J. Rheol. 32: 575-584.
- Zablotzkii, V. A. Y. Mamalui, and E. N. Soika (1996). *Magnetization Curves of Disordered Cellular Domain Patterns in Thin Magnetic-Films*. Physica Status Solidi B 193: 471-475.
- Zachariasen, W. H. (1932). *The Atomic Arrangement in Glass*. J. Am. Chem. Soc. 54: 3841-3851.